6th Numerical Towing Tank Symposium

29. September - 1. October 2003

Rome/Italy

Dedicated in memoriam Maurizio Landrini († 26.6.2003)
He was the best.

Volker Bertram (Ed)

ISTITUTO NAZIONALE PER STUDI ED ESPERIENZE DI ARCHITETTURA NAVALE

Sponsored by

INSEAN

Office of
Naval Research
(Dr. Pat Purtell)

ANSYS
Germany GmbH

FLUENT
Italia

CD Adapco

INDEX OF PAPERS (in alphabetical order of first author)

Nechita, M.; Iwashita, H.
A Hybrid Method for Seakeeping Estimation of Ships

Noblesse, F.; Yang, C.
Simple Green Functions

Ohashi, K.; Hino, T.; Ukon, Y.
Flow Computations of a Ship with a Podded Propulsor

Östman, A.
Free-Surface Flow Computations for Complex Hull Shapes

Peri, D.; Campana, E.
Hydrodynamic Design Optimization using the Navier-Stokes Equations

Salui, K.B.; Shigunov, V.; Vassalos, D.
A RANS Based Prediction Method of the Ship Roll Damping with Forward Speed

Sato, Y.; Hino, T.; Hinatsu, M.
Unsteady Flow Simulation around a Moving Body by an Unstructured Navier-Stokes Solver

Schmode, D.; Jensen, G.
Towards an Adaptive Transient Cartesian Grid Method with VoF for Floating Bodies

Schweighofer, J.
Viscous-Flow Computations at Full-Scale Ship Reynolds Numbers Using the RANS Solver FINFLO

Seif, M.S.; Saddahosseini, S.W.; Mousaviraad, S.M.
Hydrofoil Performance near the Free Water Surface

Seil, G.
RANS CFD for Marine Propulsors A Rolls-Royce Perspective

Shigunov, V.
Calculation of Fire Development and Smoke Propagation in Ship Compartments

Streckwall, H.; Hympendahl, O.
Simulation of Cavitating Flows around Propellers with a RANSE Code

Werner, S.
Adaptive Multigrid for Incompressible Navier Stokes Equations

Windt, J.
Towards Accurate Wake Predictions of Twin-Screw Ships with an Open-Shaft Stern Configuration

Woodburn, P.; Gallagher, P.; Letizia, L.
Hybrid RANSE-Potential Flow Approach to Damaged Ship in Seaways

Xing-Kaeding, Y.; Jensen, G.; Peric, M.
Ship Manoeuvring in Viscous Free Surface Flow

STEADY AND UNSTEADY RANSE SIMULATIONS FOR PLANING CRAFTS

Rodrigo Azcueta, MTG Marinetechnik, Hamburg [1]

1. INTRODUCTION

For any vessel sailing at a high F_n, like power boats, the change in the boat's running attitude (sinkage, trim, heel) due to the pressure field around the hull is quite significant so that its effects influence performance to a large extent and should be taken into account.

In this work, a general approach was implemented, extending a Navier-Stokes code to couple the fluid flow with the body motions induced by the flow and/or by external forces. This allows not only to compute dynamic sinkage and trim but also to simulate the unsteady boat motions in the 6 DOF. The methodology has been applied to several dynamic cases showing that large amplitude motions including capsizing, slamming, water entry, wave-piercing and water on deck can be simulated. The robustness of this methodology is mainly due to the simplicity of tracking the vessel's motions without deforming the numerical mesh or using complicated multi-mesh strategies. The VOF method in conjunction with a moving, rigid mesh attached to the vessel and suitable boundary conditions are shown to be very robust and efficient. In this work, only the application of this methodology to planing crafts, with the additional difficulty of the extremely high Froude numbers up to $F_n = 4$, will be demonstrated.

2. NUMERICAL METHOD

To couple the fluid flow and body motions I extended the Navier-Stokes solver COMET with a *body-motion module*. COMET is a commercial code developed in Germany by ICCM GmbH, now a member of the CD Adapco Group, the developers of the well-known multi-purpose STAR-CD code.

The general idea for coupling the fluid flow with the body motions is as follows: the Navier-Stokes flow solver computes the flow around the body in the usual way, taking into account the fluid viscosity, flow turbulence and deformation of the free surface. The forces and moments acting on the body are then calculated by integrating the normal (pressure) and tangential (friction) stresses over the body surface. Following this, the body-motion module solves the equations of motion of the rigid body in the 6 DOF using the forces and moments calculated by the flow solver as input data. The motion accelerations, velocities and displacements (translations and rotations) are obtained by integrating in time. The position of the body is updated and the fluid flow is computed again for the new position. By iterating this procedure over the time, the body trajectory is obtained.

2.1 BODY-MOTION MODULE

Two orthogonal Cartesian reference systems (RS) are used: A non-rotating, non-accelerating Newtonian RS (O, X, Y, Z) which moves forward with the mean ship speed, and a body-fixed RS (G, x, y, z) with origin at G, the centre of mass of the body. The undisturbed free-surface plane always remains parallel to the XY plane of the Newtonian RS. The Z-axis points upwards. The x-axis of the body-fixed RS is directed in the main flow direction, i.e. from bow to stern, the y-axis is taken positive to starboard and the z-axis is positive upwards. The body motions are executed using a *single-grid strategy*, where a rigid, body-fixed grid moves relative to the Newtonian RS, and the fictitious flow forces due to the grid movement are automatically taken into account in the flow equations. The body-motion module is linked and run simultaneously with the flow solver and can operate and update all flow variables, boundary conditions and parameters of the numerical method.

The motion of the rigid body in the 6 DOF are determined by integrating the equations of variation of linear and angular momentum written in the form referred to G (all vector components expressed in the Newtonian RS):

$$m\ddot{\vec{X}}_G = \vec{F} \quad , \quad \overline{\overline{T}}\,\overline{\overline{I}}_G\overline{\overline{T}}^{-1}\dot{\vec{\Omega}} + \vec{\Omega} \times \overline{\overline{T}}\,\overline{\overline{I}}_G\overline{\overline{T}}^{-1}\vec{\Omega} = \vec{M}_G \tag{1}$$

where m is the body mass, $\ddot{\vec{X}}_G$ the absolute linear acceleration of G, $\vec{F}$ is the total force acting on the body, $\dot{\vec{\Omega}}$ and $\vec{\Omega}$ are the absolute angular acceleration and angular velocity, respectively, and $\vec{M}_G$ is the total moment with respect to G, $\overline{\overline{I}}_G$ is the tensor of inertia of the body about the axes of the body-fixed RS, $\overline{\overline{T}}$ is the transformation matrix from the body-fixed into the Newtonian RS.

The contributions to the total force and to the total moment acting on G are:

---

[1] azcueta@mtg-marinetechnik.de, rodrigo@azcueta.net

$$\vec{F} = \vec{F}_{flow} + \vec{W} + \vec{F}_{ext} \quad , \quad \vec{M}_G = \vec{M}_{G_{flow}} + (\vec{X}_{ext} - \vec{X}_G) \times \vec{F}_{ext} \tag{2}$$

where $\vec{F}_{flow}$ and $\vec{M}_{G_{flow}}$ are the total fluid flow force and moment determined by integrating the normal (pressure) and tangential (friction) stresses, obtained from the Navier-Stokes solver. They include the static and the dynamic components of the water and of the air flow. $\vec{W}$ is the body weight force. $\vec{F}_{ext}$ can be any external force acting on the body which one wants to introduce to simulate for instance the towing forces and moments.

The boat motions are described in each time instant by the position of its centre of gravity $\vec{X}_G$ and the body orientation given by $\overline{\overline{T}}$. Surge, sway and heave are defined in this work as the translations of G in the directions of the Newtonian RS. The angles of rotation are defined in the following order: First the rotation around the vertical axis in the Newtonian RS (yaw or leeway angle), second the rotation around the new transverse axis (pitch or trim angle), and last the rotation around the new longitudinal axis (roll or heel angle). To integrate in time the equations of motion a first-order explicit discretisation method has shown to work well and is used preferably. Instead of integrating the angular velocity $\vec{\Omega}$ to obtain the rotation angles, the new orientation of the body is found by integrating the unit vectors of the body-fixed RS, which are the columns of $\overline{\overline{T}}$. For details on the body-motion module see [1].

2.2 FLOW SOLVER

The solution method in COMET is of finite-volume-type and uses control volumes (CVs) with an arbitrary number of faces (unstructured meshes). It allows cell-wise local mesh refinement, non-matching grid blocks, and moving grids with sliding interfaces. The integration in space is of second order, based on midpoint rule integration and linear interpolation. The method is fully implicit and uses quadratic interpolation in time through three time levels.

The deformation of the free surface is computed with an *interface-capturing scheme* of VOF type (Volume Of Fluid), which has proven to be well suited for flows involving breaking waves, sprays, hull shapes with flat stern overhangs and section flare, etc. In this method, the solution domain covers both the water and air region around the hull and both fluids are considered as one effective fluid with variable properties. An additional transport equation for a void fraction of liquid is solved to determine the interface between the two fluids. The *High-Resolution-Interface-Capturing* (HRIC) discretisation scheme for convective fluxes in the void fraction equation is used to ensure the sharpness of the interface.

The solution method is of pressure-correction type and solves sequentially the linearised momentum equations, the continuity equation, the conservation equation of the void fraction, and the equations for the turbulence quantities. The linear equation systems are solved by conjugate gradient type solvers and the non-linearity of equations is accounted for by Picard iterations. The method is parallelised by domain decomposition in both space and time and is thus well suited for 3-D flow computation with free surfaces – especially when they are unsteady, as in the case of freely-floating bodies – since they require a lot of memory and computing time. For details on the flow solver see [3].

2.3 PREVIOUS APPLICATIONS AND VALIDATION

Calculations with this method including the dynamic sinkage and trim (steady-state case) were validated for the Series 60 hull and for the model of a very fat ship with a blunt bow similar to a tanker (breaking-wave computations). These two examples showed that the method works well for very tiny changes in sinkage, trim (and also heel for the drift sailing condition) as well as for very large ones. The inclusion of the dynamic sinkage and trim in the calculations improved the agreement with experiments, and thus performance prediction.

Simulations of unsteady body motions were validated for 2-D drop tests with a wedge (used for slamming investigations). Comparisons with experiments proved very good agreement for both magnitude and timing of the accelerations, velocities and motions [1]. A validation for a 3-D case was also carried out for the model of a naval combatant in head waves and 2 DOF (heave and pitch) and showed good agreement with experiments. Slamming and green water on deck were simulated as well. In all these simulations the body trajectory, velocity and accelerations are obtained from the flow forces and/or external forces acting on the body without the need for prescribing the body trajectory.

The method has also been extensively applied to the steady flow around sailing yachts and for the simulation of the yachts responses to incident waves coming from any direction [2]. Furthermore, investigations of the dynamics of very large container vessels (up to 360 m length) sailing in extremely shallow water have been carried out (results to be published).

2.4 NUMERICAL MESH AND SIMULATION SET-UP

The model used for this investigations is a 1/4-scale model of a personal watercraft used for extensive studies in the towing tank of Osaka Prefecture University, [4]. Its main dimensions are shown in Table I and its body plan in Figure 1.

Four grids of different resolutions and size of computational domain were used to assess the influence of these parameters.

Table I. Model data

length L_{oa}	0.625 m	breath B	0.250 m
length L_{pp}	0.600 m	draft d	0.059 m
depth D	0.106 m	mass m	4.28 kg
deadrise β	22°		
KG	0.111 m	LCG-transom	0.285 m

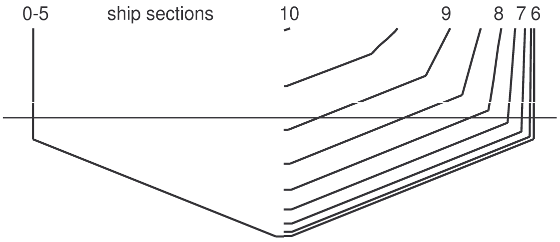

Figure 1. Body plan of planing craft model

The grids were generated using the ICEM-CFD Hexa mesh generator. The coarsest grid had around 95 000 and the finest one 230 000 CVs for one boat side (symmetry plane at the centre-line plane). Even the finest grid is still a bit too coarse in front of the model, in the wake and in transversal direction. Good resolution is achieved around the hull and in free-surface region. The differences in forces and motions as computed on the three grids were not very large, so that in the following only the results for the finest grid will be presented. The computational domain for the finest grid extends for about $1.5\,L_{oa}$ in front of the bow, $3.75\,L_{oa}$ behind the transom, $0.65\,L_{oa}$ above deck, $1.9\,L_{oa}$ below the keel and $1.9\,L_{oa}$ to the side. The mesh has such a large domain, specially above the deck, to allow large pitch motions in head waves. The CVs are mainly aligned to a water plane taking into account an average trim angle of $4.0°$. Figure 2 shows the mesh around the hull viewed from the side and slightly from the front and below and Figure 3 shows the mesh on the hull and a transverse mesh surface viewed from the front. The mesh shown in the figures is the second finest. The finest grid was obtained after a local mesh refinement in longitudinal direction in front of the model. This refinement was necessary to avoid numerical problems with the incident waves due to highly stretched cells in longitudinal direction.

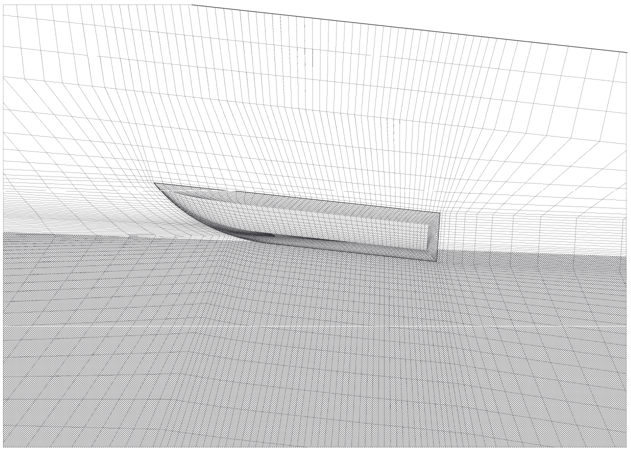

Figure 2. Numerical mesh around hull viewed from the side

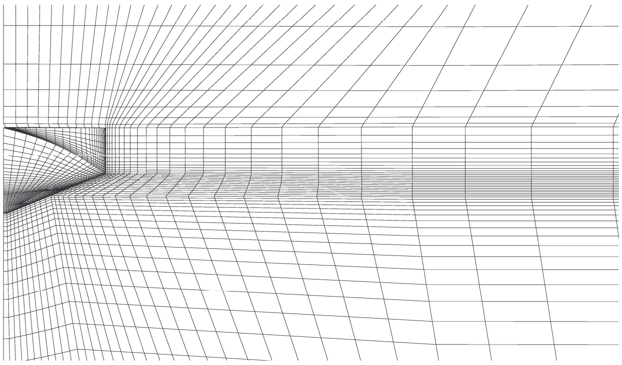

Figure 3. Numerical mesh around hull viewed from the front

The pitch radius of gyration, not known from the experiments, was estimated to be $k_{y_G} = 0.2\,L_{oa}$. The front, side, bottom and top flow-boundaries were specified as an inlet of constant known velocity (boat speed in opposite direction plus orbital velocity of the incoming waves) and known void fraction distribution defining the water and air regions (wave elevation). The wake flow-boundary was specified as a zero-gradient boundary of known pressure distribution (hydrostatic pressure). All calculations were performed using the standard k-ϵ turbulence model with wall functions ($R_n : 1.8\cdot10^6$ to $5.6\cdot10^6$).

3. RESISTANCE TESTS

RANSE computations are usually carried out for a given boat speed at a time and then repeated for as many speeds as are of interest. Here, a different approach is used: the entire resistance curve is computed in one single run. To achieve this, the boat, starting from the position at rest or sailing at a low constant speed, accelerates very slowly until it reaches the maximum boat speed expected. Since the acceleration is small and the flow basically converges for each instant boat speed, the calculation can be considered to be quasi-steady. Note that although the flow is steady once converged, since the free surface has to develop its final wave pattern, the computations (single-speed or accelerating) have to be carried out iterating in time, i.e. solving the transient terms of the flow equations.

Figure 4 shows the resistance test computed accelerating the boat from 2 m/s to 9 m/s (F_n-range from 0.8 to 4.04). The solid line represents the resistance curve. As mentioned earlier, a very important feature of these computations is that the dynamic sinkage and trim are computed throughout the entire F_n-range. These curves are given in Figure 4 as well (dashed and dotted lines respectively). The fat dots also shown in Figure 4 represent the results for the single-speed runs for $v_o = 2, 3, 4, 5, 6, 7, 8, 9$ and 10 m/s. The agreement with the resistance test calculation is good with exception of the trim angle for $F_n = 1.2$ (3 m/s).

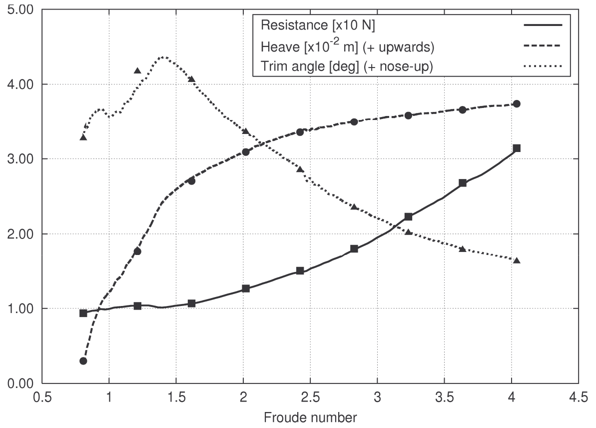

Figure 4. Numerical resistance test and computations at constant speeds

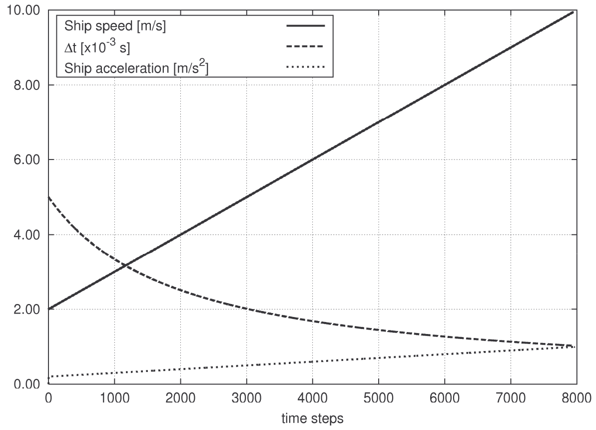

Figure 5. Curve shapes for boat speed, acceleration and Δt

The CPU time needed for computing the resistance curve over the entire F_n-range is obviously greater than when computing only one boat speed, but it pays off if many boat speeds are to be computed. 25 hrs CPU on linux cluster using 3 AMD 2000+ processors were needed to simulate the resistance curve of Figure 4. The CPU time for computing one single speed was about 8 hrs using one AMD 2000+ processor (1,000 time steps). That means that about 10 single speeds could have been computed in the time needed to compute the whole resistance curve. The resistance curve for the entire F_n-range was computed performing 8,000 time steps, cf. Figure 5, and since for each time step the boat speed has changed, 8,000 different boat speeds were computed.

One important issue to take into account when performing these kind of resistance tests is to ensure that a constant *Courant Number* $c = v\Delta t/\Delta x$ is used for the entire F_n-range. A value of $c < 0.5$ seems to be appropriate. The Courant Number is the ratio of the time step size Δt to the characteristic convection time, $v/\Delta x$, the time required for a disturbance to be convected a distance Δx. Since the mesh resolution giving Δx remains unchanged for the entire F_n-range and v is changing (the boat accelerates), Δt should the suited accordingly. This is achieved in these computations by setting $\Delta t = \Delta x_o/v$ or a minimum value for Δt when v tends to zero. Here Δx_o is a characteristic CV length, which is given as input at the beginning of the simulation.

The next issue to consider is that if a constant acceleration is used, in the high speed range where a small Δt is required, the boat's speed would change very slowly requiring too many time steps to reach the desired maximum speed. This is solved by gradually increasing the acceleration with increasing speed. The resulting curve shapes for Δt, acceleration and boat speed are given in Figure 5 as a function of the time step.

If the boat acceleration is small enough, the additional forces due to the added mass are negligible. In that case the single-speed run and the numerical resistance test will yield the same results for a given speed, as is confirmed in Figure 4 with the exception of the trim angle for 3 m/s. Furthermore, the same results should be obtained if the boat were decelerating from maximum to minimum speed. This test was also performed using inverted function shapes for acceleration and Δt. The results of the resistance test in 'decelerating mode' overlap with the lines in Figure 4 with exception of a small F_n-range between 0.8 and 1.4.

4. BOAT IN INCIDENT WAVES

This work is based on prior simulations of ship responses to incident waves coming from different directions. However, F_n in the prior simulations was moderate ($F_n < 0.5$). The obtained results were quite encouraging; some results could be successfully validated with model tests and others, for which no model tests were available, showed plausible qualitative results. Large amplitude motions including capsizing were simulated, [2]. Also the occurrence of slamming and water on deck was simulated and animated by video sequences.

The challenge the present simulations constitute, however, results from the high F_n, which introduces numerical difficulties in the generation of the incident waves, since the mean flow velocity due to the boat forward speed is 2 to 3 orders of magnitude larger than the orbital velocity of the waves. Special care is to be taken in the selection of aspect ratios of CVs to avoid non-physical wave irregularities.

The incident waves are generated at the inlet flow-boundary by imposing the instantaneous wave elevation and orbital velocities according to the linear wave theory. The orbital velocities of the waves are thus superimposed on the mean flow velocity. Three wave parameters are set at the beginning of a simulation: The wave amplitude ζ_w, the wave length λ_w and the wave direction μ relative to the boat course ($\mu = 0°$ means from astern and $\mu = 90°$ from port). Due to numerical diffusion the wave amplitude hitting the boat is reduced to some extent, although the used VOF method produces surprisingly good results on relatively coarse meshes.

Figure 6 shows a snap-shot during a simulation at an instant when the boat is completely in the air after jumping in an oblique wave. The figure shows the edges of the computational domain. Also shown is the cut of the computational domain with the undisturbed waterplane. In the single-grid strategy used in these simulations, the computational domain moves as a whole relative to this plane. The boundary conditions – the mean flow velocity, the orbital velocity, the void fraction distribution defining the wave elevations, the turbulence parameters and so on – have to be very carefully imposed at each time instant relative to the undisturbed waterplane. The VOF method and the implemented boundary conditions have proven to be very robust, since the free surface can leave the computational domain in any place, i.e. through the top flow-boundary in case that the boat heels or pitches with a large angle. Even the simulation of capsizing upside down is possible.

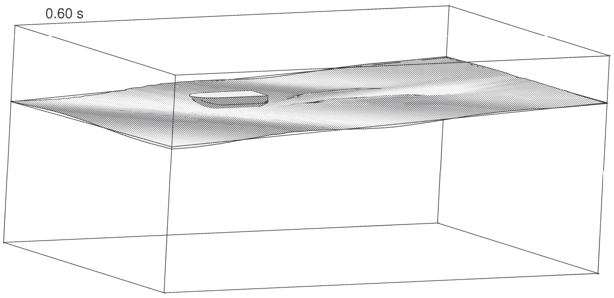

Figure 6. Power boat model jumping in oblique waves at 9 m/s

4.1 VALIDATION OF MOTIONS

Figures 7 and 8 show the motions and forces for the boat sailing at 9 m/s in head waves of 0.02 m height and 3.5 m length. Shown is also the start of the simulation: since the wave length is large in this case and the motions highly damped the motions are already periodic after 3 to 4 periods. These simulation were performed over 4,000 time steps with a time-step size $\Delta t = 0.0005$ s and 5 iterations per time step. The CPU time needed for this simulation was 33 hours on one AMD 2000+ processor or 8.5 hrs on 4 processors.

The time histories of motions and forces shown in the last figures are typical for all the simulations. However, depending on boat speed and the ratios of wave length to boat length and wave height to boat draft, the motions show sinusoidal character, not-sinusoidal periodical character with motion periods of 1, 2 or 3 times the wave encounter period, or even chaotic non-periodic character. Above certain boat speed and wave steepness the boat jumps completely out of the water. Simulations in oblique waves including the roll angle and in head waves with the boat free to surge in the waves assuming a constant drive force were also performed but will not be presented here due to lack of space.

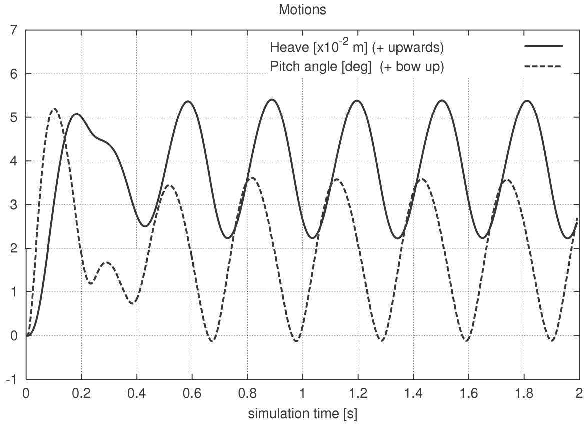

Figure 7. Motions for $F_n = 3.6$, $\mu = 180°$, $H_w = 0.02$ m and $\lambda_w = 3.5$ m. ($T_e = 0.309$ s)

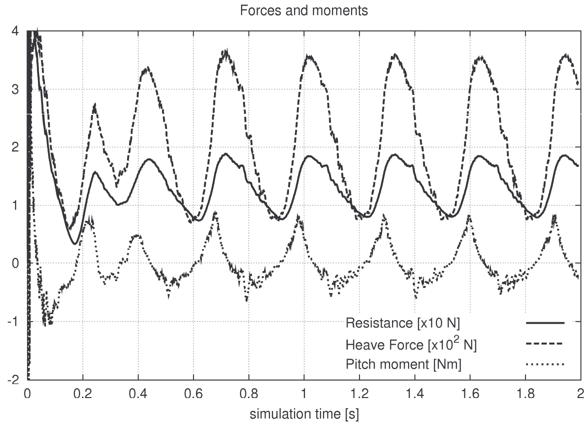

Figure 8. Forces and moments for $F_n = 3.6$, $\mu = 180°$, $H_w = 0.02$ m and $\lambda_w = 3.5$ m

The results of these simulations are compared with experiments by *Katayama et al.* [4] performed at the towing tank of the Osaka Prefecture University and with computations by *Söding* [5] based on an extension of Wagner's theory. Figures 9 and 10 show respectively the non-dimensional heave and pitch for the boat sailing at 9 m/s ($F_n = 3.6$) in head waves of 0.02 m height for varying wave lengths. The heave, measured at the centre of mass of the model G, was made non-dimensional by dividing the maximum minus the minimum heave amplitude $\zeta_{max} - \zeta_{min}$ by the wave height $H_w = 2\zeta_w$. The pitch angle was made non-dimensional by dividing the maximum minus the minimum pitch angle $\theta_{max} - \theta_{min}$ by the (linear) wave slope double amplitude kH_w where k is the wave number. In all the simulations of Figures 9 and 10, since the waves are relatively long and flat, the responses are periodic with the wave encounter period. The comparison shows in general a slight improvement in prediction by the RANSE simulations compared to the Wagner-type method although both fail to predict the peak motion by $\lambda_w/L_{oa} = 5.6$.

Sources for uncertainties in these simulations of motions in waves are the guessed pitch radius of gyration and the reduction in wave height encountered by the boat due to numerical diffusion. The latter tends to reduce the predicted non-dimensional values. On the other side, to perform experiments at such high speeds with a quite small model represents in principle a big challenge. Difficulties arise for measuring small angles and displacements, for producing regular waves in the tank and for measuring transient motions – which depend to some extent on the initial conditions – in a very short period of time. The latter also apply to the simulations, since the motions responses may i.e. switch from single-period to double-period of wave encounter after a time span which is too large for RANSE simulations. In this case the motion amplitude would change substantially. All these aspect may be deteriorating the agreement of results.

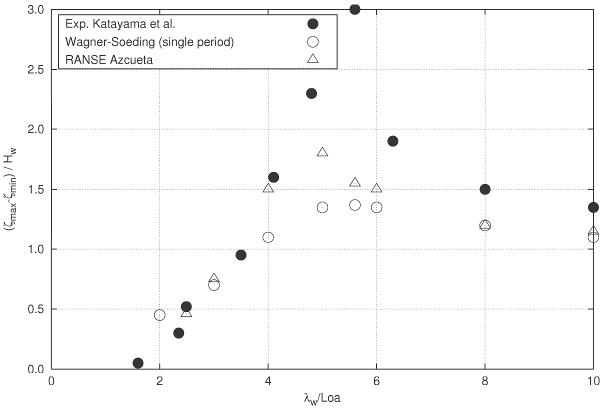

Figure 9. Non-dimensional heave over non-dimensional wave length for $H_w = 0.02$ m and $F_n = 3.6$

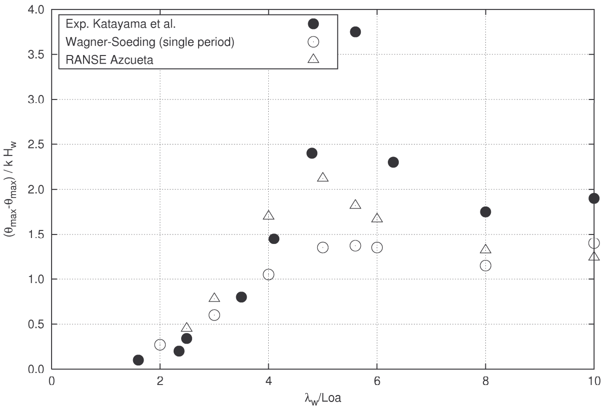

Figure 10. Non-dimensional pitch over non-dimensional wave length for $H_w = 0.02$ m and $F_n = 3.6$

References

[1] Azcueta, R., *"Computation of Turbulent Free-Surface Flows Around Ships and Floating Bodies"*, PhD. thesis, Technical University Hamburg-Harburg, 2001.

[2] Azcueta, R., *"RANSE simulations for sailing yachts including dynamic sinkage & trim and unsteady motions in waves"*, High Performance Yacht Design Conference Auckland, 2002.

[3] Ferziger, J. H. & Perić, M., *Computational Methods for Fluid Dynamics*, Springer, Berlin, 1996.

[4] Katayama, T., Hinami, T. & Ikeda, Y., "Longitudinal motion of a super high-speed planing craft in regular head waves", *4th Osaka Colloquium on Seakeeping Performance of Ships*, 2000.

[5] Caponnetto, M., Söding, H. & Azcueta, R., "Motion Simulations for Planing Boats in Waves", *Ship Technology Research*, to be published 2003.

Unsteady nonlinear flows around submerged body in water of finite depth

Malick Ba[1], Alain Rebeyrotte[1] and Michel Guilbaud[2]
Laboratoire d'Etudes Aérodynamiques (UMR CNRS n°6609)
[1]ENSMA, 1 rue C. Ader, BP 40109, 86960 Futuroscope Chasseneuil Cedex, France
Tel.: 33-5-49-49-80-87; Fax: 33-5-49-49-80-89; e-mail: ba@lea.ensma.fr
[2]CEAT-University of Poitiers, 43 rue de l'Aérodrome, 86036 Poitiers, France
Tel.: 33-5-49-36-60-27; Fax: 33-5-49-36-60-01; e-mail michel.guilbaud@lea.univ-poitiers.fr

Introduction

Behaviour of bodies in waves is often calculated by inviscid methods, fully able to represent the wave pattern. Linear calculations are limited to weak values of wave amplitudes in seakeeping computations, giving results limited to fatigue calculations in ship design. In order to extend the validity of the method to high values of wave amplitudes to predict the behaviour of ship in such seas, non linear calculations are required. In this case, Rankine methods enable to satisfy non linear free surface boundary conditions. For steady calculations, an iterative process has been often chosen, to satisfy the non linear free surface boundary conditions, Raven [1] or Scullen [2]. The full and direct resolution of the time dependent problem has been introduced by Longuet-Higgins and Cokelet [3], using a mixed Euler-Lagrange method to solve the problem of 2D wave propagation. It is based on two parts, an Eulerian one, where a linear problem has to be solved to obtain the strengths of the singularities used to represent the free surface and the body. In the second part, the Lagrangian one, it is necessary to follow the particles paths by integrating, with respect to time, the two non linear free surface boundary conditions, to update the potential and the free surface elevation. This method has been applied for 2D flows by Clément [4] and in 2D and 3D flows by Berkvens and Zandbergen [5], Berkvens [6] for freely floating or oscillating bodies, by Dommermuth and Yue [7] or Ferrant [8] in 3D flows. One of the key points is in the choice of a stable and accurate stepping technique to integrate the free surface boundary conditions. In [3], the authors use a predictor-corrector integration scheme of the Adams-Bashford-Moulton type but saw-toothed instabilities appear; they can be suppressed by a smoothing function. Park and Troesch [9] have studied the stability of the time integrations and have shown that they are depending on the geometry and of the technique used; 3D problems seem to be more stable than 2D ones. They conclude that the Euler explicit schemes were unconditionally unstable while the implicit scheme and Runge-Kutta one are stable.

In order to avoid the numerical difficulties due to singular integrals in panel method, some authors have proposed a method of desingularization (Webster [10], Schultz and Hong [11], Cao et al. [12]), that is to say putting the singularities slightly outside of the fluid domain. To reduce the CPU time, it had been shown [12] that the source distribution can be replaced by point sources without loss of accuracy. Cao et al. [12] and Lalli [13] have proposed simple formulas to calculate the desingularisation distance.

In the present paper, we use a Rankine panel method to study the 3D time dependent fully non linear flow of a submerged body moving under the free surface of an inviscid fluid, with finite or infinite water height. A Mixed Euler-Lagrange (MEL) method is used with desingularized sources above the free surface, following [13] for the desingularised distance; the body is discretised using source distributed panels. The results are compared with various linear and non linear methods available. The influence of the presence of a bottom at finite distance is investigated.

Problem to solve

We consider an incompressible and inviscid fluid, and an irrotational flow. The body motion can have unsteady velocity and direction. We use a frame of reference *Oxyz* fitted to the body. The water depth is either finite or infinite. In the fluid domain, the continuity equation together with the irrotational condition enables to use the perturbation velocity potential $\phi(x,y,z,t)$ which must satisfy the Laplace equation. The velocity is given by $\vec{V} = -\vec{U}(t) + \vec{\nabla}\phi$. One boundary condition is the condition of non perturbation at infinite distance of the body. The body condition can be written as:

$$\vec{V}\cdot\vec{n} = 0 \Leftrightarrow \vec{\nabla}\phi\cdot\vec{n} = \frac{\partial\phi}{\partial n} = \vec{U}(t)\cdot\vec{n} \tag{1}$$

where $\vec{U}(t)$ is the known body velocity and $\vec{n}$ the unit outer normal to the body. A similar condition has to be written on the bottom if it is located at finite depth. The cinematic free surface condition can be written as:

$$\frac{D\vec{X}}{Dt} = \vec{\nabla}\phi - \vec{U}(t) \tag{2}$$

where D/Dt is the material derivative and $\vec{X}(x,y,\eta)$ is the position vector of the points on the free surface. η is the free surface elevation. For the dynamic condition, we obtain:

$$\frac{D\phi}{Dt} = -g\eta + \frac{1}{2}\vec{\nabla}\phi \cdot \vec{\nabla}\phi \qquad \text{on } z = \eta \tag{3}$$

Initial conditions has to be added: η=0 and ϕ=0 (in the whole domain) for $t \le 0$.

Method of resolution

Gridding

In order to use Rankine singularities, the free surface Γ_{fs} and the body Γ_b are discretised by quadrilateral panels. For the free surface, desingularised point sources located above the nodes of these panels are used. The singularities are moved vertically with a distance Ld above the free surface. This distance is a function of the free surface grid and has been calculated in [13] in order to lead to a minimum error for the numerical solution of a wave propagation problem, the analytical solution of it being known; this distance is given by: $Ld = k \cdot \Delta x^{\mu} \cdot \Delta y^{\nu}$, (4)

with k=0.969, μ=0.294 and ν=0.016. Δx and Δy are the panel dimensions. The collocation points will be the nodes. The body is gridded with quadrilateral panels everywhere except close to the ends where triangular panels are used. The collocation points are the centres of gravity of the panels, the source strength σ_{X_s} being considered as constant on each elementary panel. Consequently, the free surface boundary conditions can be written as:

a) Dirichlet condition on the free surface $\forall X_i \in \Gamma_{fs}$; i=1, np

$$\sum_{j=1}^{np} \sigma_{Xs_j} \frac{1}{\left|X_i - Xs_j\right|} + \sum_{k=1}^{nc} \sigma_{Xs_k} \iint_{\Gamma_{b_k}} \frac{1}{\left|X_i - Xs_k\right|} d\Gamma_b = \Phi_0(X_i) \tag{5}$$

where Xs_j are the *np* desingularized sources on the free surface and Xs_k the *nc* centers of gravity of the panels on the body Γ_b. Φ_0 is the known potential on the free surface.

b) Neumann condition on the body $\forall X_l \in \Gamma_b$; l=1, nc

$$\sum_{j=1}^{np} \sigma_{Xs_j} \frac{(X_l - Xs_j)\cdot\vec{n}_{X_l}}{\left|X_l - Xs_j\right|^3} + \sum_{k=1}^{nc} \sigma_{Xs_k} \iint_{\Gamma_{b_k}} \frac{(X_l - Xs_k)\cdot\vec{n}_{X_l}}{\left|X_l - Xs_k\right|^3} d\Gamma_b = \vec{U}(t)\cdot\vec{n}_{X_l} \tag{6}$$

with $\vec{n}_{X_l}$ are for the *nc* outer unit normals of the body at the panel with center X_l.

We then obtain a linear system of order $np \times nc$ to solve.

Mixed Euler-Lagrange (MEL) scheme

This method enables to solve step by step the mixed problem defined at the previous paragraph, with a Neumann condition on the body (the normal derivative on the body is known) and a Dirichlet condition on the free surface (the potential is known). At each time step, we have to solve a linear system of equations deriving from the panel method, to calculate the strengths of the sources satisfying the previous boundary conditions, (5) and (6). Then, the free surface conditions (2) and (3) are used to update the potential and the free surface elevation.

Numerical results

Preliminary results on a single doublet

In order to check the results concerning the free surface and to optimize the calculation parameters, we have applied the method previously described with a single doublet in transient motion. The free surface grid is based on rectangular panels (with use of the symmetry of the problem, only one half of the free surface is gridded) with constant length in the streamwise direction x and with variable width (increasing of 10% from node to node in the y direction). No grid is required for the doublet.

The doublet is formed with two (positive and negative) sources with intensity μ_0, separated by 0.1m at a water depth of 1m under the undisturbed free surface. After an impulsive start, the steady forward speed is $U_0 = 1 \mathrm{m.s}^{-1}$. In order to avoid too high velocity gradients, the velocity and the intensity are given by:

$$U(t) = U_0\left(1 - e^{-kt^{\alpha}}\right) \quad ; \quad \mu(t) = \mu_0\left(1 - e^{-kt^{\alpha}}\right) \qquad (7)$$

where k and α are parameters used to avoid starting instabilities. As the location and the intensity of the doublet are known at each time, the potential on the whole free surface can be calculated. Equation (5) is reduced to the following matrix:

$$\left[A_{ij}\right]\left[\sigma_{Xsj}\right] = \left[\Phi_{0_i}\right] + \left[\Phi_{d_i}\right] \qquad (8)$$

$A_{ij} = \left|X_i - Xs_j\right|^{-1}$, X_i and Xs_j are collocation and source points of intensity σ_{Xsj} respectively.

$\Phi_{d_i} = \mu(t) * \left(\left|X_i - X_{source}\right|^{-1} - \left|X_i - X_{sink}\right|^{-1}\right)$ is the potential of the doublet in X_i.

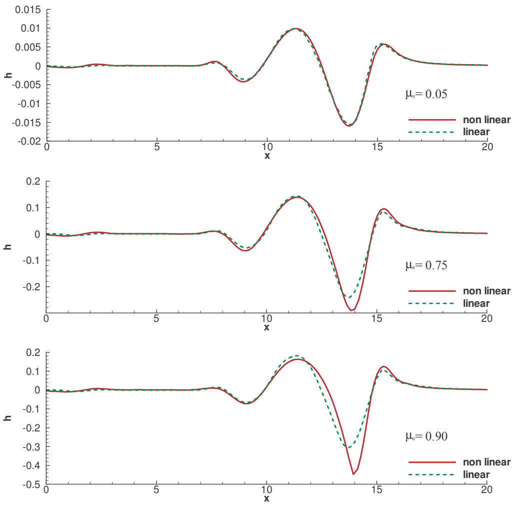

Figure 1 : Comparison of non linear and linear [14] free surface elevation above the axis of symmetry for a doublet in motion for three values of its strength (μ_0=0.05; 0.75 and 0.9)

Figure 1 plots the comparison of the present results after 10s of motion with those of King et al [14], using an unsteady linear method (time dependent Green function) for 3 values of the doublet strength. The agreement is excellent for the lower values of the strength. When the intensity increases, it can be seen that the non linear wave amplitude increases too with respect to the linear one, showing the effect of the non-linearities.

To check the obtained results, we have measured the wavelength of the waves and compared them to the values of the linear 2D theory ($\lambda = 2\pi U_0^2 / g$). The numerical values, given in table 1, are very close to the theoretical one, the maximum of the difference being smaller than 1.6%.

F	λ the	λ num	error %
0.2	2.462	2.465	0.12
0.32	6.304	6.250	0.85
0.45	12.466	12.426	0.32
0.6	22.162	22.145	0.076
0.8	39.399	40.005	1.54
1.1	74.490	73.996	0.66

Table 1 : Comparison of the wave length calculated by the present method and the 2D linear theory for various Froude numbers F

Optimisation of the parameters of the calculations

We have used the case of the doublet to optimize the parameters of the calculations as the starting function, the time step, the spatial steps in x and y, the domain truncation on the free surface for various Froude numbers ranging from 0.32 to 1.1. The comparison has been performed on the free surface elevation in the central plane and the value of the wavelength. The following parameters have been chosen:

Froude numbers	**Starting parameters k,α**	**Δt(s)**	**Δx(m)**
0.32	0.005 ; 2.	0.25	0.5
0.45	0.0001 ; 4.	0.25	0.5
0.6	0.0001 ; 4.	0.25	0.6
0.8	0.0001 ; 4.	0.2	0.8
1.1	4. ; 1.	0.1	1.0

Table 2: Parameters chosen for the calculations

We have first performed the computations in a fixed domain (first formulation) but the calculations have suffered from reflection of the waves in the downstream limit of the grid leading to too large domain of computations. The results obtained after 30s with the 2nd formulation (moving domain) are presented on figure 2. The reflected waves on the rear part of the domain are clearly removed.

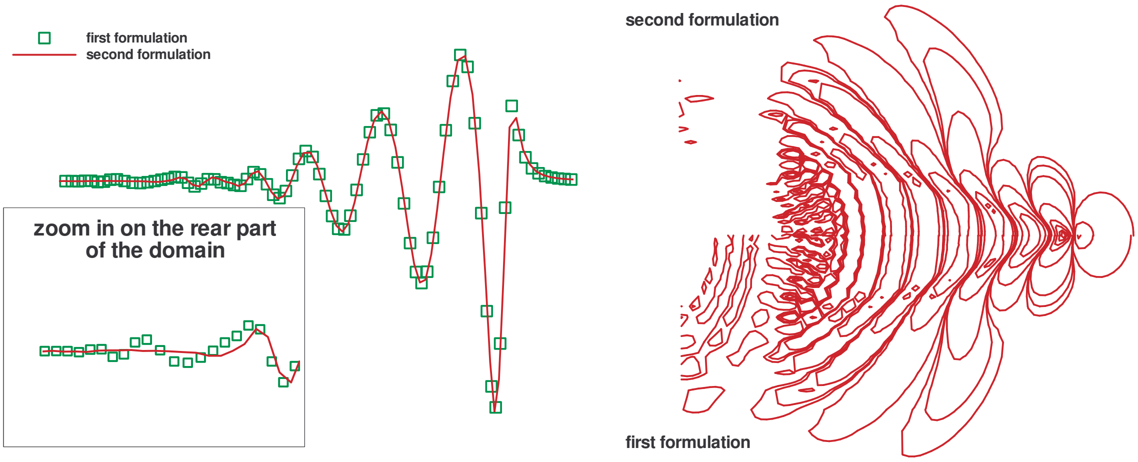

Figure 2 : Comparison of the free surface elevation for calculations in a fixed and moving domain

Submerged ellipsoid

Infinite water depth

Calculations have been first performed on an ellipsoid with an axis ratio of 5:1 using the analytical solution in unbounded fluid to choose the body grid. A 30*12 grid with step variation in power law along the x axis has been chosen. We have compared the maximum wave amplitude of the results obtained in [2] using a steady method of computation, figure 3. Our results are plotted as the symbols and the ones of [2] by lines. The agreement is excellent whatever are the values of the Froude number and of the body submersion.

In order to emphasize the non linearity effects on the wave amplitude, figure 4, we have compared our results with those of a linear computation, Ponizy et al. [15], in the same conditions. The linear results are plotted by lines and our non linear results by symbols. This figure shows that as the non linear effects are important (when the depth of immersion is weak), the wave amplitude are larger that the values given by the linear method. The difference is larger at weaker value of the Froude number.

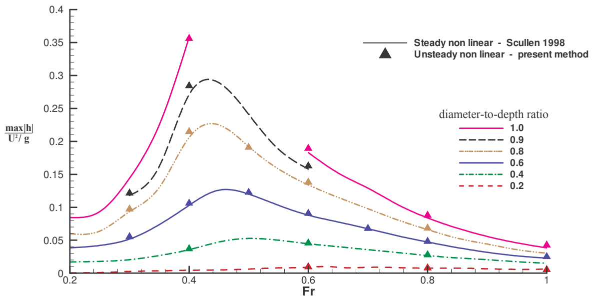

Figure 3 : Maximum wave amplitude versus the Froude number for various body depths

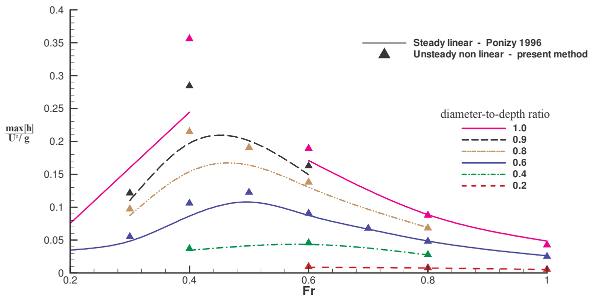

Figure 4 : Influence of the non linear effect on the maximum wave amplitude versus the Froude number for various body depths

Influence of finite water depth

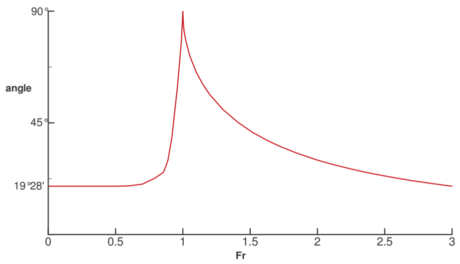

Figure 5 : Kelvin dihedral angle versus the Froude number

To check the results obtained, we have tried to compare the results obtained on the same ellipsoid than previously with the method of Havelock [16] for a submerged source. Figure 5 shows the variation of the Kelvin angle for the waves with the Froude number. This angle is plotted versus the Froude number based on the water height h, $F_h = U/\sqrt{g.h}$. For weak values of this parameter, the angle is constant with the value 19°28’, increasing sharply until 90° close to the critical value $F_h = 1$ and decreasing more slowly to reach the initial value for F_h= 3.

The figure 6 (upper part) shows the free surface elevation for Froude numbers based on the body length of 0.6, 1 and 1.2 for infinite water depth. It can be observed that the angle of the wave pattern is constant. It can be seen that the wave pattern composed of transverse and V-shape waves if F=0.6, is transformed into a pattern with only V-shape waves when the Froude number increases. Calculations have also been performed in finite water depth, figure 6 (lower part). It can be observed that the dihedral angle increases rapidly close to the critical value $F_h = 1$ and then decreases for $F_h = 1.2$.

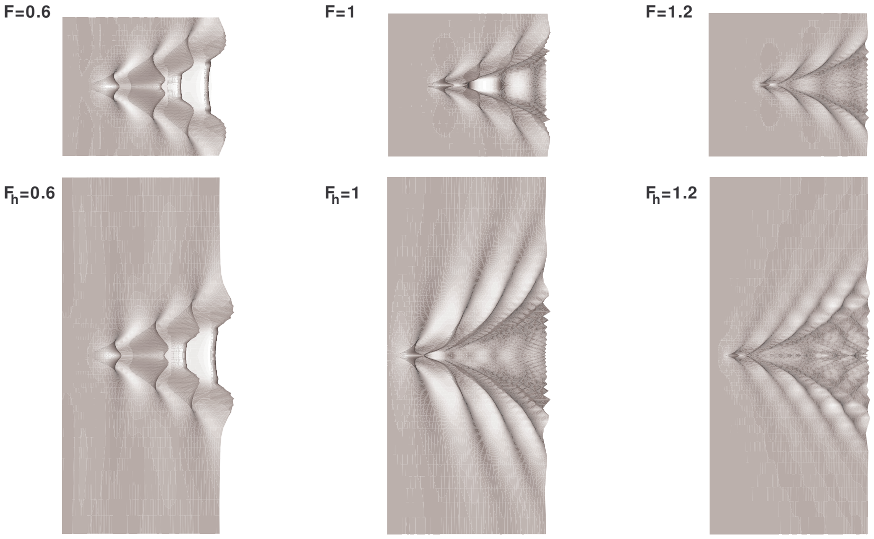
F=0.6 F=1 F=1.2

F_h=0.6 F_h=1 F_h=1.2

Figure 6 : Wave patterns in infinite depth (upper part, F=0.6-1.-1.2) and finite depth (lower part, F_h =0.6-1.-1.2)

Conclusion

We have studied the unsteady 3D flow above a submerged body, and particularly the shape of the free surface. The originality of our research is that we keep the two free surface conditions in their nonlinear formulation. We use a MEL procedure to solve the problem: at each time step we know the potential on the free surface and its position, we then solve a mixed boundary value problem to find the unknown strength of the Rankine singularities. To update the potential and the elevation of the free surface we use a 4th order Runge-Kutta scheme. In order to avoid singular kernel in the integral calculation we use a desingularized technique for the distribution of the singularities on the free surface, while the body is discretised into quadrilateral (and triangular close to the ends) panels, where the source strength is assumed to be constant. First we have applied this method to a source-sink pair moving under the free surface to validate the discretisation and to optimize the calculation procedures. Then, the motion of a submerged ellipsoid in infinite and finite water depth has been studied. The influence of a Froude number based on the water height on the dihedral wave pattern has been put in evidence; this angle increases close to F_h=1.0 and decrease then to reach the value in infinite water height. The method is also able to deal with unsteady body motions. Results concerning such motions (change of direction, circular motion,..) will be presented during the conference. Work is in progress to extend this method to a surface-piercing body.

References

[1] Raven H.C., "A Practical Nonlinear Method for Calculating Ship Wave-making and Wave Resistance", 19th Symp. On Naval Hydrodynamics, Seoul, South Korea, 1992

[2] Scullen D.C., "Accurate Computation of Nonlinear Free-Surface Flows", Ph. D., Adelaide University, Australia, 1998

[3] Longuet-Higgins M.S. and Cokelet E.D., "The Deformation of Steep Surface Waves on Water: I. A Numerical Method of Computation", Proceedings of the Royal Society, A 364, pp 1-26, Londres, 1978

[4] Clément A.H., "Coupling of Two Absorbing Boundary Conditions for 2D Time-Domain Simulations of Free Surface Gravity Waves", J. of Comp. Physics, 126, pp 139-151, 1996

[5] Berkvens P.J.F. and Zandbergen P.J., "Nonlinear Reaction Forces on Oscillating Bodies by a Time-Domain Panel Method", Journal of Ship Research, 40, pp 288-302, 1996

[6] Berkvens P.J.F., " Floating Bodies Interacting with Water Waves; Development of a Time-Domain Panel Method", Ph. D. thesis, Twente University, Enschede, Netherlands, 1998

[7] Dommermuth D.G. and Yue D.K.P., "Numerical Simulations of Nonlinear axisymmetric flows with a free surface", Journal of Fluid Mechanics, 178, pp 195-219, 1987

[8] Ferrant P., "Fully Non-Linear Interactions of Long-crested Wave Packets with a Three-Dimensionnal Body", 22nd Symp. on Naval Hydrodynamics, Washington, USA, 1998

[9] Park J.H. and Troesch A., "Numerical Modeling of Short-Time Scale Nonlinear Water Waves Generated by Large Vertical Motions of Non-Wallsided Bodies", 19th Symp. on Naval Hydrodynamics, Seoul, South Korea, 1992

[10] Webster W.C, "The Flow About Arbitrary 3D Smooth Bodies", Journal of Ship Research, pp 206-218, 1975

[11] Schultz W.W. and Hong S.W., "Solution of Potential Problems using an Over determined Complex Boundary Integral Method", J. of Computational Physics, 84, pp 414-440, 1989

[12] Cao Y., Schultz W.W. and Beck R.F., "Three-Dimensional Desingularized Boundary Integral Methods for Potential Problems", Int. J. for Num. Meth. in Fluids, 12, pp 785-803, 1991

[13] Lalli F., "On the Accuracy of the Desingularized Boundary Integral Method in Free Surface Flow Problems", Int. J. for Num. Meth. in Fluids, 1997, 25, pp 1163-1184

[14] King B.K., Beck R.F. and Magee A.R., "Seakeeping Calculations with Forward Speed using Time-Domain Analysis", 17th Symp. on Naval Hydrodynamics, La Hague, Pays-Bas, 1988

[15] Ponizy B., Guilbaud M. and Ba M., "Numerical computations and integrations of the wave resistance Green's function", Theoretic and Comp. Fluid Dynamics, 12, n°3, pp. 179-194, 1998.

[16] Havelock T.H., "The Propagation of Groups of Waves in Dispersive Media, with Application to Waves on Water produced by a Travelling Disturbance", Proceedings of the Royal Society of London, Ser. A81, pp 398-430, 1908

RANSE Simulations of Surface Piercing Propellers

Mario Caponnetto, Rolla Research, mariocaponnetto@hotmail.com

Introduction

RANSE methods have been applied to the analysis of ship propellers in open-water condition and behind ships for a good decade now. So far, these applications focused on 'conventional' propellers. These are typically modeled without consideration of the free water surface. This can be justified for conventional propellers which operate sufficiently far away from the free surface. However, high-performance boats resort often to surface-piercing propellers (SPP) which introduce several additional challenges. The propeller profiles of SPP have a cusped leading edge, do not end in a point (tapered forms), but have maximum thickness at the "trailing edge" which then becomes a trailing surface. Naturally the free surface changes the flow at the propeller considerably and we have to model rapid water exit and water entry. As in simulations of propellers interacting with ship hull or rudder, we have to combine turning grids with stationary grids in a RANSE simulation. I will present results for various SPP applications taken from the business experience of Rolla Propellers.

The simulations are performed using the commercial finite-volume RANSE solver Comet. Comet proved once again to be a rather robust code capable of handling complex free-surface applications. From a practical point of view, it is rather advantageous to have one single code to handle the hydrodynamic analyses of calm-water planing, *Caponnetto (2000),* seakeeping of planing hulls, *Caponnetto (2002)*, and propulsive organs even if these are all unconventional.

SPP work at the interface between water and air. SPP are normally used on fast yachts for a number of reasons. When speed becomes very high (>40 knots) conventional submerged propellers present the major drawbacks of erosive cavitation and high resistance of their appendages (shafts, brackets, rudders). On a properly designed SPP erosive cavitation is normally avoided since the water vapor pocket is replaced by an air pocket; the driving shafts are completely out of the water and rudders can be avoided using steerable shafts (Arneson drives). Moreover the possibility to trim the shafts and tuning the vertical force developed by the propellers, can be very useful on planing yachts to obtain the optimum running trim.

An SPP blade, during the rotation, works in the air for about 50% of the time (developing practically no thrust), is completely submerged for 25/30% of the time and for the rest is partly submerged (in the entry and exit phases). During the completely submerged phase only the face (pressure side) should be wetted, while the back side should be surrounded by an air cavity connected to the free surface. On the back side the pressure is "nominally" equal to the atmospheric pressure, while a large pressure acts on the face. SPP blades have an outline similar to conventional propellers, but the sections resemble those of a super-cavitating propeller. The leading edge is sharp and very thin to promote cavity development; the face if highly cambered with the maximum depth close to the trailing edge (cup). The shape of the back has no hydrodynamic influence as far as its contour remains inside the air pocket. For this reason and to give the required robustness, the maximum thickness of the profile is located at the trailing edge.

Compared to conventional propellers, there is a lack of data in the literature exploitable for the design of an SPP. The first complete methodical series tested in a cavitation tunnel have been developed by Rolla Propellers in 1991, *Rose and Kruppa (1991).* More recently an important experimental analysis, giving more insight in the physical phenomenon, has been performed by *Olofsson (1996),* where not only the global forces but also their instantaneous values on a single blade have been measured.

From the computational point, while in principle conventional potential flow theory could be applied to SPP design, in reality the complex free-surface effects (cavity and spray), difficult to capture with a panel method, make its accuracy insufficient for engineering purposes. Therefore Rolla started to develop a numerical tool able to calculate SPP hydrodynamics. Due to its capability to compute complex free surfaces and its feature of sliding meshes, the RANSE solver Comet has been tested for our purpose. I present here a brief description of the method used and some results.

Description of the numerical method

The flow is modeled as a two-phase flow computing both air and water flow simultaneously. The conservation equations for mass and momentum are solved in integral form using a finite volume method. The integrals are approximated using the midpoint rule. The SIMPLE algorithm couples pressures and velocities. The Reynolds stress tensor (i.e. turbulence) is modeled using the standard k-ε turbulence model. Time is discretized using an implicit Euler scheme. Demirdzic et al. (1998) give more details of the method.At the inlet, velocity components, turbulent energy and its dissipation rate are prescribed. At the outlet, zero gradients in longitudinal direction are enforced. On the propeller surface, the no-slip condition is enforced using a wall function. The interface between water and air is determined in a surface capturing method. We define a scalar function C ($0 \le C \le 1$) which describes the volume percentage of water in each cell. C=1 for cells filled completely with water, C=0 for cells filled completely with air. This scalar function allows us to model the two phases in our flow as one effective fluid with locally weighted material properties (viscosity μeff, νeff):

$\mu_{eff} = C\,\mu_{water} + (1-C)\,\mu_{air}$
$\nu_{eff} = C\,\nu_{water} + (1-C)\,\nu_{air}$

In addition to the RANSE and the turbulence transport equations, we solve one more convective transport equation to capture the convection of the water-air interface defined by C=0.5. The specially constructed high-resolution interface capturing (HRIC) scheme keeps the transition region from C=0 to C=1 relatively narrow and allows thus a quite sharp resolution of the water-air interface, *Muzaferija and Peric (1998).*

Description of the mesh

While in most of the cases performance calculations of submerged propellers can be carried on assuming steady conditions, the flow on an SPP is always unsteady and then computation must be solved marching in time, following the flow during some complete rotations of the screw. In our approach the domain mesh is composed by two cylinders. A fixed external cylinder simulates the contours of the cavitation tunnel; on its lateral surface a slip condition is imposed, while on the fore and aft surfaces the inlet and outlet condition are imposed respectively. A smaller cylinder containing the propeller is set inside the external one. At each time step the internal cylinder is rotated of a small amount, and the propeller with it. Computational variables are interpolated at the sliding interface of the common surfaces of the internal and external cylinders. The axis of rotation of the internal cylinder can be oriented arbitrarily to represent the exact propeller shaft inclination. The Fortran code that built the mesh has been in house developed. The mesh inside each block is structured and uses hexahedral cells. Local refinements can be performed splitting a cell in a number of sub-cells. In the following examples the number of cells used varied from 200.000 to 500.000.

Flow visualization

In the following series of figures the pressure distribution over the face of a blade is followed from the entry to the exit phases. The pressure peak is at the leading edge in the entry phase, but the maximum local pressure is found when the cup hits the water surface. In this moment also the thrust developed by the blade, and its mechanical stress, is maximal. When the blade is completely submerged the maximum pressure is along the leading edge (to promote ventilation) and along the trailing edge, especially close to the tip; in between the blade is relatively unloaded. When the blade is already above the undisturbed free-surface level (last image), the cup is still loaded by the water that is pushed downstream but also upward; the large spray observed behind typical SPP is generated in this phase.

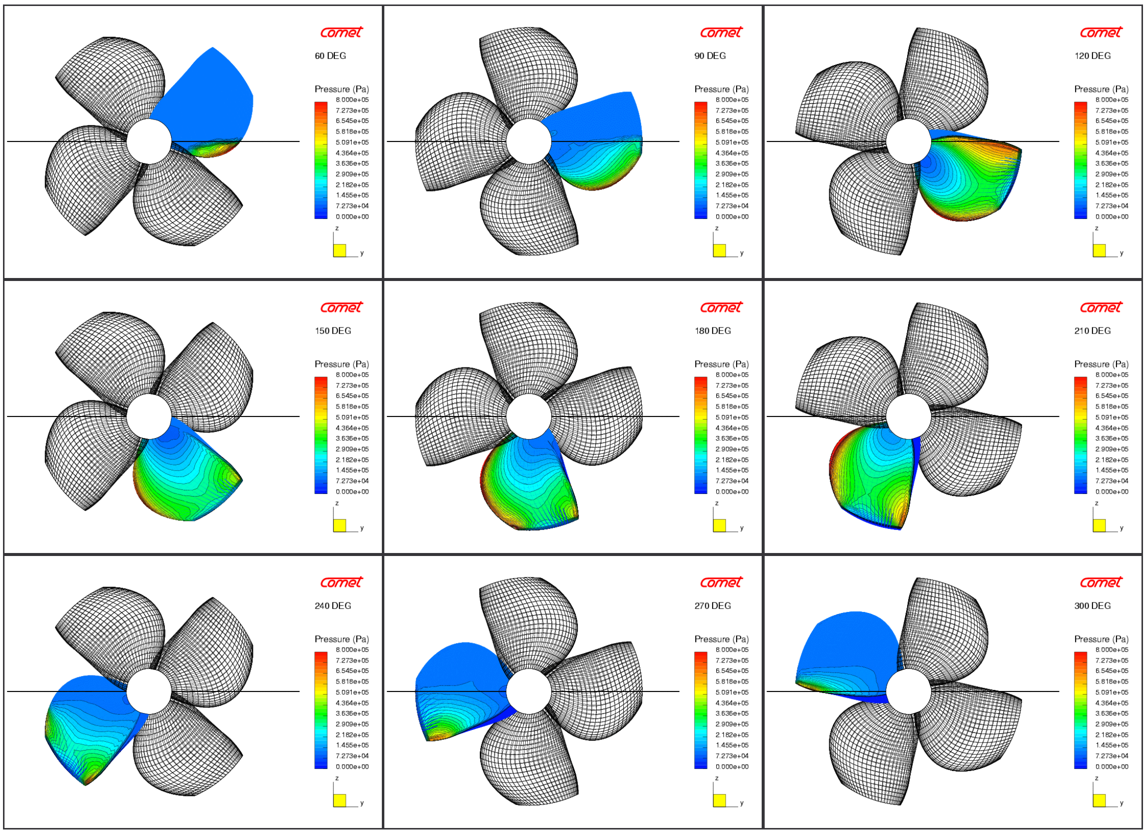

The next series of figures show a cylindrical section of the propeller at r/R=0.4. These images represent the cavity formation in the entry phase (flow from right to left). The cavity is unusually thick due the low advance ratio used for this calculation. The influence between adjoining blades is very clear.

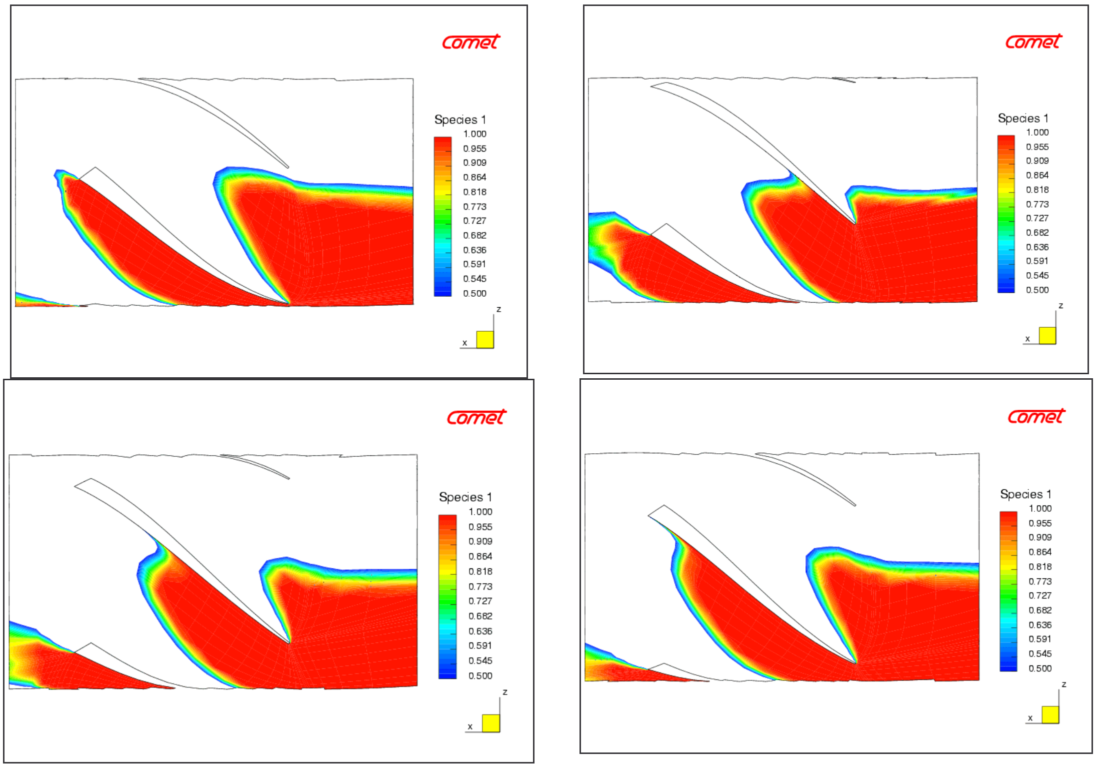

Entry phase

Similarly the last sequence of images shows the blades in the exit phase (flow from left to right). The profile approaches the free surface with the back side completely ventilated. The face carries with it some water even when it is well above the undisturbed free surface level.

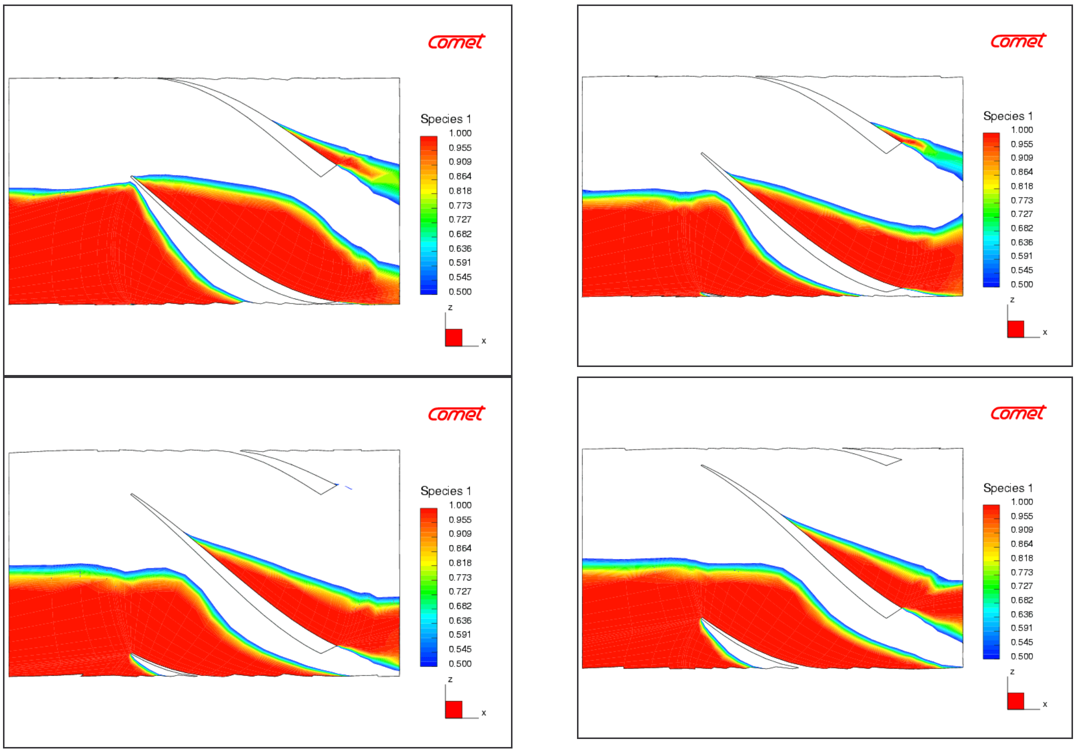

Exit phase

Forces calculation

Our main goal is to compute the correct forces and moments developed by the propeller. From our preliminary work the code seems to be able to supply the right answers even with a moderate numerical effort. The next figure compares our computation and cavitation tunnel experiments. The instantaneous non-dimensional axial force generated by one blade is plotted vs. the blade angular position. The experimental data are from Olofsson. The agreement is very good. The main characteristics of the phenomenon are captured by the code, and the integral value of the thrust is computed with an error of few percents. Also shown is the result obtained by a panel method.

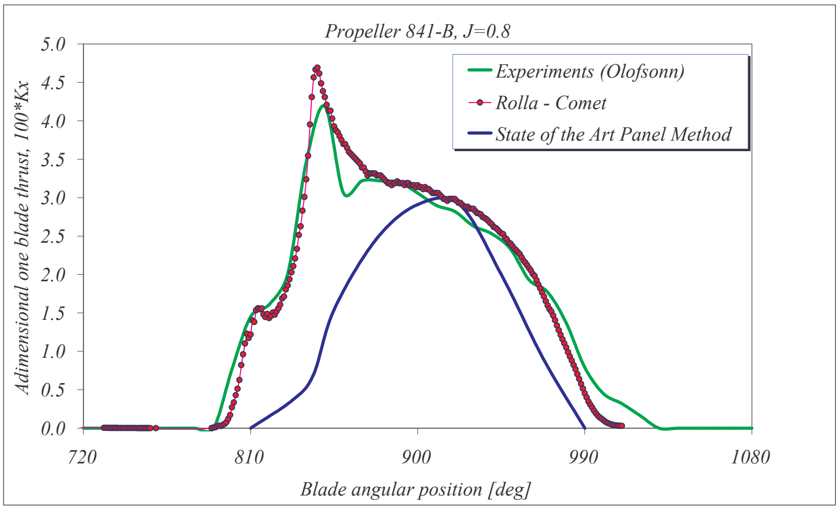

References

CAPONNETTO, M. (2000), *Numerical simulation of planing hulls*, 3rd Numerical Towing Tank Symp. (NuTTS), Tjärnö

CAPONNETTO, M. (2002), *Seakeeping of fast hard chine vessels using RANSE*, 5th Numerical Towing Tank Symp. (NuTTS), Pornichet

COMET, ICCM Institute of Computational Continuum Mechanics GmbH, Comet Version 2.004.A, Hamburg, now part of Computational Dynamics Ltd (CD Adapco Group)

DEMIRDZIC, I.; MUZAFERIJA, S.; PERIC, M. (1999), *Computation of turbulent flows in complex geometries, calculation of complex turbulent flows,* WIT Press

MUZAFERIJA, S.; PERIC, M. (1998*), Computation of free surface flows using interface-tracking and interface-capturing methods*, Nonlinear Water Wave Interaction, Comp. Mech. Publ., Southampton, pp.59-100

OLOFSSON, N. (1996), *Forces and Flow Characteristics of a Partially Submerged Propeller*, Ph.D. thesis, Chalmers Tekniska Högskola

ROSE, J.C.; KRUPPA, C.F.L (1991), *Methodical series model test results*, FAST'91, Vol. 2, Trondheim

NUMERICAL SIMULATIONS OF PODDED PROPULSORS

François DENISET *, Jean-Marc LAURENS **, Rachel JAOUEN *

* Institut de Recherche de l'Ecole Navale, BP 600, 29 240 BREST Armées, France. (*deniset@ecole-navale.fr*)
** ENSIETA, 2, rue François Verny, 29 806 BREST Cedex 09, France. (*Jean-Marc.Laurens@ensieta.fr*)

INTRODUCTION

Podded propulsors present a lot of advantages compared to classical propulsion units: better manoeuvrability [1], a more flexible installation of the engine, a more uniform wake distribution and a lower noise level. For these reasons, electrically driven pod propulsion units have gained popularity since their inception in the early 90’s. However, the constant increasing power of the units (pod + strut + propeller) mounted on ships such as cruise ships or navy ships induces new problems such as cavitation, noise and vibrations. In the early stage of the projects, CFD tools help designers to predict the hydrodynamic performance of pod units. Numerical results are compared to model measurements.

The different ongoing studies on these problems are not widely known mainly for confidentiality reasons. Szantyr [2] proposes a surface panel potential method to compute the hydrodynamic characteristics of podded propulsors in the vicinity of the design advance coefficient. Pustoshny and Kaprantsev [3] highlight problems caused by pods such as cavitation and vibrations. Terwisga et al. [4] give a review of current hydrodynamic issues in the design and application of steerable thrusters and podded propulsors. CFD and full-scale measurements are an important aid to designers. Kinnas et al. [5] use a coupled potential-Euler method to compute the entire flow around a podded propulsor. They do not predict the cavitation inception on the strut.

The aim of this study is to show the feasibility of a coupling between a potential based method and a RANSE solver to determine the hydrodynamic loading of a pod propulsor in order to determine the possible risks of cavitation.

DEFINITION OF THE PROPELLER

Based on some available geometric parameters and hydrodynamic characteristics of an existing unit, a four-bladed propeller was numerically determined using a mesh generator and a potential in-house solver. The open water dimensionless performance characteristics of the propeller are presented in Figure 1. A realistic unit similar to the one presented in Figure 2 can therefore be considered for our numerical simulations.

DESCRIPTION OF THE METHOD

The method used in this work to compute the flow around the unit (pod + strut + propeller) has been developed by Laurens [6] to predict the characteristics of the propeller-rudder interaction. Here, the velocities generated by propeller blade surface sources and doublets distributions are computed within a actuator disk located directly behind the propeller. This velocity field is then used as a velocity inlet boundary condition for the RANSE simulation of the flow around the pod and the strut. The method can be used for steady state simulations by averaging the velocities during a propeller rotation or for unsteady state simulations using the incident velocities in the rudder simulation.

A hybrid mesh of 700 000 cells has been generated around the pod. Particular attention has been paid to the mesh density close to the strut and more precisely in the strut leading edge region. The position of the leading edge of the strut is very close to the inlet boundary condition. Computational tests have shown that this proximity of the leading edge does not interfere with the inlet boundary condition. The inlet boundary condition based on the velocity field obtained by the potential flow solver respects the no slip condition on the pod surface.

In order to refine the grid within the pod boundary layer, a much larger mesh would have been required as well as a better mesh generator. At first, the intention was to solve the Euler equations around the pod. But the Neuman condition on the pod surface is then too close to the Dirichlet condition on the inlet velocity plane. It was therefore decided to solve the Navier-Stokes equations to simulate the flow around the pod. Zero velocity was also imposed at the blade root to avoid having two incompatible conditions within a same cell and to account for the forward hub boundary layer. Because of the relatively coarse grid within the pod boundary layer, there is no point at this stage to invoke a turbulent model. Simulations are therefore performed in laminar flow conditons.

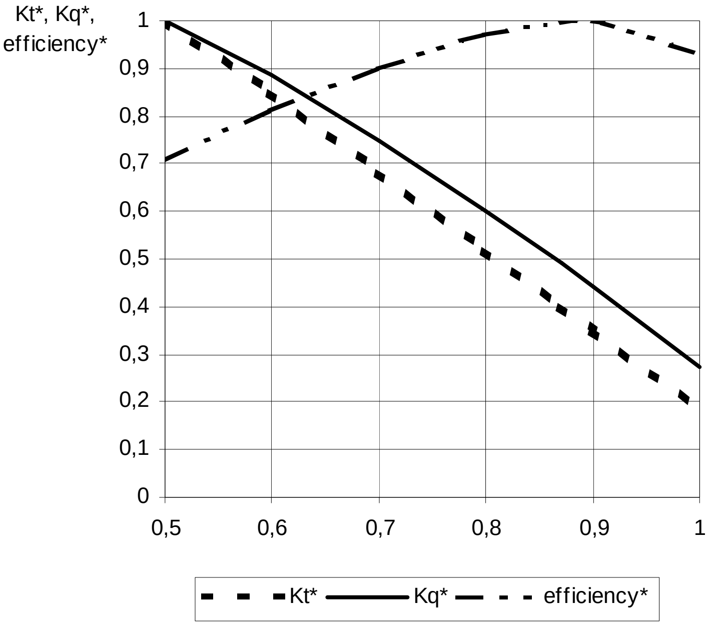

Figure 1. *Open water propeller dimensionless performance predicted by the potential flow solver.*

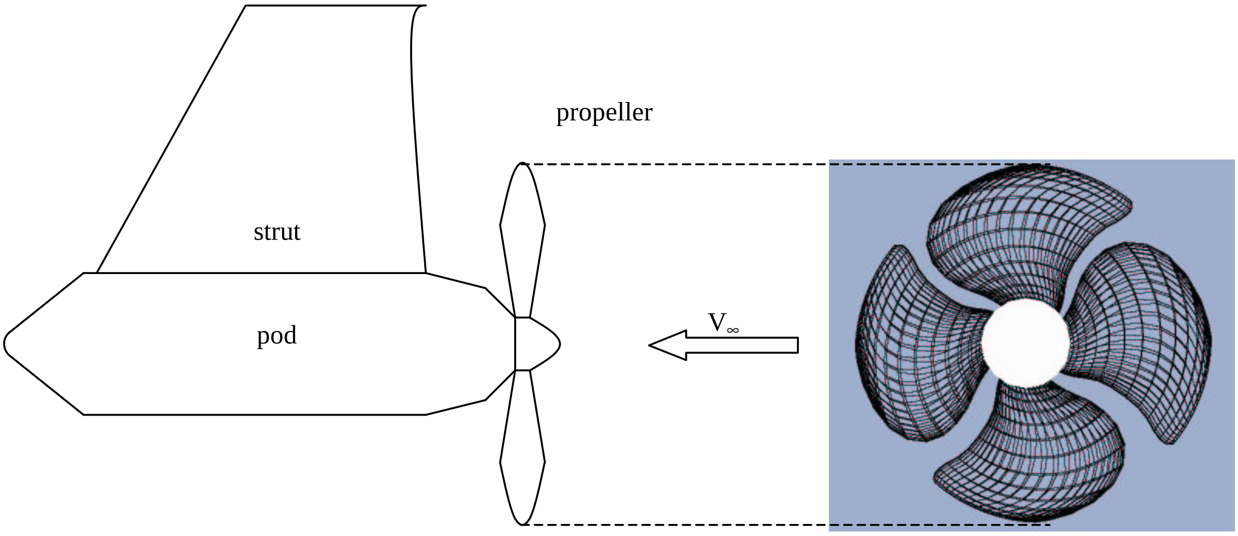

Figure 2. *Schematic view of the unit (pod + strut + propeller).*

RESULTS

Y-Lift (Cl), Z-drag (Cd) and Z-moment (Cm) hydrodynamic coefficients calculated on the strut in open water condition (without the propeller) are presented in Table 1. Although, Cl and Cm are expected to be nil because of the symmetry, we considered these values to be small enough to be regarded as negligible.

Pod without propeller	Cl	Cd	Cm
	- 0.004	0.024	-0.013

Table 1. *Hydrodynamic lift, drag and moment coefficients of the translating pod without the propeller*

The hydrodynamic coefficients computed on the strut for propulsion tests in steady state conditions are presented in Table 2. As expected the hydrodynamic coefficients of the pod change in terms of the propeller loading. The Cl and Cm values show a shift from zero which increases with the propeller loading due to the rotational flow induced by the propeller. Cd is increasing because of the lift induced drag but a better representation of the pod boundary layer may show a different result.

Pod with propeller	Cl	Cd	Cm
J = 0.87	- 0.06	0.025	- 0.162
J= 0.5	- 0.225	0.060	- 0.554

Table 2. *Steady hydrodynamic lift, drag and moment coefficients of the pod with the propeller*

The averaged hydrodynamic coefficients computed on the strut for propulsion tests in unsteady state conditions are presented in Table 3. In view of the findings of reference [6] the values of Table 3 were expected to be closer than those of Table 2. Further studies using a more refined mesh are necessary.

Pod with propeller	Cl	Cd	Cm
J = 0.87	- 0.043	0.029	- 0.108
J= 0.5	- 0.247	0.077	- 0.599

Table 3. *Unsteady hydrodynamic lift, drag and moment coefficients of the pod with the propeller*

The fluctuations of these coefficients in unsteady state conditions for both propeller loadings (J = 0.87 and J = 0.5) are presented in Figures 3 and 4. The amplitude of the fluctuations increases in accordance with the propeller loading as expected. We also note that the signals present different shapes. This behaviour which was already shown for the rudder in reference [6] tends to indicate that a complete coverage of the propeller loadings range must be simulated in order to predict the risk of vibrations occurrences which are not necessarily limited to the BR (Blade Rate).

Finally, Figure 5 shows the pressure coefficients (Cp) curve for a strut section (R = 0.9) at a given time step when J = 0.87. The same results are displayed in Figure 6 for J = 0.5. It is important to note that the Cp minimum value decreases significantly depending on the propeller loading since it may induce cavitation inception. The notch appearing on both curves around x/c = 0.1 is caused by the geometry.

DISCUSSION

The numerical method presented here can be used to estimate pressure fluctuations on the pod strut for various advance parameters. This will be useful in the early design stage and will help the designer to determine the dimensions of the propulsion unit.

The strut is not only excited at the blade rate (BR) frequency. For a low propeller loading, significant amplitudes of the fluctuating forces appear at the multiple of the BR frequency.

The pressure distributions computed on the strut show that the cavitation inception region is situated close to the strut leading edge based on the local minimal pressure value. For a more accurate prediction of cavitation risks, the whole strut has to be inspected.

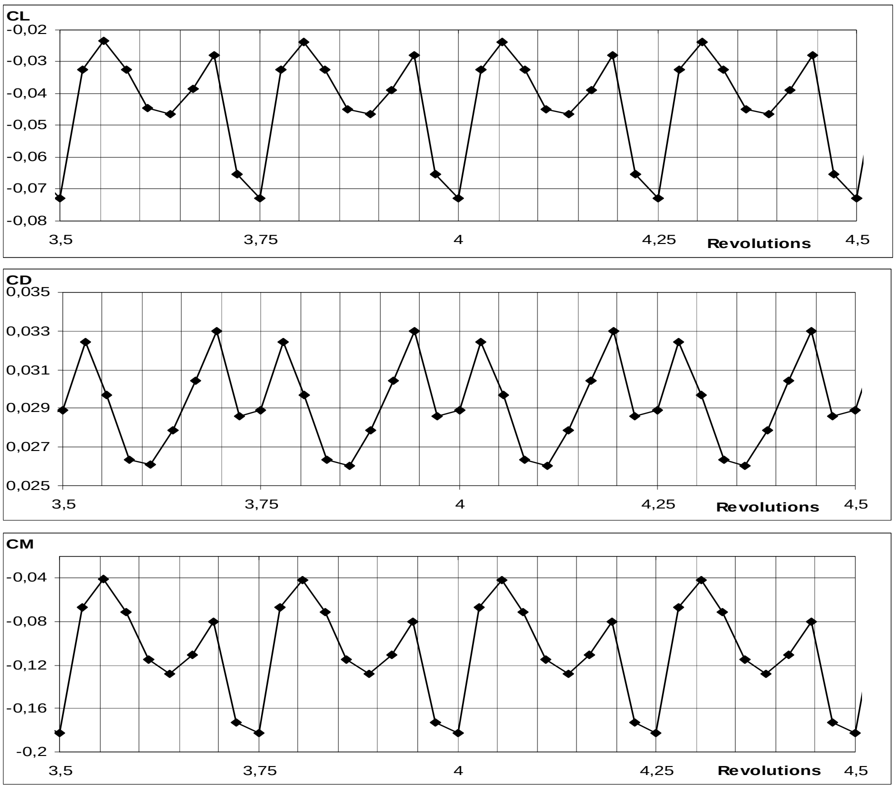

Figure 3. *Unsteady strut hydrodynamic lift, drag and moment coefficients. (J = 0.87)*

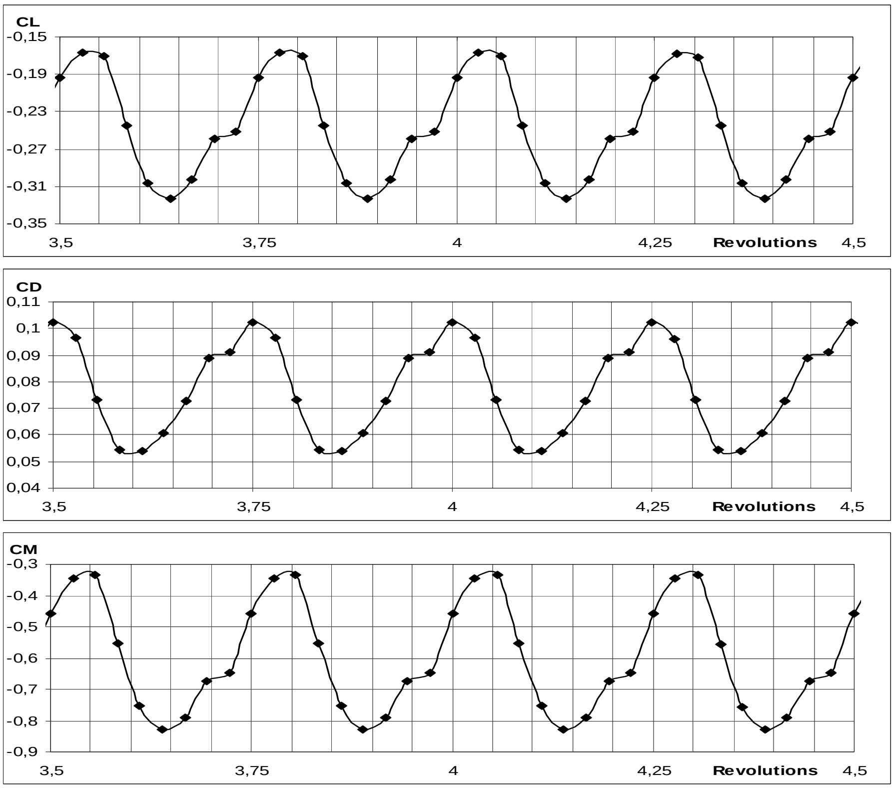

Figure 4. *Unsteady strut hydrodynamic lift, drag and moment coefficients. (J = 0.5)*

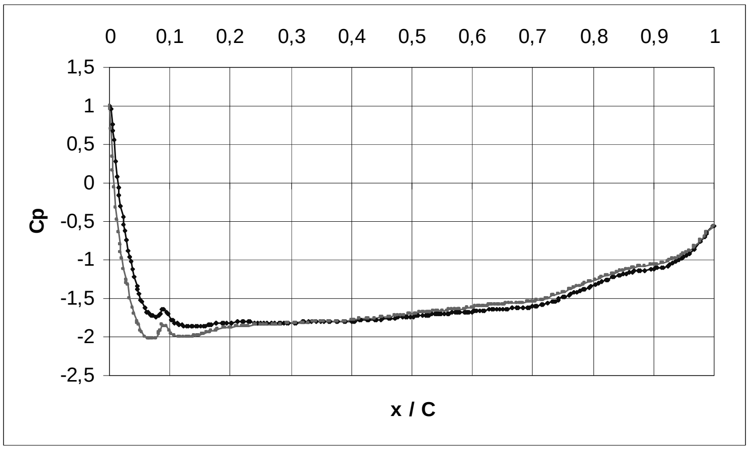

Figure 5. *Pressure coefficient distribution on the strut section situated at R = 0.9 (J = 0.87)*

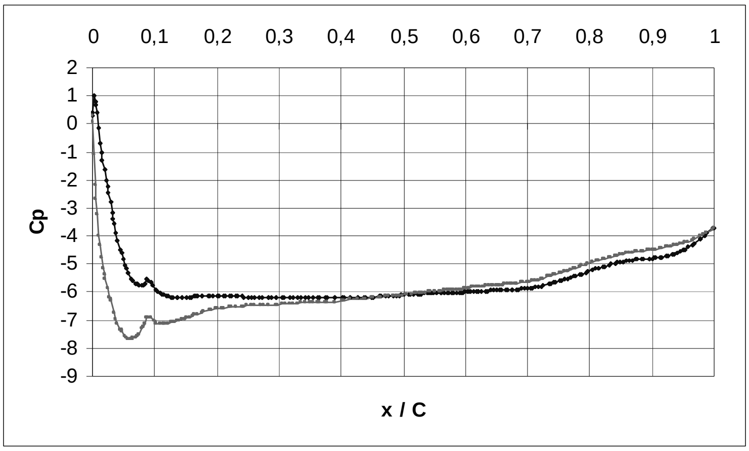

Figure 6. *Pressure coefficient distribution on the strut section situated at R = 0.9 (J = 0.5)*

PERSPECTIVES

Future studies will be devoted to mesh improvements in the boundary layer region. This will allow for a more accurate measurement of the drag effects. Additional studies of drag-induced effects will allow to determine any possible propulsion efficiency increase. Moreover, modifications of the geometry of the strut will be proposed to delay cavitation inception. Finally, estimations of vibrations induced by pressure fluctuations during manoeuvring phases will be discussed.

REFERENCES

[1] S. Toxopeus, G. Loeff , *Manoeuvring aspects of fast ships with pods*, 3rd international Euroconference on high-performance marine vehicles HIPER'02, Bergen, 14-17 September 2002, pp 392-406.

[2] J.A. Szantyr, *A surface panel method for hydrodynamic analysis of pod propulsors*, , Hydronav'2001, 14th international conference on hydrodynamics in ship design, Szczecin, Poland, 27-29 September 2001.

[3] A.V. Pustoshny, S.V. Kaprantsev, *Azipod propeller blade cavitation observations during ship manoeuvring*, CAV'2001, 4th international symposium on cavitation, Pasadena, USA.

[4] T. vanTerwisga, F. Quadvlieg, H. Valkhof, *Steerable propulsion units: hydrodynamic issue and design consequences*, 80th anniversary of Schottel GmbH & Co, August 2001.

[5] S.A. Kinnas, J.K. Choi, H. Lee, Y.L. Young, H. Gu, K. Kakar, S. Natarajan, *Prediction of cavitation performance of single/multi-component propulsors and their interaction on the hull*, SNAME annual meeting, Boston, September 2002.

[6] J.-M. Laurens, *Hydrodynamic Behaviour of a rudder operating in a propeller slipstream,* Ship Techn. Research 50, N°3, pp. 141-148, 2003.

Uncertainty Estimation :
A Grand Challenge for Numerical Ship Hydrodynamics

Luís Eça (eca@marine.ist.utl.pt)
Martin Hoekstra (M.Hoekstra@marin.nl)

1 Introduction

For many years model testing has been used as a fundamental tool of the development of ship hydrodynamics. Nowadays, it is standard practice in experimental fluid dynamics to indicate the uncertainty of a specific measurement. It is hard to believe that Computational Fluid Dynamics may establish itself as a reliable alternative and complement to model testing without indicating the numerical uncertainty of a given prediction.

The quantification of the uncertainty of a numerical prediction is commonly known as Verification of calculations, [1]. Many of the procedures proposed in the literature are based on grid refinement studies and Richardson extrapolation (RE), like the well known Grid Convergence Index (GCI) introduced by Roache, [1] and the method proposed by Stern *et al.* in [2][1]. Other alternatives are based on techniques applied to single grid calculations, which, if successful, would clearly be very powerful due to the need to compute only a single grid. Examples of this type of approaches are discussed in [4], [5] and [6].

Recently, we have investigated the difficulties of performing a reliable grid refinement study for a practical ship hydrodynamics application, which often corresponds to a complex turbulent flow, [7] to [12]. In [7], we have tried to estimate the numerical uncertainty of the calculation of the flow around the KVLCC2 tanker[2] using techniques based on RE. This effort led to a set of 24 grids where the application of the standard techniques available was found to be rather troublesome. One of the most striking features found in the data was the existence of scatter, which makes the estimation of the uncertainty from a single grid triplet less reliable.

The difficulties found in [7] led us to address simple test cases, [9], to identify the main difficulties of applying methods based on Richardson extrapolation to the uncertainty estimation in complex turbulent flows. In our tests [11] and [12], we have identified several sources of scatter in the data of a grid refinement study: the lack of geometrical similarity of the grids; the use of switches in the turbulence models; the interpolation/integration techniques required to obtain a flow variable which is not directly available from the flow solution at the grid nodes.

These difficulties are almost impossible to avoid in a complex turbulent flow and so we have tested a least squares root approach, [10], to be able to deal with the existence of scatter in the data. The reliability of such procedure has been checked in several test cases, [11], which led us to the conclusion that the establishment of a reliable procedure for a practical calculation may be more difficult and time-consuming than what would be desirable. Therefore, we have started a systematic study of the procedure based on a least squares root version of Roache's Grid Convergence Index.

The results presented in [12] for a simple turbulent boundary-layer with zero pressure gradient are encouraging. However, further testing is required to investigate the viability of such method in a practical application. Furthermore, it is important that this or other methods of uncertainty estimation are applied by different groups to assess the difficulties and usefulness of each method in order to develop robust and reliable procedures for uncertainty estimation. Therefore, we have selected two 2-D steady, incompressible, turbulent flows taken from the Ercoftac Database, [14], which we propose to the Numerical Ship Hydrodynamics community as a starting point for the joint evaluation and development of reliable tools for uncertainty estimation. For these two test cases, we have produced sets

---

[1] This method is the basis of the procedure proposed in the ITTC Quality Manual, [3].

[2] This attempt follows the citation of the mathematician George Polya cited by Roache in [13] to introduce the Method of the Manufactured Solutions: ”Only a fool starts at the beginning. The wise man starts at the end”.

of geometrically similar, single block, structured grids which can be used by almost all the numerical approaches available.

2 Uncertainty estimation with a least squares root approach

The basis of our procedure for the estimation of the uncertainty U of the solution on a given grid is the standard Grid Convergence Index (GCI) method, [1], which says

$$U = F_s|\delta_{RE}| \, . \tag{1}$$

F_s is a safety factor and δ_{RE} is the error estimation[3] obtained by Richardson extrapolation:

$$\delta_{RE} = \phi_i - \phi_o = \alpha h_i^p \, , \tag{2}$$

where ϕ_i is the numerical solution of any local or integral scalar quantity on a given grid (designated by the subscript $_i$), ϕ_o is the estimated exact solution, α is a constant, h_i is a parameter which identifies the representative grid cell size and p is the observed order of accuracy.

There are three unknowns in equation (2): ϕ_o, α and p. Therefore, three geometrically similar grids are required to estimate δ_{RE}. If solutions on more than three grids are available, more than one grid triplet can be chosen to estimate δ_{RE}. It is our experience that these estimates can vary a lot. Therefore, we compute ϕ_o, α and p in such cases with a least squares root approach that minimizes the function:

$$S(\phi_o, \alpha, p) = \sqrt{\sum_{i=1}^{n_g} \left(\phi_i - (\phi_o + \alpha h_i^p) \right)^2} \, , \tag{3}$$

where n_g is the number of grids available. The minimum of (3) is found by setting the derivatives of (3) with respect to ϕ_o, p_j and α_j equal to zero, [11].

When we only have a grid triplet, it is not difficult[4] to classify the apparent convergence condition from the convergence ratio:

$$R = \frac{\phi_2 - \phi_1}{\phi_3 - \phi_2} \, ,$$

where ϕ_1 stands for the finest grid solution, ϕ_2 for the medium grid and ϕ_3 for the coarsest grid solution. As mentioned by Roache, [15], we have:

$$\begin{array}{lcl lcl} 0 < R < 1 & \Rightarrow & \text{Monotonic convergence} & R > 1 & \Rightarrow & \text{Monotonic divergence} \\ |R| < 1 \wedge R < 0 & \Rightarrow & \text{Oscillatory convergence} & R < -1 & \Rightarrow & \text{Oscillatory divergence} \end{array}$$

When more than the three grids are available and the least squares root approach is applied this classification is not as straightforward, because the data may exhibit scatter, [11]. Therefore, we have established the apparent convergence condition using the p obtained from the least squares solution of equation (3). To identify the cases of oscillatory convergence or divergence we also perform a fit using $\phi_i^* = |\phi_i - \phi_1|$ in (3). The following four conditions are applied in sequence:

1. $p > 0$ for $\phi \Rightarrow$ Monotonic convergence.
2. $p > 0$ for $\phi^* \Rightarrow$ Oscillatory convergence.
3. $p < 0$ for $\phi \Rightarrow$ Monotonic divergence.
4. $p < 0$ for $\phi^* \Rightarrow$ Oscillatory divergence.

---

[3] In this case we are talking about the discretization error. However, one should not forget that we also have the round-off error and the iterative error that we are assuming to be negligible in this section.

[4] This does not mean that the classification based on a grid triplet is reliable.

Our experience with the GCI method has shown that its application in monotonic convergent solutions which exhibit an observed order of accuracy significantly larger than the theoretical order of accuracy may be troublesome. To avoid these problems, Roache, [16], suggests that the error estimation should be performed with the theoretical order of the method when the observed order of the method is larger than the theoretical one. This would mean in a simple three grids study, that the data of the coarsest grid would be irrelevant and that the error estimation would be performed from the data of two grids. This has been one of our criticisms, [17], on the procedure proposed by Stern *et al.* in [2]. Therefore, we have considered a different alternative based on an error representation with power series of fixed exponents, which we have tested before in [11]. The idea is simple and it has been discussed in [18]. When the observed order of the accuracy is larger than 2, we consider an alternative representation of the error estimation given by :

$$\delta_{RE2} = \phi_i - \phi_o = \alpha_1 h_i^2 + \alpha_2 h_i^3 \ . \tag{4}$$

In equation (4), there are still three unknowns: ϕ_o, α_1 and α_2. This means that we still require the information from at least three grids to perform our error estimation.

In our least square root approach, the solution of (4) becomes the minimization of the function:

$$S(\phi_o, \alpha_1, \alpha_2) = \sqrt{\sum_{i=1}^{n_g} \left(\phi_i - (\phi_o + \alpha_1 h_i^2 + \alpha_2 h_i^3)\right)^2} \tag{5}$$

that leads to a system of linear equations, [11]. The value adopted for the uncertainty estimation is the maximum of $|\delta_{RE}|$ and $|\delta_{RE2}|$.

In the cases of monotonic convergence, the standard deviation of the fit, U_s, is used as one of the contributions of the uncertainty. U_s is given by

$$U_s = \sqrt{\frac{\sum_{i=1}^{n_g} \left(\phi_i - (\phi_o + \alpha h_i^p)\right)^2}{n_g - 3}} \quad \text{or} \quad U_s = \sqrt{\frac{\sum_{i=1}^{n_g} \left(\phi_i - (\phi_o + \alpha_1 h_i^2 + \alpha_2 h_i^3)\right)^2}{n_g - 3}} \ , \tag{6}$$

depending on the equation, (2) or (4), used to estimate the error.

The procedure for the estimation of the numerical uncertainty, valid for a nominally second-order accurate method, is as follows:

1. The observed order of accuracy is estimated with the least squares root technique to identify the convergence condition according to the definition given above.

2. For monotonic convergence with $0.5 \geq p \leq 2$:

   The uncertainty is estimated with the G.C.I., equation (1), using $F_s = 1.25$ and the numerical error estimated with Richardson extrapolation, (2), using the least squares root technique. The standard deviation of the fit, U_s, is added to the uncertainty.

3. For monotonic convergence with $2 < p < 4.5$:

   The uncertainty is estimated with the G.C.I., equation (1), using $U = 1.25\max(|\delta_{RE}|, |\delta_{RE2}|)$. U_s, is added to the uncertainty.

4. For monotonic convergence with $p \leq 0.5$ or $p \geq 4.5$ and for oscillatory convergence :

   U is set equal to the maximum difference between the solutions obtained in the available grids multiplied by a factor of safety. $F_s = 3$ for $p < 0.5$ and $F_s = 1.25$ for $p > 4.5$.

5. The uncertainty estimation is not performed for the two divergence conditions.

This procedure is very similar to the one tested in [12]. However, we have introduced the power series expansion with fixed exponents in cases where the observed order of accuracy is larger than expected to serve as a confirmation of the error estimation obtained from Richardson extrapolation.

In the previous description, we have assumed that the iterative and round-off error are negligible, which may not always be possible to achieve. The iterative error is a consequence of the iterative procedures commonly applied in the solution of the non-linear systems of algebraic equations solved in Computational Fluid Dynamics. In principle, the iterative error maybe decreased as far as the machine accuracy permits, which defines the minimum level of the round-off error.

The evaluation of the discretization error requires grids in the so-called asymptotic region, which usually means highly refined grids. On the other hand, the increase of the grid density may be troublesome to ensure that the iterative error is negligible and it also increases the round-off error. Therefore, one should be aware that it is not possible to increase the grid refinement indefinitely in a grid refinement study.

3 Example of application

As an example of the problems that we may face, figure (1) presents the convergence of the friction resistance coefficient, C_F, with the grid refinement of the flow around the KVLCC2 Tanker at model scale Reynolds numbers. The calculations were performed with PARNASSOS, [19], and the integration of the wall shear stress was performed with a third order technique, [11]. The error bars estimated with our procedure for the two finest grids are plotted in figure (1). Although these results are not discouraging, it is clear that it is not easy to perform a reliable uncertainty estimation with this behaviour of the data.

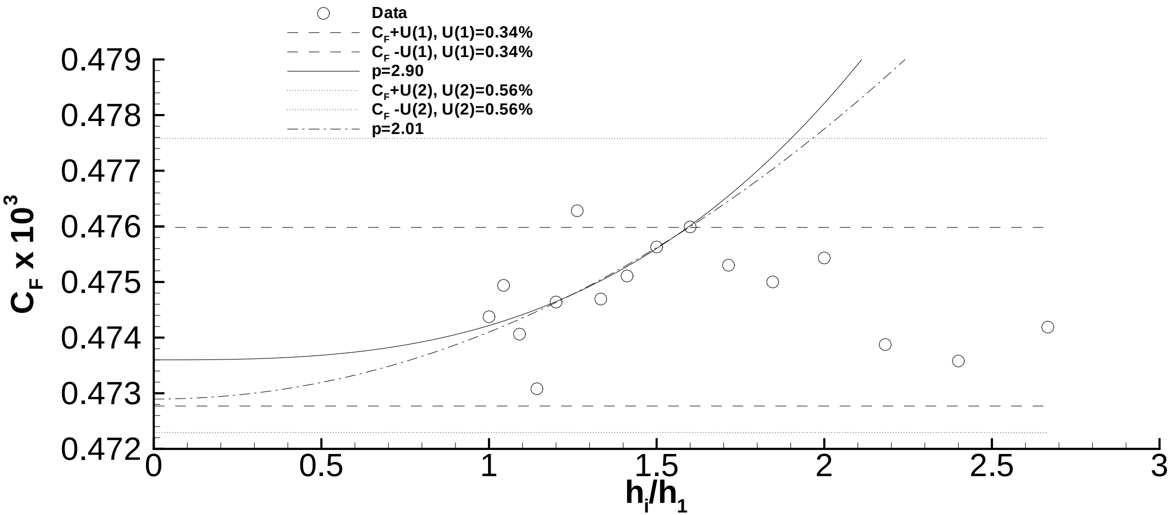

Figure 1: Friction resistance coefficients as a function of the typical cell size. Turbulent flow around the KVLCC2 tanker.

4 An invitation to the numerical ship hydrodynamics community

Our experience so far has shown that it is important to test the uncertainty estimation procedures in simple test cases to build confidence and to investigate the origins of the difficulties that we may have to face in practical applications. Therefore, we have selected two test cases of 2-D, steady, incompressible, turbulent flows from the Ercoftac Classic Database to evaluate our uncertainty estimation procedure: Case 18, [20], the flow over a hill and Case 30, [21], the flow over a backward facing step. In both cases there are experimental data available.

For the flow over the hill we have generated two sets of 11 geometrically similar, single block, structured grids. The first set includes nearly-orthogonal grids whereas the second set includes vertical straight lines. The grids range from 101 × 101 to 401 × 401 grid nodes. The coarsest grids of each set in the hill region are depicted in figure (2).

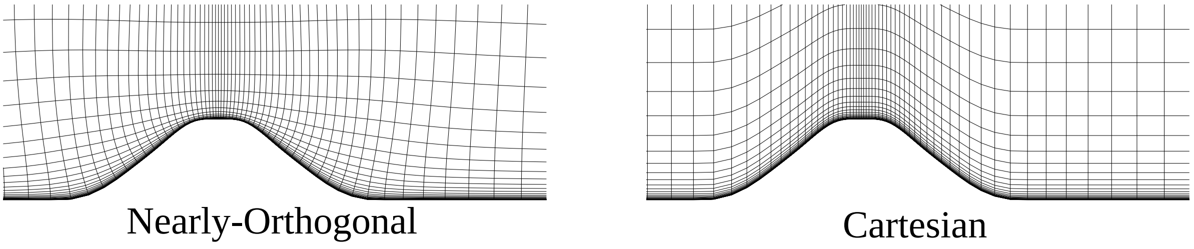

Figure 2: Coarsest grids for the flow over a 2-D hill.

For the backward facing step we have generated three sets of 7 geometrically similar grids ranging from 101 × 101 to 241 × 241 grid nodes. The grid sets include also single block, structured grids and so the two kinks of the wall geometry are included at the boundary line. In two of the sets, there is always a grid node at the two kinks, whereas for the third set there are no grid nodes at the wall kinks. Figure (3) illustrates the coarsest grids of each set.

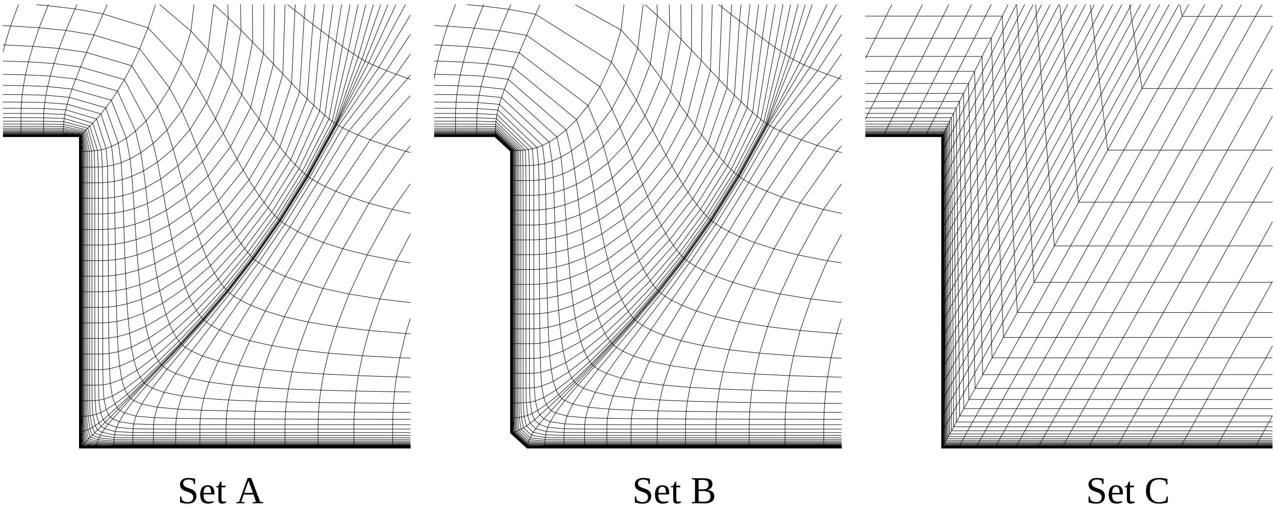

Figure 3: Coarsest grids for the flow over a 2-D hill.

For these two test cases we have generated inlet conditions for the velocity components and for the turbulent quantities of the following turbulence models: Menter's one-equation model, [22], Spalart & Allmaras one-equation model, [23], Low Reynolds Chien's $k-\varepsilon$ model, [24], and TNT and STT $k-\omega$ models, [25] and [26].

For all these turbulence models we have computed the flow field in the available grid sets and reduced the iterative error to machine accuracy. With these results we have performed uncertainty estimates with the method described above to check if the intervals of the solution of a given flow variable obtained from different grid sets overlap.

All the grids and boundary conditions of these two test cases are available to all the groups of the Numerical Ship hydrodynamics community which are interested in performing this verification exercise. We believe that we could learn a lot from the experience of performing uncertainty estimations with different procedures and using CFD methods based on different approaches in a common grid set. Therefore, we invite all the groups to perform such calculations, which could then be confronted in a Workshop that should lead us on the way to produce a reliable procedure for the uncertainty estimation in numerical ship hydrodynamics.

References

[1] Roache P.J. - *Verification and Validation in Computational Science and Engineering* - Hermosa Publishers, 1998.

[2] Stern F., Wilson R., Coleman H.W., Paterson E.G. - *Comprehemsive Approach to Verification and Validation of CFD Simulations - Part 1 : Methodologies and Procedures* - ASME Journal of Fluids Engineering, Vol. 123, pp. 803-810. December 2001.

[3] ITTC Quality Manual

[4] Jasak H. - *Error Analysis and Estimation in the Finite Volume Method with Applications to Fluid Flow* - PhD Thesis, Imperial College, University of London, 1996.

[5] Celik I., Hu G. - *Single Grid Error Estimation using Error Transport Equation* - ASME Journal of Fluids Engineering, to appear.

[6] Hay A., Visonneau M. - *Adaptative Error Control Strategy: Application to a Turbulent Flow* - AIAA meeting, Orlando, June 2003.

[7] Hoekstra M., Eça L. - *An Example of Error Quantification of Ship-Related CFD Results* - 7th Numerical Ship Hydrodynamics Conference, Nantes, July 1999.

[8] Eça L., Hoekstra M. - *On the Numerical Verification of Ship Stern Flow Calculations* - 1^{st} Marnet-CFD Workshop, Barcelona 1999.

[9] Eça L., Hoekstra M. - *An Evaluation of Verification Procedures for Computational Fluid Dynamics* - IST Report D72-7, June 2000.

[10] Eça L., Hoekstra M. - *On the Application of Verification Procedures in Computational Fluid Dynamics* - 2^{st} Marnet-CFD Workshop, Copenhagen 2000.

[11] Eça L, Hoekstra M. - *An Evaluation of Verification Procedures for CFD Applications* - 24^{th} Symposium on Naval Hydrodynamics, Fukuoka, Japan, July 2002.

[12] Eça L., Hoekstra M. - *An Example of Uncertainty Estimation in the Calculation of a 2-D Turbulent Flow* - 4^{th} Marnet-CFD Workshop, Haslar 2003.

[13] Roache P. - *Code Verification by the Method of Manafuctored Solutions* - ASME Journal of Fluids Engineering, Vol. 114, N1, March 2002, pp. 4-10.

[14] ERCOFTAC Classic Collection Database - http://cfd.me.umist.ac.uk/ercoftac

[15] Roache P.J. - *Error Bars for CFD* - AIAA-2003-048, 41^{th} Aerospace Sciences Meeting, Reno NV, January 2003.

[16] Roache P. - *Private communication*

[17] Raven H., Eça L., Hoekstra M. - *A Discussion of Procedures for CFD Uncertainty Analysis* - MARIN Report 17678 -1-RD, October 2002.

[18] Roy C.J. - *Grid Convergence Error Analysis for Mixed-Order Numerical Schemes* - AIAA Paper 2001-2606, June 2001 Anaheim.

[19] Hoekstra M., Eça L. - *PARNASSOS : An Efficient Method for Ship Stern Flow Calculation* - Third Osaka Colloquium on Advanced CFD Applications to Ship Flow and Hull Form Design, Osaka, Japan, 1998.

[20] Almeida G.P., Durão D.F.G., Heitor M.V. - *Wake Flows behind Two-dimensional Model Hills* - Experimental Thermal and Fluid Science, 7, p. 81, 1992.

[21] Driver D.M., Seegmiller H.L. - *Features of a Reattaching Turbulent Shear Layer in Divergent Channel Flow* - AIAA Journal, Vol. 23, N. 2, February 1985.

[22] Menter F.R. - *Eddy Viscosity Transport Equations and Their Relation to the $k-\varepsilon$ Model* - Journal of Fluids Engineering, Vol. 119, December 1997, pp. 876-884.

[23] Spalart P.R., Allmaras S.R. - *A One-Equations Turbulence Model for Aerodynamic Flows* - AIAA 30th Aerospace Sciences Meeting, Reno, January 1992.

[24] Chien K.Y - *Prediction of Channel and Boundary-Layer Flows with a Low-Reynolds-Number Turbulence Model.* - AIAA Journal, January 1992, pp. 33-38.

[25] Kok J.C. - Resolving the Dependence on Free-stream values for the $k-\omega$ Turbulence Model - NLR-TP-99295, 1999, http://www.nlr.nl/public/library/1999/99295-tp.pdf.

[26] Menter F.R. - *Two-Equation Eddy-Viscosity Turbulence Models for Engineering Applications* - AIAA Journal, Vol.32, August 1994, pp. 1598-1605.

RANSE and Vortex-Lattice Simulation for Podded Rudders

Ould El Moctar, Afred Junglewitz, Germanischer Lloyd, moct@GL-Group.com

Podded drives have been developed and successfully introduced in the marked during the last two decades. Despite of some problems of single components, podded drives have proven their suitability and capability as the main propulsion and steering device. They are used mostly in the segment of cruise liners and ferries which need especially at low ship speed a good manoeuvrability. The installed power ranges from 5 up to about 20 MW per piece. The most spectacular ship with podded drives will be launched this year: the Queen Mary 2 with four pods totalling about 80 MW driving power. The ship with a length over all of 345 m will have a speed of 30 kn.

In contradiction to conventional rudder propellers, podded drives produce the lateral steering force not only by changing the propeller jet direction, but also by using a considerable area of the shaft like a conventional rudder. In this respect the pod can be regarded as the Sphinx of steering.

Traditional rules can not be applied on a pod due to the mixed nature of steering device. Consequently, new approaches have to be developed based on CFD calculations and mechanical considerations. Since the traditional rules incorporate decades of positive experience a new approach should be based on traditional formulae or at least should show a connection or comparative philosophy.

The current paper deals with the steering capability of a pod. As an example a SSP-type pod (Siemens Schottel Propulsor) has been chosen. The calculation results of propeller in inclined flow obtained with different methods will be presented. Steering forces and moments are calculated with a RANSE and a Vortex- Lattice code and correlated to those of a conventional rudder. Traditional formulae are applied for both – conventional rudder and pod – and conclusions are drawn, how the gap could be closed with a view on further steps in the near future.

Numerical study of a suction anchor

François Grosjean, Steven Kerampran, Octavian Rosu, ENSIETA, grosjefr@ensieta.fr

Xavier Bompais, Ifremer, Brest, France

Introduction

The suction anchor is a new concept designed to provide strong mooring to offshore platforms. This anchor is a hollow steel cylinder (over 15 m in height) that is deeply embedded in the seabed. Part vacuum is created inside the anchor to ensure a good fixation. The positioning of such a cumbersome element causes some problems to arise, especially when the anchor is lowered from the ship to the seabed. During this translational vertical movement, the anchor is submitted to the ship heave. This additional movement is likely to generate extra constraint on the wire, which could in turn lead to its deterioration. Experimental tests have been performed by Ifremer, using a scaled model, Fig.1. This work aims at simulating the movement of the anchor using a new version a commercial code Fluent. The computations will consider a sinusoidal movement of the anchor (roughly corresponding to its heave) both in a fluid at rest and in a uniform flow. They will be validated with the experimental results provided by Ifremer.

Experimental setup

Experimental results are issued from tests realised in the basin of Ifremer, at Brest, in December 2001, in partnership with Bouygues-Offshore. The basin is 10 meters depth, 50 m long and 12.5 m large, Fig.2. For these tests, a model of suction anchor is hanged on a vertical wire loop, which is anchored at the bottom by two pulleys and moved at the top by a servomotor. The servomotor is PC-controlled. . To simulate the heave of the anchor, vertical sinusoidal motions are imposed at several periods and amplitudes, with or without superposed vertical translatory motions. Sensors measure out the displacement, speed and acceleration of the model as well as the vertical hydrodynamic forces on it.

The hydrodynamic forces are supposed to be as :

$$F_z = M_a.\frac{d_2 z}{dt_2} + B.\frac{dz}{dt}\left|.\frac{dz}{dt}\right|$$

where z is the vertical displacement of the model. M_a and B are two coefficients which characterize the hydrodynamic behaviour of the model, respectively the added mass and the quadratic damping coefficient.

A numerical identification using the Fourier series of force and displacement provides these two coefficients. The comparison between numerical and experimental results can be then more accurate.

Model description

We use the Beta version of the code FLUENT 6 which includes a new functionality enabling to deform the mesh and therefore generate the unsteady movement of a body. This version will be tested on the simple movement of the suction anchor.

We choose a computational domain according to the experimental set up, which itself has a reduction coefficient of ten. The main geometrical characteristics of the anchor are given hereafter. Its upper surface is doted with two circular holes to allow water to flow inside the anchor. These holes can be caped if need be.

- length 1730 mm, diameter 450 mm, Fig.3
- lateral thickness 4 mm, border thickness 10 mm,
- holes - diameter 31 mm, height 80 mm.
- weight 34.4 kg,

Meshing

Given the geometry of the anchor, it is tempting to use a 2D axisymmetrical mesh. In this case, the holes on the upper surface cannot be correctly modelled, and are substituted with a single hole on the axis of the anchor, with an equivalent area. Although this introduces some minor changes in the flow, we believe that these changes are well balanced by a considerable decrease of the mesh size and computational time. A very tight structured grid is generated, in particular in the zone close to the hole and along the anchor, to accurately compute the flow in the boundary layer, Fig.3. The number of hexahedral cells is 37000. In order to check the influence of the changes in the geometry of the upper face, a 3D hexahedral mesh has also been generated, Fig.4, using approximately 110000 cells.

To use the dynamic layering model implemented in Fluent 6, three zones are defined. One will move with the anchor and will include the dynamic mesh the two other zones, which surround the first one, will be fixed. In a given fixed zone, cell layers are either created or destroyed according to whether the dynamic zone moves towards or from a fixed zone. Several parameters can be used to monitor the creation and destruction of cell layers, including the layer thickness, Fig.5:

if the dimension of the cell is not between two given values [$c \cdot l, (1+s) \cdot l$], the code will add a new cell layer [1]. The addition or suppression of layers occurs in the vicinity of the dynamic grid.

The parameters for this dynamic layering are:

- $c \rightarrow$ a dislocation coefficient <<split/collapse factor>> (*c=0.4*) ;
- $s \rightarrow$ a regeneration coefficient <<spring constant factor>>(*s=1) ;*
- $l \rightarrow$ reference dimension along the *x* axis (movement axis) for elementary cell (*l = 0.015m*).

Given the fact that we used a beta version, only the movement of a rod could be modelled at first. Later on we have had the possibility to build a movement using a programmable function. This point has been very important for the success of this study.

Resolution

The fluid is incompressible but viscous. The boundary conditions are: *velocity inlet of 0.8m/s, outflow in the vicinity of the seabed, symmetry along the axis.*

The Reynolds number is $1.45 \cdot 10^{6}$ Generally we use the k-ε standard model for turbulence. The k-ω standard model has also been used on some occurrences.

Residuals are reduced to 10^{-4}. We choose an implicit segregated scheme. After convergence with ‘first-order’ scheme, we use a second-order scheme.

We do not use the gravity because the experimental set-up eliminates its effects.

First Numerical results

The first test was to compare the results in 3D with 2 holes and the results in the axisymmetrical case with a single hole. We did several calculations for a stationary flow and although some noticeable changes in the flow were observed, the net results for the drag on the anchor were strictly the same.

To compare with the experimental results, we choose the following sinusoidal movement: $z = A \cdot \cos(2 \cdot \pi \cdot t / T)$. The movement begins with the anchor first going down. The forces are positive when they are oriented toward the top.

Several cases have been simulated:

- period T=2.222s and several amplitudes *A=0.1, 0.15, 0.2 (m),*
- amplitude *A=0.1m* and several periods *T=1.389, 2.222, 3.03, 4.762 (s)*,
- in the case, *T=1.389s, A=0.2m*, we simulate both situations with the hole open and shut. The differences between the holes open or shut seem to be insignificant.

As can be seen on Fig.5, the forces on the anchor increase when the amplitude is increased.

Comparison with the experimental results shows a poor agreement, Fig.6. Important differences can be observed for the maximum and minimum effort (in the legend, 'mgama' denotes the force due to added mass).
This discrepancy between the numerical and the experimental results is observed in all cases, whatever the amplitude and the periodicity.

Displacement

The movement is given with the function $z = A \cdot \cos(2 \cdot \pi \cdot t / T)$, but in the beta version of the code we have to use the movement of a piston. When the theoretical movement: $z = A \cdot \cos(2 \cdot \pi \cdot t / T)$ (« cos » on Fig.7) is compared to the actual numerical path, it can be seen that the two curves are not superimposed. In fact, the extremes are almost identical but there is a slight difference in the medium part of the curves because the length of the piston is not large enough. The movement in the code doesn't correspond to our case. The Fourier analysis shows that the ratio L/R (length of the rod L and the diameter R of the crank) must be larger than 10 to have little influence on the symmetry of the movement.
If the length of the rod is too large, it becomes difficult to reach the convergence of the computations. By changing progressively this length from 10 to 20, this convergence is eventually obtained, and in the last step we can calculate the movement for a length of 20.
In the final version of Fluent 6, it is possible to model a real movement using a function.

Numerical results

When the movement of the anchor is corrected and is truly sinusoidal, the agreement between numerical and experimental results turns out to be very satisfying for all the studied cases. Some examples are shown on pictures 8 and 9, for the anchor in a fluid at rest. When we calculate the damping coefficients between the holes open or shut, both for the numerical and experimental results, we can see that when we shut the holes, this coefficient is reduced by 25%. For translation and heave, the comparison is again excellent, except close to the extreme where we have some discontinuities most likely due to a large time step. Unfortunately the time step could not be further decreased, since it took a week to obtain the results for 4 periods with a Sun Ultra 10 workstation.

Conclusions

Several conclusions can be drawn from this work:

- We have to be careful about the imposed movement; programming the movement with the rod isn't very convenient. The best way to create the good movement is to use the profile function in Fluent.
- The results are not affected by the opening of the holes on the upper surface of the anchor. The results are very sensitive to the movement, but if the movement is accurate, the numerical results are very close to the experimental ones.
- On this example, we consider ourselves satisfied by the new version of Fluent. We have begun to simulate other movements using programmed functions.

REFERENCES

[1] Documentation FLUENT version 6.0. 2002
Server FLUENT : *http://www.fluentusers.com*

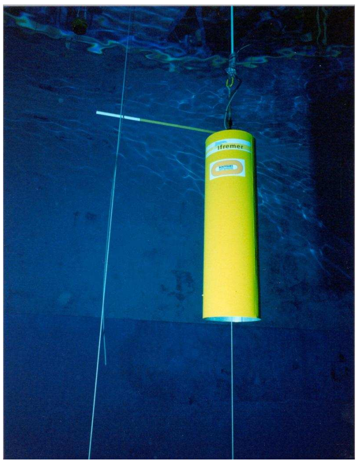

Fig.1: The experimental anchor

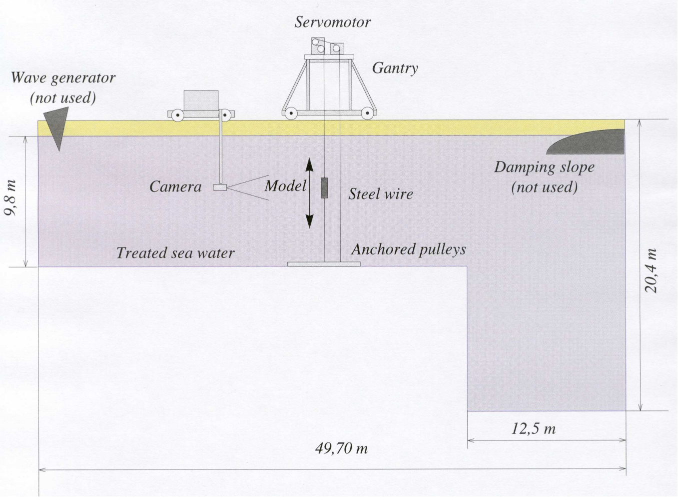

Fig.2: The experimental set-up

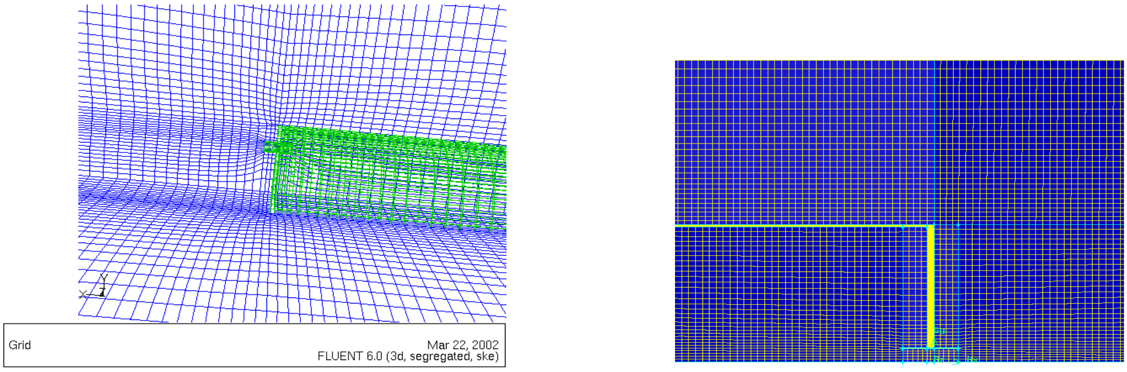

Figs.3 and 4: The 3d mesh and the axisymmetrical one in the vicinity of the hole

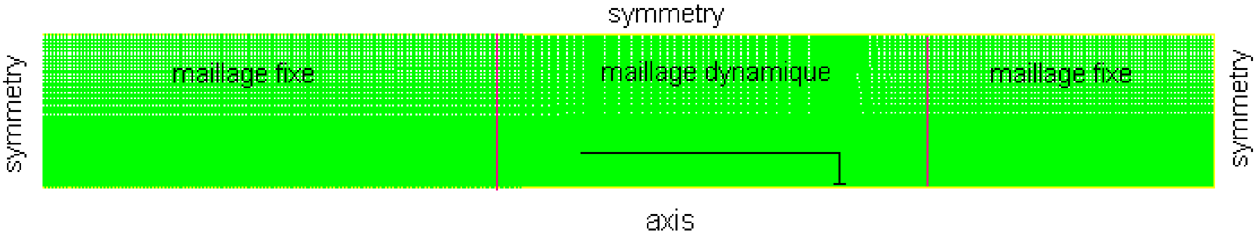

Fig.5: The grid and the boundary conditions

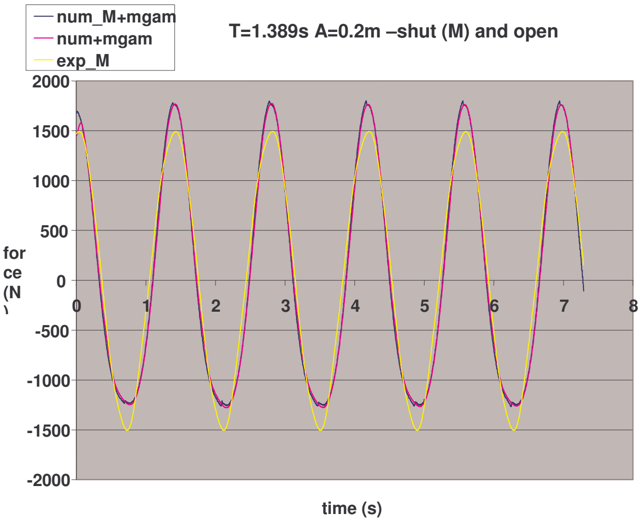

Fig6: First results

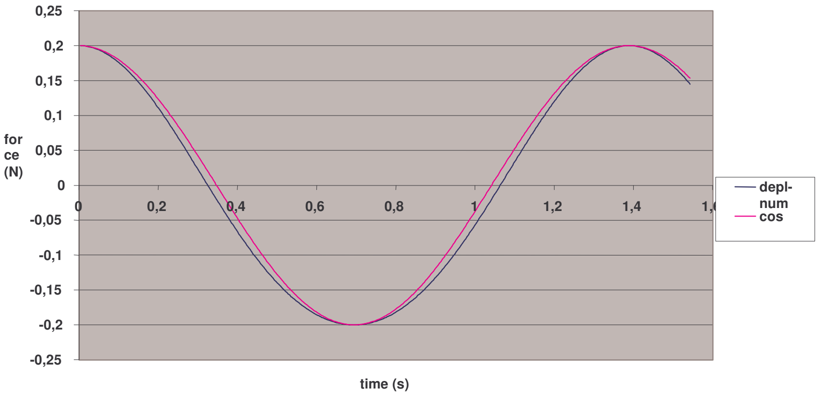

Fig.7: Experimental and numerical movements

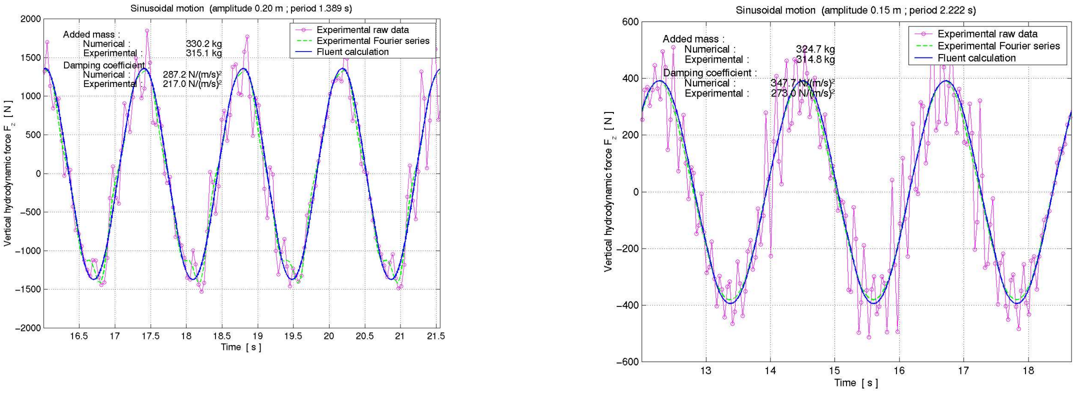

Fig.8: Comparison of experimental and numerical results for a sinusoidal movement

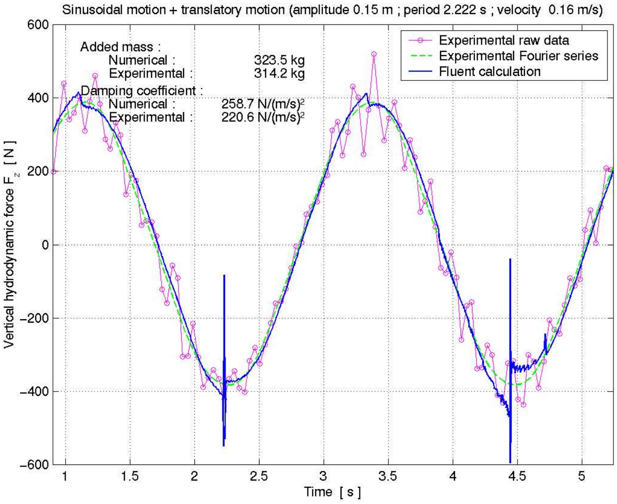

Fig.9: Comparison of experimental and numerical results for a sinusoidal movement with translation

Adaptive grids for RANSE based on numerical error

Alexander Hay and Michel Visonneau
Division Modélisation Numérique, Laboratoire de Mécanique des Fluides CNRS UMR 6598
Ecole Centrale de Nantes, B.P. 92101, rue de la noë 44321 Nantes, France

1 *Introduction*

The goal of CFD research is to find solutions free from numerical error or at least of a desired prescribed accuracy for the lowest computational and human costs. Adaptive h-refinement techniques have been designed for reaching such a solution by dynamically refining and coarsening meshes until the error is under a prescribed value.

For guiding the adaptation process both error estimator and error indicator can be used. The error estimate, considered here, is based on an equation for the error. The equation presents a source term which is approximated by the use of a higher order operator.

The whole procedure is applied to steady turbulent flows and unsteady multi-fluid flows. The gains made by the use of the adaptive mesh strategy compared to single mesh computation are evaluated.

2 *Flow Solver*

The ISIS flow solver, developed in our laboratory, uses the incompressible Reynolds-Averaged Navier-Stokes equations. The solver is based on the finite-volume method to build the spatial discretization of the transport equations on unstructured grids. The face-based method is generalized to unstructured meshes composed of arbitrary volume shapes (they are bounded by an arbitrary number of constitutive faces).

The velocity field is obtained from the momentum conservation equation and the pressure field is extracted from the mass conservation constraint transformed in a pressure equation. The whole discretization is fully implicit in space and time and is formally second order accurate. Several near-wall low-Reynolds number turbulence models, ranging from one-equation Spalart-Allmaras model, two-equation $k-\omega$ closures, to a full Reynolds stress transport $R_{ij}-\omega$ model are implemented in the code.

Incompressible and non-miscible flow phases are modeled through the use of conservation equations for each volume fraction c_i of each phase. These volume fractions permit to determine the effective physical properties of the flow. More details on this topic can be found in [1]

3 *A posteriori error estimation*

The error considered here is often called discretization error. It involves the discretization of the equations which are to be solved as well as the discretization of the geometry and the boundary conditions .

The present method is based on an equation for the discretization error in order to take into account the known transport properties of this quantity. The local error is thus potentially influenced by the whole computational domain.

Considering the exact solution ϕ which satisfies the differential operator $\mathcal{L}$ representing the PDE governing this conserved variable, and a grid G_h of size h from which a numerical solution ϕ_h is computed with the ISIS code, then the discretized error is defined as :

$$e_h = \phi - \phi_h$$

An equation for the error is derived by applying the exact operator $\mathcal{L}$ of the PDE that governs ϕ to e_h. For a linear operator the following equation can be derived :

$$\begin{aligned}\mathcal{L}(e_h) &= \mathcal{L}(\phi) - \mathcal{L}(\phi_h)\\ &= 0 - \mathcal{L}(\phi_h)\\ &= -\mathcal{L}(\phi_h) = S_h\end{aligned}$$

From this equation, it can be observed that the error is driven by *the same transport rules* than the solution ϕ itself and the extra source term comes from *the truncation of functions* that appeared in $\mathcal{L}$.

For a nonlinear operator, the same analysis is not possible but similar features are expected. Thus, the operator $\mathcal{L}$ of the Navier-Stokes equations is linearized in the Newton's sense.

The source term of the resulting equation can not be computed exactly as it involves the exact operator of the PDE. A higher order discretized operator $\mathcal{L}_h^*$ is considered in order to obtain an approximation S_h^* of S_h. For this approximation to be reliable, $\mathcal{L}_h^*$ must be more accurate than the discretized operator $\mathcal{L}_h$ of the flow solver. The higher order finite-volume discretized operator is obtained by a cubic reconstruction of ϕ_h and its derivatives at nodes and center of faces of the control volume and by integration over faces by the Simpson's rule. The whole discretization is formally fourth order accurate. And, as $\mathcal{L}_h^*$ is fourth order accurate and $\mathcal{L}_h$ is at most second order accurate, a good approximation of this source term is thus expected.

Concerning the resolution of the equation for the error, we have shown a posteriori that it is not necessary to use the higher order operator. Both $\mathcal{L}_h^*$ and $\mathcal{L}_h$ have been considered for solving the equation and close results have been obtained for the error field. Consequently, the error can be computed with the same method (and on the same grid) used for solving the PDE of ϕ. Finally, the equation that leads to an estimation of e_h is :

$$\mathcal{L}_h(e_h) = -\mathcal{L}_h^*(\phi_h) = S_h^*$$

More information on the developments of this method and its results can be found in [2].

4 *Adaptive Techniques*

During the adaptive procedure, each control volume marked for grid refinement is subdivided into several smaller ones of *the same topology*. As the initial mesh can possibly be too fine in some region for the desired accuracy, it can be coarsened by an *agglomeration algorithm*. The adaptive procedure is completely included in the ISIS code making it an automatic single numerical tool.

The adaptive procedure is summarized on figure 1. It starts with the computation of a first numerical solution on an initial uniform grid with an arbitrary number of cells. The error estimator or the error indicator is then computed to decide which changes should be made on the current mesh. The criteria of selection of a cell i on the current $Grid_j$ are the following :

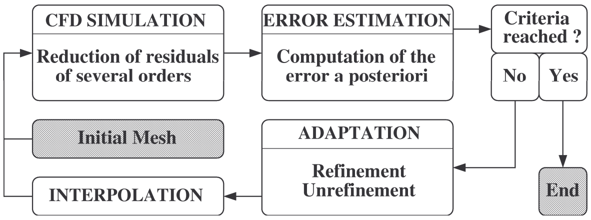

Figure 1: Adaptive procedure

Refinement : $Err_{Grid_j}(i) > \mathsf{TolR} * ||Err_{Grid_1}||_{L1}$
Unrefinement : $Err_{Grid_j}(i) < \mathsf{TolD} * ||Err_{Grid_1}||_{L1}$

The parameters TolR and TolD control the intensity of the procedure during one adaptive step for the refinement and the unrefinement process respectively. The numerical solution is then “mapped” on the new adapted mesh and the computation is resumed on this grid. If an error estimator is considered, this procedure is repeated until the error estimate is below a desired value. In practice a reduction of a factor Red of the L_1 norm of the error over the domain is asked for handling the accuracy of the numerical solution. Thus, the procedure ends when the current $Grid_j$ satisfies :

$$||Err_{Grid_j}||_{L1} < \frac{||Err_{Grid_1}||_{L1}}{\mathsf{Red}}$$

All these possible grid alterations can be canceled as the initial mesh can be recovered by the use of connectivities between the different generations of meshes. Thus, the regions of the mesh that must be adapted are allowed to change during the computation as it is the case for unsteady computation.

5 *Numerical application*

5.1 Turbulent flow around a square-cross section cylinder

The problem consists in simulating the flow of air for a Reynolds number of 22000 around a square-cross section cylinder located in the vicinity of a solid wall. The geometry is described on figure 2. With a gap between the plate and the bottom square-cross section cylinder of $S/D = 0.25$, the flow is stationary.
The two-equation $k - \omega$ turbulence model of *F.R. Menter* is considered in this study. Details on the computational domain and boundary conditions can be found in [2]. For this non-linear problem, the exact solution is not known. In order to evaluate the quality of the adapted solutions, a uniform grid refinement study has been performed. Six uniform grids of increasing fineness have been considered for making single mesh computations (see table 2). The different solutions obtained from the considered grids converge to a practically mesh independent solution (see figure 5) which will be used as a reference for evaluating the quality of the adapted solution.

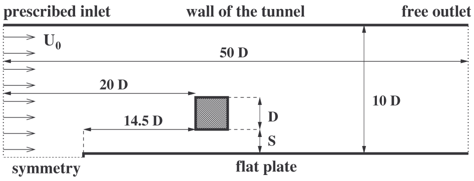

Figure 2: Computational domain

The coarsest uniform mesh (Grid 1) is used as the starting point of the present computation. The norm of the error vector of the velocity, and the error for the kinetic turbulent energy k were considered in the adaptive process. It is believed *a priori* that taking into account the error for k allows to resolve accurately the turbulent properties of the flow since the kinetic turbulent energy is linked to the intensity of turbulence.

The parameters that control the adaptive procedure are $\mathsf{TolR} = 0.4$, $\mathsf{TolD} = 0.08$ and $\mathsf{Red} = 5$. The same tolerance of refinement TolR is applied for the treatment of $\overrightarrow{U}$ and k. For reaching the chosen criterion, three adaptive steps of isotropic refinement were performed and the resulting final adapted mesh has 35314 computational points. The initial uniform mesh and the final adapted mesh obtained after the three cycles of adaptation are presented in figure 4. The regions that were refined or coarsened can clearly be seen along with the agglomerated cells created by unrefinement of the initial mesh.

Figure 5 presents a comparison of the profiles of the normalized streamwise component of the mean flow U/U_∞, for the all the grids considered, extracted at $X/D = 0$, i.e. on the middle top face of the square cylinder. The profiles of the normalized shear component of the Reynolds stress are also given. It can be concluded from these profiles that the solution of the adaptive procedure has reached the fine grid solution. This is especially true for the turbulent correlation. More precisely, the adapted solution profiles are close to the ones obtained on the uniform grid 5 so that the two computations can be considered as comparable in terms of accuracy. In figure 6, the same profiles are extracted at $X/D = 2$, i.e. in the wake of the square cylinder. Once again, these profiles indicate that the solution of the adaptive computation is comparable to the uniform grid 5 solution. From these results, it can be concluded that the adapted grid solution is at least of comparable accuracy to the one of the uniform grid 5 solution.

In order to quantify the gains obtained by the use of the adaptive procedure compared to single uniform mesh computation, table 2 presents also the number of computational points of the different meshes considered in this study and the CPU time (relative to the one of the coarsest uniform grid) needed for reaching a converged solution. The CPU time for the adaptive computation referred to the whole adaptive procedure from the initial grid to the final adapted grid including error estimations. Compared to the uniform grid 5, which has been demonstrated of the same accuracy, the adaptive computation requires almost 4 times less computational points and more than 10 times less CPU time.

5.2 Unsteady multi-fluid flows

The free oscillations of a free surface in a tank are considered here. The initial state of the interface between air and water is a half-cosinusoide of amplitude $0.005m$ for a mean level h of $0.05m$ as illustrated on figure 3. As the main feature of interest is an accurate capturing of the interface, the adaptation process will be guided by the norm of the gradient of the volume fraction so that it will occur around the free surface. Changes in the mesh are performed 20 times per period. Examples of meshes generated during the adaptive computation are shown on figure 7. The force applied during two periods by the flow on the left-hand side wall of the tank computed by the adaptive computation is plotted on figure 8. This result is compared with the one of a uniform mesh as fine as the adapted meshes in the region of the free surface (Grid 2) and the one of a uniform mesh with almost the same number of points than the adaptive grids (Grid 1). The table 1 gives the CPU times consumed by the different computations. It can be concluded that the adaptive solution is more accurate than the solution on Grid 1 and in close agreement with the fine solution on Grid 2 for almost 6 times less CPU time requirement and 7 times less computational points.

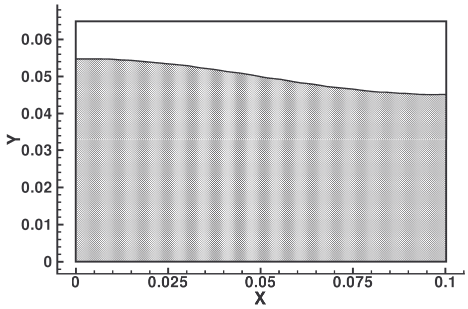

Figure 3: Computational domain

	Grid 1	Grid 2	Adaptive
Nb of Cells	1748	11781	1668-1785
CPU Time	438.94	4737.73	719.00

Table 1: Informations on computations

More complex multi-fluid flow problems will be treated using the adaptive procedure for the final presentation.

6 *Conclusions*

An adaptive h-refinement procedure guided by both error estimator and error indicator has been presented. It has been shown to be general since the initial mesh can be both refined and coarsened. The adaptive procedure included in the ISIS flow solver is a complete automatic single tool for reaching accurate solutions for a low computational cost. This tool has shown interesting gains for two-dimensional flows in term of CPU time and memory requirement compared to single mesh computations.

References

[1] G.B. Deng, E. Guilmineau, P. Queutey and M. Visonneau, Interface capturing and interface tracking of incompressible and immiscible viscous flows, Huitièmes journées de l'hydrodynamique, March 5-7, Nantes , France, 2001.

[2] A. Hay and M. Visonneau, Adaptive error control strategy : Application to a turbulent flow, AIAA 16th Computational Fluid Dynamics Conference, AIAA Paper 2003-3848, June 23-26, Orlando, FL, 2003.

	Grid 1	Grid 2	Grid 3	Grid 4	Grid 5	Grid 6	Adaptive
Nb of Cells	4288	8355	16733	68293	135436	550609	35314
CPU Time	1	3.27	13.89	138.06	709.65	7162.86	69.77

Table 2: Informations on computations

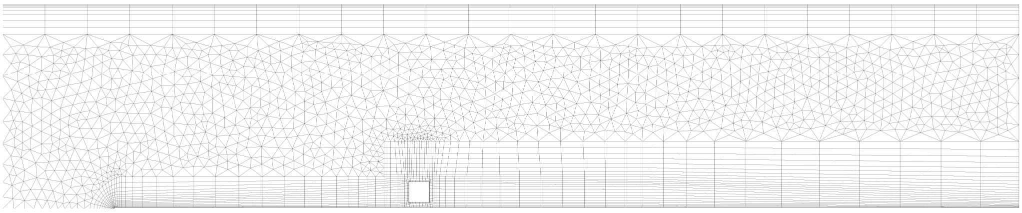

(a) Initial Uniform Mesh (4288 cells)

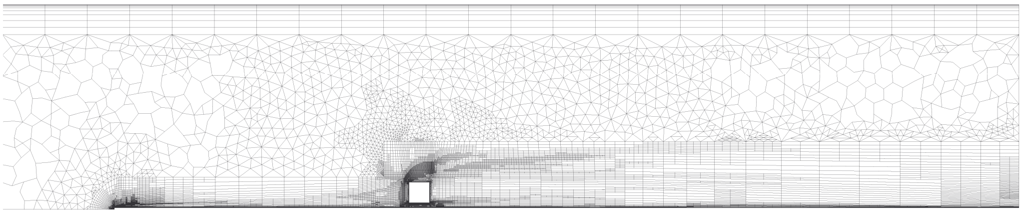

(b) Final Adapted Mesh (35314 cells - 3 adaptive steps)

Figure 4: Global view of the meshes

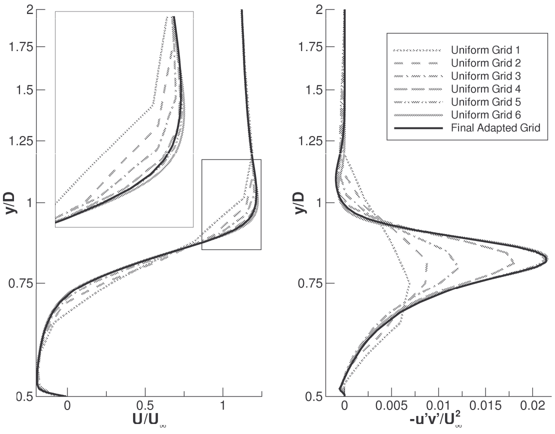

Figure 5: Profiles extracted at $X/D = 0$

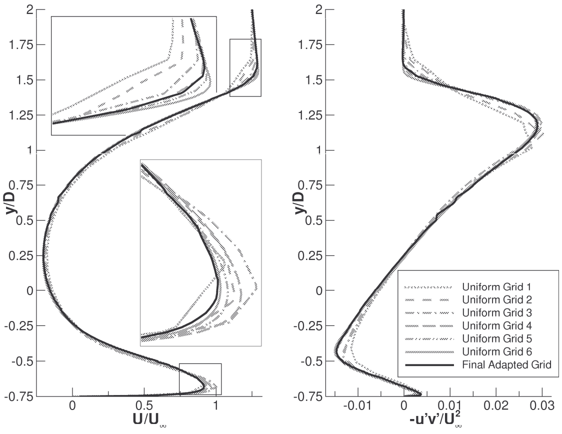

Figure 6: Profiles extracted at $X/D = 2$

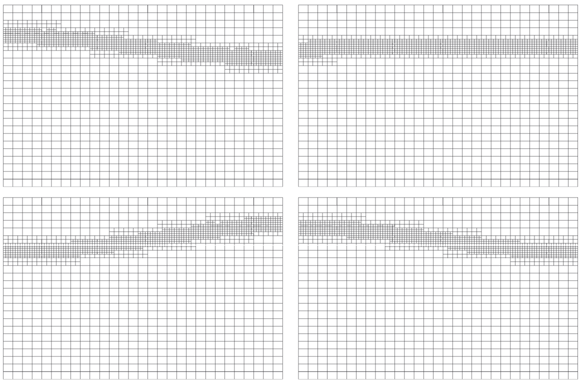

Figure 7: Examples of meshes

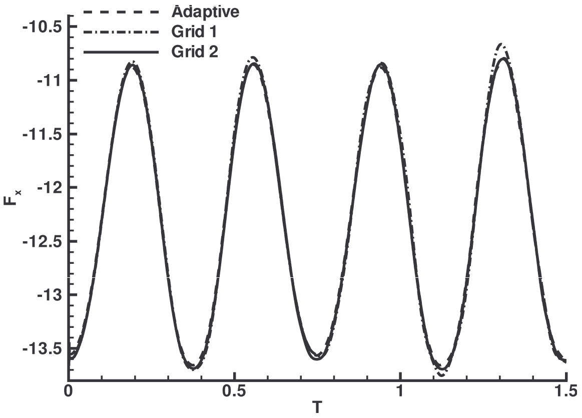

Figure 8: Effort on the left-hand wall

Surface ripples past breaking waves generated by a submerged hydrofoil

A. Iafrati, E.F. Campana,
INSEAN - Via di Vallerano, 139 - 00128 - Roma (ITALY)

1 Abstract

The bulge-capillary wave system generated by a hydrofoil moving beneath the air-water interface is numerically investigated via a heterogeneous domain decomposition technique that uses a two-fluid Navier-Stokes solver to describe flow about the free surface. Attention is here focused on the surface ripples generated by a gentle spilling breaker at small scales when surface tension effects significantly affect the dynamics of the air-water interface. As a matter of fact, at the smallest scales, surface tension suppresses the formation of the plunging jet and the breaking wave establishment takes place without water impact and no air is entrapped. A bulge grows about the wave crest which slides down upon the forward face of the wave and an intense shear layer develops beneath. Instabilities of this shear layer is found to be the mechanism responsible for the generation of coherent vortex-structures which interact with the free surface and lead to the formation of large downstream propagating free surface ripples.

2 Introduction

In [8] it is shown how the wave breaking establishment is affected by surface tension when reducing the length scale. The air entrapment and the plunging jet, characterizing large scale wave breaking, progressively disappears. The plunging jet is replaced by a growing bulge that eventually slides down on the forward face of the wave. This mechanism characterizing the establishment of gentle spilling breaking has been experimentally found by Qiao & Duncan [6] and reference cited therein.

During the downslope motion of the bulge toward the forward wave trough, an intense shear layer develops as a result of the interaction with the upslope incoming flow beneath. Although with a reduced intensity, the shear layer is still present when the bulge reaches its final, quasi-steady, configuration near the wave trough. In this conditions, downstream propagating ripples have been observed experimentally. With the help of a stability analysis, in [3] it is shown that their characteristic wavelength matches rather well that of the most unstable modes of the shear layer.

In this paper the small scale wave breaking flow generated by a submerged hydrofoil is numerically investigated through a heterogeneous domain decomposition technique [4] which makes use of a potential flow solver to describe the flow about the body and of a viscous flow solver to describe the flow about the air-water interface. To allow the description of the complex interface topology changes, the flow in air and water is simulated as that of a single incompressible fluid physical properties of which smoothly changes about the interface. The latter is captured via a Level-Set approach.

The numerical model is used to simulate the unsteady flow generated by a towed hydrofoil starting from rest. Results showing the surface ripples formation and their downstream propagation are presented in terms of free surface profiles. The evolution of the vorticity field is also presented clearly showing the shear layer instabilities as the responsible mechanism for the surface ripples generation.

3 Numerical model

An unsteady heterogeneous domain decomposition approach has been developed to tackle the wave breaking flow induced by a submerged hydrofoil moving beneath the free surface [4]. In the free surface region, a viscous flow model with an interface capturing technique is adopted, while, in the body region, a potential flow approximation is used. To dynamically couple the flows in the two subdomains, a procedure is developed which allows exchange of information without overlapping between the subdomains.

In the body subdomain the flow is governed by a Laplace equation for the velocity potential ϕ which satisfies Neumann boundary conditions at the inflow, the outflow, the bottom of the channel and all along the body contour. Along the matching line between the subdomains, the velocity potential is assigned by the integrating in time t the unsteady Bernoulli equation:

$$\varphi = \int_0^t \frac{\partial \varphi}{\partial t}\, dt \tag{1}$$

with

$$\frac{\partial \varphi}{\partial t} = -\frac{p^B}{\varrho} - gy - \frac{|\boldsymbol{u}|^2}{2} \quad ,$$

where ϱ is the fluid density, g is the acceleration of gravity, y is the vertical coordinate oriented upward and $\boldsymbol{u}$ is the local fluid velocity. To enforce continuity of normal stresses, the pressure acting on the body domain p^B is related to that provided by the Navier-Stokes solver in the free surface domain p^F by the equation

$$p^B = p^F - 2\mu \frac{\partial u_n}{\partial n}$$

$\boldsymbol{n}$ being the normal vector and μ the local fluid viscosity, as evaluated in the free surface domain. Furthermore, a steady Kutta condition is applied at the trailing edge of the hydrofoil to properly account for the vortex shedding.

In the free surface region, the two phase flow of air and water is approximated by that of a single incompressible fluid with density and viscosity varying smoothly through the interface. The system of Navier-Stokes equations is solved by using a finite volume method on a non staggered grid. A fractional step approach is used: the momentum equation is advanced in time neglecting pressure contributions whose effects are successively reintroduced by enforcing continuity of the velocity field. Integration in time is carried out with a three-step Runge-Kutta scheme.

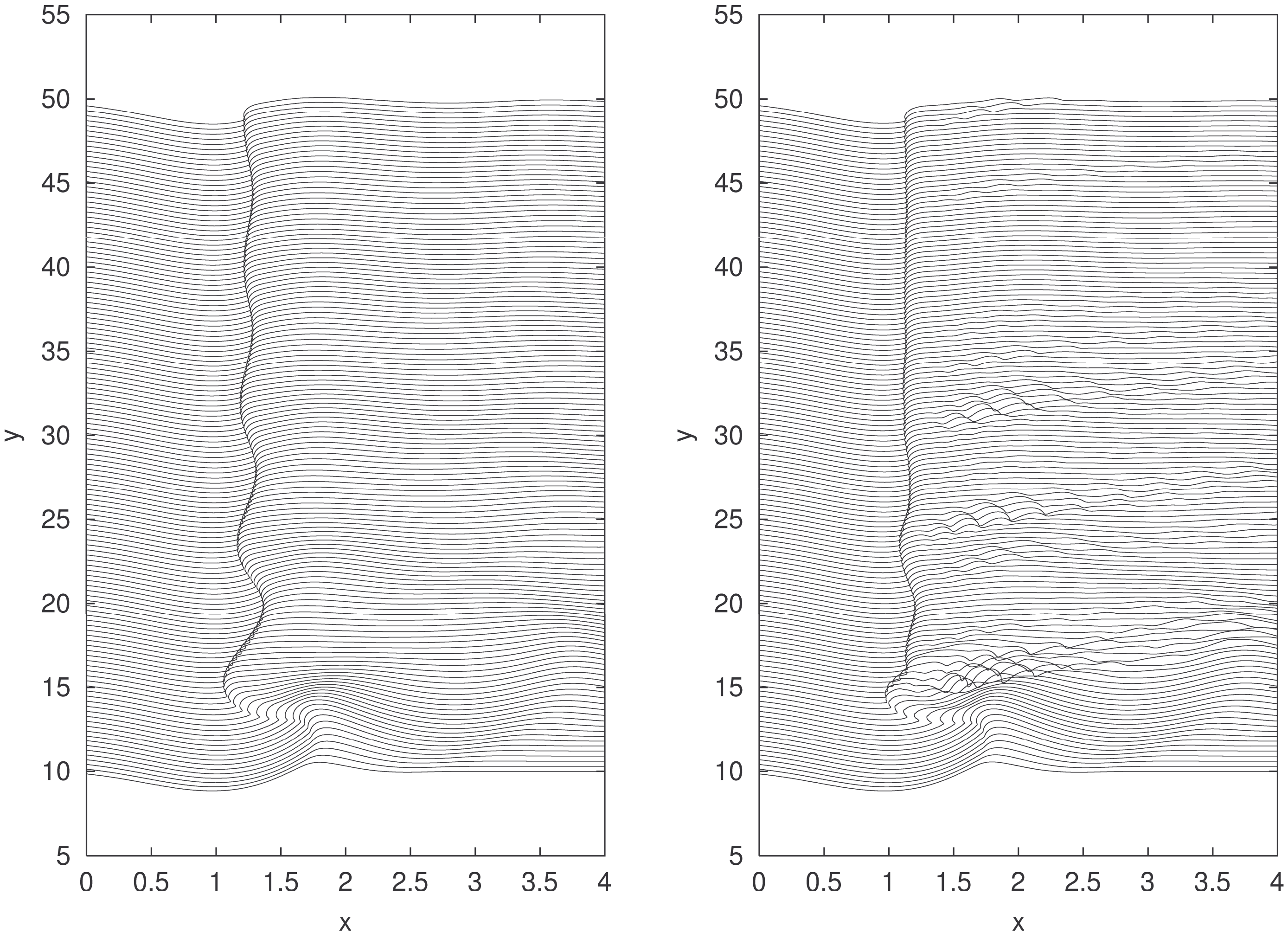

Figure 1 Time sequence of free surface profiles for $Re = 1000$ (*left*) and $Re = 2480$ (*right*). Here $\Delta t = 0.1$ is the time delay and also the vertical shift between two successive profiles.

The air-water interface is captured as the zero level-set of a signed normal distance d from the interface which is initialized as $d > 0$ in water, $d < 0$ in air. During the motion, the distance is transported by the flow and the interface at the new time is given by the level-set $d = 0$ of the new distribution of the distance function. To avoid difficulties in evaluating derivatives, fluid properties are assumed to vary smoothly in a small neighborhood of the interface. To keep constant in time the width of the jump region, the distance function is periodically reinitialized as the minimum distance from the interface [7].

4 Some numerical results

The numerical model is used to simulate the unsteady free surface flow generated by a NACA 0012 hydrofoil moving at a depth $d = 0.783$ beneath the still water level (length is nondimensionalised by the chord L) with an angle of attack $\alpha = 5°$. Starting from the experimental data by Duncan [2], wave breaking conditions are found for

$$Fr = \frac{U}{gL} = 0.576 \quad We = U\sqrt{\varrho_w L \sigma} = 10.5$$

where ϱ_w is the water density and σ is the surface tension coefficient. Numerical simulations are carried out at two different values of the Reynolds number $Re = \varrho_w UL/\mu_w$ based on water properties, that is $Re = 1000$ and $Re = 2480$.

The computational domain extends from $x = -15$ to $x = 15$, the leading edge of the hydrofoil being located at $x = 0$. The matching surface between the lower and upper subdomains is located at $y = -0.2$ and the top boundary is at $y = 0.4$. The grid has 768×192 cells, and is clustered about the breaking region where we have $\Delta y = 0.0025$ and $\Delta x \simeq 0.0027$. The density and viscosity jumps, ratios of which is the same as that of air and water, are spread on a stripe which thickness is 0.04. In order to reduce the formation of forward propagating waves, the hydrofoil is smoothly accelerated up to the final speed which is reached at $t = 10$. Two numerical beach models are introduced about the two ends of the computational domain. In these regions an additional term is introduced in the equation governing the interface dynamics aimed at damping disturbances outgoing from the computational domain.

In Fig. 1 the sequence of free surface profiles obtained for $Re = 1000$ in the hydrofoil frame of reference is plotted. It shows the initial steepening of the crest, the bulge growth and its subsequent sliding motion as a consequence of the breaking establishment. Next, the front of the bulge experiences damped oscillations which are due to the start from the rest [1]. Although this picture exhibits a rather smooth and regular behaviour, a closer inspection (not shown here) reveals the presence of small amplitude ripples which propagates downstream.

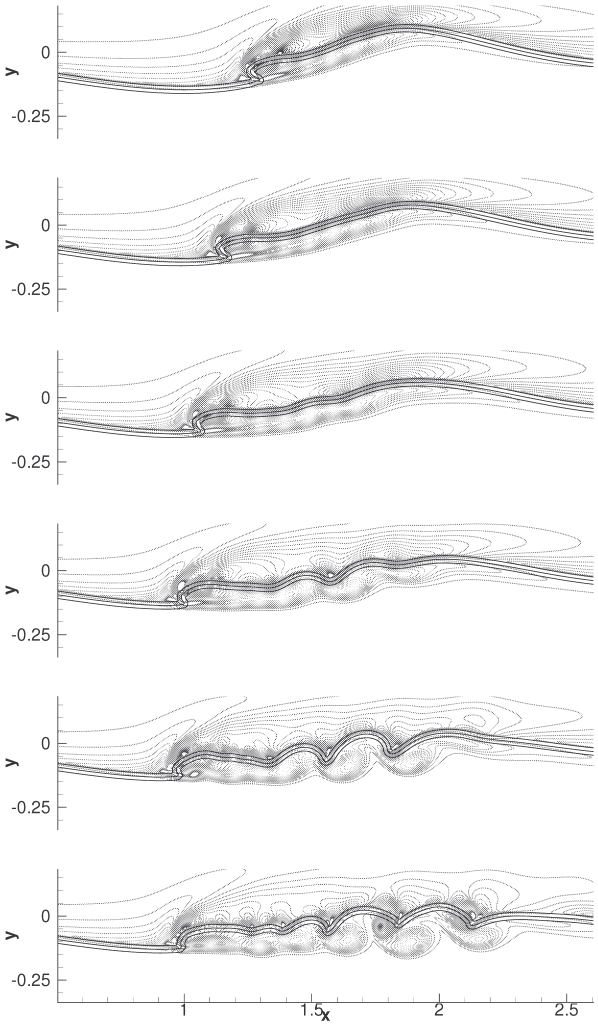

Figure 3 Sequence of vorticity contours during the first upstream motion of the bulge, revealing the development of shear layer instabilities and the corresponding formation of free surface ripples.

To get more insights about the nature of these ripples and of the mechanisms governing their propagation, the numerical simulation is repeated by using $Re = 2480$. The resulting profile history, reported in Fig.2, exhibits significant differences with respect to the previous case. In particular, the bulge reaches an upstream foremost position and much larger downstream propagating ripples appear. Clearly evident is also the recurrence of ripples formation and the faster damp of the bulge oscillations, likely due to the increased energy dissipation provided by the larger ripple formation. A deeper discussion is reported in [5] where frequency-wavenumber spectra of the free surface fluctuations are evaluated. From the spectra it is seen that the ripples wavelength grows during the downstream propagation while their amplitude decays rather slowly. In [5] it is speculated that the lower decay rate of the numerical results compared to the experimental results reported in [3] has to be ascribed to the lower Reynolds number and, more important, to the neglected three dimensional effects.

A better understanding of the ripples formation can be drawn by looking at the sequence of vorticity contours shown in Fig. 3. In this picture three density levels are also depicted to show the interface position. The three levels denote the air, average and water values, respectively. The sequence shows the development of a shear layer at the toe between the flow into the bulge and the incoming upslope flow. Hence, shear layer instabilities are generated which give rise to separated coherent structures that strongly interacts with the free surface. As a consequence, free surface ripples are just traces on the free surface of the underlying vortex blobs and their propagation speed is the same at which vortex-blobs are convected into the water. This mechanism agrees with that experimentally observed in [6] and also speculated in [3].

It is worth of noting that the interaction of the coherent structures with the wave troughs induces a strong vertical asymmetry of the free surface profiles. Furthermore, this continuous interaction can lead to the formation of secondary vortex structures, as it can be noted in the last configuration of Fig. 3. Once secondary vorticity structures appear, they acts to slow down the primary ones and, as a consequence, the curvature at the wave troughs is progressively reducing.

References

[1] Duncan J.H., *An experimental investigation of breaking waves produced by a towed hydrofoil*, Proc. R. Soc. Lond., vol. A 377, 331–348 (1981)

[2] Duncan J.H. *The breaking and nonbreaking wave resistance of a two–dimensional hydrofoil*, J. Fluid Mech., vol. 126, pp. 507-620 (1983)

[3] Duncan J.H., Dimas A.A., *Surface ripples due to steady breaking waves*, J. Fluid Mech., vol. 329, pp. 309-339 (1996)

[4] Iafrati A., Campana E.F., *A domain decomposition approach to compute wave breaking*, Int. J. Numer. Meth. in Fluids, vol. 41, 419-445 (2003)

[5] Iafrati A., Campana E.F., *Flow field evolution beneath microbreakers*, submitted for publication of the J. Fluid Mech. (2003)

[6] Qiao H., Duncan J.H., *Gentle spilling breakers: crest flow field evolution*, J. Fluid Mech., vol. 439, pp. 57-85 (2001)

[7] Sussman M., Smereka P., Osher S., *A level set approach for computing solutions to incompressible two-phase flow*, J. Comput. Phys., vol. 114, pp. 146-159 (1994)

[8] Tulin M.P., *Breaking of ocean waves and downshifting*, Waves and Nonlinear Processes in Hydrodynamics, Grue J., Gjevik B. and Weber J.E. Eds., Kluwer Acad., Dordrecht, Netherland, pp. 170-190 (1996)

Water entry of 2D finite wedges

Alessandro Iafrati, Davide Battistin
a.iafrati@insean.it,d.battistin@insean.it
INSEAN - Via di Vallerano, 139 - 00128 - Roma (ITALY)

Abstract

The free surface flow generated during water entry of 2D finite wedges is here investigated. The flow is potential and the fluid incompressible. Attention is devoted to the analysis of the transition from the chine-unwetted to the chine-wetted condition, when flow separation from the body corner takes place. To achieve this goal, the spray developing about the intersection of the free surface with the body contour is accurately described by a hybrid finite-element model coupled with the boundary-element approach that is adopted to describe the solution in the whole of the fluid. When the spray tip reaches the separation point, a Kutta condition is applied requiring slope continuity of the fluid boundary at the corner. Free surface shape, pressure distribution and history of the hydrodynamic force throughout the water entry process are presented.

1 Introduction

The free surface flow taking place during the water entry of 2D finite wedges is investigated. The study is carried out by assuming the flow to be potential and the fluid incompressible. Gravity and surface tension effects are also neglected.

Attention is mainly concerned with the development of a numerical model to describe the free surface flow taking place during the flow separation taking place when the thin spray reaches the wedge corner. This rather complicated problem has been analysed in the past by Vorus [5] and by Zhao *et al.* [7]. In [5] the water entry problem is analysed with the help the so called flat cylinder theory which enforces nonlinear boundary conditions on a linearized body contour (that is on the horizontal axis). Within this approach the occurrence of flow separation is handled in terms of a suitable boundary condition.

In [7], under the same potential flow assumptions, the problem has been investigated through an extension of the fully nonlinear numerical model originally proposed in [6]. In this latter a model is introduced which cuts off the spray that develops about the intersection between the free surface and the body contour as a result of the local flow singularity and replaces it by an appropriate boundary condition applied at the truncation. In [7] a Kutta condition is enforced at the separation point as soon as the jet truncation passes through it.

In the present paper a fully nonlinear numerical model able to deal with flow separation from body contour is developed. Differently from the model adopted in [7], here the spray is not cut off but, instead, is accurately described in terms of a simplified model based on a finite element discretization of the thin layer [2].

The set of differential equations governing the free surface flow is solved with the help of a mixed Eulerian-Lagrangian (MEL) formulation [3]. The jet layer is discretized into small control volumes and the velocity potential within each one is written as an harmonic expansion in power series. The coefficient of the power series are derived from the boundary conditions applied at the free surface and at the body contour. Additional matching conditions among adjacent elements are also applied to guarantee regulatity of the solution. When the first control volume of the jet approaches and crosses the separation point, a Kutta condition is locally applied requiring that fluid particles have to leave the body tangentially.

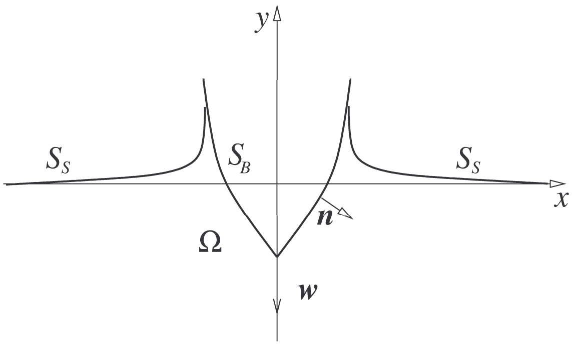

Figure 1: Sketch of the system.

2 Mathematical model

Within the above assumptions, let φ denotes the velocity potential, the free surface flow is governed by the following set of equations

$$\begin{aligned} \Delta\varphi &= 0 && \Omega \\ \varphi_n &= -V n_y && S_B \\ \frac{D\varphi}{Dt} &= \frac{|\nabla\varphi|^2}{2} && S_S \\ \frac{D\boldsymbol{x}}{Dt} &= \boldsymbol{u} && S_S\ , \end{aligned} \qquad (1)$$

where V is the entry velocity which is assumed to be constant (Fig. 1). This initial value problem is solved through a MEL technique and at each time step a boundary value problem is solved by using an integral representation of the velocity potential φ.

The hydrodynamic load acting on the impacting body is calculated through integration of the pressure field along the wetted portion of the contour, evaluated by means of the unsteady Bernoulli equation

$$p = -\rho_0 \left(\varphi_t + \frac{|\nabla\varphi|^2}{2} \right) . \qquad (2)$$

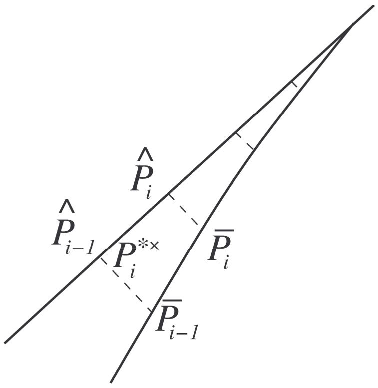

Figure 2: Sketch of the definitions used for the control volume V_i in the modelled jet region.

where ρ_0 is the fluid density. The unsteady contribution φ_t is obtained first by exploiting its harmonic properties. Hence a boundary value problem is formulated similar to that used for the velocity potential itself. As for the velocity potential problem, the boundary condition on the body is of Neumann type [1]:

$$(\varphi_t)_n = -V_\tau (u_n)_\tau + V_n (u_\tau)_\tau - k_\tau \boldsymbol{V} \cdot \boldsymbol{u} \tag{3}$$

where k_τ is the local curvature of the body contour. On the free surface a Dirichlet type condition holds instead, that is easily derived from the Bernoulli equation (here the atmospheric pressure is set equal to zero):

$$\varphi_t = -\frac{|\nabla \varphi|^2}{2} \tag{4}$$

The numerical solution of the water entry flow is rather challenging because of the particular features of the flow about the intersection between the free surface and the body contour. A great simplification of the problem is achieved through a model which cut off the thin layer from the computational domain and replaces it with a suitable boundary condition [6]. Although this model does not significantly affect the pressure distribution and total hydrodynamic load [1], details about the fluid motion inside the truncated part of the jet are completely lost. For this reason a new model has been developed in [2] which is based on a subdivision of the modelled part into small control volumes. Within each one the velocity potential is written in the form of an harmonic Taylor series, up to the second order, about the corresponding centroid (x_i^*, y_i^*) (see Fig.2):

$$\begin{aligned} \varphi_i^J(x,y) = A_i + B_i(x - x_i^*) + C_i(y - y_i^*) + \qquad (5) \\ \frac{D_i}{2}\left[(x - x_i^*)^2 - (y - y_i^*)^2\right] + E_i(x - x_i^*)(y - y_i^*) \ . \end{aligned}$$

The coefficients appearing in eq. (5) are obtained by enforcing boundary conditions on the body and free surface side. Furthermore, an additional matching condition is applied among adjacent elements to guarantee regularity of the solution [2]. A completely similar model is used when evaluating the time derivative of the velocity potential, φ_t.

Once flow separation from the corner of the wedge takes place, we assume that particles which were moving along the body contour, continue moving along the tangent to the body at the separation point. This aim is achieved by enforcing a Neumann boundary condition on a very small part of the free surface adjacent to the wedge corner.

From the numerical point of view, once the fluid starts leaving the body, the jet model is simplified, by reducing the series expansion to the first order. This assumption gives to any pair of points $(\hat{P}_i, \bar{P}_i)$ lying on the two free surface pieces that bounds the control volume V_i, the same velocity and then the thickness of the jet layer remains "frozen". Although this assumption does not allow to strictly conserve the mass, it is of great help in terms of stability of the numerical algorithm.

3 Numerical discretization

The numerical discretization is zero order in space, thus approximating the unknowns with piecewise constant functions on straight panels, and second order in time, making use of a Runge-Kutta integration scheme. For stability reasons, the time step is chosen such that the (maximum) displacement of the centroid is smaller than one fourth of the corresponding panel length. At each time step, centroids of the free surface panels are moved in a Lagrangian way. Their position is interpolated with splines and panel vertices are located along the interpolating contour. Once flow separation takes place, a Neumann condition is applied at the first panel of the free surface, requiring that the normal velocity is equal to that of the last panel on the body.

To account for the finite extension of the computational domain, the far field behavior of the solution is profitably used. At very large distances r_F from the body, the potential is approximated by that of a vertical dipole

$$C_D(t)\varphi_D(x,y) = C_D(t)\frac{y}{x^2 + y^2} = C_D(t)\frac{\sin\theta}{r_F} \ . \tag{6}$$

A far field domain boundary of circular shape ($r = r_F$) is introduced, which joins the two ends of the free surface portions lying inside the computational domain. Along this far field boundary a Dirichlet condition is applied and the normal derivative of the velocity potential is obtained from the solution of the boundary integral problem. The dipole constant C_D is derived by assuming that the total incoming flow obtained as the integral of the inflow from the far field boundary equals that provided by the dipole solution, that is:

$$-\int_{S_F} \varphi_n(Q)\, dS(Q) + C_D \int_{S_F} \varphi_{Dn}(Q)\, dS(Q) = 0 \ . \tag{7}$$

4 Numerical results and model validation

The fully nonlinear numerical model so far discussed has been already deeply validated in [2] for what concerns the

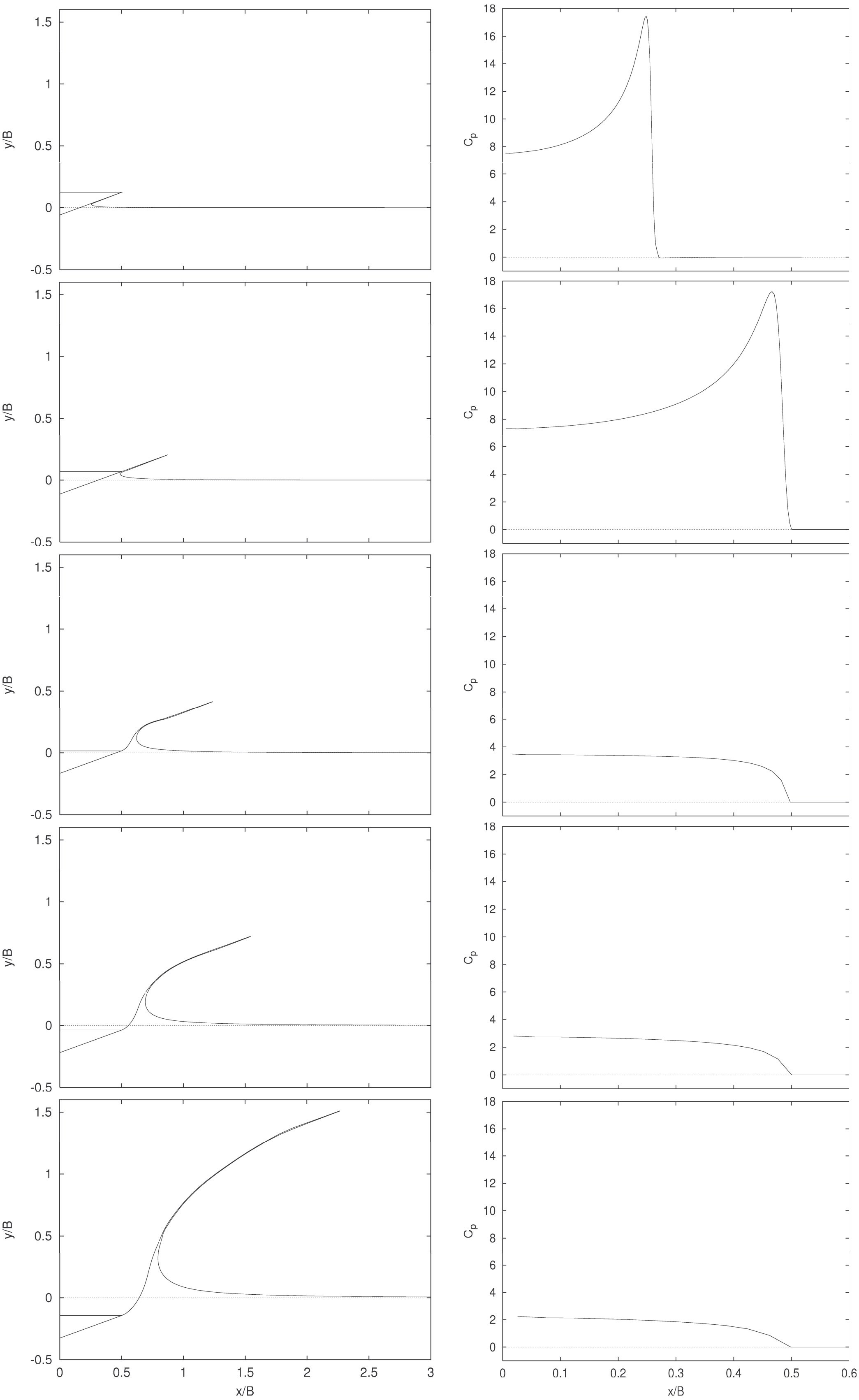

Figure 3: Free surface configurations and pressure distributions at five time instants, for a 20° wedge.

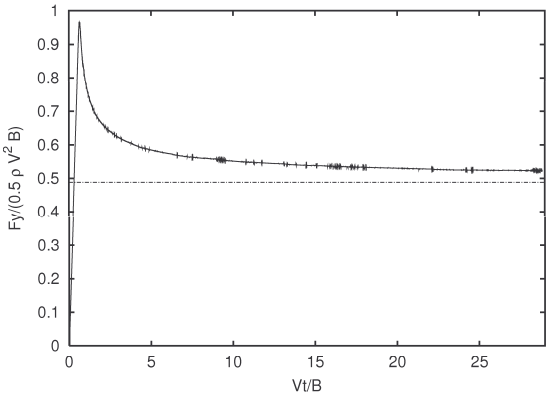

Figure 4: Force history for a 60° wedge. The horizontal line is the value of the corresponding cavity flow solution [4].

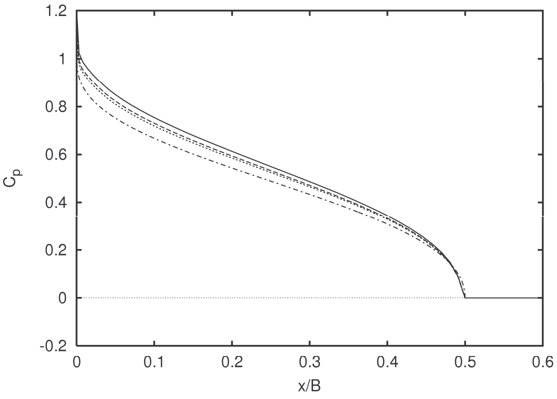

Figure 5: Asymptotic pressure distribution on a 60° wedge, at $Vt/B = 11.3$ *(solid)*, 19.7 *(dashed)*, 28.1, *(dotted)*. The dash-dotted line represents the cavity flow solution.

free surface evolution and the modelling of the thin jet.

Here, attention is mainly focused on the use of the numerical model to describe the free surface flow during the separation phase. In Fig.3, some results in terms of free surface configurations and distributions of pressure coefficient are presented for the impact of a finite wedge with 20° deadrise angle. In the early stage, the jet still entirely lies along the solid body contour, therefore the free surface configuration and the pressure distribution coincide with those predicted by the similarity solution with a peak occurring about the jet root. As the jet detaches from the body, this pressure peak progressively disappears and the distribution becomes monotonic. Concerning the free surface dynamics, since gravity effects are neglected in the present work, the separated jet does not collapse onto the free surface and no waves are produced.

If the water entry is followed for quite a long time evolution, it is expected that the cavity flow solution for the considered wedge shape is approached. To prove this conjecture, a very long simulation is performed for a wedge with 60° deadrise angle. The resulting history of the total hydrodynamic load is depicted in Fig.4 along with the theoretical asymptotic value of the cavity flow solution as provided by [4]. Although the numerical solution seems to provide an asymtotic trend, the final value is about 5% larger than the theoretical value. Reason for this disagreement are still under investigation.

The pressure distribution at three different stages of the wedge entry are evaluated and compared with the theoretical solution for the cavity flow in Fig.5. The time delay among the three numerical pressure distributions is constant thus making it evident the reduction of the convergence rate with time. The comparison shows that the shape of the pressure curves is rather similar to the theoretical one.

References

[1] Battistin D., Iafrati A., *Hydrodynamic loads during water entry of two-dimensional and axisymmetric bodies*, J. Fluids and Struct., vol. 17, pp. 643-664 (2003)

[2] Battistin D., Iafrati A., *A numerical model for the jet flow generated by water impact*, J. Engng. Math., to appear (2003).

[3] Longuet-Higgins M., Cokelet E., *The deformation of steep surface waves on water. i. a numerical method*, Proc. R. Soc. London, vol. A 350, pp. 1-26 (1976).

[4] Milne-Thomson L.M., Theoretical hydrodynamics, 5 th edn., Macmillan & Co. Ltd., London (1968).

[5] Vorus W., *A flat cylinder theory for vessel impact and steady planing resistance*, J. Ship Res., vol. 40(2), pp. 89-106 (1996).

[6] Zhao R., Faltinsen O., *Water entry of two-dimensional bodies*, J. Fluid Mech., vol. 246, pp. 593-612 (1993).

[7] Zhao R., Faltinsen O., Aarnes J., *Water entry of arbitrary two-dimensional sections with and without flow separation*, Proc. of the 21^{th} ONR Symp. on Naval Hydrod., Trondheim (Norway) (1996).

Preliminary Investigations for CFD Fire Simulations in Ship Rooms

Bruno Junalik, Volker Bertram, ENSIETA, Volker.Bertram@ensieta.fr
Ould (Bettar) El Moctar, Germanischer Lloyd, moct@GL-Group.com

Testing a commercial CFD code for fire simulations was the subject of a final year research project at ENSIETA, *Junalik (2003),* conducted at Germanischer Lloyd. Calculations covered four different scenarios typical for ships: (1) a cabin arrangement, (2) an atrium and a shopping mall, (3) an engine room, (4) a Ro-Ro ship deck.

RANSE simulations for fires cannot reproduce the evolution of large eddy structures observed in most fire plumes. Thus fire turbulence models resort sometimes to “Large Eddy Simulation” (LES) or even Direct Numerical Simulation (DNS). For ship rooms, LES can be performed at best for single rooms and DNS is prohibitively expensive. The employed commercial code FDS (Fire Dynamics Simulator) solves a low-mach number form of the Navier-Stokes equations using a fast Fourier transform solver for pressure, a LES turbulence model (the original Smagorinsky model) and a mixture fraction combustion model. The energy conservation equation is not explicitly solved, but its source terms are included in the expression for the flow divergence. FDS has sub-models for radiative and conductive heat transfer, sprinkler nozzles, droplet transport and evaporation, simple pyrolisis, fuel sprays, liquid fuel pool and multi-grid operation. Fire simulations require in addition a combustion model. Combustion models tracking the significant species required to calculate the heat release rate are often computationally too expensive due to the require fine grid resolution. Mixture fraction models offer a relative simple alternative. All of the species are described in terms of a mixture fraction Z(x,t). The mixture fraction, defined as the fraction of the fluid mass that originated as fuel, is a single scalar quantity that obeys a conservation equation.

A simple test case served to familiarize with the code: A cubical room (L=B=H= 5m) with two holes with the outside and a fire from burning heptane on an area of A=0.25 m^2 (0.5m·0.5m). According to classical theory, we expect for a heptane fire a heat release $\dot{Q}=\dot{m}''A\Delta H_C$ of 715 kW. $\dot{m}''$ is the maximum burning flux value (65 g/m^{2}s for heptane), ΔH_C the effective heat of combustion (44 kJ/g for heptane). According to classical theory we expect a flame length L_f=0.23 $\dot{Q}^{0.4}$-1.02D = 2.93 m. D is the hearth diameter. The temperature expected at the tip of the flame is 400°C. The temperature of the fire plume should decrease with height. The heptane fire was described in FDS with the following combustion parameters:

- Stoechiometric coefficients: NU_O2=11, NU_H2O=8, NU_CO2=7
- Heat Release Rate per Unit Area of 2860 kW/ m^2 (giving the theoretical heat release)
- CO and soot yields are set to 0.010 and 0.037 (g/g) based on the FDS manual.

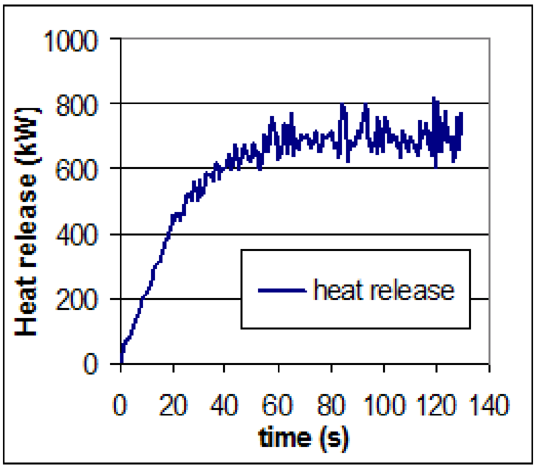

Fig.1: Heat release for single-fire, single room case

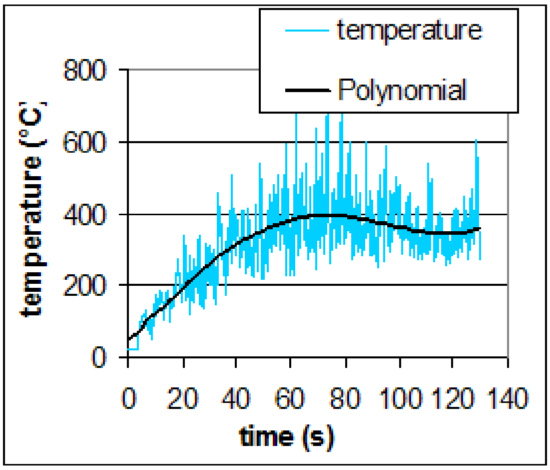

Fig.2: Temperature for single-fire, single room case

The evolution of this fire in time was realistic, Fig.1. The heat release rate grew within one minute to 700 kW which is 2% below the expected 715 kW. Fig.2 shows the temperature recorded at a height of 3 m, just above the fire in the middle of the room. The temperature does not evolve smoothly over time: Air does not rise continuously above the fire due to the fire plume turbulence: Hot smoky eddies raise until the ceiling, those eddies alternate with cooler air. This explains the fluctuations. The spatial temperature distribution was realistic, Fig.3. In the center, a fire plume comprises the burn-out zone and the buoyant rise of the combustion gas. The hot upper gas layer is indicated by its temperature. A layer of cold gas is lying beneath. Indicated temperatures agreed well with values from classical fire plume theory. At a height of approximately 3 m (the theoretical flame length) the average temperature was 400°C as expected.

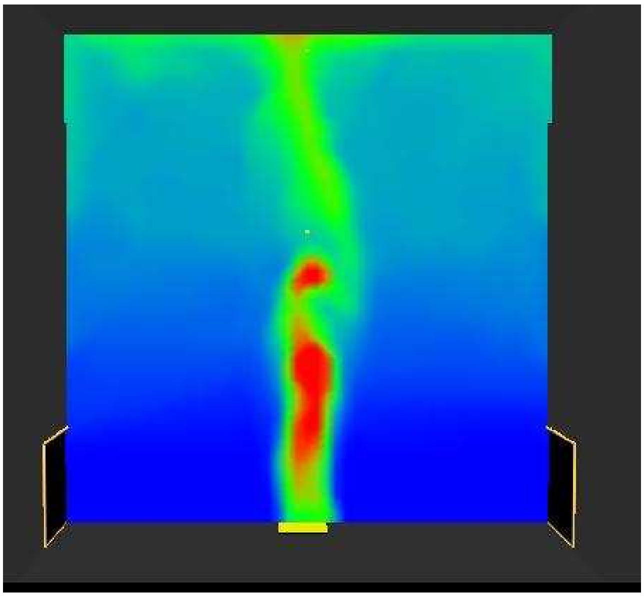

Fig.3: Temperature distribution in single-fire, single-room test simulation as predicted by FDS

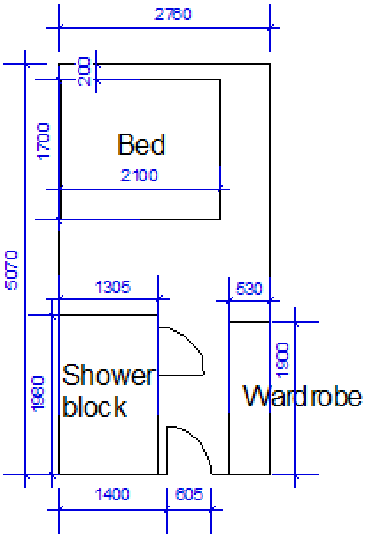

Fig.4: Cabin plan, height 2100mm

A standard passenger cabin with door closed was selected as test case, Fig.4. Bed and wardrobe as biggest furniture were modeled as cubical obstacles. The cabin is equipped with a shower block. The inlet of the cabin ventilation (0.4m·0.4m) is in the ceiling above the bed. One outlet (0.5m·0.1m) is in the lower part of the shower block (60 Sm^3/h), another (0.6m·0.2m) on the lower part of the wall with the corridor, under the wardrobe. The strength of the inlet ventilation was varied in the different simulations. Values tested were 350, 110 Sm^3/h and no ventilation. 110 Sm^3/h is the standard comfort value of the ventilation in a cabin

FDS allows specifying different boundary conditions for the obstructions:

- Walls and ceiling (mineral wool) were defined as thermally-thick solid with thermal diffusivity $\alpha=0.35\cdot10^{-6} m^2/s$, thermal conductivity KS=0.04 W/m·K, and thickness $\Delta=0.025$ m. Thus FDS performed a one-dimensional heat transfer calculation in the material.
- Floor (concrete) was defined as a thermally-thick solid with $\alpha=0.57\cdot10^{-6}$ m^2/s, KS=1 W/m·K, $\Delta=0.03$ m.
- Wardrobe and bed frame (wood) were defined as a thermally-thick solid with $\alpha=8.3\cdot10^{-8}$ m^2/s, KS=0.0611 W/m·K, $\Delta=0.016$ m. To prevent heat loss from the backside of the material, the option backing='insulated' was activated.
- Bed upholstery was defined as a thermally-thin material. C_DELTA_RHO (the product of the specific heat (kJ/kg·K), density (kg/m^3) and thickness (m) of the liner) was set to 1.29 $kJ/m^2\cdot10^{-6}K$. The ignition temperature of the upholstery was set to a high temperature to avoid the phenomenon of flashover.

For reasons of simplicity, polystyrene was used as a combustible. This fire was set in the cabin on the floor, with an area A=0.4m·0.4m. The fire parameters set in FDS followed data from classical theory. For an assumed polystyrene pellet fire ($\dot{m}''$=38 g/m^{2}s; ΔH_C =39.8 kJ/g for polystyrene), we expect then a heat release $\dot{Q}$= 240 kW, a flame length L_f=1.6 m, a temperature at flame tip 400°C. The following combustion parameters were set in FDS:

- Stoechiometric coefficients: NU_O2=10, NU_H2O=4, NU_CO2=8
- Heat Release Rate per Unit Area = 1500 kW/ m^2 (giving the theoretical heat release 240 kW)
- CO yield = 0.06 g/g, soot yield = 0.164 g/g
- 30 s ramp-up time of the heat release

LES computations with FDS were compared with a classical zonal approach (code Multi Room Fire Code MFRC) deemed reliable and well validated up to the point of flashover. Same geometry and fire parameters were used.

Two discretizations in FDS were tried: (1) a discretization consisting of a fine mesh for the fire (5cm cubic cells) and 4 coarser overlapping meshes (10 cm cubic cells) for the cabin. (2) A discretization with a fine mesh for the fire (5cm cubic cells) and a mono-block mesh (10 cm cubic cells) for the cabin. Test computations showed similar results for distributions of temperature, carbon monoxide, and smoke density. However, for a test computation without fire considering just the mechanical ventilation, the grid with overlapping grids did not converge to the expected results even after 300 s of simulated flow, while the simulation with the second grid converged within 15 s to the expected results, Fig.5. Therefore all following simulations used the second grid.

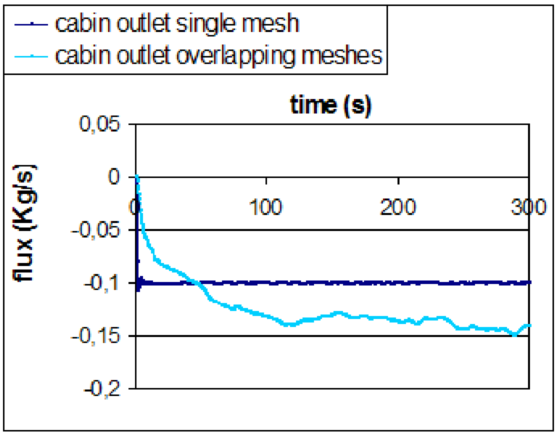

Fig.5: Flux for overlapping mesh and single mesh

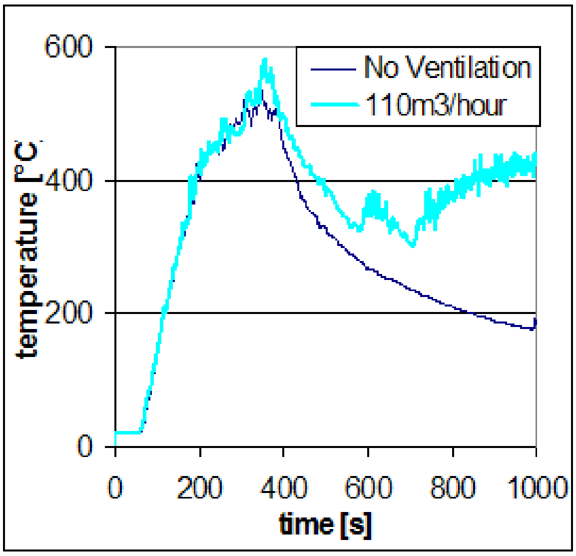

Fig.6: Influence of ventilation on temperature

Fig.6 shows the influence of ventilation on the temperature in the cabin. This temperature is the one recorded at a point, situated between the shower block and the wardrobe, at z=1.1m. Two ventilation cases were investigated (110 and 0 Sm^3/h). Perhaps contrary to intuition, ventilation increases in this case the temperature, because ventilation provides oxygen to the combustion. The more oxygen you provide, the more fuel you burn, the higher the temperature. In the simulation without ventilation, the temperature reaches 500°C within 400 s and then decreases slowly. There is no more oxygen in this room and the fire is smoldering. In the simulation with the 110 m^3/hour ventilation, the temperature also reaches 500/600°C within 400 s and then, starts to decrease before being stabilized. The fire is ventilation controlled.

For strong ventilation of 350 Sm^3/h, results between MFRC and FDS differ considerably, Figs.7 and 8. 350 Sm^3/ h ventilation is in theory just enough to over-ventilate the fire. Thus we should expect after a transition time a constant heat release rate of 240 kW. This is the case with MRFC, but in the FDS model, after reaching this value, the heat release decreases slowly to considerably lower values, Fig.7 (left). Correspondingly, the temperatures (in an upper layer, averaged for MRFC; single point for FDS) develop quite differently with a constant rise for MRFC, and a fluctuation around a rather constant plateau for FDS, Fig.7 (right). Maximum temperatures predicted are for both simulations around 400°C. The explanation for the differences is probably that (unlike FDS) MRFC does not consider the exact geometry of the room and its obstacles that could disturb the oxygen flow from the inlet ventilation to the hearth of the fire.

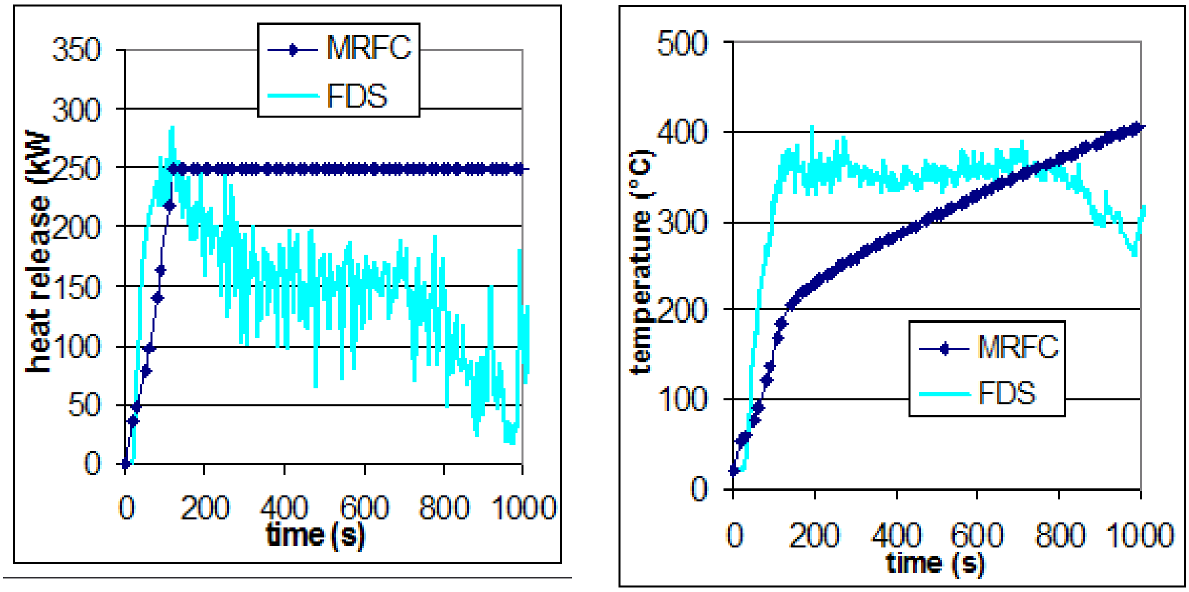

Fig.7: Heat release and temperature in the upper layer results of MRFC (zone model) and FDS (CFD model) for a 350m^3/hour ventilation

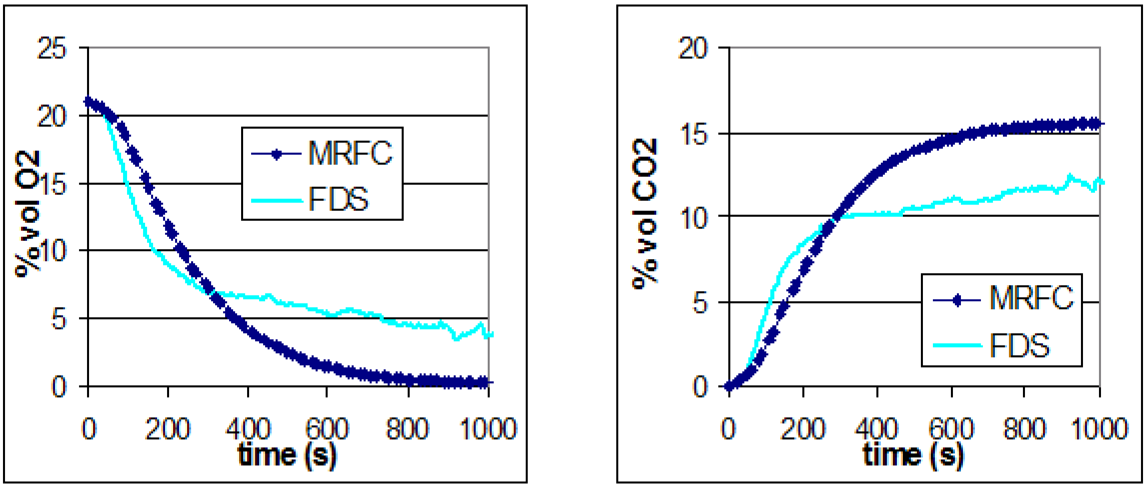

Fig.8: O_2 and CO_2 concentrations in the upper layer for a 350 m^3/hour ventilation

Fig.8 shows the oxygen and the carbon dioxide rates given by MRFC and FDS. Predictions of the oxygen and the carbon dioxide rates are close with both codes. Rates predicted by MRFC are after 800 s constant, while rates given by FDS still fluctuate even after 1000 s of simulation. But FDS rates tend to MRFC rates. FDS indicated also a concentration of 4000 ppm CO in the hot gas. MRFC did not indicate any CO, although a theoretical value of 6000 ppm is expected from theory in stoechiometric combustion.

JUNALIK, B. (2003), *Fire simulation*, final thesis, ENSIETA

SIMULATION OF SHIPS IN LARGE WAVES USING A FINITE-VOLUME-METHOD

Matthias Klemt, Technical University of Hamburg-Harburg, klemt@tu-harburg.de
Milovan Peric, CD adapco Group - Nuremberg
Gerhard Jensen, Technical University of Hamburg-Harburg, g.Jensen@tu-harburg.de

1. INTRODUCTION

Ship motions and associated loads on a ship hull are usually predicted with methods based on potential flow assumptions. Large errors can be introduced by these assumptions for a few practically important cases like ship motions in large amplitude waves, ship responses under a wave impact (slamming), or ship capsizing etc. The need for a numerical tool that can predict the motions and loads in large waves, taking into account viscous effects, turbulence, flow separation and wave-breaking phenomena is obvious.

The objective of this research is to develop and validate a computional technique for the coupled analysis of viscous flow and flow-induced body-movements in large waves. For this purpose, some cases are selected to be investigated using this method and compared with experimental results.

2. NUMERICAL METHOD

OVERLAPPING GRID-METHOD

The Navier-Stokes-Equations and the body dynamic equations are to be solved in a coupled manner. A Finite-Volume-Method on block structured grids is used to predict the viscous flow around a floating-body. The velocity of the floating-body is corrected by a Crank-Nicholson-Method after every iteration (fully implicit). An Approximation for the hydrodynamic masses is used to make the coupled procedure robust. An approach with overlapping grids has been employed to avoid the difficult grid-management caused by changing of the body position. There is a space-fixed grid with a hole close to the body and a body-fixed grid. Fig. 1 shows the principle of this approach.

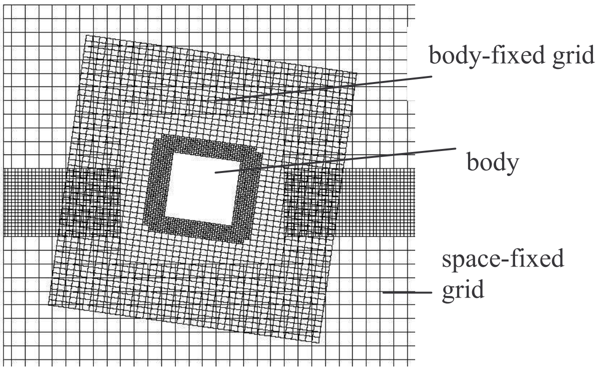

Fig. 1 2-dimensional body with overlapping grids

The flow solution has to be interpolated on the boundaries of every grid from each other to force a unique solution on both grids in the overlapping area. Finally a correction of the convective velocities makes sure that the mass conservation law will be satisfied.

There are two ways to calculate the flow in the case of body-movement. First by changing the coordinates of the bodyfixed grid in every iteration (moving grid) and after that solving the Navier-Stokes-Equations in the space-fixed coordinate system. The disadvantage of this method is that the geometry in the program is only written in single precision while all variables are in double precision. In case of small timesteps this could lead to problems.

The other way, which is employed here, is to keep the coordinates of the body-fixed grid fixed and the Navier-Stokes-Equations will be solved in the body fixed coordinate system. In that case the consideration of the grid-accelarations and velocities is necessary. This could be done in double precision. Another advantage is the reduced requirement of memory because there is no need for saving the updated vertex nodes of the grid during the calculation.

NUMERICAL TANK

The numerical tank consists of a fluid domain with two phases (water and air) bounded by a layer of air on top, a bottom surface in water and four vertical boundaries. Regular waves are generated by giving inlet velocity and waterheigt based on potential theory (Airy, Stokes I-IV) at the inlet boundary [1]. At the other side of the tank a numerical beach is defined to avoid reflection of the waves.

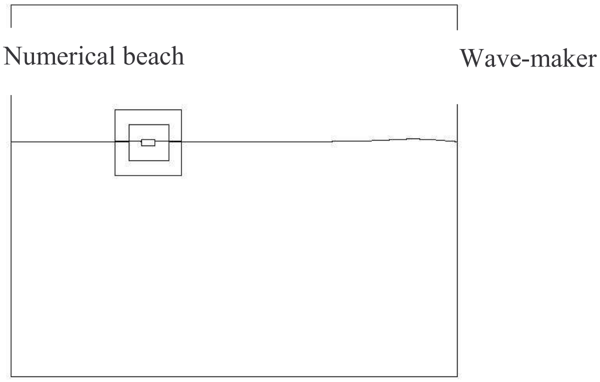

Fig. 2 Numerical tank

3. APPLICATIONS

MOTIONS OF A FAST CONVENTIONAL PASSENGER FERRY

A fast conventional RoRo passenger ferry was selected as reference ship for the study. The ship was designed by IZAR for the Eurpean research project DEXTREMEL [3]. Model tests were carried out at a scale of 1/40 in a seekeaping basin by MARIN. Figure 4 shows the discretisation of the ship and its main particulars are listed in Table 1.

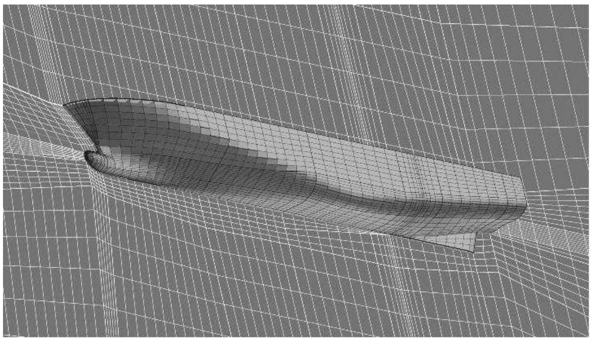

Fig. 3 Discretisation of the ship

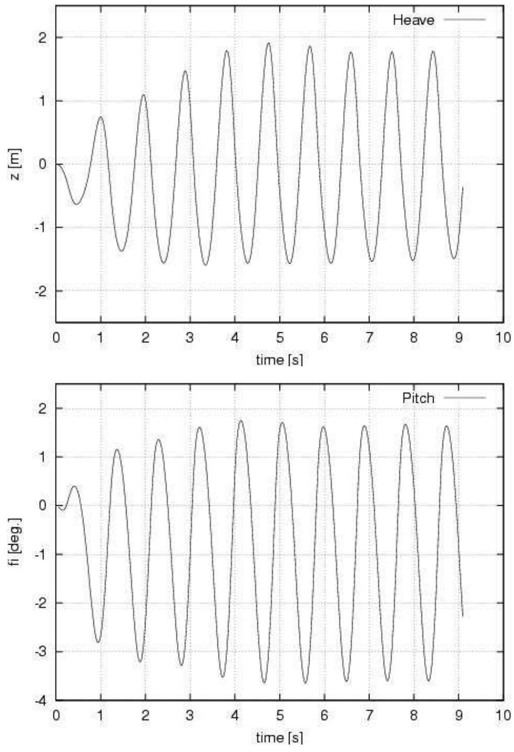

Fig. 4 Calculated heave and pitch motions

The computation was done for a ship speed of 26 kn (93 % of full speed) in head waves. Only half of the ship at model scale has been discretized and pitch and heave were the degrees of freedom. At the beginning of the calculation the whole computation domain was initialised with undisturbed waves and the ship was at rest. Figure 5 shows the calculated heave and pitch motion in waves with ω=0.6, H=8m and a plot of the situation at t=8.7 s is presented in Fig. 6.

Table 1 Main particulars of reference ship

	Symbol	Value	Unit
Length between perpendiculars	Lpp	173.00	m
Beam	B	26.00	m
Draft	T	6.50	m
Displacement	Δ	16800	t
Service Speed	Vs	28	kts

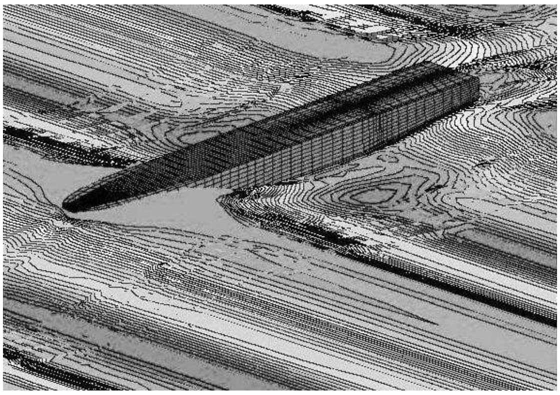

Fig. 5 Ship in head waves, ω=0.6, H=8.0 m, t=8.7 s

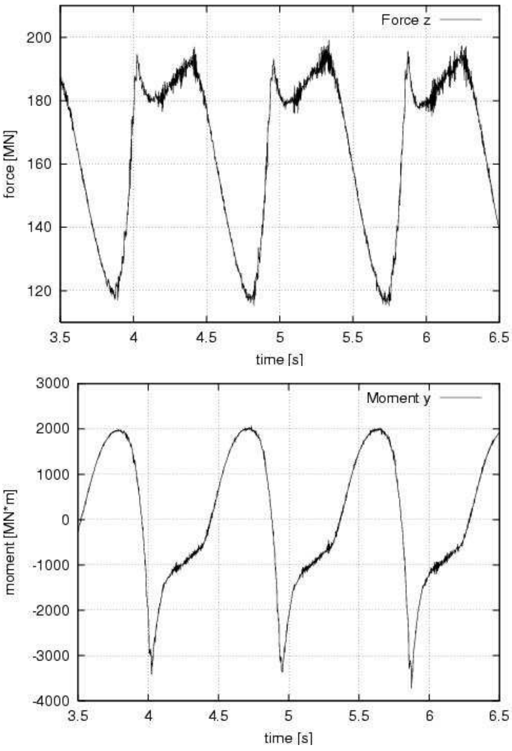

Fig. 6 Calculated heave force and pitch moment

Noted is that the amount of the negative pitch angle is much higher than the positive one caused by bow flare effects and impact loads.

The corresponding force and moments acting on the hull are shown in Fig. 6.

The time traces of the forces have a nonlinear appearance due to the impact loads during the water entry. Fig. 7 presents the comparison of calculated and measured RAOs of heave and pitch motion.

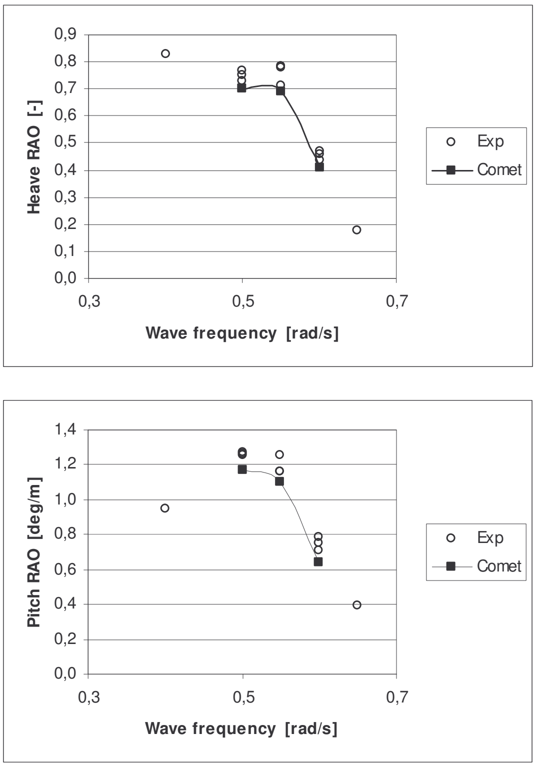

Fig. 7 Predicted RAOs of heave and pitch motion compared with measurements

The heave and pitch response were a bit underpredicted by the computional method. This effect might be caused by the coarse discretisation of the ship. The refinement of the whole computation domain has to be investigated in the next time.

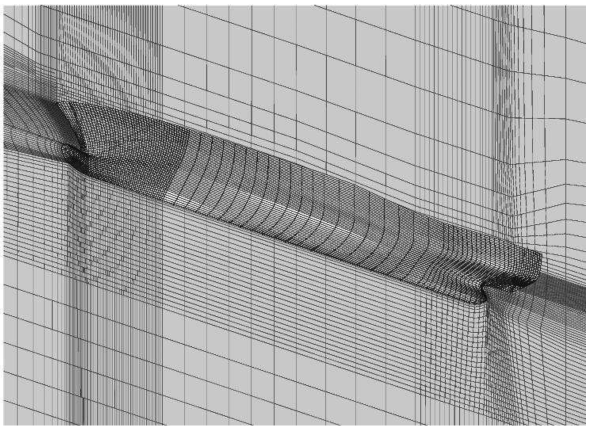

Fig. 8 Discretisation of the container ship

CONTAINER SHIP IN LARGE WAVES

A container ship travelling in an extreme wave situation was selected to test the numerical properties of the computational method. The ship was built on the shipyard HDW in Kiel. The objective were to measure shipmotions and local loads on the bow flare during the bow water entry. Figure 8 shows the discretisation of the ship and its main paritculars are listed in Table 2.

Table 2 Main particulars of the container ship

	Symbol	Value	Unit
Length between perpendiculars	Lpp	204.00	m
Beam	B	26.66	m
Draft	T	8.70	m
Service Speed	Vs	25	kts

The computation was done without forward speed in head waves. The wave length was equal to the ship length (204 m) and the wave height has been choosen H=21m. Figure 9 shows the calculated heave and pitch motion.

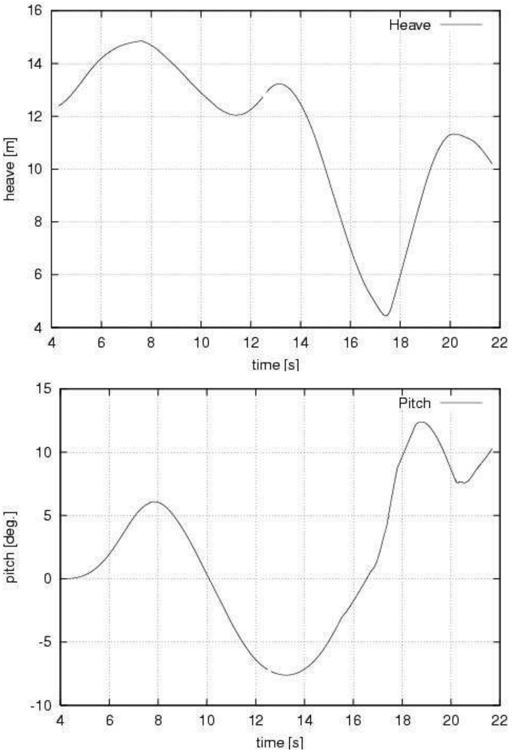

Fig. 9 Calculated heave and pitch motions

The calculated motions are very strong caused by the extreme wave. No stationary solution in the ship behavior can be observed until now. In Fig. 10 can be seen that green water effects play an important role in such a high wave.

4. POSTPROCESSING

A lot of data are generated during a CFD-Simulation using the Finite-volume-method. A saved restart-file contains the data of every control volume for one or two time steps in case of using three-time-level-scheme, so you can't hold much of these data on the hard disk for long. The standard way of postprocessing is to make one or two pictures of the situation in the computation area and save the time traces of several local and global variables like ship motions or local impact loads. Once the restart-file is deleted, an external viewer has no chance to get further information of the remaining results. The objective was to improve the postprocessing-procedure and to extract the most important information from a restart-file. The "Virtual Model Language (VRML)" [6] has been used to visualize the extracted information in one 3D-model. The interpreter is a share-ware plug-in for a standard internet browser and can be downloaded by everyone.

For that purpose the region elements of the ship-geometry was reduced. This has been done by joining some faces to larger polygons [7]. The arbitrary free surface of both computation domains has been extracted and a bit simplified for the region far from the ship. The distribution of pressure and friction forces has been mapped on the hull and is shown by coloring the values. Some interaction buttons was added to switch between pressure and friction forces. There is also the possibility of coloring the wave height by pressing another button or to make the surface transparent in steps. Further interaction is to start and stop the animation, to set the speed and to go through it stepwise. Figure 9 shows a picture of the model.

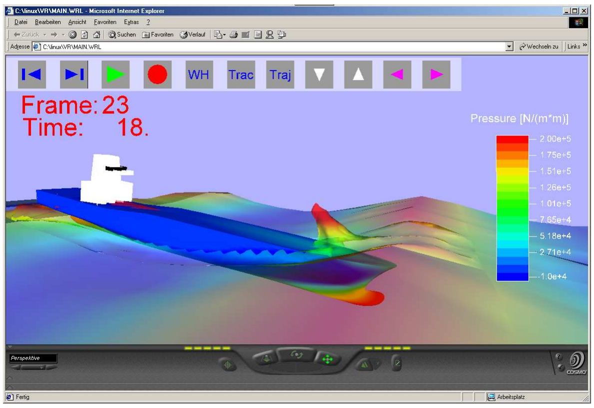

Fig. 10 VRML model of the container ship in head waves, H=21m, t=18.0 s

The advantage is to give the viewer the chance to view the results in more detail by going around the ship and viewing one or more variables alone or together. In this model we included the possilbility to select some points of a set and to follow the particle traces in time. Noted is that the particles didn't take the way of a circle like in linear waves. In such a high wave a mass transfer in direction of the wave propagation can be observed.

Another advantage of using such a VRML-database is the use of internet-abilities. The results are loaded by giving internet-addresses, so the files or parts of them could be saved and changed on a physical space far away from the viewer.

REFERERENCES

1. Clauss, G., Lehmann, E. and Östergaard, C. (1998): Meerestechnische Konstruktionen, Springer-Verlag Berlin Heidelberg New York

2. Comet user manual, ICCM (Institute of Computional Continuum Mechanics GmbH), Hamburg, 2001

3. DEXTREMEL (1997): Design for Structural Safety under Extreme Loads, BriteEuRam project, contract BPPR-CT97-0513,

http://research.germanlloyd.org/Projects/DEXTREMEL/index.html

4. Muzaferija, S. and Peric, M. (1999): Computation of free -surface using interface-tracking and interface-capturing methods

5. Sames, P. C., Klemt ,M. and Schellin, T. E. (2001): Prediction of Wetdeck Slamming Loads for a Catamaran, HIPER 2001, Hamburg

6. Däßler, R. (1999) : Das Einsteigerseminar VRML, bhv Verlag, Germany

7. Lindenau, O., Bertram, V. (2003) : The Making of an SES with Streamlines and Pressure Distribution, COMPIT ’03, Hamburg

Numerical Simulation of Passive Anti-Roll Tank Devices

Jean-Marc Laurens, Eric Frébet (Ensieta), laurenje@ensieta.fr

Introduction

Since their introduction by Frahm in 1911, U-tanks as passive dampers have been chosen as the stabilisation system of many ships. Using a fluid tank for roll damping is an ancient and attractive idea. The principle is simple, if the water motion in the tank and the ship's roll are in the opposite phase, the weight of the water in the tank acts as a counteractive force which dampens roll motion. Among the several types of existing fluid tanks, U-tanks are recognised to be more difficult to tune than free surface tanks, Barr (1975). That is simply because their natural frequencies depend on more parameters. Partially because of the progress made to simulate unsteady state two-phase flow at low computing costs and also because of the advent of double hull tankers, renewed interest for the device seems to exist. At first, the present study only intended to test the feasibility of U-Tanks numerical simulations using an existing RANS solver with a VOF model but once the Pandora box opened it was impossible to refrain ourselves from looking at its content.

Numerical simulations

The RANSE solver Fluent version 6.1 was used for the simulations presented here. Unsteady state two-phase flow is solved using the VOF model.

We noted that a better behaviour is obtained when imposing a pressure inlet condition at tank extremities. To simulate to roll motion, the gravity force was forced to vary in a cyclic way. This would normally impose a correction of accelerations because of the moving referential system but since they are only a fraction of the gravity we leave that minor correction aside for the time being. Preliminary computations showed that results are not sensitive to grid refinement.

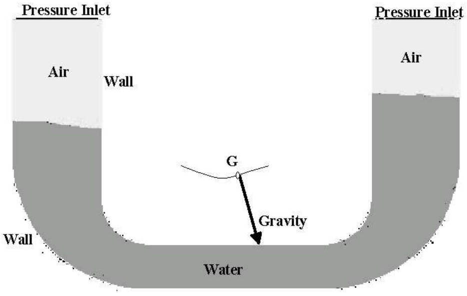

Figure 1. *Boundary conditions*

Because of the pressure inlet condition, the water is evacuated from the computational domain when it reaches the top of a reservoir which does not allow simulations under such conditions and as a result amplitudes of oscillations must be kept low.

Validation

To validate our simulations, we used the experimental results obtained by Field and Martin (1975) later used by Van Daalen et al. to validate their own computations. The set-up is presented in Figure 2.

Water level
Case A : 3 feet, Case B : 5 feet

Reservoir width : 9 feet
Distance between reservoirs : 24 feet
Duct height : 1 foot
Amplitude of forced motion : 5°

Figure 2. *Experimental set up used by Martin and Field (1975) used for validation*

Figure 3 is an example of the curves obtained after simulation. The coordinates of the water centre of gravity in the U-Tank, Xg and Yg, are computed at each time step. The righting moment will of course mostly depend on Xg. The dynamics of the water produces higher amplitudes of movements for Xg then steady state hand computations as we approach the tank natural frequency and the obtained non zero phase shows that the water in the U-Tank does not roll in phase with the boat; which is as expected.

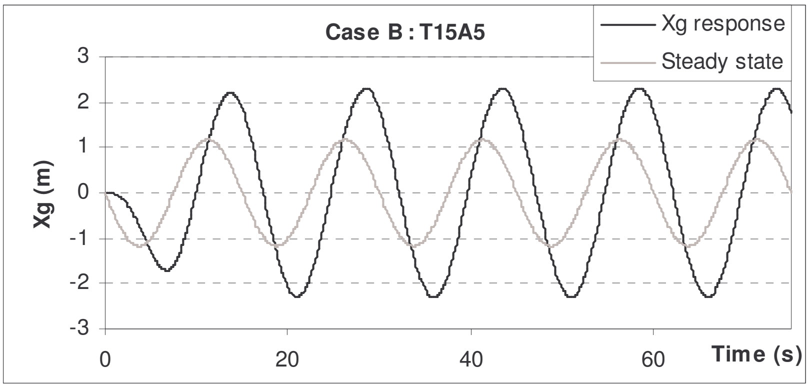

Figure 3. *Example of response obtained compared to steady state (Period 15s, Amplitude 5°)*

Based on curves such as the curve presented in Figure 3, we computed amplitudes and phase angles obtained for the range of forced oscillations expressed as ω. In order to comply with the presentation of results by Van Daalen et al. (2000), the amplitude of response is given in terms of Am/Aφ which represents the righting moment (N.m) per degree of forced oscillation. All the results are compiled in Figure 4 where they are compared with both the computations of Van Daalen et al. (2000) and the experimental results of Fields and Martin (1975).

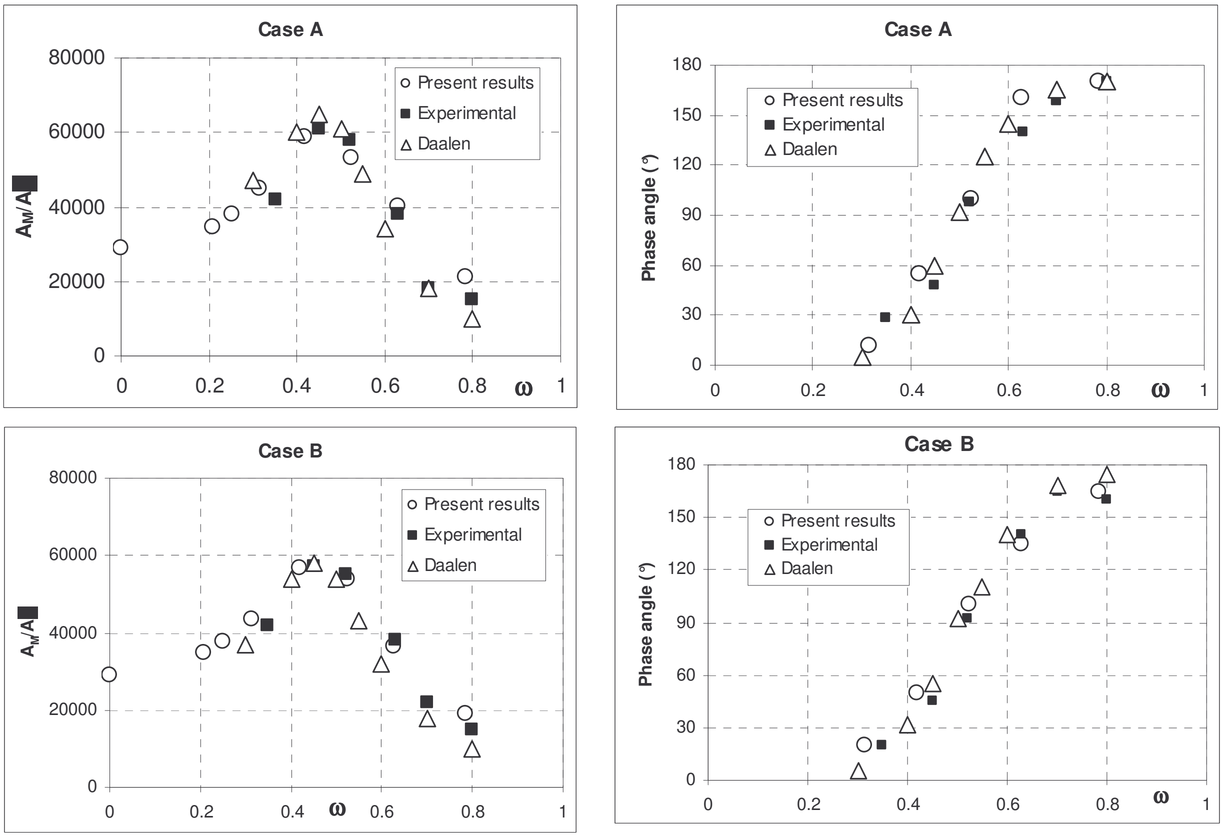

Figure 4. *Amplitude of the righting moment (left) and phase angle (right) versus forced pulsation obtained in the present calculations compared to computations performed by Van Daalen et al. (2000) and experiments by Field and Martin (1976). First row (Case A), water level 3ft and second row (Case B), 5ft of water.*

Although our results are in excellent agreement with these two aforementioned references, we verified that the amplitude of the response and the amplitude of forced motion are indeed linear. We noted from these simulations that the response phase angle is also linearly dependent to the amplitude of the forced motion.

Effects of geometrical parameters: attempting to tune the system

The first question is to determine what is really driving the response of the system. Since gravity is the main force, a scale model should be based on the Froude number. Hence, if the model is 10 times smaller its period of forced motion should be made $\sqrt{10}$ times shorter. Respecting the transit time of a water particle from one end to the other would have lead to a scale model period of forced motion which is 10 times smaller.

As confirmed by the results of Figure 5, the Froude number does indeed as for seakeeping problems drive the system. The little difference between scale:1 Xg and extrapolated Xg from 1/10 scale model indicates the negligible influence of viscous effects. Additional simulations using various viscosity factors confirmed this observation.

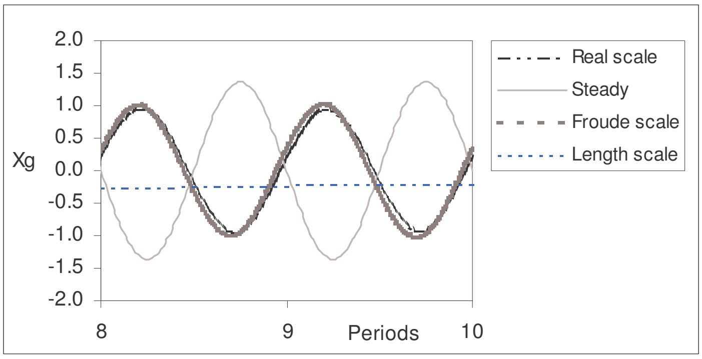

Figure 5. *Scale (metric symposium)*

Figure 6. *Rounding the U-tank angles*

Because viscous effects appear to be negligible here, rounding the angles of the U-shape tank should not greatly affect the response behaviour. The set up of Figure 6 was used to confirm that results were not greatly affected by this geometrical parameter although the flow presents important vortices.

Other geometrical parameters have been tested. Main tendencies are summarized in Table 1. A '+' indicates that the response variable increases with the parameter.

***Table 1**. Effect of geometrical parameters on amplitude and phase of the response*

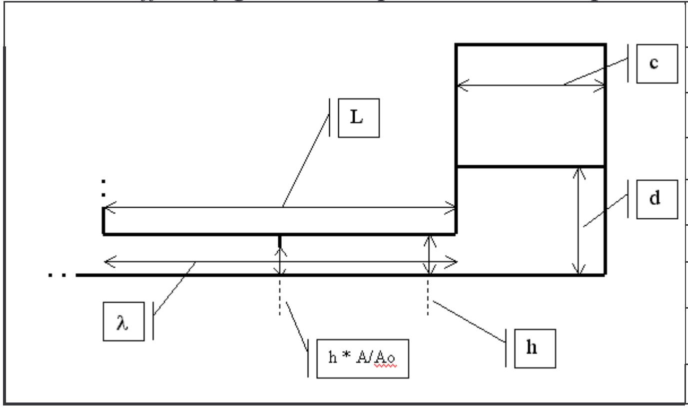

	Amplitude	Phase
A/Ao	+	+
C	+	-
d	~	.
H	-	-
L	+	-
λ	-	+
µ	-	-
ρ	-	-

In order to determine the significance of the effect of a particle transit time, or travelling distance λ, from one end to the other compared to the more important effect of L measuring the distance between the two reservoirs, the set-ups of Figure 7 were used and their results compared.

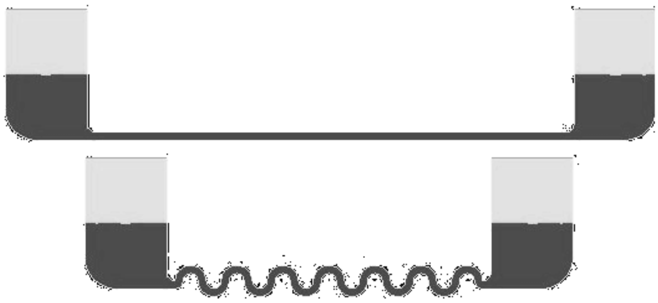

Figure 7. *The two set-ups present the same value of λ for two different values of L. Results using these two geometries showed that L, the distance between the two tanks is far more significant for the response of the system than the path length. It only emphasizes that the system is driven by the Froude number.*

The size of a U-tank is made to fit the inner hull. This way its natural roll period should be close to the natural roll period of the vessel. The ratio C/L can be adjusted to tune the U-tank. The natural ship roll period depends upon the GM value and therefore varies with the cargo for example. We saw that adjusting the water level in the tank does not significantly affect the response. The only reasonable geometrical modification would be to partially close the pathway between the two reservoirs. As presented in Table 1, increasing the blockage, A/Ao, decreases the response phase and amplitude. The U-tank geometry has to be designed for the smallest value of GM so the pathway section can be reduced when this value increases. Figure 8 shows the effect of reducing the pathway cross-section of a given U-Tank geometry. As expected, when totally blocked (A/Ao=1), the system is almost neutralised.

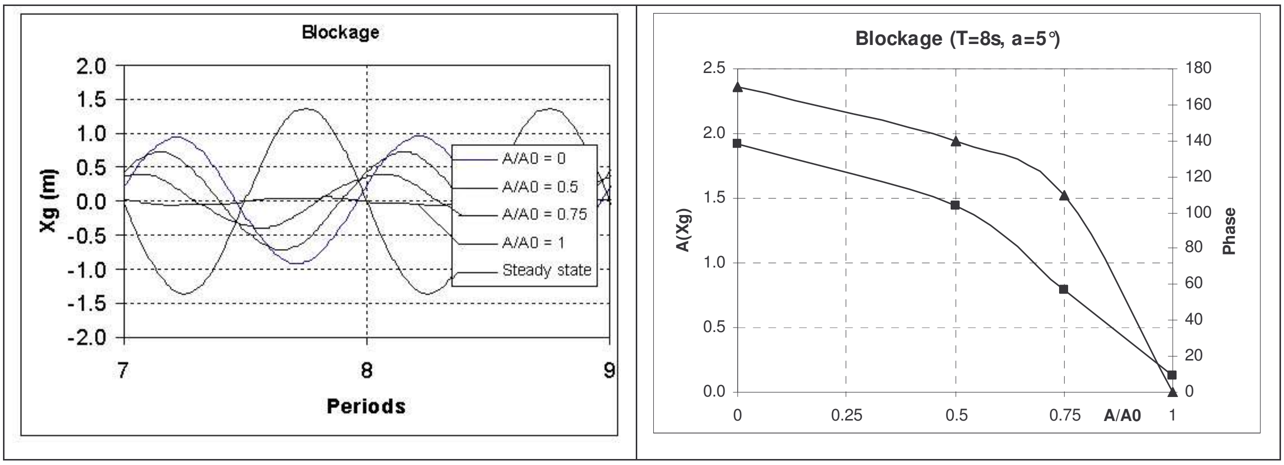

Figure 7 *Effect of increasing the blockage (A/Ao).*

Several studies exist on the possibilities of the active or semi-active tuning of free surface tanks and U-Tubes. Birmingham et al. (2002) for instance, have designed a system involving baffles and valves mechanism whilst Van Daalen et al. (2000) suggest to prevent the water from rising in one arm of the U-Tube alternatively on the starboard and port side. All systems have their advantages but will suffer from severe maintenance problems. Without pretending to make a final statement, the best strategy is probably to adjust the system for each encountered sea state which renders it unadvisable for warships for instance because they are often changing course unless equipped with an additional system such as fin stabilisers.

Irregular motions

Finally, it is natural to ask how effective a U-Tank would be when the ship is animated with irregular motions. Simulating such motions does not involve any additional problems since our simulations are performed in the time domain. We restricted our investigations to bi-chromatic oscillations. We considered that the main roll period was accompanied by a secondary roll period four times smaller in length and in amplitude. The responses obtained, such as in Figure 8, shows that the secondary frequency has very little influence. Compiled results presented in Figure 9, confirm this observation.

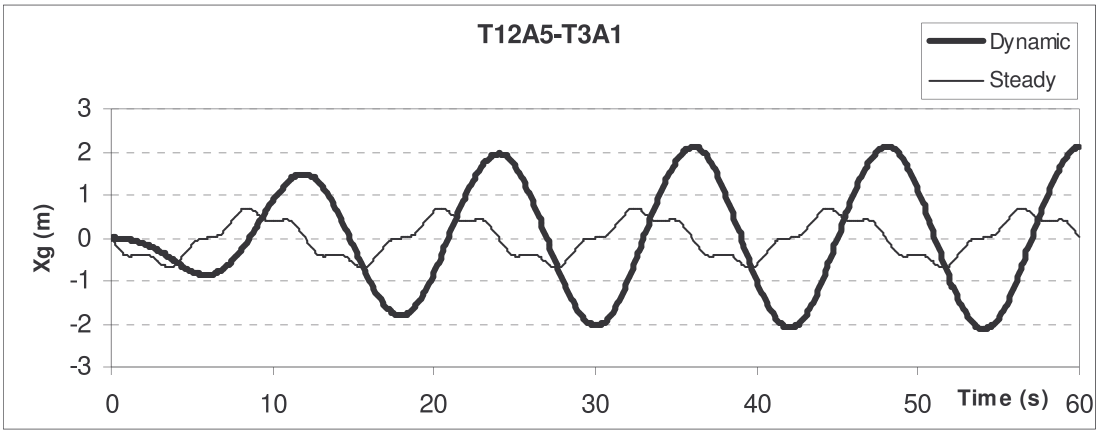

Figure 8. *Example of response for an irregular forced motion*

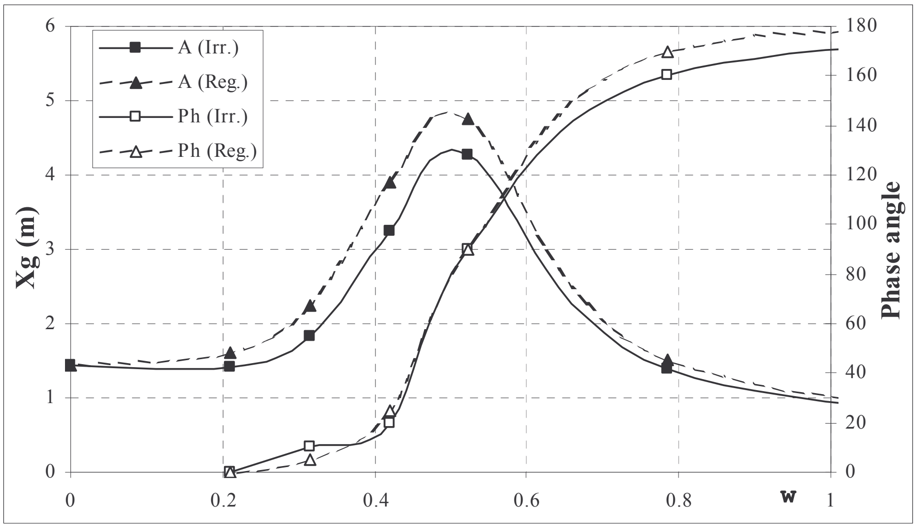

Figure 9*. Compared responses for regular and irregular forced motions.*

Conclusion

The primary objective of our work has been achieved since our results are in excellent agreement with the experimental results of Fields and Martin (1975) and the earlier simulations performed by Van Daalen et al. (2000). The effects of the principal parameters involved were examined. However we recognise that we achieved very little in comparison to the full extent of the subject.

As stated in Birmingham et al. (2002), it is surprising that systems such as free surface tanks or U-Tanks are not more frequently installed on vessels whilst they are increasingly used as anti-seismic devices in architecture, Yalla (2001). Using a RANSE solver for their simulations is certainly an advantage but not an absolute necessity. Experimental set-ups do not seem to involve considerable investments. Simplified mathematical models developed prior to computer age have shown perfectly valid results: Stigter (1966), Van den Bunt (1969), Van den Bosch (1966), Journée (2000), etc. General recommendations to fit such systems in ships exist. Perhaps this information is not widely available and accessible. Ship stability is also perhaps regarded as of secondary importance compared to economical considerations. In that case, it can be purported that a stabilised ship can shut down its propulsion and drift.

Scope for future work

The work reported here only consists of a preliminary study. We showed that the numerical tools available produce results in agreement with experimental data. Computing requirements are reasonable enough to plan full 3D simulations. Coupling these simulations with a potential flow seakeeping code should permit to simulate the ship movements equipped with U-tanks or free surface tanks. In parallel with these developments an experimental system should be designed to confirm the findings. Ideally, such a development program should also include trials in a towing tank on a ship model scale equipped with passive anti-roll devices.

Acknowledgements

We would like to thank J. Journée for some fruitful discussions at TU-Delft and for having lend us some TNO reports otherwise sometimes difficult to obtain within reasonable delays. This study has been partially funded by the Bassin d'essais des carènes.

References

BARR, R.A. (1975), *Written discussion concerning the presentation of FIELDS and MARTIN (1975).*

BECK, R.F ; CUMMINS, W.E. ; DALZELL, J.F. MANDEL, P. and WEBSTER, W.C. (1989), *Principles of Naval Architecture Vol.3 : Motions in waves*. Published by the SNAME, NJ, USA.

BENFORD, H. (1991), *Naval Architecture for non-naval architects.* Published by the SNAME, NJ, USA.

BIRMINGHAM, R.; WEBSTER, B.; ROSKILLY T. and JONES E. (2002), *The application of artificial intelligence to roll stabilisation for a range of loading and operation conditions*, HISWA 2002.

FIELD, S.B. ; and MARTIN, J.P. (1976), *Comparative effects of U-tube and free surface type passive roll stabilization systems,* Transactions of the Royal Institution of Naval Architects, Vol.118, pp.73-92.

JOURNEE, J.M.J. (2000), *Fluid tanks and ship motion*, Lecture held at Kyushu University. TU Delf Report 1237.

STIGTER, C. (1966), *The performance of U-tanks as a passive anti-roll device,* TNO Report N°81 S

VAN DAALEN, E.; KLEEFSMAN, GERRIT, J.; LUTH, H.R.; VELDMAN, A. (2000), *Anti-Roll Tank Simulations with a Volume of Fluid (VOF) Based Navier-Stokes Solver.* 23rd Symposium on Naval Hydrodynamics, Val de Reuil, Vol. 3, pp.28-43.

VAN DEN BOSCH, J.J. and VUGTH, J.H. (1966), *Roll damping by free-surface tanks.* TNO Report N°83 S

VAN DEN BUNT, J.D. (1969), *The design of U-tanks for roll damping of ships,* TNO Report N°124 S

YALLA, S.K. (2001), *Liquid dampers for mitigation of structural response : Theoretical development and experimental validation,* Ph.D. Thesis, University of Notre Dame, Australia.

Moving bodies in viscous flow simulation

Alban LEROYER and Michel VISONNEAU
Laboratoire de Mécanique des Fluides UMR-CNRS 6598
Ecole Centrale de Nantes, B.P. 92101, 1 rue de la Noë 44321 Nantes Cedex 3
Alban.Leroyer@ec-nantes.fr , Michel.Visonneau@ec-nantes.fr

1 Introduction

The growth of storage capacity and computers power enables more and more complex simulations. Therefore, Navier-Stokes flow solvers integrate new physical features to deal with more and more realistic applications. Viscous flows around moving bodies is one of them. Applications are numerous, especially in the hydrodynamic field : seakeeping, slamming, bio-mimetism, ...

This paper deals with this feature recently implemented into the ISIS flow solver developped by D.M.N. (i.e. CFD Department of the Fluid Mechanics Laboratory). In particular, it describes the methods used to achieve such simulations (regridding strategies induced by bodies motion, Fluid-Structure coupling). Lastly, some applications are presented to illustrate the new possibilities of the flow solver.

2 Description of the ISIS features

ISIS uses the incompressible unsteady Reynolds-Averaged Navier-Stokes equations (RANSE). The solver is based on a finite-volume method to build a second order accurate spatial discretization of the transport equations on unstructured grids. Pressure field is obtained from the mass conservation constraint transformed in a pressure equation. Hydrodynamic flows can be simulated by using a capturing method with appropriate discretisation schemes to keep the sharpness of the interface between air and water. Several turbulence models ranging from one equation to full RSTM closures are also available.

Flows around an arbitrary number of bodies in free or imposed 3D motion can now be simulated by ISIS. Bodies can be rigid or flexible with a prescribed law of deformation in time.
For each body, the motion can be :

- imposed by giving an explicit temporal law providing the space position of the body.
- resolved at each time step by coupling the RANS equations and Newton's Laws. Only the intial kinematic screw is imposed. Imposed external forces or moments can be added too.

One can freeze some degrees of freedom (DOF) to control possible kinematic links.

3 Resolution of the Newton's Laws

The aim is to calculate the temporal evolution of the kinematic characteristics of a rigid or flexible body submitted to the hydrodynamic forces.

The first step consists in the definition of an initial inertial frame of reference $\mathcal{R}_0$, linked to the physical space, assimilated to a Galilean referential. It is called the primary referential. The origin of this referential is fixed to the mass center of the body at the initial time. Then, one specifies the referential $\mathcal{R}_1$ linked to the body, coincident with $\mathcal{R}_0$ at initial time. Therefore the transformation $\mathcal{R}_0 \longrightarrow \mathcal{R}_1$ can be parameterized (position and orientation).

Note : as far as flexible bodies are concerned, their shape is imposed in the primary configuration. Their position in space is obtained after carrying out the transformation $\mathcal{R}_0 \longrightarrow \mathcal{R}_1$.

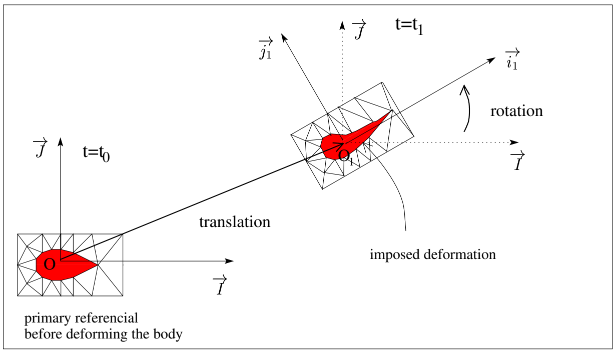

FIG. 1 – Flexible body with rigid transformation

In the frame of this general 3D resolution, classical description of the body orientation by 3 successive rotations (like Euler Angles), written (ψ,θ,ϕ), is unsuitable because of singular configurations for which the triplet (ψ,θ,ϕ) is not unique. The use of a quaternion eliminates these problems (quaternion can be roughly considered as a spatial extension of the plane representation of complex number). The integration scheme to solve motion is second-order accurate as in the flow solver.

4 Regridding strategies

To implement bodies motion in a flow solver, the mesh must be adapted to the new position of bodies in time. In order to keep an appropriate grid, three methods have been integrated :

- Spring analogy regridding
- Rigid transformation of the mesh
- Analytical weighted regridding

4.1 Spring analogy regridding

With this method, the mesh is viewed as a mechanical structure composed by compression and torsion springs ([1]) The new mesh is obtained by resolving a system after imposing the new position of nodes belonging to bodies. This technique is very convenient because of its capacity to deal with any deformation. Nevertheless, the calculation cost is quite expensive.

4.2 Rigid transformation

Here, all the nodes are moved with the solid motion of the body, coming from the resolution of the Newton's Laws or from an imposed law. This approach is operational only for a simulation with one body in an infinite fluid domain, but tolerates movement of arbitrary amplitudes.

4.3 Analytical weighted regridding

This method can be considered as an alternative to the spring analogy for solid motion. It is derived from the rigid transformation. But in this case, the displacement of each node is weighted by a factor varying between one and zero according to the distance of the body. This factor is allocated to each node of the mesh. It is imposed to one for nodes belonging to the studied body and zero for nodes of other domain boundaries. The values of this factor are calculated at the beginning of the simulation by solving a Laplacian operator. This approach is faster than the spring analogy one because nodes position are recomputed analytically without solving any system.

Note : in the flow solver, mesh mobility is taken into account by calculating on each face a moving velocity flux. The latter is obtained by computing the exact volumes swept by cell faces, which ensures the space conservation law ([2]).

5 Fluid-Structure coupling

In the case of prescribed motions, bodies are displaced at every time step. After recomputing the new mesh, flow is solved. Therefore, there is no real coupling when motion is imposed, due to the lack of fluid feedback on the body position. Problem is different when motion is solved with Newton's Law. As a matter of fact, bodies kinematic is linked to the flow at the same time step by forces carrying on them.

In the first method, called weakly coupled method, hydrodynamic forces and moments provided by the RANS equations are calculated only at the end of every time step. They are used to obtain the new position of bodies. In this case, a one time step discrepancy between flow and bodies motion appears in the resolution (hydrodynamic forces on bodies calculated at time t are used to create the t+dt kinematic configuration). Consequently, errors may be accumulated. Moreover, instabilities may appear as soon as a body density is close to the density of one fluid. A stronger coupling is then necessary.

5.1 Non-linear coupling

In order to stabilize coupling, the estimated flow during the non-linear iteration is used to calculate forces and moments acting on bodies and then new bodies position.
This is described by algorithm Fig. 2.

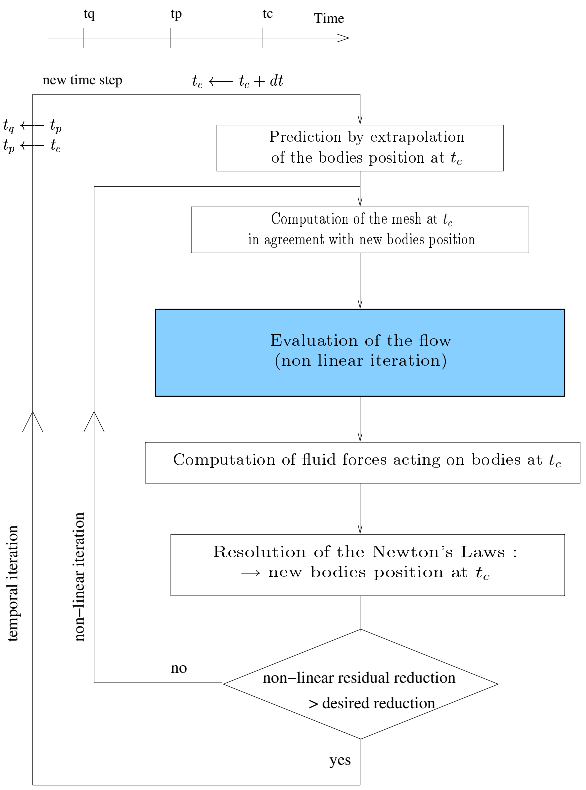

FIG. 2 – Non-linear coupling

This coupling clears away the time discrepancy problem between flow and bodies kinematic. However, even if this procedure is definitely more stable, divergent oscillations may remain in severe configurations. To achieve a stable coupling, a specific treatment of the equations of motion needs to be applied.

5.2 Stabilization of the non-linear coupling

As Söding showed in [3], the instability comes from the dependence of fluid forces on body acceleration. This force is usually formulated by splitting it in an unlinked part with acceleration and in a linear linked one. The latter is the added mass term.

$$f = \bar{f} - a\gamma \text{ with } \gamma : \text{body acceleration}$$

This characteristic is used to modify the resolution of the Newton's Laws equations in order to produce a stable coupling.
Look at the 1D problem. The equation of the motion is reduced to :

$$m\gamma = f$$

The two side of this equation are increased of an added mass term in which the right hand side is evaluated at the previous non-linear iteration.
The equation to solve is then :

$$(m+a)\gamma^{nlit} = f + a\gamma^{nlit-1}$$

At convergence ($\gamma^{nlit} = \gamma^{nlit-1}$), the initial equation is recovered. The term a needs not be accurately assessed, since it does not affect the converged solution. It must only be chosen just high enough to ensure stability.

6 Application

6.1 Free fall of a prismatic hull

These simulations are based on experimental symmetric and asymmetric drop tests with a 20° deadrise prismatic wedge (See [4] and [5]). The hull is dropped with an initial zero speed from different heights H, with various heel angle α (Fig. 3). The dynamic characteristics of the hull (mass, inertia, position of the mass center) are parameters of experiments too.

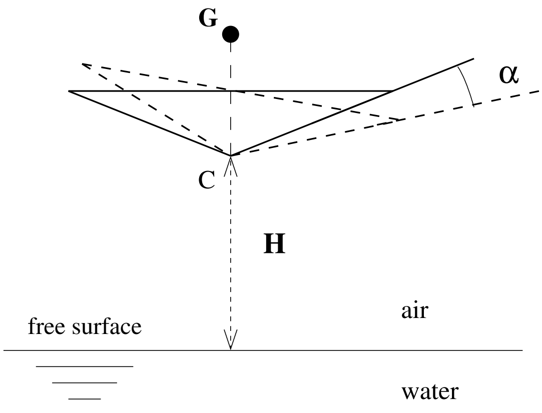

FIG. 3 – Experimental overview

Owing to the high aspect ratio of the hull (0.61m x 2.44m) , 2D hull section simulations were able to be done. The results of vertical and angular accelerations were compared with the experimental data (Fig. 4).

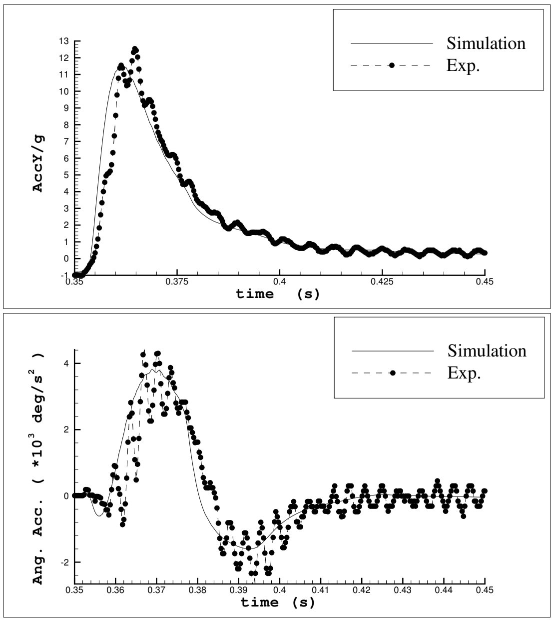

Definition of this test case

Kinematic conditions	
H	0.61 m
α	5 °

Dynamic conditions	
M	124 kg
I_G	8.85 $kg.m^2$
CG	0.216 m

FIG. 4 – Example of comparaison for an asymmetric case

Good agreement is noticed. Fast variations on experimental data are not captured by simulations since they are produced by structural vibrations.

6.2 The self-propelled fish-like body

This case deals with the free motion of one flexible body (Fig. 5).

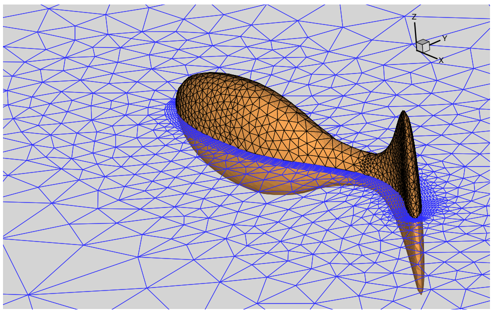

FIG. 5 – 3D fish-like body

Only the shape of the body is imposed, and the response of the fluid induced by the deformation of the body creates fluid forces on it and then movement. Hence, the position of the "virtual fish" in space is an additional unknown of the computation.

The deformation of the body shape imposes to have recourse to the spring analogy method at every new step time to compute a fish-fitted mesh. This mesh is then moved by a rigid transformation to position the body in space. Here, a non-linear coupling with an added mass term is required to achieve a stable coupling.

2D and 3D simulations were already performed by imposing a periodical fish-like deformation law, with an initial zero body speed. One observes that after a transitional state, the speed of the fish becomes periodical with a constant mean speed (Fig. 6).

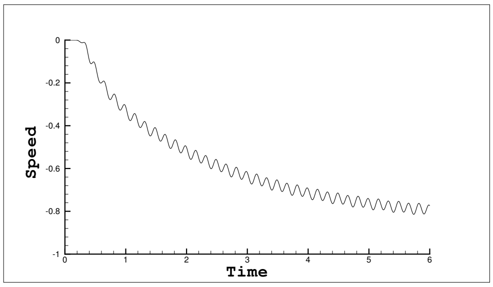

FIG. 6 – Time evolution of the speed of the fish

This periodical behaviour can also be viewed on Fig. 7 since the curve tends to be superimposed on itself.

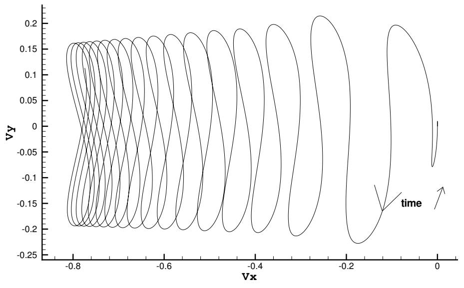

FIG. 7 – Transerval versus longitudinal velocity

6.3 Free motion of a floating box on waves generated by a wave-maker

This study used experiments realized at the Technical University of Berlin and described in [6]. Here, two bodies are involved. The water-maker which angle is imposed in time by experimental data, generates a large wave package. The other one is the free-floating box, which density is $0.68 g/cm^3$ (See Fig. 8).

Preliminary simulations were performed. The non-linear coupling without added mass term ensures the stability of the coupling for the floating body. The spring analogy technique is invoked at each new time step. Additionally, the analytical weighted reggridding is required during the non-linear iterations to adjust the body position. Two meshes have been employed, one with a no-slip condition on the body surfaces, the other with a slip condition. Comparisons with the experimental body position measurements already show that viscous effects are important. Fig. 10 confirms that the motion of the floating box is greatly influenced by the type of boundary condition on it. Nevertheless, these meshes have to be improved even these first simulations are encouraging.

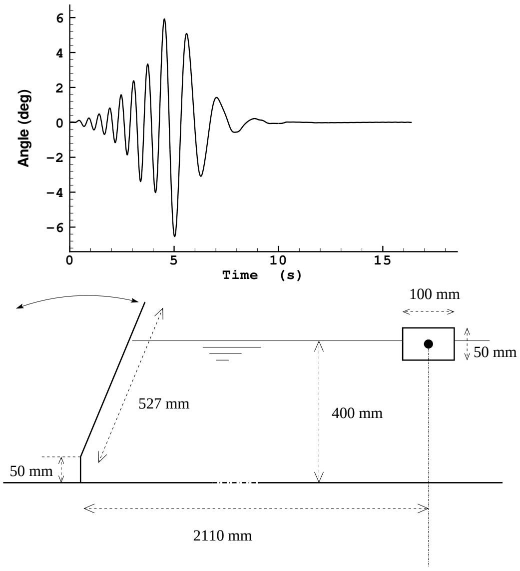

FIG. 8 – Experimental Case

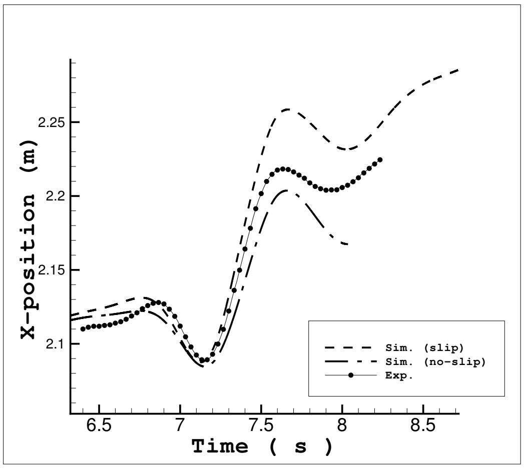

FIG. 9 – Horizontal motion of the body

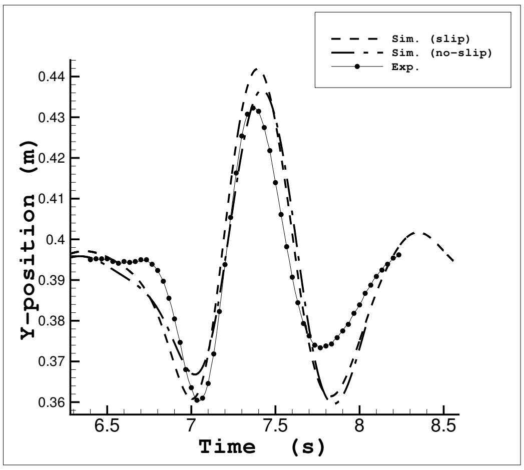

FIG. 10 – Vertical motion of the body

7 Conclusion

This paper was focused on techniques which were added in the flow solver ISIS, to achieve coupling between body motion and flow simulation. These described applications demonstrated the robustness of the chosen methodology.

However, parallelization of the spring analogy regridding remains to be completed to compute finer grids within reasonable CPU time. All the presented test cases will be assessed to evaluate the influence of the discretization error before the computation of seakeeping configuration.

Références

[1] C. Farhat, C. Degand, B. Koobus, and M. Lesoinne, “Torsional springs for two-dimensionnal dynamic unstructured fluid meshes.,” *Comput. Methods Appl. Mech. Engrg.*, vol. 163, pp. 231–245, 1998.

[2] J. H. Ferziger and M. Peric, *Computational Methods for Fluid Dynamics*, ch. 12.1. Springer, 1996.

[3] H. Söding, “How to Integrate Free Motions of Solids in Fluids,” in 4^{th} *Numerical Towing Tank Symposium, Hambürg*, 2001.

[4] L. Xu, A. Troesch, and R. Peterson, “Asymmetric Hydrodynamic Impact and Dynamic Response of Vessels,” in 17^{th} *International Conference on Offshore Mechanics and Arctic Engineering, Lisbon*, 1998.

[5] R. Azcueta, *Computation of Turbulent Free-Surface Flows Around Ships and Floating Bodies*. PhD thesis, Université d’Hambourg, 2001.

[6] Y. Xing, I. Hadzic, and M. Peric, “Predictions of Floating-Body Motion in Viscous Flow,” in 4^{th} *Numerical Towing Tank Symposium, Hambürg*, 2001.

Comparison of VOF and Spectral-potential models on three-dimensional sloshing

David LE TOUZÉ, Yann ANDRILLON,
Pierre FERRANT and Bertrand ALESSANDRINI

Division Hydrodynamique Navale,
Laboratoire de Mécanique des Fluides (CNRS UMR6598)
École Centrale de Nantes, 1 Rue de la Noë,
B.P.92101 44321 Nantes cedex 3, France.
Email : david.letouze@ec-nantes.fr

1 Introduction

This paper intends to show a comparison between two different free surface flow solvers.

The first one is a fast potential flow method based on a spectral technique. This one-phase potential flow model is limited to non-breaking flows, due to a single-valued free-surface formulation. However, its features of fast calculation, high accuracy and robustness up to almost vertical slopes may be of interest. It will also be the occasion to compare different spectral techniques, including a new variant of fully-dealiased High-Order Spectral method.

The second model solves the Navier-Stokes equation and uses a 'Volume Of Fluid' method for predicting the free surface in a fully-coupled approach to calculate the flow motion. This VOF method includes no reconstruction. Indeed, to ensure the accuracy of the method, the sharpness of the interface is conserved using a High Resolution scheme for the convection discretisation. The discretisation is made by a finite volumes technique such that structured or unstructured meshes are usable.

Previous validating two-dimensional cases will first be presented. Comparisons of simulations of sloshing waves in a three-dimensional tank will then be presented and discussed, including the post-breaking stage in the VOF-model calculations.

2 Spectral Solver

The application of spectral methods to potential flow simulations are limited to a few examples up to now (including e.g. [13] [8], [10], and [14]), despite their well-known quick convergence and high accuracy features. However, their application was limited until recently to simulations of wave fields starting from an initial sea-state. Le Touzé & Ferrant [15] have proposed an extended model able to generate and propagate accurately fully-nonlinear wave fields starting from the rest. This model is included in the novel Spectral-Wave Explicit Navier-Stokes Equations (SWENSE) model recently derived by Ferrant *et al.*[1] to calculate the diffraction on bodies submitted to a fully-nonlinear wave field in viscous flow. To compare with the VOF method here, only the kernel of the spectral model is employed, i.e. a three-dimensional wave tank without generating device, in which fully-nonlinear free surface conditions (FNFSCs) are modelled. Both the direct method by Fenton & Rienecker [9], and the High-Order Spectral technique by West *et al.*[10] will be used and compared.

Under potential flow theory considering the free surface to be single-valued, the potential and the free surface elevation verify in the fluid domain D of the $L_x \times L_y \times 1$ tank :

$$\begin{aligned}
\Delta\phi &= 0 && \text{in } D \\
\frac{\partial\eta}{\partial t} &= \frac{\partial\phi}{\partial z} - \frac{\partial\phi}{\partial x}\frac{\partial\eta}{\partial x} - \frac{\partial\phi}{\partial y}\frac{\partial\eta}{\partial y} && \text{on } z=\eta \\
\frac{\partial\phi}{\partial t} &= -\eta - \frac{1}{2}|\nabla\phi|^2 && \text{on } z=\eta \\
\frac{\partial\phi}{\partial n} &= 0 && \text{on } x=0,L_x\,;\quad y=0,L_y
\end{aligned} \tag{1}$$

Then the potential is expressed by means of a spectral expansion on the natural modes of the fluid domain D [9] :

$$\phi(x,y,z,t) = \sum_{(n_x,n_y)} A_{n_x n_y}(t)\frac{\cosh[k_{n_x n_y}(z+1)]}{\cosh[k_{n_x n_y}]}e^{i(k_{n_x}x+k_{n_y}y)} \qquad \text{in } D \tag{2}$$

This expansion is plotted in the preceding set of equations. Then collocation nodes are spread over the free surface at its instantaneous position, and from the two FNFSCs one can get the time derivatives of η and of the time modal amplitudes $A_{n_x n_y}(t)$ in a pseudo-spectral manner, involving the resolution of a linear system at each sub-step of the time-marching process. η at the collocation nodes and the $A_{n_x n_y}(t)$ are then advanced in time using a 4^{th}-order Runge-Kutta scheme.

Alternatively, the FNFSCs can be written by means of the Zakharov surface potential [17]. The only remaining non-surfacic quantity in their expression is the potential vertical derivative $\partial\phi/\partial z$. The so-called High-Order Spectral (HOS) technique consists then in expanding this last quantity located at the *exact* free surface position, in Taylor series about the undisturbed free surface position $z = 0$. An iterative process can then be settled to obtain $\partial\phi/\partial z$ through that development, starting from known surface quantities (such as the surface potential). This iterative process is also solved in a pseudo-spectral manner, this time by means of FFTs, benefiting from the evaluation at the fixed surface $z = 0$. However, by plotting in the FNFSCs the solution obtained for $\partial\phi/\partial z$ out of this iterative process, one gets the full expression of these FNFSCs still *at their exact position*. The surface quantities, again at this exact position, can next be updated through the time-marching scheme. This is to say that *the HOS technique retains the fully-nonlinear feature of the solution*, despite the Taylor expansion and the following iterative resolution, which is *inner* and *not correlated* to the main resolution. This model is therefore not linked to classical perturbation series expansions.

This HOS technique has been proposed independently and almost simultaneously by Dommermuth & Yue [8] and West *et al.*[10]. However, as noticed by Tanaka [14], the West *et al.*version should rather be considered since its consistent development in orders of η fully retains the Hamiltonian conservative structure of the solution. So here a new fully-dealiased version of the West *et al.*solution is used, formulated in a bounded tank whereas theirs is for unbounded periodic free surfaces.

3 Free Surface Capturing Solver

The 2D Free Surface Capturing method used in this comparison has been presented during the Nutt's of 2002 [4]. The novelty in the code is the used of a new correction method for volume fraction field, and the new ability of it to simulate three dimensional application. Practically, the 'Volume Of Fluid' method employed has been investigated by several authors as Ubbink[16], Perić[11, 5] and Didier[7]. This method calculate the flow in the two fluids (air and water), considered as one single fluid whose physical properties vary across the interface. The physical characteristics ρ and μ are determined using the value of an additional variable (c) the volume fraction, given in equation (3). The value of (c) is such that, if a cell is filled with fluid 1, (c=0), and if it is filled with fluid 2, (c=1). The behaviour of the free surface is calculated through an additional advection equation (4). Consequently, the computation is performed on one a large fixed grid, which is one of the advantages of the method.

$$\rho = \frac{c\rho_1 + (1-c)\rho_2}{\rho_1} \qquad \mu = \frac{c\mu_1 + (1-c)\mu_2}{\mu_1} \tag{3}$$

$$\frac{\partial c}{\partial t} + \overrightarrow{\nabla}\cdot(c\overrightarrow{u}) = 0 \tag{4}$$

The disadvantage of the method is the difficulties to conserve correct global volume of fluid. In the correction method employed, different level of neighbour of the free surface are defined, the level 1 corresponding to the cells crossed by the interface. Then the cell which have a level higher to 4, the volume fraction is corrected to 0 or 1. The others with a level lower than 4 is corrected in order to obtained the exact initial volume of fluid. So, the conservation of the global volume is ensured and the transition is thin.

The flow is calculated using the incompressible Navier-Stokes equations which drive the motion of the fluid. In order to discretise the system, their dimensionless conservative form, as presented below (5, 6), is employed using a fully implicit finite volume method. To ensure the accuracy of the solver, the integrals are approximated to second order and the flux approximation is evaluated with a deferred correction. One critical issue of the VOF method is the choice of the differencing schemes employed to solve the convective term of the volume fraction equation. Low order schemes like central differencing schemes are not suitable because bounded solution is not ensured. And other differencing schemes like first-order upwind scheme are too diffusive, smear the interface and introduce artificial mixing of the two fluids over a wide region. Therefore high order mixing schemes have been designed for this application such as the CICSAM scheme developed by Ubbink[16]. It preserves a sharp transition zone with a checked boundedness criterion.

$$\begin{aligned} \int_V \frac{\partial \rho u_i}{\partial t} dV + \int_S \rho u_i \, (\overrightarrow{u} . \overrightarrow{n}) \, dS + \int_S P \, \overrightarrow{i}_i . \overrightarrow{n} \, dS + \int_S \frac{\mu}{Re} \left(\overrightarrow{\nabla} \overrightarrow{u} . \overrightarrow{n} \right) dS \\ = \int_V \frac{1}{Re} \left(\overrightarrow{\nabla} \mu \right) . \left(\overrightarrow{\nabla} . \overrightarrow{u} \right) dV + \int_V \rho \frac{1}{Fr^2} \frac{\overrightarrow{g}}{g} dV \end{aligned} \tag{5}$$

$$\int_S \overrightarrow{u} . \overrightarrow{n} \, dV = 0 \tag{6}$$

As indicated before the system is built through a Fully Coupled method. Numerically this technique presents the advantage of accelerating the velocity-pressure coupling and fasten the convergence. More precisely, the Rhie and Chow[12] velocity flux reconstruction is applied to the conservation of momentum Navier-Stokes equation to obtain a single system using the pressure, the velocity and an added variable the second velocity. The solution is calculated with an iterative algorithm BiCGSTAB-ϖ using an incomplete LU decomposition preconditionner.

The VOF solver capabilities have been checked on different applications [3, 4, 2], such as the flow in a sloshing tank or the simulation of a Rayleigh-Taylor instability.

4 Results

The first sloshing flow used to compare the solver is an two-dimensional test case . It has been compared to experiment made by Corrignan[6]. The tank employed is 0.4 m wide, 0.2 m high and is filled to 60% of water. The movement of the tank is an horizontal oscillating displacement. It is ruled by the equation (7). The VOF calculations were performed on a structured of about 3500 control volumes and the time step is about $dt = 0.001$.

$$x(t) = \begin{cases} A \cdot (sin(2\pi f_1 t) - sin(2\pi f_2 t)) \text{ if } 0 \leq t \leq 3.43s \\ 0 \text{ otherwise} \end{cases} \tag{7}$$

$$\begin{aligned} A &= 7.5.10^{-3} m \\ f_1 &= 1.598 Hz \\ f_2 &= 1.307 Hz \end{aligned} \tag{8}$$

On the following figures, the exact interface shape of the experiment, the spectral and the VOF simulation is showed. the numerical results are in good agrement withe the experimental one. And it can be notice that the transfers between the potential energy and kinetic energy seem to be correctly simulated for the VOF solution and the numerical diffusion seems to be negligible.

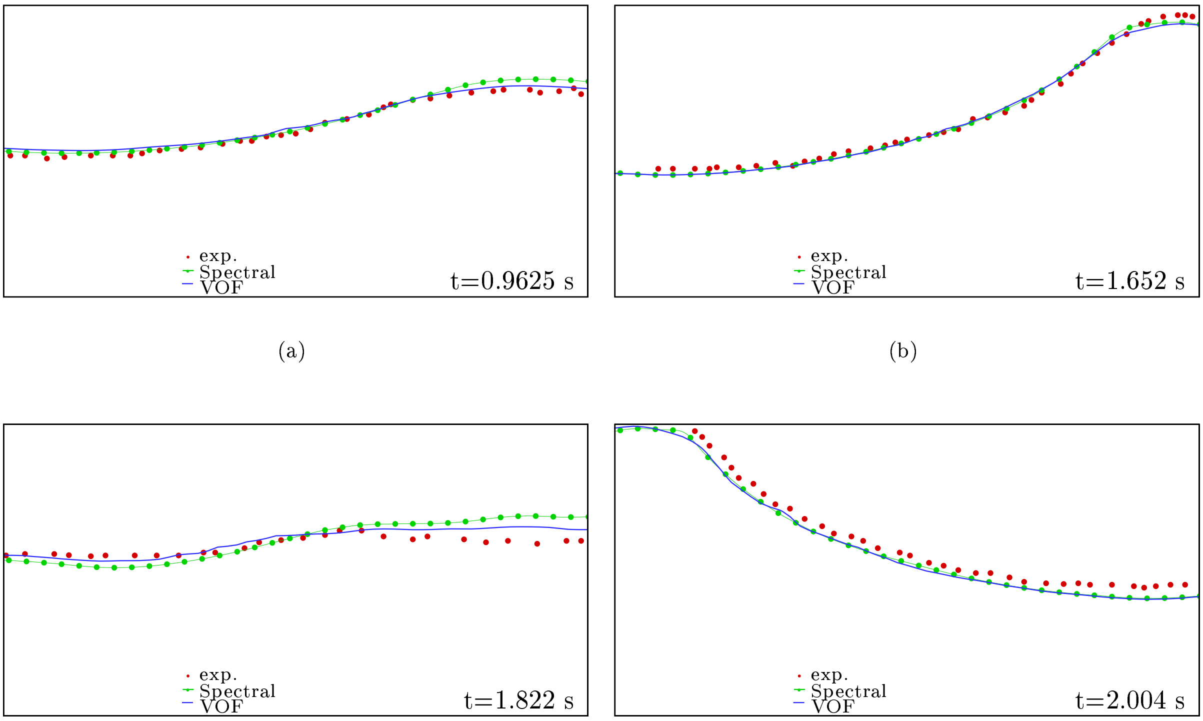

(a) (b)

(c) (d)

The second application has been made in a three-dimensional tank. The tank is B=25 m and L=25 m wide and contains 1 m fluid. The translational movement is explain in 9, where ω_{0x} and ω_{0y} are calculated using 10, the terms with m=1,3,5... ,n=0 and n=1,3,5... m=0 correspond to the symmetric motions in the x and y directions, respectively. in our case each first frequencies are obtained by taking m=1, n=0 and n=1, m=0.

$$\begin{cases} x(t) = A \cdot sin(0.998\omega_{0x}t) \\ y(t) = A \cdot sin(0.998\omega_{0y}t) \end{cases} \tag{9}$$

$$\begin{aligned} &A = 1.2m \\ &\omega_0 = \sqrt{\sqrt{\left(\frac{m\pi}{L}\right)^2 + \left(\frac{n\pi}{B}\right)^2} tanh\left(\sqrt{\left(\frac{m\pi}{L}\right)^2 + \left(\frac{n\pi}{B}\right)^2}\right)} \end{aligned} \tag{10}$$

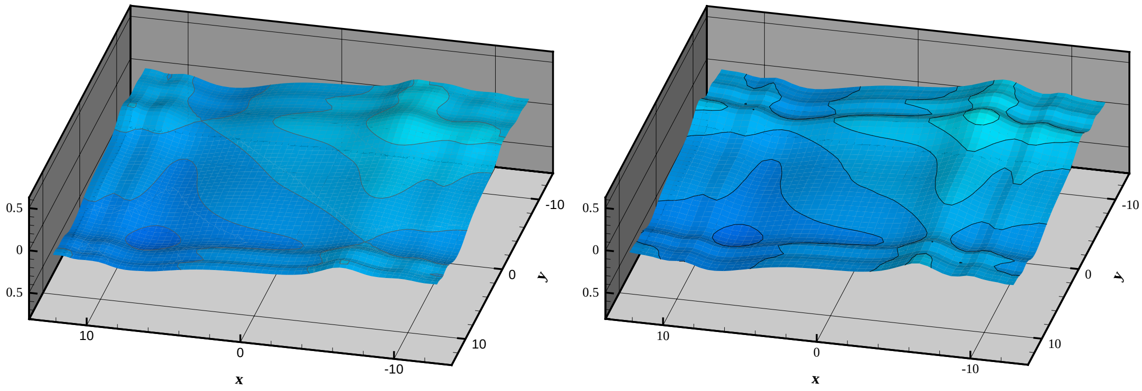

FIG. 1: Free surface elevation in the tank at t=10

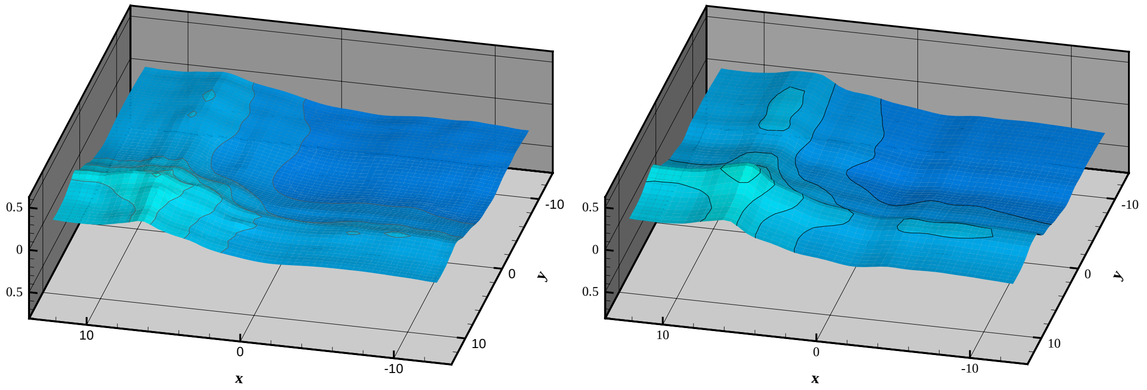

FIG. 2: Free surface elevation in the tank at t=21

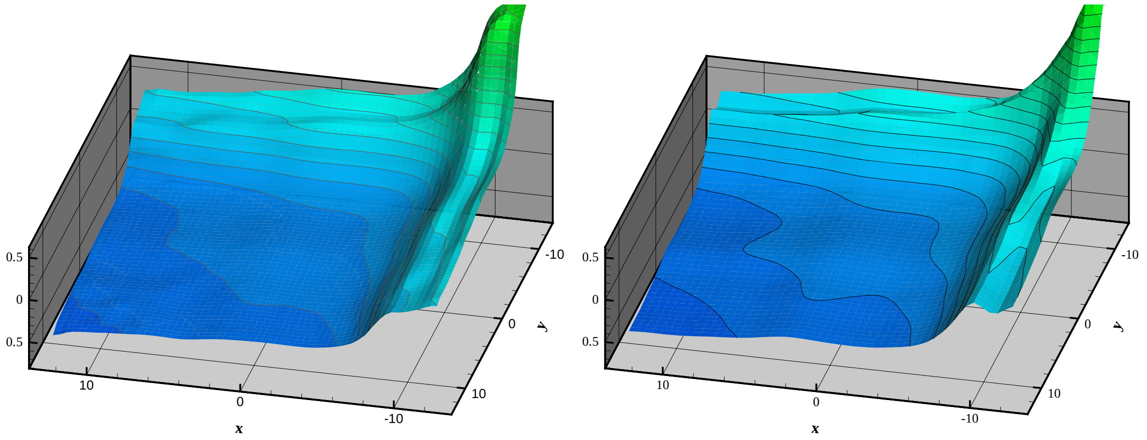

FIG. 3: Free surface elevation in the tank at t=44.1

The different views show the free surface shape obtained using the VOF (left) and spectral (right) models. Four selected instants of the simulation are presented, as the forced motion of the tank leads to steeper and steeper slopes in the free surface. Contours on the various snapshots represent the water elevation, the levels shown are exactly the same in the two simulations. On the first pair of views, one can notice a nice agreement between the two potential and viscous flow models. With the increase of the energy given to the fluid, the free surface motion becomes more and more violent, leading to dissipation in the viscous model. Therefore one can observe small differences increasing with time between the two solutions, in particular less pronounced crests and slopes in the VOF results. However, the much faster potential model and the VOF solution are in close agreement up to the time of the third pair of views, where a violent crest occurs in one corner of the tank. Of our two spectral models, only the direct method is able to keep on, with the inclusion of smoothing, up to the time of first breaking shortly after (fourth pair of snapshots). The very fast HOS technique (without smoothing) stops at the time of the third views, where very steep slopes close to breaking are already present. A finer comparison of the direct and HOS spectral methods will be presented at the workshop, as well as the post-breaking stage of the VOF calculation.

Références

[1] P Ferrant L Gentaz B Alessandrini and D Le Touzé. A potential / RANSE approach for regular water wave diffraction about 2d structures, (accepted for publication). *Ship Tech. Res. / Schiffstechnik*, 50, 2003.

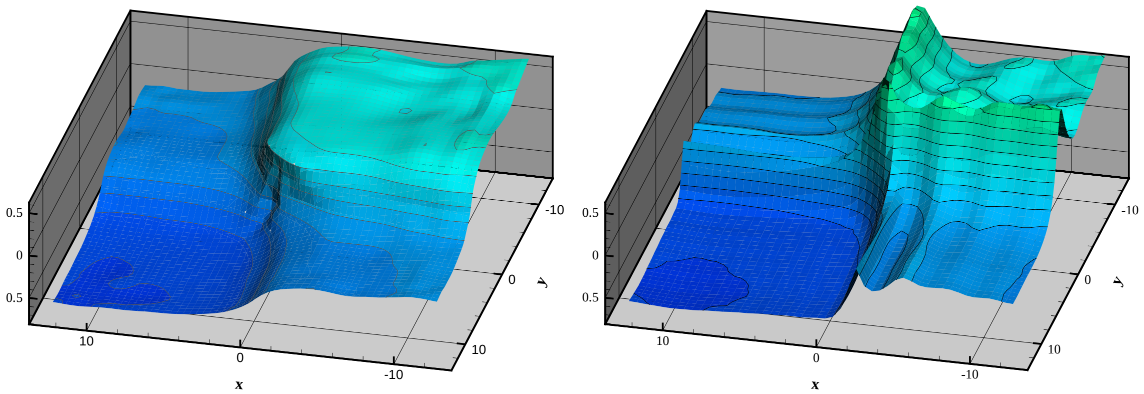

Fig. 4: Free surface elevation in the tank at t=54

[2] Y Andrillon M Doring B Alessandrini and P Ferrant. Comparison between sph and vof free surface flow simulation. In *5th Numerical Towing Tank Symposium*, September 2002.

[3] Y Andrillon and B Alessandrini. A 2D+T VOF fully coupled formulation for calculation of breaking free surface flow. In *24^{th} Symposium on Naval Hydrodynamics*, July 2002.

[4] Y Andrillon and B Alessandrini. A fully-coupled VOF method for free surface simulation. In S F Lee R C T Rainey, editor, *International Workshop on Water Waves and Floating Bodies*, April 2002.

[5] R Azcueta, S Muzaferija, and M Perić. Computation of water and air flow around ships. In *EUROMECH*, pages 121–131, 1998.

[6] P Corrignan. Analyse physique des phénomènes associés au ballotement de liquide dans les réservoirs (sloshing). *Thèse de Doctorat*, 1994.

[7] E Didier. *Simulation D'écoulements À Surface Libre sur Des Maillages Destructurés*. PhD thesis, Ecole Centrale de Nantes, 2001.

[8] D G Dommermuth and D K P Yue. A high-order spectral method for the study of nonlinear gravity waves. *J. Fluid Mech.*, 184 :267–288, 1987.

[9] J D Fenton and M M Rienecker. A fourier method for solving nonlinear water-wave problems : application to solitary-wave interactions. *J. Fluid Mech.*, 118 :441–443, 1982.

[10] B J West K A Brueckner R S Janda M Milder and R L Milton. A new numerical method for surface hydrodynamics. *J. Geophys. Res.*, 92 :11803–11824, 1987.

[11] S Muzaferija, M Peric, P Sames, and T Schellin. A two-fluid navier-stokes solver to simulate water entry. In *22nd Symposium on Naval Hydrodynamics*, pages 638–649. The National Academy of Sciences, 2000.

[12] C M Rhie and W L Chow. A numerical study of the turbulent flow past an isolated airfoil with trailing edge separation. *AIAA J.*, 21 :1525–1532, 1983.

[13] W J Bateman C Swan and P H Taylor. On the calculation of the water particle kinematics arising in a directionally spread wavefield. *J. Comput. Phys.*, 186 :70–92, 2003.

[14] M Tanaka. A method of studying nonlinear random field of surface gravity waves by direct numerical simulation. *Fluid Dynamics Res.*, 28 :41–60, 2001.

[15] D Le Touzé and P Ferrant. On the optimal use of submerged dipoles for the generation of unsteady nonlinear waves. *Proc. of the 18^{th} Int. Workshop on Water Waves and Floating Bodies, Le Croisic*, pages 109–112, 2003.

[16] O Ubbink. *Numerical Prediction of Two Fluid Systems with Sharp Interfaces*. PhD thesis, Imperial College, 1997.

[17] V E Zakharov. Stability of periodic waves of finite amplitude on the surface of a deep fluid. *J. Appl. Mech. Tech. Phys.*, 9 :190–194, 1968.

Numerical and Experimental Study of Sloshing in Partially Filled Rectangular Tanks

Andrea Colagrossi, Claudio Lugni, INSEAN, Rome/Italy, a.colagrossi@insean.it
Vincent Dousset, Volker Bertram, ENSIETA, Brest/France
Odd M. Faltinsen, Dept. of Marine Technology, NTNU, Trondheim/Norway

A 2D Smoothed Particles Hydrodynamics (SPH) code has been developed at INSEAN and applications to the breaking-dam problem have been described at a previous NuTTS, *Colagrossi et al. (2001)*, and expanded in *Colicchio et al. (2002)*. *Landrini et al. (2003)* applied INSEAN's SPH code to sloshing. *Colagrossi and Landrini (2003), Landrini et al. (2003)* give details of the theory. The described SPH method is rather robust (even for large free-surface fragmentations and folding), efficient and simple to code. CPU times are comparable to other techniques capable of modeling breaking waves.

The SPH technique studies the fluid flow as the movement of fluid particles, which have their own mass, density, velocity, and pressure. Each particle is influenced in its evolution by the evolution of the neighbor particles. Consequently, the characteristics of the particles are estimated through interpolation equations, which are weighted sums of the characteristics of the nearby particles. These equations are governed by a kernel function W which assigns its weight in the sum to each particle involved in the computation of a given property. We use a Gaussian kernel function with cut-off limit of $3h$. Fig.1 explains how a Gaussian kernel of length h influences the computations of the properties of the particle centered on x^*.

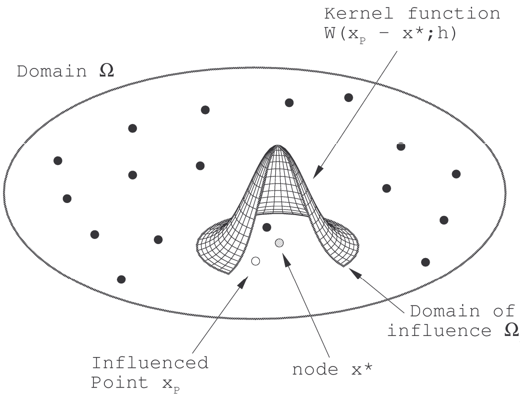

Fig.1: Implementation of the kernel function W on the fluid domain Ω

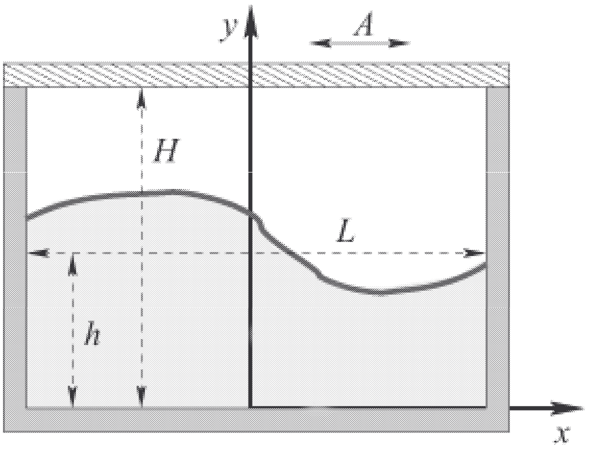

Fig.3: Coordinates and nomenclature

The SPH code solves the Euler equations in Lagrangian formulation together with an equation of state for the pressure. This suffices for the sloshing problem which is substantially governed by inviscid mechanisms. The method treats the flow as a weakly-compressible inviscid fluid for numerical efficiency, ensuring that this does not introduce errors in representing the actual physics. We consider a reference system fixed relative to the tank, Fig.2.

The fluid equations for a generic excitation of the tank are:

$$\frac{d\rho_i}{dt} = -\rho_i \sum_j M_{ij} \tag{1}$$

$$\frac{du_i}{dt} = -\frac{1}{\rho_i} \sum_j F_{ij} - f_i \tag{2}$$

$$\frac{dx_i}{dt} = u_i \tag{3}$$

$$p(\rho) = P_0\left[\left(\frac{\rho}{\rho_0}\right)^{\gamma} - 1\right] \tag{4}$$

ρ_i is the fluid density of the i^{th} particle, u_i its velocity, and x_i its position; in the following only the liquid phase will be modeled, while a two phase flow SPH model are described in *Colagrossi and Landrini (2003)*. The interaction terms M_{ij} and F_{ij} follow from the discretization of the mass and momentum conservation equations. Finally, $\rho_i f_i$ represents any body force; here we account for gravity and apparent forces. The interaction terms can be computed independently, resulting in an explicit method easily implemented on parallel computers. The state equation (4) must be satisfied by the particle pressure and depends only on the value of the density. The parameters P_0, ρ_0 and γ are chosen to have maximum density oscillations of order of 1% around the reference value ρ_0. The reference value is obtained by choosing the speed of sound $c_s = (dp/d\rho)$ at least ten times larger than the highest fluid velocity expected in the analyzed physical problem.

To maintain consistency between mass, density and occupied area during the simulation (correcting for accumulating numerical errors), the density field is periodically re-initialized by applying:

$$\rho_i = \sum_j m_j W_{ij} \tag{5}$$

This is not straight-forward along the fluid domain boundaries. In these areas, the number of particles seen by a given particle decreases, i.e. the computed density is smaller than the original value. By adapting the kernel function to account for the fluid boundary, Eq.(5) is adapted to this demand. This gives slightly longer computations, but mass conservation is restored, a more regular pressure distribution is derived and total energy is better conserved. An artificial viscosity is included in the discretized momentum equation to increase the stability of the numerical algorithm. Time integration follows a fourth-order Runge-Kutta method.

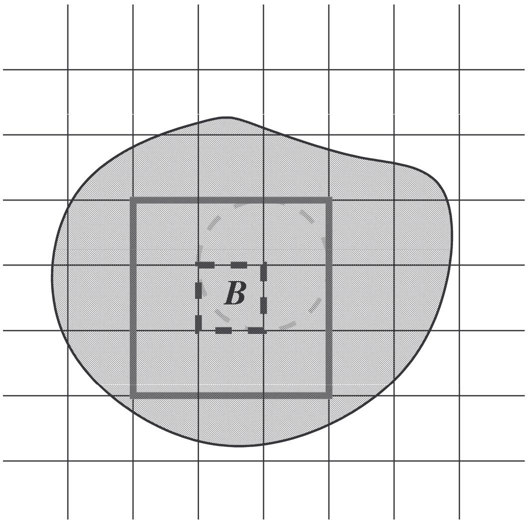

Fig.3: Limits of the particle searching algorithm Ω

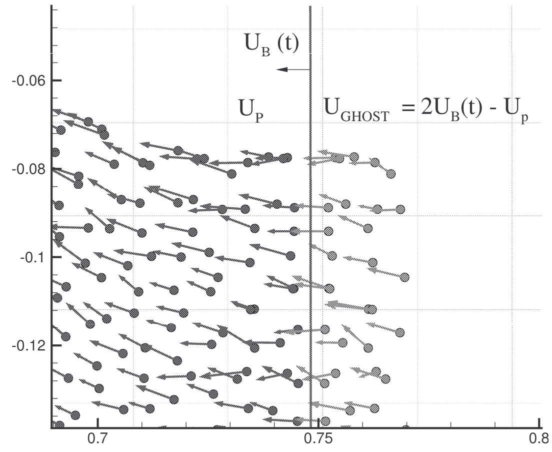

Fig.4: Location and velocity of the ghost particles for a straight wall

For the weakly-compressible treatment of liquids and to prevent particle inter-penetration, we implemented a velocity (XSPH) correction Δu_i in the equations of particle motion following *Monaghan (1994)*. This correction considers the neighbor velocities through a mean velocity evaluated within the particle support. A background Cartesian grid covers the whole fluid domain and beyond. This grid consists of square cells of length $3h$. The particle searching algorithm to compute F_{ij} and M_{ij} is implemented only for the cell where the particle is and the eight closest adjacent cells, Fig.3. In Fig.3, the cell which contains the particle is in the dashed line, the cells taking part in the interpolation equations are included in the thick-sided square. The dashed circle represents the influence domain for a particle located on a vertex of the dashed-limited cell. In practice, a first list collects all the cells with their respective particles at a given time. A second list contains pointers from a given particle to the cell containing it. These lists are updated at each time step.

Pressure continuity at the free surface is granted by the definition of the kernel function W. The kinematic condition is satisfied by the Lagrangian tracking of the particles. A no-penetration condition on solid boundaries (walls) is imposed using 'ghost particles'. Density, pressure, and velocity of these fictitious particles are deduced from those of the physical particles adjacent to the solid boundary. At each time step, all the particles within a layer with $3h$ thickness from the wall are mirrored inside the body. Fig.4 shows the case of a straight wall, giving also the velocity law for the ghost particles.

The code has been validated against an extensive series of sloshing experiments performed recently at INSEAN. *Faltinsen et al. (2000)* proposed a multimodal approach, improved in *Faltinsen et al. (2001)* to solve a pitch and surge-excited sloshing problem in a rectangular tank. They compare their theoretical results with the sloshing experiments in a rectangular tank with sinusoidal surge excitation performed by *Olsen and Johnsen (1975).* We compared these theoretical and experimental data for $h/L = 0.35$ and excitation amplitudes $A = 0.05 \cdot L$ and $A = 0.1 \cdot L$. Fig.5 compares SPH results, original experiments of Olsen and Johnsen, multimodal approach and our own experiments for the maximum free-surface elevation ζ measured (= maximum absolute value measured by the gauge within the steady-state flow) at 5 cm from the right wall as a function of the excitation period T. The results fit well except for the $T/T_1 \leq 1$ for $A/L = 0.1$. T_1 is the first natural period according to linear theory. Since we do not know the details of the experimental set-up used by Olsen and Johnsen and their procedure for evaluating ζ/L, it is not straightforward to explain the disagreement. The two experiments diverge for high excitation frequencies. There, flow non-linearities will be more relevant making steady-state flow conditions in the tank difficult. Thus the results could be sensitive to the used transient. Olsen and Johnsen initiated the measurements 5 minutes after the tank motion started; we did so after 4 min and 10 s. Also, we used a crank-connecting rod system to drive the excitation. As a consequence, for excitation frequency larger than resonance frequency, during the initial transient the resonance frequency was excited (briefly) which could affect the resulting sloshing conditions. In particular for $T/T_1 \leq 1$ and for $A/L = 0.1$, we observed in the experiments during the transient regime water impact on the tank roof which will modify the steady-state conditions. This could explain also differences between our experiments and the multimodal approach. Current research focusses on a more detailed investigation of the transient regime.

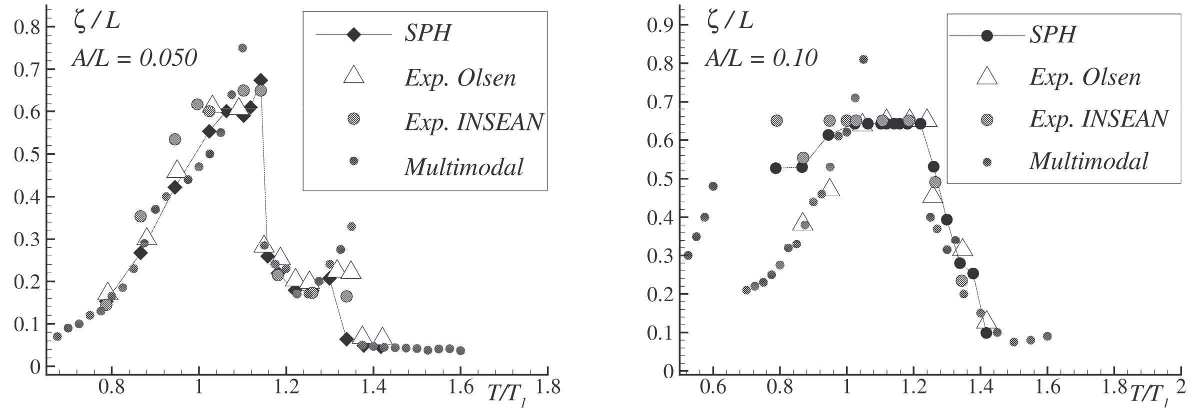

Fig.5: Max. wave amplitude vs. period of oscillation; $A/L = 0.05$ (left), $A/L = 0.1$ (right)

In the SPH simulations, a linear ramp was enforced numerically to gradually reach the desired excitation frequency. Then, the frequency was maintained constant during 32 periods. The SPH results were finally obtained by analyzing the last 20 simulated periods. SPH predictions agree generally with experiments. For $T/T_1 \leq 1$ they agree better with Olsen and Johnsen's measurements and multimodal approach results for $A/L = 0.05$, better with our measurements for $A/L = 0.1$. However, the numerical simulations consider an evolution of only 40 periods. Therefore the considered time history is earlier than the time range used in either experiments. Thus, there are no definite conclusions possible.

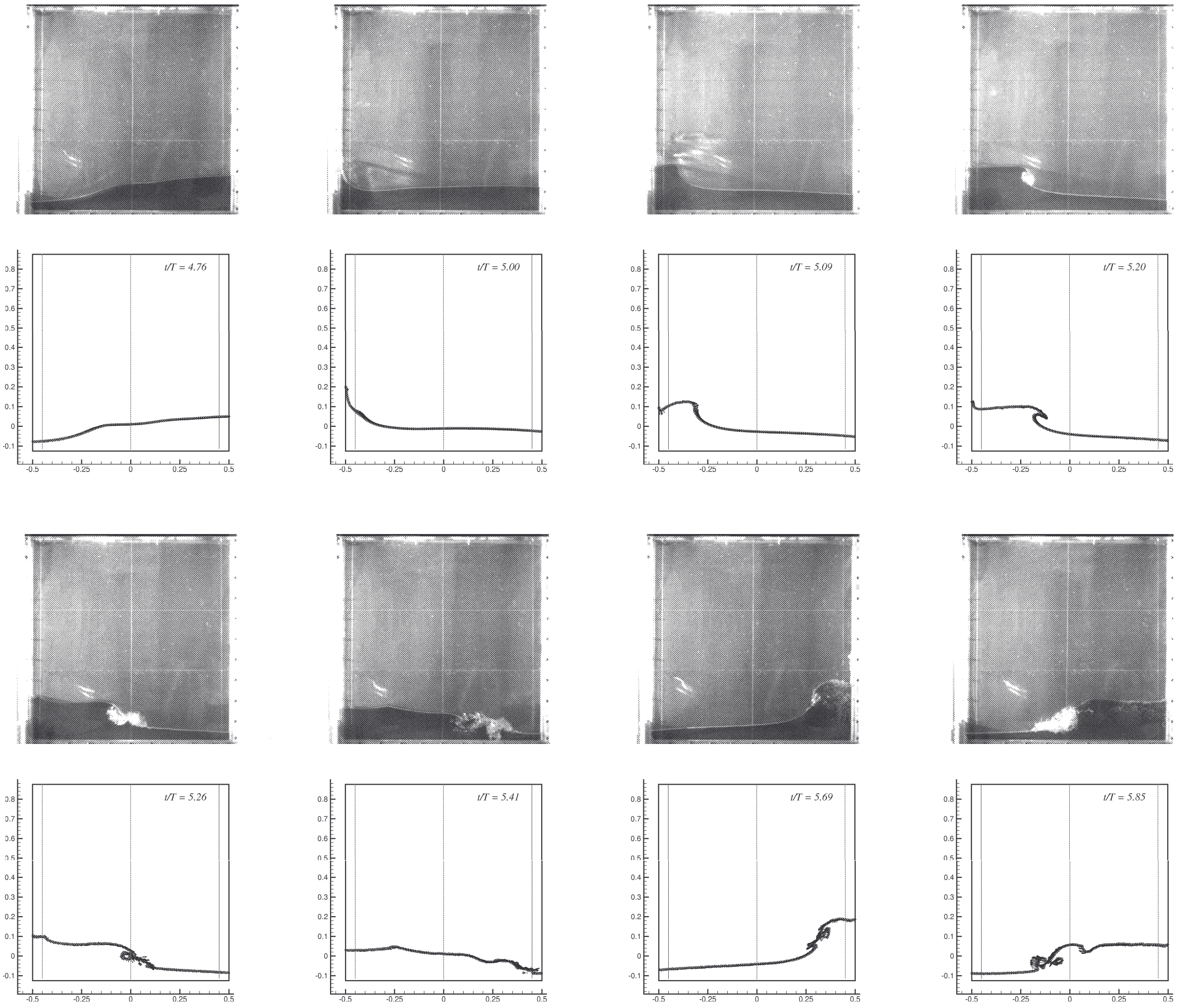

Fig.6: Experimental observations and SPH simulations for $h/L = 0.125$, $A/L = 0.1$, $T/T_1 = 1$. Related time instants from left to right, top to bottom: $t = 8.82s$, $t = 9.21s$, $t = 9.43s$, $t = 9.65s$, $t = 9.82s$, $t = 10.09s$, $t = 10.65s$, and $t = 10.91s$

SPH simulations have also been compared for shallow filling height to experiments performed at INSEAN. Flow features differ substantially from those at $h/L = 0.35$. Fig.6 compares SPH results and experimental observations for $h/L = 0.125$, $A/L = 0.1$, and $T/T_1 = 1$. A linear ramp was used to reach gently the excitation period, then the excitation frequency was kept constant. The shown sequence refers to the evolution phase between the end of the linear ramp and a few cycles after it. The water moves first from the right to the left of the tank, hits the left wall and creates a very thin jet flow along the structure. Then under the action of gravity a reversed motion is caused with the formation a plunging wave traveling towards the other side. The plunging wave quickly breaks on the underlying water and generates a splash-up series. The moving wave forms then a bore finally hitting the opposite wall. From this time on, the bore travels back and forth along the tank alternatively hitting the side walls. SPH results give free surface and velocity vectors of free-surface particles.

Experimental snapshots are in good agreement with the SPH predictions until the last time instant shown. Here, SPH predicts an earlier break-down of the wave than observed in the experimental recordings. Therefore, the subsequent wall impact will differ in energy and the maximum free-surface elevation experienced in the tests was higher than predicted by the SPH code, Fig.7. Results agree well up to $t/T \approx 6$, then start to deviate. The numerical maximum free-surface elevations predicted after this initial phase are lower than measured.

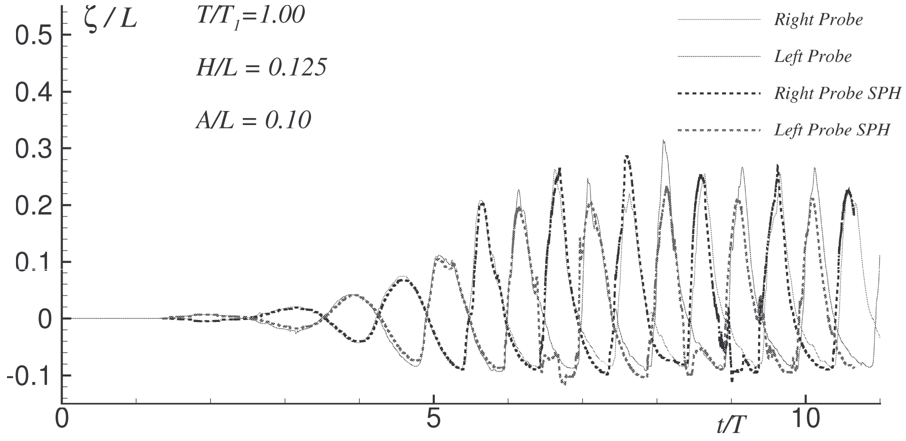

Fig.7: Time history of the free-surface elevation and related SPH predictions

Acknowledgment

This work is dedicated to Maurizio Landrini who contributed substantially to this paper. We miss him.

References

COLAGROSSI, A.; LANDRINI, M. (2003), *Numerical simulation of interfacial flows by smoothed particle hydrodynamics*, J. Comp. Phys. (to appear)

COLAGROSSI, A.; LANDRINI, M.; TULIN, M. (2001), *A Lagrangian meshless method for free-surface flows*, 4th NuTTS, Hamburg

COLICCHIO, G.; COLAGROSSI, A.; GRECO, M.; LANDRINI, M. (2002), *Free-surface flow after a dam break: A comparative study*, Ship Technology Research 49/3

LANDRINI, M.; COLAGROSSI, A.; FALTINSEN, O.M. (2003), *Sloshing in 2-D flows by the SPH method*, 8th Int. Conf. Num. Ship Hydrodynamics, Busan

MONAGHAN, J.J. (1994), *Simulating free surface flows with SPH*, J. Comp. Dyn. 110, pp.399-406

OLSEN, H.; JOHNSEN, K.R. (1975), *Nonlinear sloshing in rectangular tanks - A pilot study on the applicability of analytical models*, Det Norske Veritas report 74-72-S, Vol.II

FALTINSEN, O. M.; ROGNEBAKKE, O.; LUKOVSKY, I.A.; TIMOKHA, A.N. (2000), *Multi-dimensional modal analysis of nonlinear sloshing in a rectangular tank with finite water depth*, J. Fluid Mechanics 407, pp.201-234

FALTINSEN, O. M.; TIMOKHA, A.N. (2001), *An adaptive multimodal approach to nonlinear sloshing in a rectangular tank*, J. Fluid Mechanics 432, pp.167-200

RANSE analysis of 2D flow about a submerged body using explicit incident wave models

R. Luquet, B.Alessandrini, P. Ferrant & L. Gentaz
Ecole Centrale de Nantes[1]

Introduction

Today a lot of ocean or coastal engineering problems involving wave-body interactions is numerically treated by solving Reyolds Averaged Navier-Stokes Equations (RANSE). This is quite interesting because vorticity and viscosity effects can be very important for understanding of wave-body interactions.

However numerical simulations under viscous flow theory lead to very large CPU requirements because grids must be very refined between location of the structure and location of wave generation (for structured or non-structured grids used with finite differences or finite volumes). This is indeed necessary to propagate the wave signal from the paddle to the structure with no noticeable damping. Moreover successive wave reflections on the body or the paddle affect the incoming wave train and reduce the useable duration of the numerical simulation. However this kind of problem which concerns Numerical Wave Tanks (NWTs) based on potential or viscous flow theory can be easily largely avoided by using immersed singularities (spinning dipole is the most efficient because it can be generate waves in downstream direction only) or pressure patch *(Armenio & Favretto, 1997).*

To overcome these problems an original formulation is used here by modifying the initial problem in order to solve the diffracted flow only. This approach has previously been used in the frame of potential theory , by *Di Mascio et al. (1994)* or *Ferrant (1996)* in three dimensions, and e.g. *Schønberg and Chaplin (2001*) in two dimensions. It consists in splitting all unknowns of the problem (potential and free-surface elevation) in a sum of an incident term and a diffracted term. The incident terms are described explicitly. Thus only the part of the grid in the vicinity of the structure needs to be refined. Far from the body a stretched grid allows an efficient damping of the diffracted flow.

Here splitting of unknowns will be applied to a 2D viscous flow solver, *Gentaz et al. (2000*). The incident flow is supposed to verify a non-linear potential flow and the diffracted flow is solved by assuming that the total flow verifies RANS Equations : modified RANS Equations verified by the diffracted flow are named in the following SWENS (Spectral Wave Explicit Navier-Stokes) Equations.

This technique has been already successfully used for the case of a non-linear regular wave train on a submerged square cylinder (with its axis parallel to the wave crest) – see *Ferrant et al. (2002)* – and hydrodynamic forces had been compared with numerical and experimental data. Here an submerged horizontal circular cylinder under regular waves is considered in order to focus on free-surface elevations and its harmonic components on lee the side of the cylinder and to compare them with numerical and experimental results by *Schønberg & Chaplin (2001)* and *Chaplin (2001)* respectively.

Modification of the RANSE Solver to solve the diffracted problem

The viscous flow solver used in this study solves 2D RANS (Reynolds Averaged Navier-Stokes) Equations under laminar flow assumption and non-linear free-surface boundary conditions.

In the initial formulation of the problem primitive variables are Cartesian components of velocity (u^1, u^2), pressure *p* and free-surface elevation *h*. Dependant space unknowns are (x^1, x^2) horizontally and vertically upward oriented respectively.

To consider the single diffracted problem, primitive unknowns (Cartesian components of velocity (u^α) with $\alpha \in \{1,2\}$, pressure *p* and free-surface elevation *h*) are decomposed as follows :

---

[1] LMF/DHN, UMR 6598 du CNRS, 1, rue de la Noë, F-44321 Nantes Cedex 03, France

$$\begin{cases} u^{\alpha} = u_I^{\alpha} + u_D^{\alpha} \\ p = p_I + p_D \\ h = h_I + h_D \end{cases} \qquad \alpha \in \{1,2\} \tag{1}$$

Variables with the subscripts *I* and *D* represent incident and diffracted variables, respectively.

This decomposition is then introduced in the set of initial equations assuming that the incident wave flow fulfils the Euler equations and non-linear free surface boundary conditions in potential flow theory :

- Transport equations :

$$\frac{\partial u_D^{\alpha}}{\partial t} + \left(u_I^j + u_D^j\right)\frac{\partial u_D^{\alpha}}{\partial x^j} - \nu \frac{\partial^2 u_D^{\alpha}}{\partial {x^j}^2} + \frac{1}{\rho}\frac{\partial p_D}{\partial x^{\alpha}} = -u_D^j \frac{\partial u_I^{\alpha}}{\partial x^j} + \nu \frac{\partial^2 u_I^{\alpha}}{\partial {x^j}^2} \qquad \alpha \in \{1,2\} \tag{2}$$

- Mass conservation :

$$\frac{\partial u_D^j}{\partial x^j} = 0 \tag{3}$$

- Free-surface boundary conditions :

(i) kinematic condition
$$\frac{\partial h_D}{\partial t} + u_D^1 \frac{\partial h_I}{\partial x^1} + \left(u_I^1 + u_D^1\right)\frac{\partial h_D}{\partial x^1} = u_D^2 \tag{4}$$

(ii) normal dynamic condition
$$p_D = \rho g h_D + 2\rho\nu \frac{\partial}{\partial x^j}\left(u_I^j + u_D^j\right) n_i n_j \tag{5}$$

(iii) tangential dynamic condition
$$\left(n_j t_i + n_i t_j\right)\frac{\partial}{\partial x^j}\left(u_I^i + u_D^i\right) = 0 \tag{6}$$

In Equations (2) to (6) terms with incident variables (velocities, velocity gradients, free-surface elevations and free-surface elevation gradients …) are explicitly computed knowing kinematics and interface position of the incident flow. This set of equations will be named in the following SWENS (Spectral Wave Explicit Navier-Stokes) Equations. Note that the equations have been given for laminar flow, which is consistent with numerical examples given in the sequel. SWENS equations for turbulent flows are easily obtained by taking the turbulent viscosity ν_t into account.

In order to compute the set of equations defined previously the fluid domain is discretised by a structured monoblock grid. The equations (2) to (6) are modified by using a set of curvilinear space variables fitted to the geometry of the fluid domain to simplify the implementation of boundary conditions. A free-surface tracking method is used to update the interface : at each time step the mesh is regridded following the new shape of the free surface. Equations are discretised by second-order finite difference schemes in space and time. A pressure equation is obtained by combining the equation of mass conservation (3) with transport equations (2) following the Rhie & Chow procedure (Rhie & Chow, 1983) : thus checkerboard oscillations classically associated with centered second-order schemes are suppressed.

An original fully-coupled method, developed by *Alessandrini* and *Delhommeau* (*1995*), is used to solve the discretised set of equations : at each iteration all equations (RANS Equations, pressure equation, free-surface boundary conditions, no-slip conditions) are assembled in a single large and sparse linear system which is solved using a bi-CGSTAB algorithm with an incomplete LU preconditioning.

Models of incident flows

To consider a non-linear regular incident wave train an algorithm based on the stream function theory of *Rienecker & Fenton (1981)* has been implemented.

A irregular wave train could be prescribed as well by using a spectral formulation. This kind of procedure has been already developed by *Ferrant & Le Touzé (2002)* combining a spectral formulation and a Boundary Element Method (BEM) to simulate an irregular wave train interacting with a 3D body under potential flow theory.

Finally the combination of incident potential flow and RANS solvers for the diffracted problem can be summarized as follows : At each time step of the computation the geometry of the fluid domain is updated. The kinematics of the incident wave flow is calculated on this updated grid and then the diffracted problem defined by the set of SWENS Equations (2) to (6) is solved using the viscous flow software described previously.

Preliminary results

Two unnecessary approximations used previously (*Ferrant et al., 2002*) have been modified in the present work. First, finite differences methods were used to determinate the derivatives of the incident flow variables. However this flow is known analytically so the formulas of its derivatives can be directly obtained. These analytical terms have been implemented and the results obtained by simulations including the two kinds of derivatives have been compared. As shown in the numerical results on the left of figure 1 the differences between the two ways of calculating the derivatives is sizeable and can reach 10 %. However the consequences on global quantities like the free surface profiles are almost negligible (figure 1, on the right).

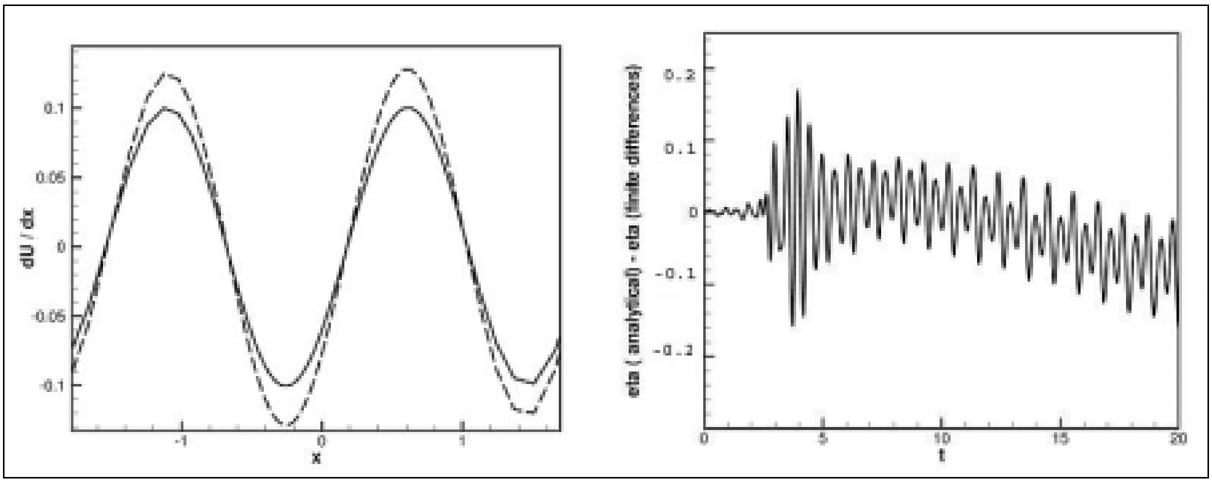

Figure 1 : Deep water wave diffracted by a circular cylinder at *x*=0.
Left : variation of $\frac{\partial U}{\partial x}$ for the incident flow at *t*=12 s, solid : finite differences; dashed line : analytical derivative .
Right : Difference in percentages between the two free-surface elevations at *x*=0.2.

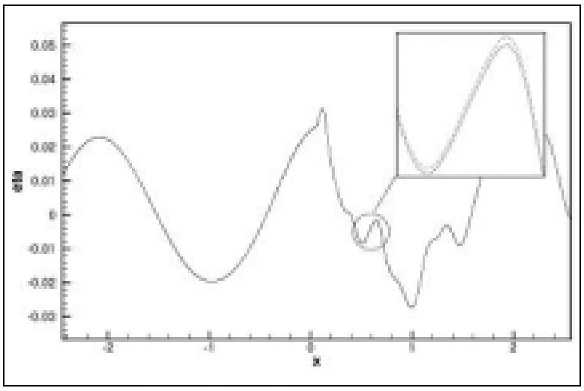

Figure 2 : Free-surface profile of deep water wave diffracted by a circular cylinder.
Dashed and solid lines correspond respectively to results from Euler and RANS assumption.

In the other approximation the incident wave flow was assuming to verify RANS Equations in order to simplify the equation set (2) to (6). This was not strictly exact because the incident non-linear flow model of *Rienecker & Fenton (1981)* used here is based on potential flow theory and verifies Euler equations only. That is why equations (2) to (6) have been modified consequently. Figure 2 gives a comparison between two free-surface profiles corresponding to results from Euler or RANS assumption for the incident flow and shows that profiles are very close.

Finally verification of volume conservation has been made: the variation is smaller than 1 % for simulations longer than 40 s.

Results

A non-linear regular wave train is propagating above an immersed horizontal circular cylinder in deep water is computed here following numerical study of *Schønberg & Chaplin (2001)* and measurements by *Chaplin (2001)*. Parameters of computation are normalised by taking the cylinder radius c and $(c/g)^{1/2}$ as length and time scales respectively. Thus the cylinder submergence is d/c=1.5, the angular frequency kc=0.56 and the amplitude of the fundamental frequency component a/c is 0.107. With these parameters, the Keulegan-Carpenter number is KC=0.15.

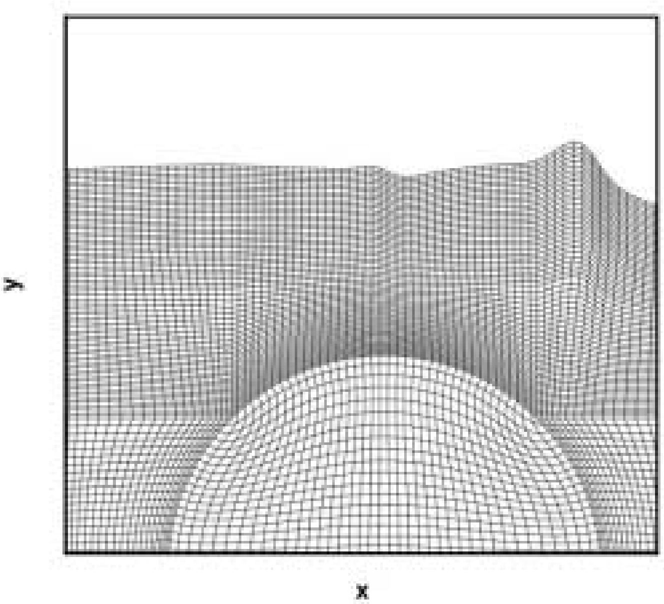

Figure 3 : details of the grid used in computations

For present computation under viscous flow theory a 300000 nodes grid has been used in order to compute properly higher order harmonic components of the free surface elevation – about 40 points per wavelength for the third harmonic to compare with 10 points in the same case for the potential flow computations of *Schønberg & Chaplin (2001)* – A part of this grid is shown on figure 3.

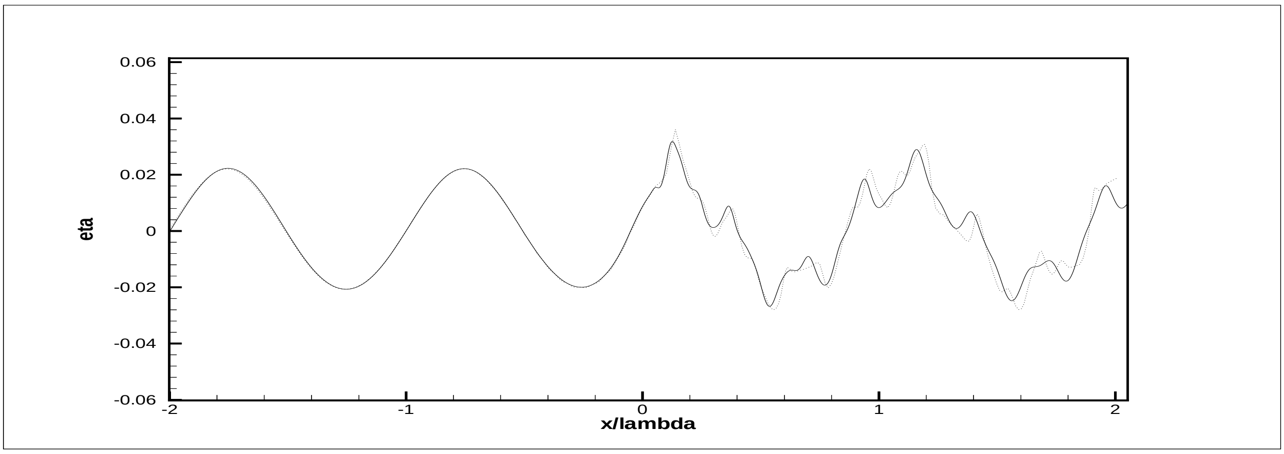

Figure 4 : Free-surface profile for *d/c*=1.5, *kc*=0.56 and *a/c* = 0.107.
Solid line : present computations; dotted line : computations from *Schønberg & Chaplin (2001)*

On figure 4 instantaneous free-surface profiles are compared with potential flow computations made by *Schønberg & Chaplin (2001*) with a quite good agreement. These profiles are plotted at the instant at which the undisturbed wave filed would have a zero up-crossing at *x*=0.

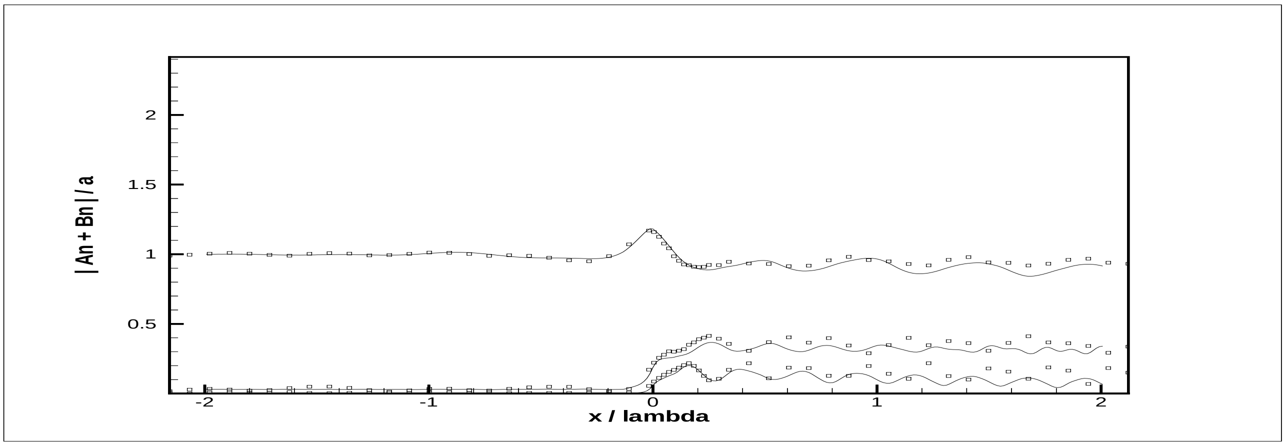

Figure 5 : Fourier components of the free surface elevation.
Symbols : measurements from *Chaplin (2001)*; solid line : present computation.

Figure 5 shows the spatial variations of the first three harmonic components of the free surface elevation. For several locations in the numerical wave tank these components have been computed using a Fourier decomposition of the time history of free-surface elevation signal in a moving window of one wave period long. Present computations are in good agreement with Chaplin's experiments for the first wave crest located behind the cylinder. For the following crests, present results underestimate the amplitudes of the harmonics because the grid is stretched in this part of the wave tank. Concerning reflections of the incident signal – they must be zero according to linear theory *(Dean, 1948)* or second-order accuracy *(Mc Iver & Mc Iver)* and cannot be measured with enough confidence experimentally (*Chaplin, 1984*; *Grue, 1992*)– present computations show a small spatial variation for the first harmonic component. This agrees with recent measurements from *Chaplin (2001)* who attributes these results to reflection at the fundamental frequency : according to him the corresponding reflection coefficient follows $a_-^{(1)} / a \approx (ka)^3$ for large values of $(ka)^3$ and thus reflection is not significant (*Schønberg & Chaplin, 2001*).

Conclusion

Diffraction of a non-linear regular wave train by an submerged circular cylinder has been studied with an original approach combining viscous flow solver and explicit modelling of the incident waves. Instead of computing the whole velocity, pressure and free surface fields, the diffracted flow only is computed solving SWENS Equations (RANS Equations where variables have been decomposed in incident and diffracted variables).

First results are encouraging and other comparisons will be undertaken for this case (harmonic components of hydrodynamic forces or free wave amplitudes at the lee side of the cylinder).

References

Alessandrini, B., Delhommeau, G., (1995), *A multigrid velocity-pressure-free surface elevation fully coupled solver for calculation of turbulent incompressible flow around a hull*, 9th Int. Conf. Num. Methods Laminar and Turbulent Flows, Atlanta, pp.1173-1184.

Armenio, V. ; Favretto, M., (1997), *Development of a viscous numerical wave tank and numerical evaluation of dynamic loads on submerged bodies at small KC numbers*, 7th Int. Offshore and Polar Eng. Conf., Honolulu, Vol. 3, pp.98-105.

Chaplin, J. R., (1984), *Non-linear forces on a horizontal cylinder beneath waves*, J. Fluid Mech., 449-464.

Chaplin, J. R., (2001), *Non-linear Wave Interactions with a Submerged Horizontal Cylinder*, 11th Int. Offshore and Polar Eng. Conf., Stavanger, Vol. 3, pp. 272-279.

Dean, W. R., (1948), *On the reflexion of surface waves by a submerged circular cylinder*, Proc. Camb. Phil. Soc., 483-491.

Di Mascio, A., Landrini, M., Lalli, F., Bulgarelli, U., (1994), *Three Dimensional non linear diffraction around fixed structures*, Proceedings of 20th ONR Symposium on Naval Hydrodynamics.

Ferrant, P., (1996), *Simulation of strongly non-linear wave generation and wave-body interaction using a 3D MEL model*, Proceedings of 21st ONR Symposium on Naval Hydrodynics, Trondheim.

Ferrant, P., Gentaz L., Le Touzé, D., (2002) *a new potential / RANSE approach for water wave diffraction*, 5th Numerical Towing Tank Symposium, Pornichet.

Ferrant, P., Le Touzé, D., (2002), *Fully-non-linear spectral/BEM solution for irregular wave interactions with a 3D body*, OMAE Conference, Oslo.

Gentaz, L. ; Maury, C. ; Alessandrini, B. ; Delhommeau, G., (2000), *Numerical simulation of a two-dimensional wave tank in viscous fluid*, Int. J. Offshore and Polar Eng. (IJOPE), pp.1-9.

Grue, J., (1992), *Non-linear water waves at a submerged obstacle or bottom topography*, J. Fluid Mech., 455-476.

Mc Iver, M., Mc Iver, P., (1990), *Second-order wave diffraction by a submerged circular cylinder*, J. Fluid Mech., 519-529.

Rhie, C. M., Chow, W. L., (1983), *A numerical study of the turbulent flow past an isolated airfoil with trailing edge separation*, AIAA Journal, vol. 21, pp. 179-195.

Rienecker, M.M.; Fenton, J.D., (1981), *A Fourier approximation method for steady water waves*, J. Fluid Mech. 104, pp.119-137.

Schønberg, T.; Chaplin, J.R., (2001), *Computation of Non-Linear Wave Reflections and Transmissions from a Submerged Horizontal Cylinder*, 11th Int. Offshore and Polar Eng. Conf., Stavanger, vol. III, pp.280-287

DEVELOPMENT AND APPLICATION OF AN UNSTRUCTURED FINITE VOLUME SOLVER FOR FREE SURFACE FLOWS IN 2D

Tommi Mikkola[1]
Ship Laboratory, Helsinki University of Technology

1 INTRODUCTION

Within the field of ship research, viscous free surface flows have commonly been solved using surface tracking methods based on structured boundary fitted grids. Due to the use of structured grids, these methods are, however, not very well suited for cases involving complex geometries and large deformations of the free surface. Unstructured methods, having the capability to cope also with geometrical complexities, are therefore a more suitable choice for these kind of cases. An equally important feature of unstructured grids is adaptivity, i.e. the possibility to regenerate the grid locally during the solution process without affecting the rest of the grid.

The purpose of the on-going research at Helsinki University of Technology Shiplaboratory is the development of an unstructured, finite volume flow solver for free surface flows with surface tracking, adaptive grid reconstruction. The first part of the work was the development of a basic laminar 2D solver without free surface for triangles based on the pressure correction method.[8] In this paper the solver is extended for free surface flows with emphasis on the coupling of free surface solution and pressure correction method. Two approaches for the solution of the free surface deformation, with partial coupling to the bulk flow solution, are presented. As the interest is on the free surface solution approach, only Eulerian flow is considered. The surface tracking is implemented with a well known spring analogy model.

2 GOVERNING EQUATIONS

The flow is assumed to be incompressible, inviscid and isothermal in 2D. The governing equations for the flow are the incompressible 2D continuity and momentum balance equations. In conservation form these are

$$\int_{\partial\Omega} \rho v_i n_i dS = 0 \qquad \text{and} \qquad \int_{\Omega} \rho \frac{\partial v_i}{\partial t} dV + \int_{\partial\Omega} \rho v_i v_j n_j dS = -\int_{\partial\Omega} p n_i dS \tag{1}$$

respectively. Here ρ is the density, v_i are the velocity components and n_i are the components of the outer normal for domain Ω respectively. The piezometric pressure p includes the effect of gravity and is given by

$$p = p^{\mathrm{tot}} + \rho g x_2 \ , \tag{2}$$

where p^{tot} is the total physical pressure and gravity points in the negative x_2-direction.

The bulk flow and free surface are connected through boundary conditions, which have to be satisfied on the deforming surface. As a material interface, the free surface introduces two types of conditions on the flow quantities. The first one of these is the kinematic boundary condition stating that there is no flow through the interface. This requires that

$$\left(v_i - v_i^{\mathrm{fs}}\right) n_i = 0 \qquad \text{, where} \qquad v_i^{\mathrm{fs}} = \frac{\partial h}{\partial t} \delta_{i2} \tag{3}$$

is the velocity of the surface parallel to the x_2-axis. Wave height h is measured from some reference level parallel to the x_1-axis. Writing out Eq. (3) gives the kinematic boundary condition

$$\frac{\partial h}{\partial t} = v_2 + v_1 \frac{n_1}{n_2} \ . \tag{4}$$

The second condition to be satisfied on the free surface is the dynamic boundary condition. This states, that stresses have to be continous across the free surface. In this work, the inviscid approximation of this without surface tension effects is used. Assuming zero atmospheric pressure and taking into account Eq. (2) leads to the dynamic boundary condition

$$p = \rho g h \tag{5}$$

for the piezometric pressure on the free surface.

---

[1] Ship Laboratory, Helsinki University of Technology, Otakaari 4, FIN-02015 Espoo, Finland – E-Mail: Tommi.Mikkola@hut.fi
This work has been carried out in 'Ship Flows' project funded by the Academy of Finland (project 49846)

3 NUMERICAL METHOD

The numerical method used in this work is based on the unstructured, triangle based, finite volume method and the flow equations are solved using a SIMPLE-type [4], collocated pressure correction method.[8] Boundary conditions are taken into account by setting appropriate values for the variables in ghost cells on the boundaries. Velocities and pressures are defined at the centres of the control volumes and wave heights at the centres of the free surface faces.

The solution process is based on a velocity-pressure decoupling, in which the velocities and pressures are solved separately in an iterative manner. In each iteration, the velocity field is first updated from momentum balance using the current pressure field and corrected after this by altering the pressure according to the resulting mass balance error in the continuity equation. This process is repeated until a steady state is reached. Each global iteration can be divided into three parts: the velocity update, calculation of the mass balance error and the pressure correction stage.

A common approach to solve free surface problems is to decouple the bulk flow and free surface problems. In that case, the solution of the flow consists of two independent steps iterated in turns until a converged solution is reached. For each iteration, the bulk flow is updated first with boundary conditions according to the current free surface. This is followed by the solution of the new free surface location based on the updated bulk flow and adjustment of the grid to match the new boundary. Calculation of the new wave height can be based on either the kinematic or dynamic boundary condition. The next bulk flow step is then based on boundary conditions on the updated free surface.

In the current method, the approach above is improved slightly by partially coupling the bulk flow and free surface solutions through the pressure correction equation.

3.1 Kinematic free surface approach

In this approach the update of the wave height is based on the kinematic boundary condition. The grid is assumed to be fixed and to coincide with the instantaneous free surface at the current time step. Velocity components are updated from the momentum balance using dynamic boundary condition (5) for the pressure and either zeroth or first order extrapolation for the velocities on the free surface.

Full decoupling of the bulk flow and free surface solutions would result into a constant pressure boundary condition on the free surface, implying zero pressure correction on the free surface. On the other hand, the deformation of the free surface combined with the dynamic boundary condition changes the pressure on the free surface. This incompatibility of boundary conditions would lead to a jump in the pressure across the free surface during the iteration, affecting the stability of the method. In order to avoid this complication, the deforming free surface is taken into account during the pressure correction stage using the dynamic boundary condition as follows.

After the calculation of the mass balance error, the change of wave height is evaluated by integrating the kinematic boundary condition (4) in time with the explicit Euler scheme. Pressure on the new free surface has to satisfy the dynamic boundary condition, giving with the resulting change in wave height

$$p'^{\text{fs}} = \rho g \left(v_2 + v_1 \frac{n_1}{n_2} \right) \Delta t \, , \tag{6}$$

which is used as a boundary condition for the pressure corrections on the free surface. Due to the relaxation of the pressure corrections in SIMPLE method, wave heights have to be relaxed similarly with

$$h^{n+1} = h^n + \alpha_p \Delta h \tag{7}$$

in order to get a free surface compatible with the corrected pressure field.

3.2 Dynamic free surface approach

In the second approach used in the current method, the calculation of the new wave height is based on the dynamic boundary condition. Each iteration starts with the calculation of the current wave height from the pressure on the surface:

$$h = \frac{p^{\text{fs}}}{\rho g} \, . \tag{8}$$

As with the kinematic approach, the grid is assumed fixed. Time integration of the momentum equations is done assuming slip condition on the free surface. The pressures are thus extrapolated linearly into the ghost cells and velocity vector is mirrored with respect to the surface, resulting into zero mass flux through the surface. This same condition is used for the calculation of the mass balance error as well.

Test calculations showed, that full decoupling of the solutions would lead to large deformations on the free surface, making the method very unstable, unless considerable under-relaxation of the pressures is applied after the solution of the pressure correction equation. Heavy under-relaxation would, however, have a dramatic effect on the convergence speed of the solution process.

In this approach, the partial coupling of the bulk flow and free surface solutions is in a form of under-relaxation in the pressure correction stage based on the deforming free surface. As in the first method, the pressure correction on the free surface and the change in wave height can be related through the dynamic boundary condition giving

$$\Delta h = \frac{p'^{\mathrm{fs}}}{\rho g} \, . \tag{9}$$

If the grid is assumed fixed, this movement of the free surface results into a mass flux through the face of the fixed grid given by the kinematic boundary condition as

$$\dot{m}^{*\mathrm{fs}}_{lm} = \frac{f_1 p'_l + (1 - f_1)\, p'_m}{g \Delta t} S_{lm} n_{2,lm} \, . \tag{10}$$

Here l is the computational cell with a face on the free surface and m the associated ghost cell. This mass flux is added to the mass balance error in the pressure correction equation. By using zeroth order extrapolation for the pressure corrections in Eq. (10), i.e. $p'_m = p'_l$ the contribution can be transfered to the diagonal of the pressure correction equation, giving for the diagonal term

$$\alpha^{\mathrm{fs}}_{ll} = \alpha_{ll} + \frac{S_{lm} n_{2,lm}}{g \Delta t} \, . \tag{11}$$

3.3 Grid update

The wave heights are given at the centres of the faces on the free surface. Before the grid can be updated, these values have to be transformed to the grid points on the surface. A centred scheme for the transformation leads to decoupling of the neighbouring wave heights, when calculating normal vectors, and therefore an upwind scheme is used instead. Assuming that the flow is from left to right, the wave height at the right hand end point of the face h^{r} is approximated by a third order scheme

$$h^{\mathrm{r}} = \frac{2\bar{h}^{\mathrm{r}} + 2h - \bar{h}^{\mathrm{l}}}{3} \, . \tag{12}$$

Here $\bar{h}^{\mathrm{r}}$ and $\bar{h}^{\mathrm{l}}$ are the weighted averages of neighbouring wave heights at the right and left hand ends of the face respectively. An alternative to this scheme is zeroth order extrapolation of wave height, which can be used close to boundaries to damp out transient waves.

The updating of the grid is based on the well known linear spring analogy model first presented by Batina [1], in which the edges of the grid connecting the grid points are assumed to be linear springs. The grid points are moved by searching for the equilibrium of the spring system knowing the displacements on the free surface.

4 NUMERICAL TESTS

The free surface solution approaches described above have been tested with two test cases. These are a flow over a bump on the bottom of an infinitely wide channel [3] and flow over a submerged hydofoil with an angle of attack [5].

Results are presented for three different free surface solution approaches. These are:

a. kinematic free surface approach with zero gradient condition for the velocity components

b. kinematic free surface approach with linear extrapolation for the velocity components

c. dynamic free surface approach

Local time stepping is used for the bulk flow and free surface solutions in order to accelerate the convergence of the solution process. These are controlled separately through nondimensional CFL-numbers given by

$$\mathrm{CFL} = \max_{m=1,3} \frac{v_{i,l} n_{i,lm} S_{lm} \Delta t_l}{V_l} \qquad \mathrm{CFL}^{\mathrm{fs}} = \frac{v_1 \Delta t^{\mathrm{fs}}}{S n_2} \tag{13}$$

for bulk flow and free surface time steps respectively.

4.1 Flow over a bump

This case was chosen for the overall comparison of different approaches during the development of the free surface solution method due to its simplicity and the prior experience [7] with the case. The bump on the floor of the channel is of Gaussian bell shape with a height of 0.1 and the centre at $x_1 = 10$. In x_1-direction the domain extends from -20 to 50, with damping zones from -20 to 0 and from 30 to 50 on the free surface. Undisturbed water level is at $x_2 = 0$. The grid for the case was created with EasyMesh grid generator [9] and has 1533 nodes, 4123 sides and 2591 triangles. The number of points on the free surface is 279. Cell size in the grid increases towards the inflow and outflow boundaries.

Testing has been performed with both a subcritical and supercritical cases, with Froude numbers based on depth below and above unity respectively. The results presented below are for the subcritical case with Froude number of 0.567. At low inflow velocity, both free surface approaches performed well in terms of convergence. The time step parameters CFL and $\mathrm{CFL}^{\mathrm{fs}}$ were 5.0 and 1.0 respectively for both approaches. Pressure corrections were under-relaxed slightly more in the case of the dynamic approach, with relaxation factor 0.3 for the kinematic and 0.2 for the dynamic approach. With these choices the residuals converged to machine accuracy after around 6000 iterations for the kinematic approach and after around 8000 iterations for the dynamic approach, where the slower convergence of the latter is probably due to the smaller pressure relaxation factor. For comparison, the case was tested also with fully decoupled approaches. In this case, the dynamic approach was extremely unstable and, even with radical reduction of the pressure under-relaxation factor, computations diverged. For the kinematic approach, the difference was more subtle. With fully decoupled approach, the free surface CFL-number had to be limited to roughly 0.5. As the limiting factor with the above choice of parameters seemed to be the free surface evolution, the reduction of the free surface time step resulted into roughly twice as slow convergence of the total solution.

At higher velocities considerable difference emerged between the approaches. As the inflow velocity was increased, the dynamic approach became highly unstable with large free surface deformations leading to the divergence of the solution, unless the final pressure corrections were heavily under-relaxed. The kinematic approaches on the other hand required very few changes to the input parameters.

Some differences can also be seen in the wave profiles compared in Fig. 1 with a result from a previous test with FINFLO flow solver [7]. The damping with the dynamic approach is slightly stronger than with the kinematic approach and linear extrapolation for the velocity components. For the kinematic approach with zero gradient condition, the damping is considerably stronger than with cases b and c. The location and depth of the first through as well as the location of the first peak for all cases agree well with the previous results for FINFLO. The strong damping of the wave field in the FINFLO result is partially due to the rapid increase of the cell size towards the outflow boundary, and therefore further away from the obstacle the results are not comparable.

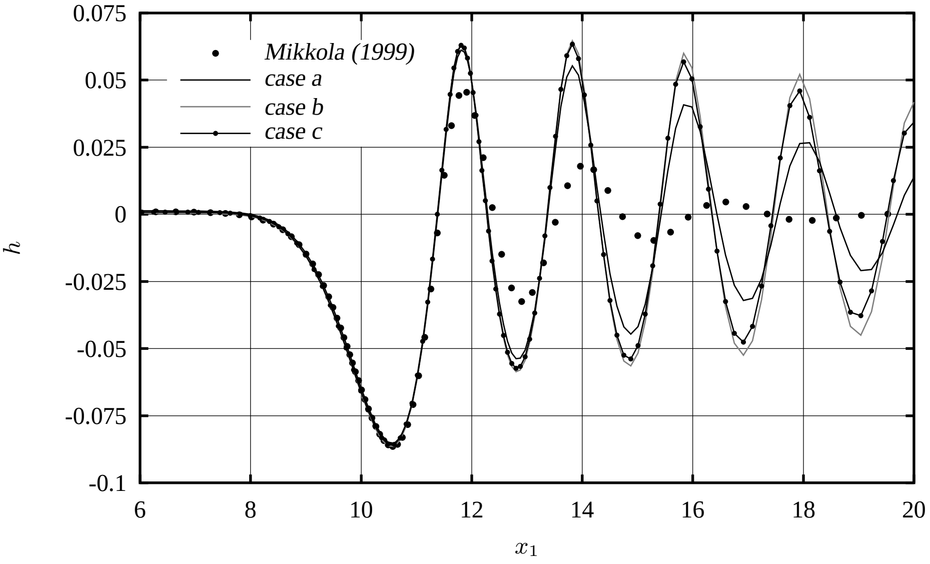

Figure 1: Wave profiles for flow over a bump compared with results for FINFLO [7].

Differences in the flow field are most easily seen from the contours of v_2-velocity shown in Fig. 2 for cases a and c. The results for cases b and c were practically identical. Here the contours are drawn using the values at the cell centres as well as the averaged values at the grid points. Cases b and c give relatively smooth and almost identical velocity distributions, whereas the velocity field from case a has some oscillations close to the free surface. It can be seen, that because of the zero gradient condition the contours cross the free surface orthogonally for a large part, which clearly should not be the case. Due to an incompatible boundary condition there is thus a jump in the gradient field close to the free surface.

4.2 Flow over a submerged hydrofoil

The accuracy of the free surface approaches was checked with a flow over a submerged NACA-0012 hydrofoil with an angle of attack of 5 degrees. The Froude number based on the chord length is 0.567. Experimental results for this case have been presented by Duncan [5]. It has also been extensively used for numerical testing, see e.g. [6] and [2].

The chord length of the hydrofoil is 1 and the leading edge is at (0,-0.99). The grid consists of 2996 points, 8699 sides and 5703 triangles. There are damping zones on the free surface from the inflow boundary to -7 and from 6.25

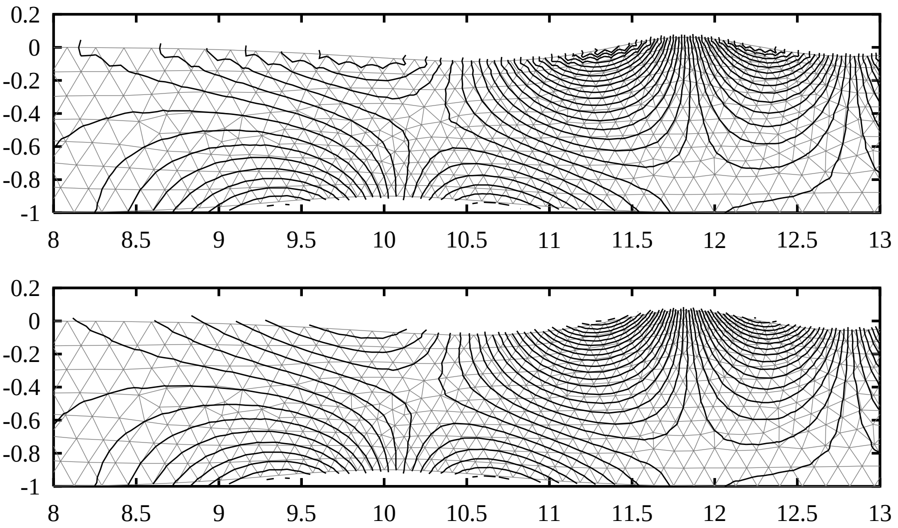

Figure 2: Contours of v_2-velocity for flow over a bump in cases a and c respectively. Contour interval is 0.02.

to the outflow boundary. The resolution of the grid is increased around the leading and trailing edges of the foil as well as close to the free surface between $x_1 = 0$ and $x_1 = 6.25$. The number of points on the hydrofoil and on the free surface are 128 and 115 respectively.

The CFL-numbers for the bulk flow and free surface solutions were set to 1.0 and 0.5 respectively. For pressure correction factor 0.2 machine accuracy for the residuals was reached after 4000 to 5000 iterations in all cases, with slightly more iterations required for the dynamic approach.

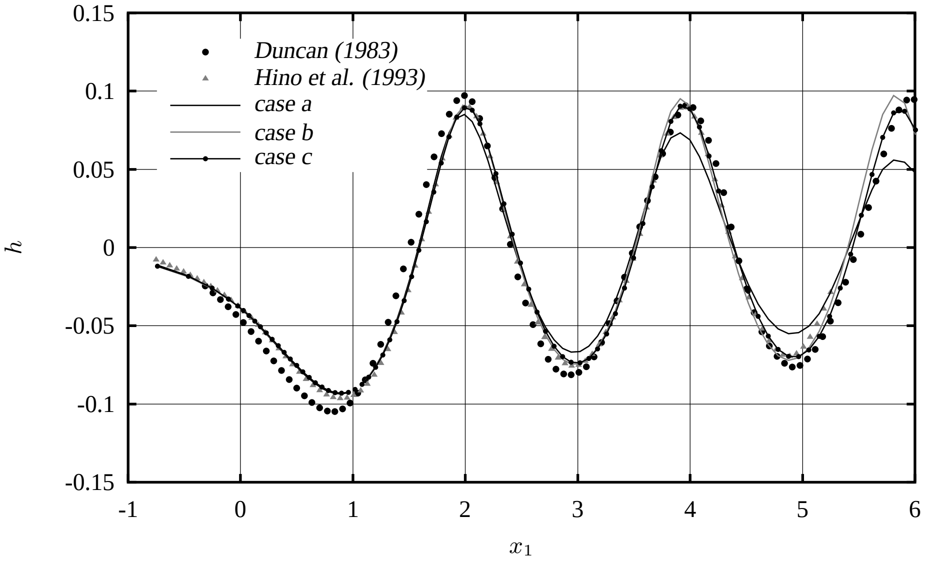

Figure 3: Wave profiles for flow over a submerged hydrofoil compared with measurements by Duncan [5] and numerical reference data by Hino et al. [6].

Wave profiles for different approaches are compared with experimental and numerical references in Fig. 3. Good agreement with the numerical and experimental results can be seen with similar damping to the first test case. Compared to the experiment, the depth of the first through is however under-estimated. This may be due to an insufficient resolution of the grid in front of the through, where the cell size can be seen to increase quite rapidly. There is also a small difference in the wave length between the computations and the measurement.

Comparison of the contours of velocities and pressure showed again, that cases b and c give practically identical results, while the contours in case a oscillate slightly close to the free surface. Despite the differences close to the free surface, discrepancies close to the hydrofoil are negligible. Pressure contours for case b are shown in Fig. 4.

5 CONCLUSIONS

Unstructured pressure correction solver based on triangle meshes has been extended for free surface flows. Two kind of approaches for free surface solution with partial coupling to the pressure correction method have been studied.

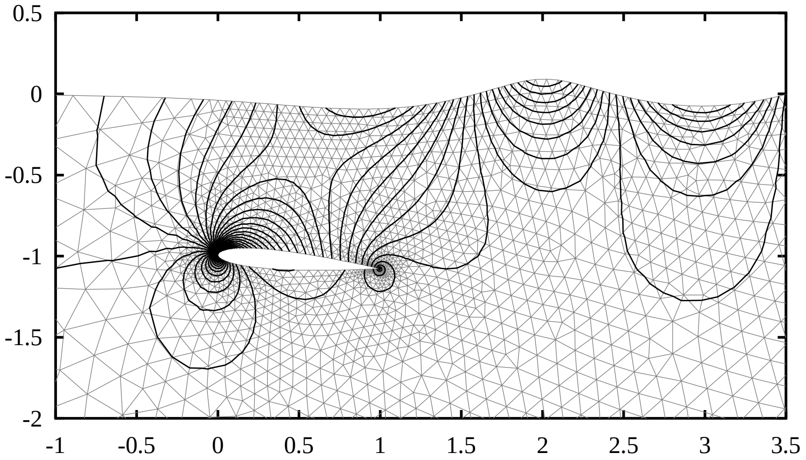

Figure 4: Contours of pressure for flow over a submerged hydrofoil in case b. Contour interval is 100.

In the kinematic approach the updating of the wave field is based on the kinematic boundary condition, whereas in the dynamic approach the new wave height is evaluated from the dynamic boundary condition. Additionally, the kinematic approach has been tested with two different velocity boundary conditions.

Comparison with the fully decoupled approaches showed, that at low inflow velocity the stability of the dynamic approach was greatly improved by the partial coupling of the solutions. Some improvement was also shown for the kinematic approach. Both approaches performed roughly equally well in terms of convergence speed. At higher velocities partial coupling was effective only in the case of kinematic approach.

Wave profiles agreed well with experimental and numerical reference data. Numerical damping of the wave field was marginally stronger in the dynamic approach, as long as linear extrapolation was used for the velocity components on the free surface with the kinematic approach. Zeroth order extrapolation resulted into considerably stronger damping of the wave field.

The next phase of the research will concentrate on the development of the adaptive, surface tracking grid reconstruction. The proposed approach consists of two parts. The first part is the identification of the areas requiring updating and regridding of these areas, while the second one is the initialization of the solution in the updated parts of the grid. Because the intended approach is very similar to more common forms of adaptivity, it should be possible to make good use of existing research on adaptive methods.

REFERENCES

[1] BATINA, J. T. Unsteady euler algorithm with unstructured dynamic mesh for complex-aircraft aerodynamic analysis. *AIAA Journal 29*, 3 (1991), 327–333.

[2] BERTRAM, V., LANDRINI, M., AND LUGNI, C. An unsteady model for free surface flows around hydrofoils. In *NuTTS'98, Numerical Towing Tank Symposium* (Hamburg, Germany, 1998).

[3] BET, F., HÄNEL, D., AND SHARMA, S. D. Simulation of hydrodynamical free-surface flow. In *ECCOMAS'96* (1996), Elsevier.

[4] CARETTO, L. S., GOSMAN, A. D., PATANKAR, S. V., AND SPALDING, D. B. Two calculation procedures for steady, three-dimensional flows with recirculation. In *Proc. Third Int. Conf. Numer. Methods Fluid Dyn.* (Paris, 1972).

[5] DUNCAN, J. The breaking and non-breaking wave resistance of a two-dimensional hydrofoil. *Journal of Fluid Mechanics 126* (1983).

[6] HINO, T., MARTINELLI, L., AND JAMESON, A. A finite-volume method with unstructured grid for free surface flow simulations. In 6^{th} *International Conference on Numerical Ship Hydrodynamics* (Iowa, 1993).

[7] MIKKOLA, T. Testing of Two FINFLO-based Free-surface Codes Using Eulerian Flow Over a Gaussian Ground Elevation. Internal report D-56, Helsinki University of Technology, Ship Laboratory, 1999.

[8] MIKKOLA, T. Development of an unstructured pressure-correction solver based on triangle meshes. In 5^{th} *Numerical Towing Tank Symposium* (Pornichet, France, 2002), G. Delhommeau and M. Visonneau, Eds., Ecole Centrale de Nantes.

[9] NICENO, B. Easymesh. `http://www-dinma.univ.trieste.it/˜nirftc/research/easymesh/`.

A Hybrid Method for Seakeeping Estimation of Ships

Mirel Nechita
National University of Singapore,
Blk EA #07-26,
9 Engineering Drive 1,
Singapore 117576
Email: mpemn@nus.edu.sg

Hidetsugu Iwashita
Hiroshima University,
1-4-1 Kagamiyama,
Higashi-Hiroshima
Japan 739-8527
Email: iwashita@naoe.hiroshima-u.ac.jp

Introduction

Structural analysis of ships and floating structures using finite elements requires accurate seakeeping computations concerning the local wave pressure distribution in addition to the calculation of total hydrodynamic forces and ship motions. In this paper we present a numerical method for seakeeping estimation of ships, which take into account the influence of the steady wave field through body and free surface boundary conditions. The method is applied to a blunt ship and to a slender ship. The numerical results are carefully compared with experimental data and other computational methods in a wide frequency range (including τ<0.25).

A hybrid method is proposed for extending the Rankine panel method to the low frequency range. For the prediction of the unsteady wave field is necessary an accurate estimation of the steady wave field; this is done by using a fully nonlinear Rankine panel code for the steady problem.

Mathematical Formulation

Considering a ship advancing with constant forward speed U in regular waves encountered at angle χ, we adopt the coordinate system presented in Fig. 1. The linear theory is employed for the problem assuming incompressible, inviscid and irrotational fluid. The wave field is decomposed into a near field and a far field. The near field is constituted by a closed region bounded by ship surface S_H, free surface S_F and artificial surface S_C. The far field is an open region bounded only by the artificial surface S_C and the free surface S_F^*. We apply the RPM (Rankine Panel Method) in the near field and GFM (Green Function Method) in the far field and connect both solutions on the artificial surface S_C.

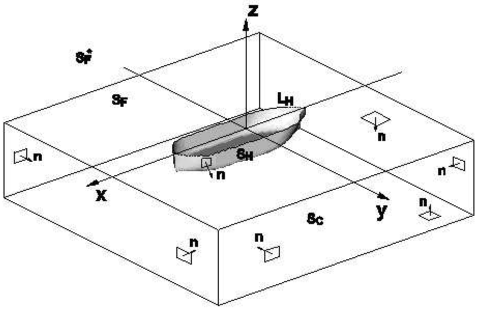

Fig. 1 Coordinate system

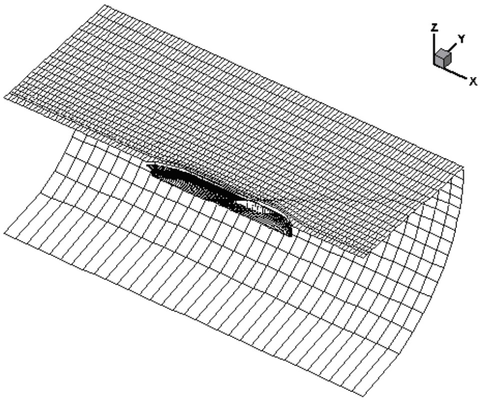

Fig. 2 Computational grids for Series-60

The total potential is decomposed into steady velocity potential Φ and unsteady velocity potential ϕ:

$$\Psi(x,y,z;t) = U\Phi(x,y,z) + \Phi_t(x,y,z;t) = U\Phi(x,y,z) + \Re[\phi(x,y,z)e^{i\omega_e t}] \tag{1}$$

For the near field, the boundary conditions to be satisfied by the unsteady potentials ϕ_j (j=1~7) are given in [1]. For the far field, according to the Green function method, the unsteady potentials ϕ_j^* can be expressed as:

$$\begin{aligned}\phi_j^* &= -\iint_{S_C}\left[\frac{\partial\phi_j^*(Q)}{\partial n} - \phi_j^*(Q)\frac{\partial}{\partial n}\right]G^W(P,Q)dS \\ &+ \frac{1}{K_0}\oint_{L_C}\left[\frac{\partial\phi_j^*(Q)}{\partial x'} - \phi_j^*(Q)\frac{\partial}{\partial x'} - 2i\tau K_0\phi_j^*(Q)\right]G^W(P,Q)dy'\end{aligned} \tag{2}$$

$G^W(P,Q)$ denotes the Green function which satisfies the following linearized free-surface condition and the radiation condition at infinity:

$$\left[\left(i\omega_e - U\frac{\partial}{\partial x}\right)^2 + \mu\left(i\omega_e - U\frac{\partial}{\partial x}\right) + g\frac{\partial}{\partial z}\right]G^W(P,Q) = 0 \quad \text{on} \quad z = 0 \tag{3}$$

Due to continuity of the fluid between the near field and the far field, the conditions

$$\phi_j = \phi_j^*, \ \frac{\partial\phi_j}{\partial n} = -\frac{\partial\phi_j^*}{\partial n} \tag{4}$$

must be satisfied on the artificial surface S_C.

Numerical Method

The discretization of the boundary surfaces S_H and S_F is made in accordance with RPM discretizations for the Series-60 presented in [2]. After pilot computations, which analyzed the flow over a source pulsating with $\tau = 0.2$ at depth $d = 0.2m$, moving with constant speed $U = 1.0m/s$, it was found that the appropriate shape of the artificial surface S_C is semi-cylindrical. The computational grid used in the proposed hybrid method for Series-60 hull forms is shown in Fig. 2. The number of elements used for the computations are presented in the Table 1.

Table 1. Number of elements on boundary surfaces

Hull Form	N_H on S_H	N_F on S_F	N_C on S_C	N_T Total
Series-60, $C_b = 0.6$	1320	1919	480	3719
Series-60, $C_b = 0.8$	1320	1717	480	3517

For the near field, the unsteady potentials ϕ_j (j=1~7) are expressed by source distributions on the body surface S_H, the free surface S_F and the artificial surface S_C.

$$\phi_j(P) = -\int_{S_H+S_F+S_C}\sigma_j(Q)G(P,Q)dS \tag{5}$$

where $G(P,Q) = 1/4\pi\sqrt{(x-x')^2 + (y-y)^2 + (z-z')^2}$, $P \equiv (x,y,z)$, $Q \equiv (x',y',z')$

Hydrodynamic forces

The importance of the steady wave field on hydrodynamic forces is demonstrated through numerical results for the added mass, damping coefficients and the wave exciting forces. This method is able to estimate in good accuracy the unsteady waves for high and low frequency range.

Fig. 3 and Fig. 4 present a comparison between the results of strip method, hybrid methods (based on a double-body formulation and based on fully nonlinear steady wave field) and the experiment. Continuous arrow and dashed arrow show $\tau = 0.25$ and $\tau = 0.5$, respectively. The results for the hybrid methods are noted with (DBF) for double-body formulation and (FNL) for fully nonlinear formulation. It is known that desingularized Rankine panel method gives good results only for the range $\tau > 0.5$. For the low frequency region, the hybrid methods predict fairly the experimental values for the added mass and damping coefficients. Especially for pitch added mass (Fig. 3), the results of hybrid method forecast the experimental jumps in the low frequency region. Also for the coupled damping coefficient between pitch and heave we can remark the reasonable numerical results in the range of $\tau < 0.5$ (Fig. 4).

Fig. 5 presents surge and heave exciting forces and pitch exciting moment for Series-60 (C_b=0.6). For surge and heave exciting forces there are no significant differences between computations. All computations appear to predict quite accurate the experimental values. Distinction between computations appears for pitch exciting moment where for the values $\lambda / L > 1.5$ ($\tau < 0.57$) we can observe a small difference between the hybrid methods.

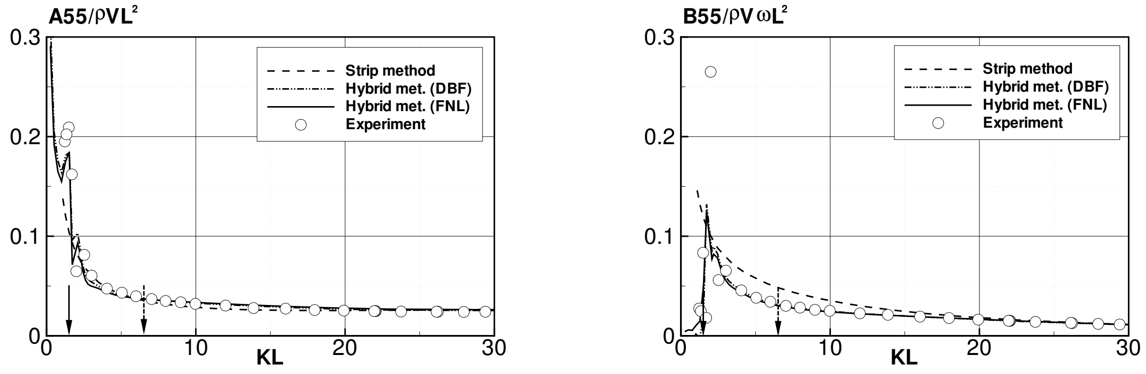

Fig. 3 Added mass and damping coefficients for pitch for Series-60 (C_b=0.6) at F_n=0.2

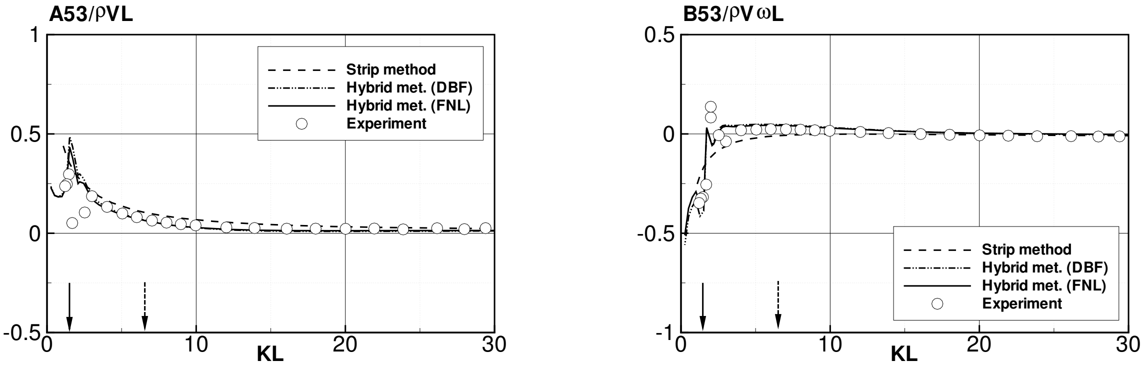

Fig. 4 Coupled added mass and damping coefficients between pitch and heave for Series-60 (C_b=0.6) at F_n=0.2

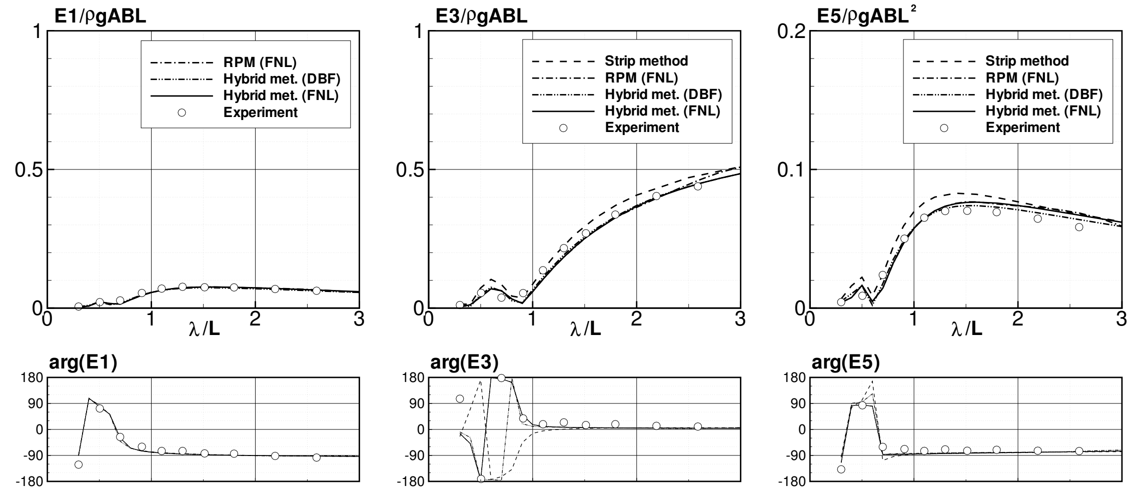

Fig. 5 Wave exciting forces and moment for Series-60 (C_b=0.6) at F_n=0.2 in regular head waves

Unsteady Wave Field

In order to validate the newly developed hybrid method, we proceed with analysis of the unsteady wave field. Low frequency range ($\tau < 0.25$) is selected for investigation of the unsteady wave field. In this range we used heave radiation wave for validating the numerical results of hybrid method. Fig. 6 presents wave contour plots of heave radiation wave for $\tau = 0.23$ for Series-60 (C_b=0.8). This frequency was selected because the side wall effect does not contaminate the k_1 wave system which propagates from downstream toward the ship and has only minimal influence on the k_2 wave system which propagates from the ship toward upstream region.

For this case of a blunt model we can observe the two wave crests near ship side as for the slender model and also a new wave crest near the ship's bow. This local wave is captured only by hybrid method taking into account the fully nonlinear steady wave field. Along the ship side, the waves are overall better estimated by hybrid method (FNL).

Conclusions

The presented hybrid method was applied to Series-60 hull forms, blunt and slender model and the numerical results were compared with experiments taking into account the side wall effect of the towing tank. Through this study the following conclusions can be reached:

- The developed hybrid method is able to predict the hydrodynamic forces in good accuracy. The numerical results of the hybrid method cover the whole frequency range, combining the advantages of RPM for high frequency range and the GFM for the low frequency range. The influence of the steady wave field on hydrodynamic forces seems not so remarkable and can be detected in the numerical results of the pitch exciting moment.
- The hybrid method is able to estimate in good accuracy the unsteady waves for high and low frequency range. For the sensitive range of $\tau < 0.25$, fully nonlinear approach of the method gives better results than linear approach for the k_2 wave system and for the local wave system along ship side.

- For improving unsteady wave estimation in the low frequency range, for the case of blunt ship's forms, it is necessary to evaluate more carefully the steady wave in the downstream region of the computational domain.

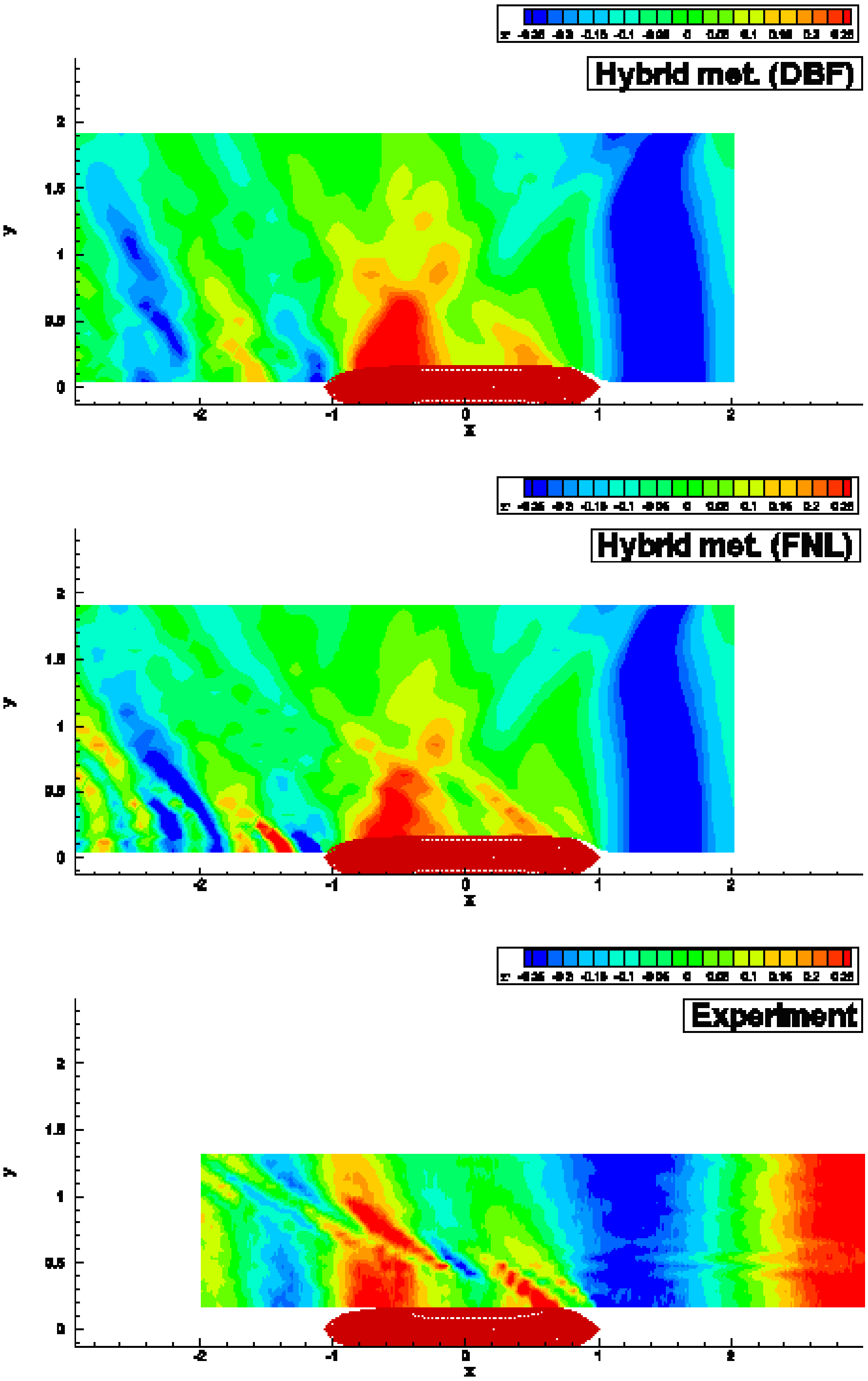

Fig. 6 Contour plot of heave radiation wave for Series-60 (C_b=0.8)
at F_n=0.2, KL=1.32, τ=0.23

References

[1] Nechita, M.: *Study on a Seakeeping Computation Method of Ships Considering Fully-Nonlinear Steady Wave Field*, PhD Thesis (2001), Hiroshima University Press, Japan.

[2] Nechita, M., Iwashita, H., Iwasa, H., Hidaka, Y., Ohara, H.: *Influence of the Fully Nonlinear Steady Wave Field on the Unsteady Wave Field of a Blunt Ship Advancing in Waves*, Transaction of the West-Japan Society of Naval Architects, No. 101 (2000) pp.37-48.

[3] Iwashita, H., Hidaka, Y., Kishimoto, K., Nechita, M.: *Side Wall Effects of a Towing Tank on the Measurement of Unsteady Waves of Ships Advancing in Waves*, Transactions of the West-Japan Society of Naval Architects, No.102(2001), pp.21-33.

[4] Iwashita, H., Lin, X., Takaki, M.: *Combined Boundary Integral Equations Method for Ship Motions in Waves*, Transaction of the West-Japan Society of Naval Architects, No. 85 (1993) pp.37-55.

Simple Green Functions

Francis Noblesse[1] and Chi Yang[2]
[1] NSWC-CD, 9500 MacArthur Blvd, West Bethesda, MD 20817-5700
[2] School of Computational Sciences, George Mason University, Fairfax, VA 22030-4444

This study is dedicated to the memory of Dr. Maurizio Landrini, with great sadness and respect.

Introduction

Theoretical prediction of the behavior of ships and offshore structures in time-harmonic ambient waves is one of the most important core issues in free-surface hydrodynamics. For offshore structures, robust and highly-efficient panel methods have been developed, and are routinely used, to solve the canonical wave diffraction-radiation problems associated with the definition of added-mass and wave-damping coefficients, and wave-exciting forces and moments. These potential-flow methods are based on numerical solution of a boundary-integral equation formulated using the Green function that satisfies the linear free-surface boundary condition for diffraction-radiation of time-harmonic waves without forward speed. Application of this classical approach, often identified as the free-surface Green-function method, to wave diffraction-radiation by ships (i.e. with forward speed) has also led to useful methods—see e.g. *Diebold (2003), Boin et al. (2002,2000), Chen et al. (2000), Guilbaud et al. (2000), Fang (2000), Wang et al. (1999), Du et al. (2000,1999), Iwashita and Ito (1998), Iwashita (1997)*—although not to a comparable degree of practicality because forward speed introduces major difficulties (not present for wave diffraction-radiation at zero forward speed). A fundamental difficulty, considered in the present study, of the forward-speed wave diffraction-radiation problem is that the Green function that satisfies the linear free-surface boundary condition for diffraction-radiation of time-harmonic waves (frequency ω) with forward speed $\mathcal{U}$ is much more complicated than the Green functions corresponding to the special cases $\mathcal{U}=0$ or $\omega=0$, which can be evaluated simply and efficiently, at least in deep water; see e.g. *Ponizy et al. (1994)*.

The Green function $G(\vec{\xi}\,;\vec{x}\,)$ for wave diffraction-radiation with forward speed, which represents the velocity potential of the flow created at a field point $\vec{\xi}=(\xi\,,\eta\,,\zeta\,)$ by a moving pulsating source located at a singular point $\vec{x}=(x\,,y\,,z)$, vanishes in the farfield limit $\|\vec{\xi}-\vec{x}\|\to\infty$ and satisfies the Poisson equation

$$G_{\xi\xi}+G_{\eta\eta}+G_{\zeta\zeta}=\delta(\xi-x)\,\delta(\eta-y)\,\delta(\zeta-z) \tag{1a}$$

and the Michell linear free-surface boundary condition

$$G_{\zeta}+F^2G_{\xi\xi}-f^2G+i\,2\tau\,G_{\xi}-\varepsilon\,(FG_{\xi}+ifG\,)=0 \tag{1b}$$

at $\zeta=0$; see e.g. *Noblesse (2001)*. Here, $0<\varepsilon\ll1$, $F=\mathcal{U}/\sqrt{gL}$ is the Froude number, $f=\omega\,\sqrt{L/g}$ is the nondimensional wave frequency and $\tau=Ff=\mathcal{U}\,\omega/g$, where g is the acceleration of gravity, $\mathcal{U}$ is the ship speed, ω is the frequency of the waves encountered by the ship, and L is a reference length (typically the ship length). The coordinates $\vec{\xi}$ and $\vec{x}$ are nondimensional in terms of the reference length L. The Green function G is nondimensional with respect to a reference potential UL, where the reference velocity U may be chosen as $\sqrt{gL}$; two alternative choices for U are $\omega\,L$ and the ship speed $\mathcal{U}$. The flow is observed from a Cartesian system of coordinates that moves with speed $\mathcal{U}$ along the path of the ship. The x-axis is chosen along the ship path and points toward the ship bow. The z-axis is vertical and points upward, and the mean free surface is taken as the plane $z=0$.

A number of free-surface Green functions, based on alternative mathematical representations, have been proposed and used in the literature on wave diffraction-radiation with forward speed. Briefly, two main types of free-surface Green functions have been used. (i) Green functions defined by single Fourier integrals that involve relatively complicated special functions (related to the complex exponential integral) of a complex argument, and (ii) Green functions expressed as single Fourier integrals along a steepest-descent integration-path (that must be determined numerically) in the complex Fourier plane (Bessho's method). These free-surface Green functions, and related singularity distributions over flat rectangular or triangular panels, have been considered in numerous studies, and relatively efficient numerical-evaluation methods have been developed; see e.g. *Maury (2000), Chen (1999), Boin et al. (1999), Brument and Delhommeau (1997), Ba and Guilbaud (1995), Iwashita and Ohkusu (1992), Bougis and Coudray (1991), Jankowski (1990), Hoff (1990), Wu and Eatock Taylor (1987), Guevel* *and Bougis (1982), Inglis and Price (1982), Kobayashi (1981), Bessho (1977).* Nevertheless, Green functions that satisfy the free-surface boundary condition for wave diffraction-radiation with forward speed are relatively complicated building blocks that may not necessarily be best suited for practical applications.

These free-surface Green functions are commonly expressed in the form

$$4\pi\, G = -1/r + R + W + L \tag{2}$$

where $1/r$ is the fundamental free-space Green function, R is defined in terms of elementary Rankine sources, and the components W and L account for free-surface effects. The component W, dominant in the farfield, accounts for the waves included in the Green function G, and is defined by one-dimensional Fourier superpositions of elementary waves (i.e. single Fourier integrals). The component L in (2) accounts for nearfield free-surface effects and is defined by a singular double Fourier integral, which can be expressed in terms of single Fourier integrals involving the complex exponential integral or related special functions. Alternative mathematical expressions for the wave component W and the local-flow component L in (2) are given in the literature; e.g. see the studies of free-surface Green functions listed in the previous paragraph, *Noblesse and Yang (1996), Noblesse (1981).* The most complicated of the three components in the decomposition (2) is the local-flow component L.

The Green function (2) satisfies the Michell linear free-surface boundary condition (1b) everywhere, i.e. in both the farfield (where the linearized free-surface condition is valid) and the nearfield (where the linear free-surface condition is only an approximation, due to nearfield effects). Thus, a natural alternative to the Green function (2) is a Green function that satisfies the Michell linear free-surface boundary condition accurately in the farfield, but only approximately in the nearfield. Such a Green function cannot be obtained by merely ignoring the local-flow component L in the alternative mathematical representations (2) given in the literature, as can be seen—for instance—from the representation of the Green function for steady flows given in *Noblesse (1981).* Specifically, the wave component W and the local component L in this representation of the steady-flow Green function $G(\vec{\xi}\,;\vec{x}\,)$ involve the sign function $\text{sign}(\xi - x)$ and the absolute value $|\,\xi - x\,|$, respectively. Thus, the wave component W and the local component L do not satisfy the Laplace equation (although the sum $W + L$ does), and expression (2) with $L = 0$ therefore does not yield a satisfactory Green function.

Simple Green function for wave diffraction-radiation with forward speed

A Green function that satisfies the Poisson equation (1a), the radiation condition, and the Michell free-surface boundary condition (1b) in the farfield, and approximately in the near field, is obtained in *Noblesse and Yang (2003)* by extending the analysis of generic Green functions given in *Noblesse (2001).* This Green function can be expressed as

$$4\pi\, G = -1/r + 1/r_* - 2/r_*^F + 2/r_*^{Ff} + i\,(\,W^+ - W^- - W^i\,) \tag{3}$$

where r, r_*, r_*^F, r_*^{Ff} are defined as

$$\left\{\begin{array}{ll} X = \xi - x & r = \sqrt{h^2 + Z^2} \\ Y = \eta - y & r_* = \sqrt{h^2 + (Z_*)^2} \\ Z = \zeta - z & r_*^F = \sqrt{h^2 + (Z_* - F^2)^2} \\ Z_* = \zeta + z & r_*^f = \sqrt{h^2 + (Z_* - 1/f^2)^2} \\ h = \sqrt{X^2 + Y^2} & r_*^{Ff} = \sqrt{h^2 + (Z_* - F^2 - 1/f^2)^2} \end{array}\right\} \tag{4}$$

and $W^{\pm}$ and W^i stand for wave components that are given by one-dimensional Fourier superpositions of elementary waves. These wave components—defined below—depend on the coordinates X, Y, Z_* given by (4), and involve a function Θ that is defined as

$$\Theta = \frac{\sinh(2\,\Phi/\sigma) + i\,\sin(2\,V/\sigma)}{\cosh(2\,\Phi/\sigma) + \cos(2\,V/\sigma)} \qquad \text{with} \qquad V = \frac{Z_*\,k}{1 + (Z_*\,k)^4/(C\sigma)^4} \tag{5}$$

and $\Phi = X\alpha + Y\beta$; furthermore, σ and $C < 2\,\pi/3^{\,3/4} \approx 2.756$ are positive real numbers that may be chosen as $\sigma = 2.5$ and $C = 2$.

Wave component W^+

The wave component W^+ in (3) is defined as

$$W^+ = \frac{1+\sqrt{1+4\tau}}{4F^2}\int_{-\infty}^{\infty} dt\, \frac{(1-\Theta)\,|\,t\,|\,e^{Z_*\,k\,-\,i\,\Phi}}{(1+t^2)^{1/4}\sqrt{1+t^2-a^2}} \tag{6a}$$

where the wavenumber k and the function Φ are given by

$$k = k_o^+\sqrt{1+t^2} \qquad \Phi = k_o^+\Big(Xa + (\mathrm{sign}t)\,Y\sqrt{1+t^2-a^2}\,\Big) \tag{6b}$$

with the function a and the reference wavenumber k_o^+ defined as

$$a = 1 + \frac{(1+t^2)^{1/4}-1}{\sqrt{1/4+\tau}+1/2} \qquad k_o^+ = (\sqrt{1/4+\tau}+1/2\,)^2/F^2 \tag{6c}$$

The function Θ is given by (5) with (6b).

Wave component W^- for $\tau < 1/4$

If $\tau < 1/4$, the wave component W^- in (3) is defined as

$$W^- = \frac{1+\sqrt{1-4\tau}}{4F^2}\int_{-\infty}^{\infty} dt\, \frac{(1+\Theta)\,|\,t\,|\,e^{Z_*\,k\,-\,i\,\Phi}}{(1+t^2)^{1/4}\sqrt{1+t^2-a^2}} \tag{7a}$$

where the wavenumber k and the function Φ are given by

$$k = k_o^-\sqrt{1+t^2} \qquad \Phi = k_o^-\Big(-Xa + (\mathrm{sign}t)\,Y\sqrt{1+t^2-a^2}\,\Big) \tag{7b}$$

with the function a and the reference wavenumber k_o^- defined as

$$a = 1 + \frac{(1+t^2)^{1/4}-1}{\sqrt{1/4-\tau}+1/2} \qquad k_o^- = (\sqrt{1/4-\tau}+1/2\,)^2/F^2 \tag{7c}$$

The function Θ is given by (5) with (7b).

Wave component W^- for $1/4 < \tau$

If $1/4 < \tau$, the wave component W^- in (3) is defined as

$$W^- = \frac{f}{F}\int_{-\infty}^{\infty} dt\, \frac{(1+\Theta)\,|\,t\,|\,e^{Z_*\,k\,-\,i\,\Phi}}{(1+t^2)^{1/4}\sqrt{1+t^2-a^2}} \tag{8a}$$

where the wavenumber k and the function Φ are given by

$$k = 4f^2\sqrt{1+t^2} \qquad \Phi = 4f^2\Big(-Xa + (\mathrm{sign}t)\,Y\sqrt{1+t^2-a^2}\,\Big) \tag{8b}$$

with the function a defined as

$$a = [\,2\,(1+t^2)^{1/4}-1]/(4\tau) \tag{8c}$$

The function Θ is given by (5) with (8b).

Wave component W^i for $1/4 < \tau$

If $1/4 < \tau$, the wave component W^i in (3) is defined as

$$W^i = \frac{f/F}{1+\sqrt{1+4\tau}}\int_{-\sqrt{(1+\sqrt{1+4\,\tau}\,)^4-1}}^{\sqrt{(1+\sqrt{1+4\,\tau}\,)^4-1}} dt\, \frac{(1-\Theta)\,|\,t\,|\,e^{Z_*\,k\,-\,i\,\Phi}}{(1+t^2)^{1/4}\sqrt{1+t^2-a^2}} \tag{9a}$$

where the wavenumber k and the function Φ are given by

$$k = k_i^+\sqrt{1+t^2} \qquad \Phi = k_i^+\Big(Xa + (\mathrm{sign}t)\,Y\sqrt{1+t^2-a^2}\,\Big) \tag{9b}$$

with the function a and the reference wavenumber k_i^+ defined as

$$a = 1 - \frac{(1+t^2)^{1/4}-1}{\sqrt{1/4+\tau}-1/2} \qquad k_i^+ = f^2/(\sqrt{1/4+\tau}+1/2)^2 \tag{9c}$$

The function Θ is given by (5) with (9b).

Wave component W^i for $\tau < 1/4$

If $\tau < 1/4$, the wave component W^i in (3) is defined as

$$W^i = f^2\,\frac{K_i^+ + K_i^-}{2}\int_{-\pi}^{\pi} dt\,\frac{(1-\Theta)\,|\sin t\,|\,e^{Z_*\,k - i\,\Phi}}{\sqrt{1-a^2/(1-\tau a)^4}} \tag{10a}$$

where the wavenumber k and the function Φ are given by

$$k = f^2(1-\tau a)^2 \qquad \Phi = f^2\Big(Xa + (\mathrm{sign}\,t)\,Y\sqrt{(1-\tau a)^4 - a^2}\Big) \tag{10b}$$

Furthermore, the function a in (10b) and $K_i^{\pm}$ in (10a) are defined as

$$a = \frac{K_i^+ - K_i^-}{2} + \frac{K_i^+ + K_i^-}{2}\cos t \qquad \begin{Bmatrix} K_i^+ \\ K_i^- \end{Bmatrix} = \begin{Bmatrix} 1/(\sqrt{1/4+\tau}+1/2)^2 \\ 1/(\sqrt{1/4-\tau}+1/2)^2 \end{Bmatrix} \tag{10c}$$

The function Θ is given by (5) with (10b).

Simple Green function for special case $\omega = 0$

For steady free-surface flow about a ship advancing in calm water, the Green function (3) becomes

$$4\pi\,G = -1/r + 1/r_* - 2/r_*^F + W^o \tag{11a}$$

where r, r_*, r_*^F are given by (4), and the wave component W^o is defined as

$$W^o = \frac{1}{F^2}\int_{-\infty}^{\infty} dt\,\frac{\sqrt{T+1}}{T}\,e^{Z_*\,k}\,\mathcal{I}m\,(1-\overline{\Theta})\,e^{i\,\Phi} \tag{11b}$$

Here, $\mathcal{I}m$ stands for the imaginary part, and the wavenumber k and the function Φ are given by

$$k = T/F^2 \qquad \Phi = \Big(X + (\mathrm{sign}\,t)\,Y\sqrt{T-1}\Big)\sqrt{T}/F^2 \qquad \text{with} \quad T = \sqrt{1+t^2} \tag{11c}$$

The function $\overline{\Theta}$ is the complex conjugate of the function Θ defined by (5) with (11c).

Simple Green function for special case $\mathcal{U} = 0$

For diffraction-radiation without forward speed, the Green function (3) becomes

$$4\pi\,G = -1/r - 1/r_* + 2/r_*^f - i\,W^i \tag{12a}$$

where r, r_*, r_*^f are given by (4), and the wave component W^i is defined by

$$W^i = f^2\int_{-\pi}^{\pi} dt\,(1-\Theta)\,e^{Z_*\,k - i\,\Phi} \tag{12b}$$

Here, the wavenumber k and the function Φ are given by

$$k = f^2 \qquad \Phi = f^2(X\cos t + Y\sin t) \tag{12c}$$

The function Θ is given by (5) with (12c).

Conclusion

The Green function (3) satisfies the Poisson equation (1a), the radiation condition, and the Michell linear free-surface boundary condition (1b) in the farfield. Unlike usual free-surface Green functions, which satisfy the free-surface condition (1b) exactly everywhere, the Green function (3) only satisfies the free-surface boundary condition (1b) approximately in the nearfield. Although the linear free-surface boundary condition (1b) is valid far away from a ship advancing in regular waves (i.e. in the farfield), this boundary condition can only be regarded as an approximation in the vicinity of the ship (i.e. in the nearfield) due to nearfield effects. Thus, it is not evident that a Green function that satisfies the Michell condition (1b) everywhere is necessarily superior to a Green function that only approximately satisfies the Michell boundary condition in the nearfield.

The Green function (3) is expressed as the sum of four elementary Rankine sources, defined by (4), and the three wave components $W^{\pm}$ and W^i, defined by (5)–(10) in terms of one-dimensional Fourier superpositions of elementary waves. The Green functions (11) and (12), which correspond to the special cases $f = 0$ and $F = 0$, are expressed in terms of three elementary Rankine sources and a single wave component. The Rankine components in (3), (11a) and (12a) account for the leading terms in both the nearfield and farfield asymptotic approximations to the nonoscillatory local-flow components associated with the boundary condition (1b) and the related conditions for the special cases $f = 0$ and $F = 0$, which thus are satisfied approximately in the nearfield and accurately in the farfield. The integrands of the Fourier integrals that define the wave components $W^{\pm}$ and W^i in (3), W^o in (11), and W^i in (12) are continuous and only involve trigonometric and hyperbolic functions of real arguments, and the limits of integration in these Fourier integrals are independent of the coordinates X, Y, Z_*. Thus, the Green functions (3)–(10), (11) and (12) are remarkably simple.

The Green function (3) is considerably simpler than the free-surface Green functions that have been used in the literature. The frequency-domain Green function (3) is no more complicated than the Green function associated with a time-domain analysis, which requires a time-history convolution. The frequency-domain Green function (3) is more complicated, but includes considerably more physics, than the elementary Rankine source $1/r$ used as Green function in Rankine-source panel methods, which require appropriate numerical-differentiation schemes to enforce the radiation condition (an unsolved nontrivial problem for wave diffraction-radiation in a regime approximately defined by $\tau < 0.5$) and truncation of an unbounded free-surface distribution of singularities; see e.g. *Bertram and Yasukawa (1996)* and *Bertram (2000).*

No distribution of singularities over the free surface is required to compute diffraction-radiation of time-harmonic waves by a ship within the linear approximation associated with the Michell free-surface boundary condition if a usual free-surface Green function is employed (although free-surface distribution of singularities are required to account for nearfield free-surface effects; e.g. if free-surface linearization about the zero-Froude-number double-body flow is used). However, use of a simple Green function like (3) requires a distribution of singularities over a nearfield portion of the free surface in the vicinity of the ship waterline. An important property of the free-surface distribution of singularities associated with the use of such a simple Green function is that it rapidly vanishes in the farfield (in practice, at a small distance from the ship) because the linearized free-surface boundary condition becomes exact in the farfield. This property is a significant difference with panel methods based on Rankine sources.

The analysis used in *Noblesse and Yang (2003)* to obtain the Green functions (3)–(10), (11), (12) for deep water can be extended to the more general case of uniform finite water depth. This extension will be given elsewhere. Numerical comparisons of the simple Green functions (3)–(10), (11), (12) with the corresponding usual Green functions, which satisfy the linearized free-surface boundary condition everywhere, will also be reported elsewhere.

References

Ba M., Guilbaud M. (1995) *A fast method of evaluation for the translating and pulsating Green function*, Ship Tech. Res. 42:68-80

Bertram V. (2000) *Practical ship hydrodynamics*, Butterworth-Heinemann, 270 pp.

Bertram V., Yasukawa H. (1996) *Rankine source methods for seakeeping problems*, Jahrbuch Schiffbautechnische Gesellschaft, Springer, 411-425

Bessho M. (1977) *On the fundamental singularity in the theory of ship motions in a seaway*, Memoirs

Defense Academy Japan, Vol. XVII, 95-105

Boin J.P., Guilbaud M., Ba M. (2002) *Forward speed effects on diffraction-radiation computations*, 5^{th} Numerical Towing Tank Symposium (NuTTS'02) Pornichet, France

Boin J.P., Guilbaud M., Ba M. (2000) *Seakeeping computations using the ship motion Green function*, ISOPE Seattle, USA, 398-405

Boin J.P., Ba M., Guilbaud M. (1999) *Précision des intégrations surfaciques de la fonction de Green dans un code de tenue à la mer avec vitesse d'avance*, 7^e Journées de l'Hydrodynamique, 1-14

Bougis J., Coudray T. (1991) *Méthodes rapides de calcul des fonctions de Green des problèmes de Neumann-Kelvin et de diffraction-radiation avec vitesse d'avance*, 3e Journees de l'Hydrodynamique, Grenoble, France, 17-30

Brument A., Delhommeau G. (1997) *Evaluation numérique de la fonction de Green de la tenue à la mer avec vitesse d'avance*, 6^e Journées de l'Hydrodynamique, 147-160

Chen X.B. (1999) *An introductory treatise on ship-motion Green functions*, 7th Itl Conf. Numerical Ship Hydrodynamics, Nantes, France, 1.1, 1-20

Chen X.B., Diebold L., Doutreleau Y. (2000) *New Green-function method to predict wave-induced ship motions and loads*, 23^{rd} Symp. Naval Hydro. Val de Reuil, France

Diebold L. (2003) *Etude du probleme de tenue a la mer avec vitesses d'avance*, These de Doctorat, Universite de Poitiers, France

Du S.X., Hudson D.A., Price W.G., Temarel P. (2000) *A validation study on mathematical models of speed and frequency dependence in seakeeping*, Proc. Inst. Mech. Engrs 214:181-202

Du S., Hudson D.A., Price W.G., Temarel P. (1999) *Comparison of numerical evaluation techniques for the hydrodynamic analysis of a ship travelling in waves*, Royal Inst. Naval Arch. 141:236-258

Fang M.C. (2000) *The effect of the steady flow potential on the motions of a moving ship in waves*, J. Ship Res. 44:14-32

Guevel P., Bougis J. (1982) *Ship motions with forward speed in infinite depth*, Itl Shipbuild. Progr. 29:103-117

Guilbaud M., Boin J.P., Ba M. (2000) *Frequency domain numerical and experimental investigation of forward speed radiation by ships*, 23^{rd} Symp. Naval Hydro. Val de Reuil, France

Hoff J.R. (1990) *Three-dimensional Green function of a vessel with forward speed in waves*, Thesis, Division of Marine Hydrodynamics, Norwegian Inst. of Tech., Trondheim, Norway

Inglis R.B., Price W.G. (1982) *A three-dimensional ship motion theory - the hydrodynamic coefficients with forward speed*, Trans. Royal Inst. Nav. Arch. U.K. 124:141-157

Iwashita H. (1997) *Numerical seakeeping calculations based on the 3D Green function method*, Ship Tech. Res. 44:111-132

Iwashita H., Ito A. (1998) *Seakeeping computations of blunt ship capturing the influence of steady flow*, Ship Tech. Res. 45:159-171

Iwashita H., Ohkusu M. (1992) *The Green function method for ship motions*, Ship Tech. Res. 39:3-21

Jankowski J. (1990) *Fundamental solution of linear hydrodynamic boundary-value problems*, Polski Rejestr Statkow, Gdansk, Poland, Report No. 45

Kobayashi M. (1981) *On the hydrodynamic forces and moments acting on a three-dimensional body with a constant forward speed*, J. Soc. Nav. Arch. Japan, 150:175-189

Maury C. (2000) *Etude du problème de tenue à la mer avec vitesse d'avance quelconque par une méthode de singularité de Kelvin*, Thèse de Doctorat, Université de Nantes, France

Noblesse F. (2001) *Analytical representation of ship waves*, Ship Tech. Res. 48:23-48

Noblesse F. (1981) *Alternative integral representations for the Green function of the theory of ship wave resistance*, J. Engg Math. 15:241-265

Noblesse F., Yang C. (2003) *Practical free-surface Green functions for wave diffraction-radiation with forward speed*, 8th Itl Conf. Numerical Ship Hydrodynamics, Busan, Korea

Noblesse F., Yang C. (1996) *Fourier representation of near-field free-surface flows*, Ship Tech. Res. 43:19-37

Ponizy B., Noblesse F., Ba M., Guilbaud M. (1994) *Numerical evaluation of free-surface Green functions*, J. Ship Research, 38:193-202

Wang C.T., Chiu F.C., Horng S.J. (1999) *Hydrodynamic forces on the advancing slender body with speed effects: wave exciting forces*, Itl Shipbuild. Progr. 46:29-41

Wu G.X., Eatock-Taylor R. (1987) *A Green's function form for ship motions at forward speed*, Itl Shipbuild. Progr. 34:189-196

Flow Computations of a Ship with a Podded Propulsor

Kunihide Ohashi, Takanori Hino, Yoshitaka Ukon
National Maritime Research Institute, Japan
e-mail: k-ohashi@nmri.go.jp, hino@nmri.go.jp, ukon@nmri.go.jp

1.Introduction

In recent years, various podded propulsors with an electrical propulsion system are being developed aiming at better hydrodynamic performance. Among them, a system with electric motors inside a pod is considered to be most promising. For the optimized design of ships with a podded propulsion system, methods for predicting hydrodynamic performances of a ship with a podded propulsor are required. CFD(Computational Fluid Dynamics) methods with an unstructured grid approach are expected to be the most powerful tool for this purpose, since it can analyze turbulent viscous flows around a complex geometry. For the analysis of self propulsion condition by CFD methods, propeller effects should be taken into account in a Navier-Stokes solver. It can be achieved by the use of a body force distribution representing propeller effects. This approach has been applied to analysis of ship flows with a conventional propeller and generally showed good agreements with measured data[1].

In this paper, a Navier-Stokes solver with an unstructured grid method is applied to the prediction of the performances of a ship with a podded propulsor. The numerical results are shown and compared with measured results. Also, the discussions are made for the performances of the two ways of podded propulsor arrangement, a pusher type and a tractor type. Through these applications, capability of the numerical method is demonstrated

2.Numerical Method

Since a basic numerical procedure for the Navier-Stokes equations are described in references[2][3], only the brief outline is given here.

Spatial discretization is based on a cell-centered finite-volume method. A computational domain is divided into unstructured polyhedral cells and flow variables (pressure, velocity and eddy viscosity) are stored in the center of each cell. Cells whose shape are hexahedra, tetrahedra, prisms or pyramids can be used and the combinations of these cells give greater flexibility for handling complex geometry.

For the inviscid fluxes (convection terms and pressure gradient terms), the second order upwind scheme based on the flux-differencing splitting of Roe with the MUSCL approach is employed. The viscous fluxes are evaluated by the second order central scheme. Thus, the overall accuracy in space is the second order.

The backward Euler scheme is used for the time integration. Local time stepping method is used, in which time increment is determined for each cell in such a way that the CFL number is globally constant. The linear equations derived from the time linearization of the fluxes are solved by the Gauss-Seidel iteration.

The propeller effects are represented using the body force distributions which are calculated by a simplified propeller theory[4].

3.Results and Discussions

Table 1 shows the principal particulars of the ship model used.

Table 1 Principal Particulars of Ship Model

	Model	Ship
Lpp(m)	6.6667	78.00
B(m)	0.9966	13.00
d(m)	0.2492	4.61
Cb	0.682	

A ship type is a coastal cargo ship and its design speed is 12.0 kt. In the numerical simulation, the Reynolds number is set 4.096 $\times 10^6$ and free surface effect is not considered for simplicity. As a turbulence model, Spalart-Allmaras model is adopted.

All the measurement, which include resistance and self propulson tests and wake measurement, were conducted at the NMRI.

3.1 Towing Condition

In towing condition, the solution domain is set for the left half side due to flow symmetry. Its size is,

$-1.0 < x < 3.0, -2.0 < y, z < 0.0$

which are nondimensionalized by L_{pp} and the origin of the coordinate is set FP.

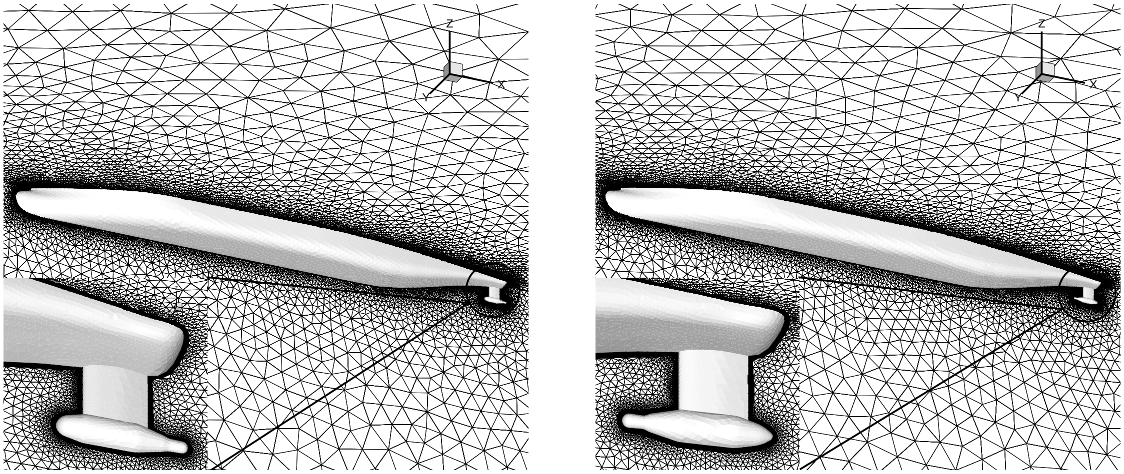

Pusher type

Tractor type

Figure 1 Computational grids

The computational grids consist of 0.8 million cells (0.3 million prisms and 0.5 million tetrahedra) and 0.3 million vertices (Figure 1). The grids are hybrid, that is, prisms are used in the region near the hull surface and tetrahedra are used in the far field. Minimum spacing adjacent to the hull surface is set as 1.0×10^{-6}

The computed result of pressure distributions on the hull surface are shown in Figure 2. The pressure distributions of pusher and tractor types are almost same on the hull and the strut surface. On the pod surface, on the other hand, low pressure area are observed at the discontinuity of the pod surface and pusher and tractor types show quite different pressure patterns.

Comparison of the nominal wake distributions are shown in Figure 3. The wake measurement was performed only for the pusher type. The computed result shows a agreement with the measured result. The wake shape can be considered as the superposition of the wakes of a ship hull and a pod and also a strut.

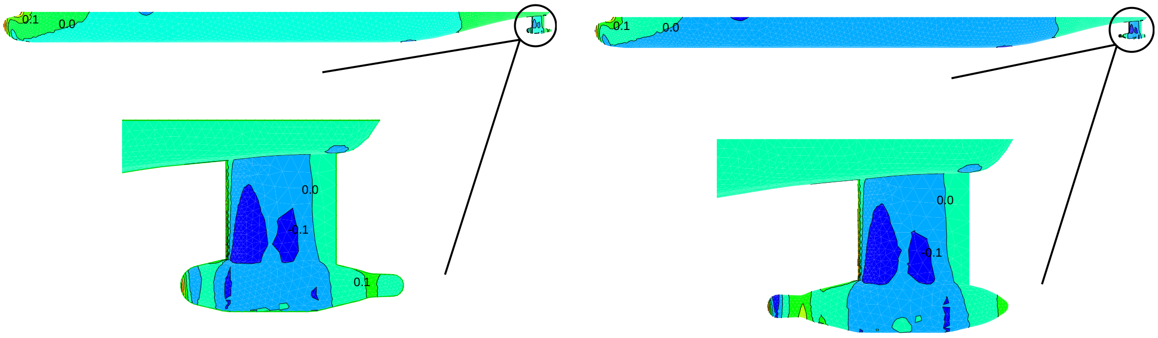

Pusher type Tractor type

Figure 2 Pressure distributions on the hull surface(Δ p=0.1)

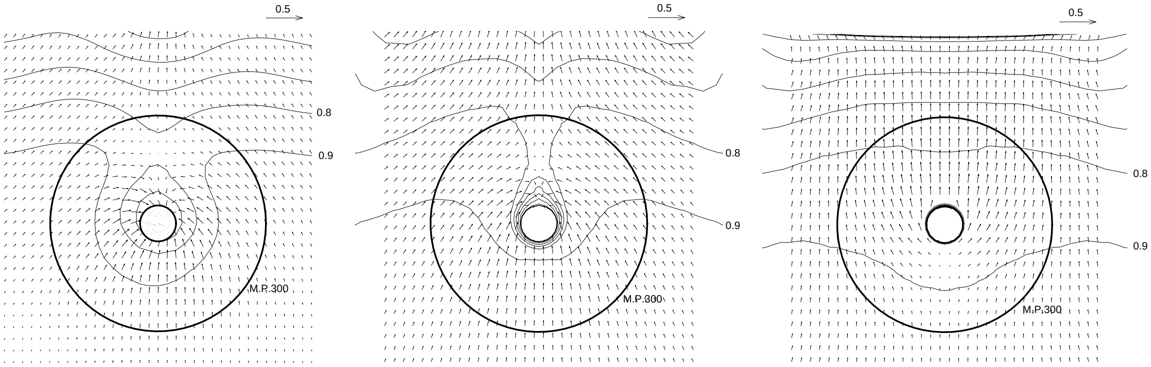

Measured Computed Pusher type Computed Tractor type

Figure 3 Nominal wake distribution at propeller plane(Δ u=0.1)

Table 2 shows the computed and measured results of the form factor 1+K and the nominal wake coefficient 1-w_n. The computed form factor is larger than the measured results. Nominal wake coefficients show good agreement with the measured result and exhibit the same tendency that 1-w_n of the tractor type is lower than that of the pusher type. As shown in Figure 3, in case of a tractor type, a propeller plane is closer to the hull surface than in case of a pusher type, thus, the nominal wake coefficient becomes lower.

Table 2 Comparisons of form factor and nominal wake coefficient

	Measured		Computed	
	Pusher	Tractor	Pusher	Tractor
1+K	1.13	1.14	1.28	1.24
1-w_n	0.880	—	0.885	0.863

3.2 Self-propulsion Condition

For the self propulsion condition, the Reynolds number is set to be the same as the towing condition. The computational grids are made from the grids of towing condition, that is, the grids of towing condition are mirrored on the y-plane. Thus the computational grids of self propulsion condition consist of 1.6 million cells(0.6 million are prisms and 1.0 million are tetrahedra). The solution domain is as follows:

$-1.0 < x < 3.0, -2.0 < y < 2.0, -2.0 < z < 0.0$

The computation of a self propulsion condition starts from the convergence results of a towing condition. Propeller revolution number is changed automatically to match the propeller thrust to ship drug at the ship point. Iterations are performed until the propeller revolution and the flow field converge. Self propulsion factors are computed by the thrust identity method.

Table 3 shows the principal particulars of propeller model. Propeller open test result are depicted in Figure 4 together with the prediction with the simplified propeller theory. The result of the simplified propeller theory shows good agreement with the measured result.

Table 3 Principal Particulars of M.P.No.300

Diameter(m)	0.1965
Boss ratio	0.1665
Pitch ratio(0.7R)	0.6800
Blade width ratio	0.3423
Number of blades	4
Direction of turning	Right
Blade section	NACA

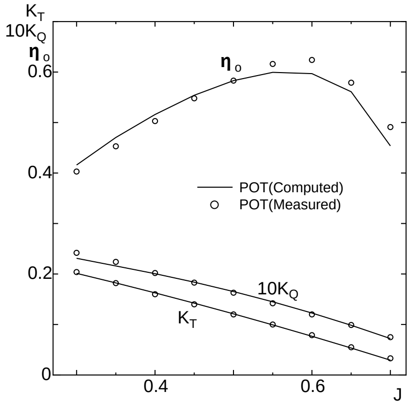

Figure 4 Propeller open test result

Figure 5 depicts the pressure distributions on the hull surface. Surface pressure distributions on the ship hull show little difference between in pusher and tractor types. In case of a pusher type, surface pressure distributions of pod are lower than the towing condition due to the propeller suction. Also pressure distributions in port and starboard sides of a pod surface are almost same. On the other hand, surface pressure distributions of a tractor type are quite different between port and starboard sides. Because a propeller slipstream hits the strut, lower pressure arises in starboard side. While high pressure area arises in port side. These asymmetric forces cause problems in manoeuvrability. In such a case, a fin is attached under the pod casing for the force balance. Also, informations of the pressure distributions are important for the self propulsion performance and a propeller design.

The wake distributions behind the propeller slipstream(x=1.03) are shown in Figure 6. In case of a pusher type, swirling velocities are kept in a propeller slipstream. On the contrary, in case of a tractor type, they are deformed due to interaction with the strut.

Finally, comparison of self propulsion factors are shown in Table 4. The computed results are compared with the measured results on the lowest Froude number Fn=0.18.

The computed results show the same tendency with the measured results, thus, all self propulsion factors of a pusher type are larger than those of a tractor type. The thrust deduction coefficients of a tractor type become lower than those of a pusher type due to drag increase of a pod in the propeller slipstream. The effective wake coefficients of a tractor type is also smaller than those of a pusher type. This is because the thrust of a tractor type is larger due to the displacement effect of a strut and a pod, and also because a wake gain of a tractor type is larger than a pusher type. In the present computation, the difference between a pusher and tractor types is very small in total efficiency.

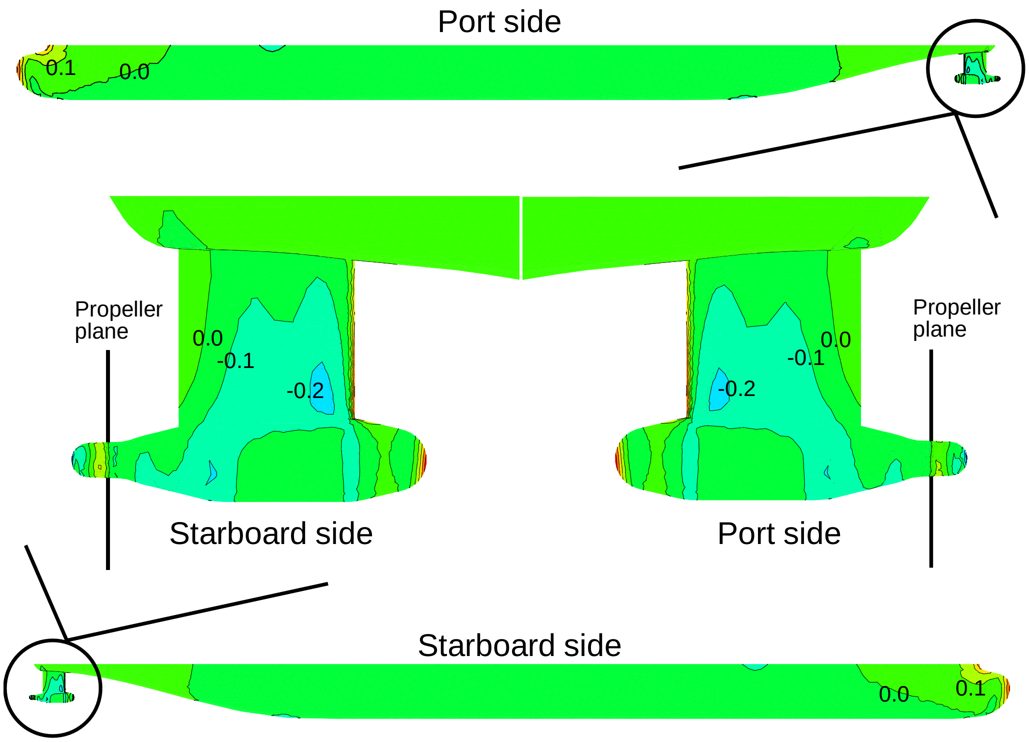

Pusher type

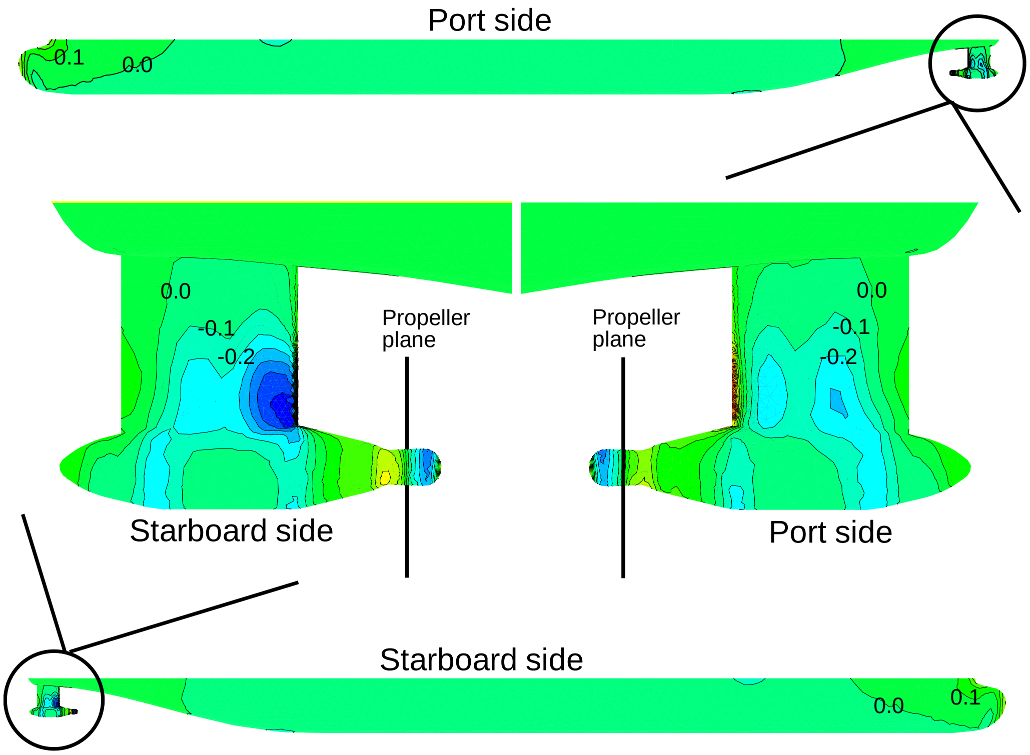

Tractor type

Figure 5 Pressure distributions on the hull surface(Δ p=0.1)

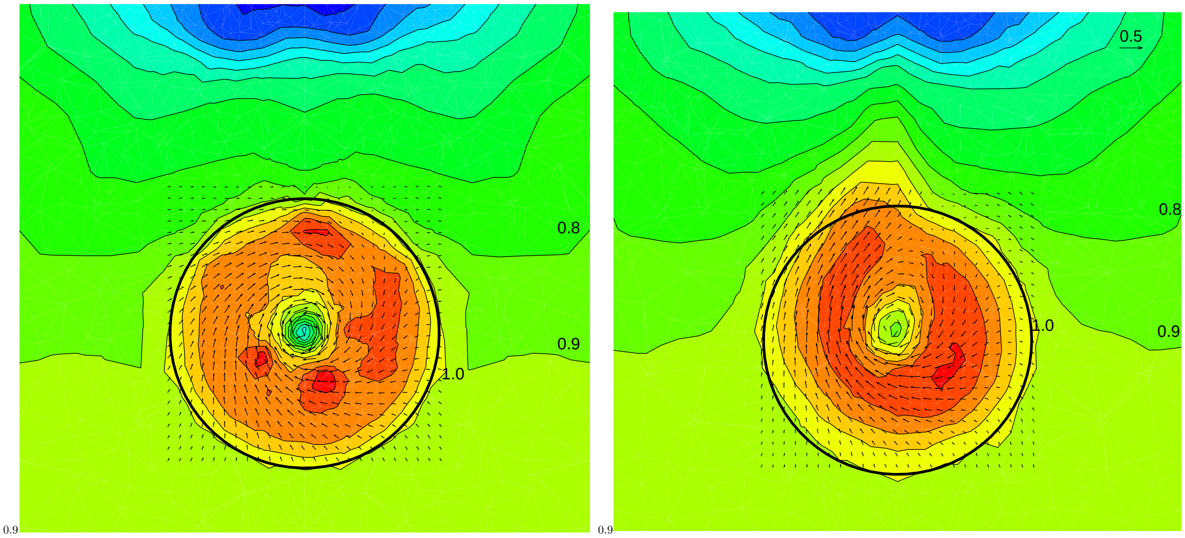

Pusher type

Tractor type

Figure 6 Wake distributions at propeller race(x=1.03, Δ u=0.1)

Table 4 Comparisons of self propulsion factor

	Measured(Fn=0.18)		Computed	
	Pusher	Tractor	Pusher	Tractor
1-t	0.933	0.894	0.904	0.889
1-w_t	0.930	0.856	0.904	0.867
η_r	1.011	1.001	1.029	1.010
η_o	0.595	0.580	0.578	0.573

4.Conclusion

Flow computations of a ship with a podded propulsor have been performed. The performances of the two ways of podded propulsor arrangement, i.e., a pusher type and a tractor type, are compared. The informations of flow fields and self propulsion factors are useful for a ship hull design.

References

[1]Ohashi, K., Hirata, N., Hino, T. : A Comparative Study of Body Force Models Representing Effects of Contrarotating Propellers, Trans. of the West-Japan Society of Naval Architects, Vol.105, (2003)

[2]Hino, T. : Navier-Stokes Computations of Ship Flows on Unstructured Grids, Proc. of the 22nd Symp. on Naval Hydro., (1998)

[3]Hino, T. : An Intefrace Capturing Method for Free Surface Flow Computations on Unstructured Grids, J. of the Soc. Naval Archit. Japan , Vol.186, pp.173-183, (1999)

[4]Moriyama, F. : On an Approximate Numerical Method for Estimating the Performance of Marine Propellers, (in Japanese), Papers of Ship Research Institute, Vol.16 No.6, pp.361-376, (1979)

FREE SURFACE FLOW COMPUTATIONS
FOR COMPLEX HULL SHAPES

Anders Östman, CFD norway, Norway
E-mail: anders.ostman@cfdnorway.no

INTRODUCTION

The flow field around realistic hull types might generate a very complex wave pattern. The transom stern may be partly wetted, a bulbous bow generates a complex bow wave, and the physical bow wave tends to break in the high Froude number range. All this presents challenges from the numerical simulation point of view. When computing flow fields where the physical bow wave breaks, it is necessary to add additional numerical diffusion locally in the vicinity of the breaking wave. In the present paper this is done by means of two of schemes from the LED-family. These models are thereafter used to compute the flow field around the DTMB 5415 test case.

GOVERNING EQUATIONS

Conservation of mass and momentum of a inviscid, incompressible fluid flow with a gravitational acceleration in the z-direction can be written on dimensionless form as

$$\begin{aligned} &\frac{\partial u_j}{\partial x_j} = 0 \\ &\frac{\partial u_i}{\partial t} + u_j \frac{\partial u_i}{\partial x_j} = -\frac{\partial \psi}{\partial x_i} \end{aligned} \tag{1}$$

where Re is the Reynolds number, ψ is a variable for the pressure, containing both the static and the hydrostatic component of the pressure,

$$\psi = p + \frac{1}{Fr^2} x_3 \tag{2}$$

where Fr is the Froude number, $Fr = U / \sqrt{gL}$.
The Froude number now enters explicitly in the boundary condition for ψ instead of in the governing equations.

The physical requirement that there can be no mass flux through the free surface gives a kinematic boundary condition that has to be fulfilled at the surface. The condition states that the boundary has to move as a material surface, and is written as

$$\frac{d\beta}{dt} = w = \frac{\partial \beta}{\partial t} + u \frac{\partial \beta}{\partial x} + v \frac{\partial \beta}{\partial y} \tag{3}$$

where $\beta(x,y,t)$ is the location of the free surface. An additional dynamic condition has to be fulfilled at the surface. In case of large values of the surface curvature, the surface tension can be neglected, and the dynamic condition at the free surface becomes $p = p_{atm}$. The corresponding boundary condition for ψ, Eq.(2) becomes

$$\psi = p_{atm} + \frac{1}{Fn^2} \beta \tag{4}$$

Viscous effects are neglected on the free surface, a consequence of this assumption is that there can be no velocity gradients normal to the free surface yielding a Neumann boundary conditions for the velocities,

$$\frac{\partial u}{\partial n} = \frac{\partial v}{\partial n} = \frac{\partial w}{\partial n} = 0 \tag{5}$$

NUMERICAL METHOD

The method used for the solution of the incompressible Euler equations is a finite-volume method based on central differences in space co-ordinates and an explicit Runge-Kutta method for the integration in time. This method is marching in time from an initial field until a stationary condition is reached and the conservation equations for mass and momentum are satisfied.
The flow solver facilitates multi-block grids with a general and flexible specification of boundary conditions. The cell-centred finite-volume discretisation stems from the integral form of the Euler equations. On a finite control volume Ω this reads

$$\begin{aligned} &\frac{\partial}{\partial \mathrm{t}} \int_{\Omega} \mathrm{U}\, \mathrm{d}\Omega + \oint_{\mathrm{S}} \mathrm{F} \cdot \mathrm{n}\, \mathrm{dS} = 0, \\ &\mathrm{U}^{\mathrm{T}} = \left[\mathrm{p}/\mathrm{c}^2, \mathrm{u}, \mathrm{v}, \mathrm{w}\right] \end{aligned} \tag{7}$$

where p is static pressure and c is an artificial speed of sound. The variables u, v, and w are the Cartesian velocity components in x -, y-, and z-direction respectively. The variables are assumed averaged over each control volume. In Eq. (7) $\boldsymbol{F}$ refers to the common flux vector containing the convective flux terms while the vector $\boldsymbol{n}$ is the outward unit normal of the surface with area S. At each cell face the characteristic variables are obtained using a 3rd-order accurate upwind-biased interpolation stencil. After a transformation back to primitive variables the fluxes are assembled.

Solution of the Free Surface Kinetic Boundary Condition

The iterations of the bulk flow equations and the free surface equation are done in two independent loops. They are not coupled in a way that would prevent flux to go through the surface in every intermediate time step. However, as the solution converges, the flux through the surface will go to zero, the velocity at the boundary will become parallel to the surface, and the surface will behave as a material surface. This approach follows the method presented in [1]. The equation for the free surface is solved in the same way as the equations for bulk flow, i.e. by a three stage Runge-Kutta algorithm.

Numerical diffusion at the free surface

For flow fields around realistic hull shapes, designed for high speeds, the physical bow wave tends to break in the higher range of speed. For computations of such flows it is necessary to add additional diffusion in the wave breaking area. This can be done in a number of ways. As an example, Mascio et al. [3], achieved excellent results using ENO-type schemes. In the present method two types of local extremum diminishing, LED [2], schemes are implemented and applied on the free surface. The implemented schemes are ELED (essentially local extremum diminishing) and USLIP (upstream limited positive) some details of these schemes will now be described; the reader is referred to [2] for further details.

A diffusive flux through a cell face located at i+1/2 can be written,

$$d_{i+1/2} = \alpha_{i+1/2}(\Delta h_{i+1/2} - \frac{1}{2}(\Delta h_{i+3/2} + \Delta h_{i-1/2})), \qquad \text{where } \Delta h_{i+1/2} = \beta_{i+1,j} - \beta_{i,j} \tag{8}$$

This scheme gives the well known fourth order dissipation. The scheme is frequently used to eliminate spurious oscillations of smooth flows. As mentioned above, additional diffusion has to be added locally for flows with extreme gradients, such as breaking waves or shock waves in super sonic flows. A family of diffusive flux limited schemes with the possibility of increasing the diffusion at local extremum can be written in the form,

$$d_{i+1/2} = \alpha_{i+1/2}(\Delta h_{i+1/2} - L(\Delta h_{i+3/2}, \Delta h_{i-1/2})) \tag{9}$$

where L(p,q) is a limited average with the natural properties of an average.
In addition, L(p,q) has a special property needed for the scheme to be LED, namely, L(p,q)=0 if p and q have opposite signs. This property is essential for the scheme to be LED (and TVD). It is convenient to rewrite L(p,q) is the following form,

$$L(p,q) = \frac{1}{2} D(p,q)(p+q) \tag{10}$$

where D(p,q) is a function introduced to deflate the arithmetic mean, and become zero if p and q have opposite signs. In ELED and USLIP schemes the function D(p,q) is defined as,

$$D(p,q) = 1 - \left| \frac{p-q}{\max(|p|+|q|, \varepsilon\Delta x^r} \right|^s \tag{11}$$

The term $\varepsilon\Delta x^r$ is introduced to activate a threshold in the limited average. The values for the parameters in function are chosen as, ε=1.0, r=1.5 and s=2.

In the USLIP-scheme, the diffusive flux is evaluated from the upstream side of the cell face. We then get the following scheme,

$$\begin{aligned} & d_{i+1/2} = \alpha_{i+1/2}(\Delta h_{i+1/2} - L(\Delta h_{i+1/2}, \Delta h_{i-1/2})) \\ & \text{if } u_{i+1/2} > 0 \text{ or} \\ & d_{i+1/2} = \alpha_{i+1/2}(\Delta h_{i+1/2} - L(\Delta h_{i+1/2}, \Delta h_{i+3/2})) \\ & \text{if } u_{i+1/2} < 0 \end{aligned} \tag{12}$$

It can be shown that the LED-type schemes satisfy the TVD-property, while the opposite is not necessarily true. By increasing s, a sequence of limited averages is generated. If s=1 we get the minmod limiter, while s=2 is equivalent to Van Leer's limiter. Furthermore, it can be shown that the numerical diffusion from ELED-type schemes is of order Δx^2 at smooth extremum.

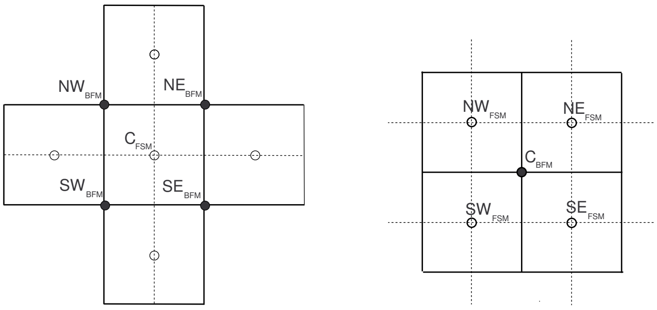

Figure 1 a) Interpolation stencil from the bulk flow mesh (BFM) to the free surface mesh (FSM).
b) Interpolation stencil from the FSM to the BFM

Free surface discretisation

The free surface kinetic boundary condition, KFSBC, is discretised by means of a finite-difference method. A new two-dimensional free surface mesh, FSM, is introduced beside the original finite-volume bulk-flow mesh, BFM. The node points in the FSM are constructed to be located in the centres of the BFM free surface cell face, Figure 1. At the beginning of each iteration the location of the node point, C, is found as an average of its surrounding bulk flow vertex points.

$$z_C^{FSM} = \frac{1}{4}\left(z_{NW}^{BFB} + z_{NE}^{BFB} + z_{SW}^{BFB} + z_{SE}^{BFB}\right) \tag{13}$$

Each free-surface iteration gives a new location of the FSM, and the vertex points on the free surface of the BFM can thereafter be updated. This is done by interpolating the deflection of the FSM to the vertex points of the bulk flow mesh,

$$\left(z_C^{BFM}\right)_{i+1} = \left(z_C^{BFM}\right)_i + \frac{1}{4}\left(\Delta\beta_{NW}^{FSM} + \Delta\beta_{NE}^{FSM} + \Delta\beta_{SW}^{FSM} + \Delta\beta_{SE}^{FSM}\right) \tag{14}$$

The bulk flow mesh can now be redistributed. The mesh is forced to move along the grid lines of an underlying grid.

RESULTS

The computations are performed on a two block grid, with 187*63*61 node points in the main block and 35*29*61 nodes in the block behind the transom stern. The computed wave profile at the hull is compared with INSEAN experimental data in Figure 2. The computations gives a bow wave that is located just ahead of the bow wave found in the experiments. Downstream the bow wave is the wave profile below the data along the entire hull. This is however in line with the results computed by many others, se the proceeding from the Gothenburg Workshop [4]. The USLIP and ELED schemes give nearly the same results, although the USLIP-scheme gives a slightly higher peak in the bow wave. The results along a cut at y/L=0.172 is shown in Figure 2. The computations under predicts the wave crest at x/L=0.5, again this is a problem encountered at the Gothenburg Workshop. There is a small shift in phase between the USLIP and ELED results at the local extremum, this is probably due to the fact that the ELED scheme is symmetric, while the USLIP is asymmetric.

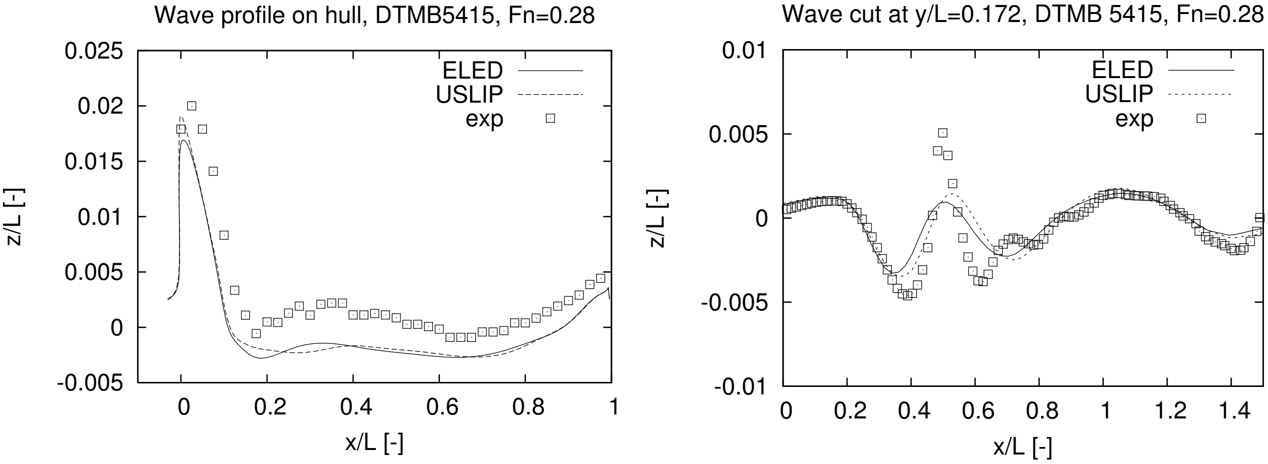

Figure 2 a) Wave profile along the hull. b) Wave profile at a cut at y/L=0.172

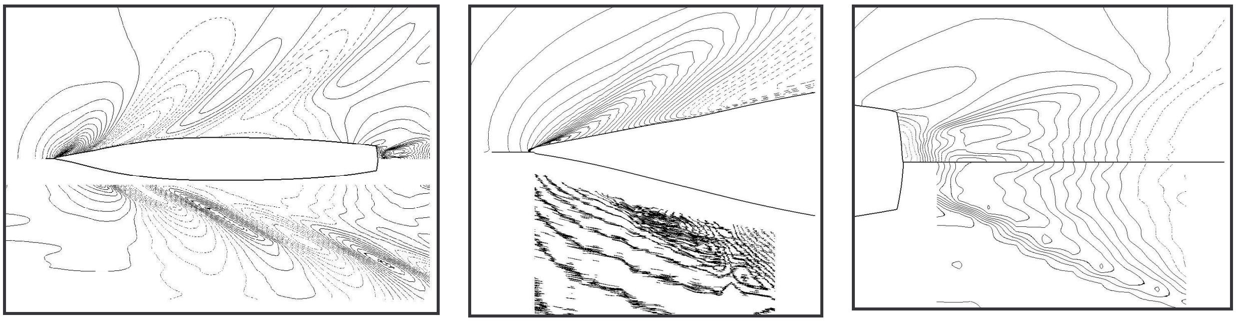

Figure 3 a) Overall wave pattern. b) Wave pattern at the bow. . c) Wave pattern behind the stern. Computations are in the upper half and experimental results in the lower half in all the figures.

The wave pattern is shown in Figure 3. The overall pattern is in reasonable agreement with the experimental results, although the computed results are more diffusive further away from the hull. It is difficult to interpret the experimental results in the bow area, but it seams that the computed bow wave is in good agreement with the experiments. In the stern area there are reasonably good agreement between computations and experiments.

CONCLUSIONS

The free surface flow around the DTMB 5415 test case has been computed using a finite volume flow solver with a surface tracking method at the free surface. Two LED-type numerical diffusion schemes for the free surface boundary condition have been tested. Both schemes are capable of handling the breaking bow wave, and there are small differences in the computed wave profile between the two schemes.

REFERENCES

1. FARMER J., MARTINELLI L., JAMESON A., "*Fast multigrid method for solving incompressible hydrodynamic problems with free surfaces*", AIAA Journal, Vol. 32, No. 6, 1994.

2. JAMESON A., "*A perspective on computational algorithms for aerodynamic analysis and design*", Progress in Aerospace Sciences, Vol. 37, 2001, p.197-243.

3. DI MASCIO, A., MUSCARI R., BROGLIA R., L., "*Computation of the flow past the U.S. Navy Combatant DTMB 5415 by a Godunov-type scheme*", Gothenburg 2000, Chalmers University of Technology, Gothenburg, Sweden, 2000.

4. LARSSON L., et al. "*Gothenburg 2000, A workshop on numerical ship hydrodynamics, Preprints*", Chalmers University of Technology, Gothenburg, Sweden, 2000.

Hydrodynamic Design Optimization using the Navier-Stokes Equations[1]

Daniele Peri, Emilio F. Campana, INSEAN, d.peri@insean.it

The use of high fidelity, CPU time expensive solvers is now quite common in the trial-and-error ship design process. Their use in simulation-based design is however still limited by the large amount of computational effort needed in the optimization cycles [2] and only few examples are available in optimal ship design literature [3, 5]. Research is moving toward the use of Variable Fidelity modelling techniques to reduce the CPU time needed [1].

The aim of this kind of *global approximation*, is to maximize the use of low-fidelity, cheap models, less accurate but also less expensive than high-fidelity models. With the use of some consistency conditions, the response of the low-fidelity models can be corrected during the optimization cycles, approximating the high fidelity predictions up to first order.

A first example is regarding a containership (KRISO KCS) in which the uniformity of the axial flow at the propeller at Fr $= 0.26$ has been assumed as objective function, by partially modifying the shaft log only, as shown in Fig. 1. The objective function is evaluated by using a high fidelity RANSE code. Being the code a multigrid one, the two finest grid levels are adopted as high and low fidelity models, allowing a CPU time reduction of about 75%. An example of the obtained results is reported in Fig.2, where the axial velocity of the original and optimzed models are compared. Here the variance of the axial velocity at the propeller disk is lowered of about 13%, obtaining a much more uniform flow at the propeller: this gives an improvement of the propulsive qualities without a dramatic change of the hull form.

A Multidisciplinary Design Optimization (MDO) problem for a surface ship is solved considering five objective functions and three different PDE are solved numerically, including a high-fidelity RANSE code for the prediction of the free-surface flow past the ship.

The description of the ship MDO problem is the following. The goal is the minimization of five objective functions at service speed (20 knots). Function F_1, computed by using a non-linear potential solver for steady free surface flows, is connected with the drag reduction. Functions F_2 and F_3, estimated applying a 3D panel code in the frequency domain, represent the seakeeping performances of the vessel (i.e. the response of the ship in waves) and define the operativity of a ship. To compute functions F_4 and F_5, a RANSE solver for steady free surface flows has been used. F_4 is related to the minimization of the so called "sonar dome vortices", produced at the junction of the sonar dome with the hull, while F_5 is an index of the quality of the flow and it is the parameter normally considered in the design of the propeller. 15 design variables have been used for the optimization of the shape.

The key point of the algorithm is the use of Response Surfaces as low fidelity models, whose degree of accuracy is improved at each optimization cycle. The kernel of method adopted here is the combined use of variable fidelity models, in which the low fidelity models, computationally inexpensive, *evolve* during the optimization cycles.

As a preliminary result, Fig.3 shows a typical sub-optimal solution. Modifications in the fore region are related with the geometry of the sonar dome. Large modifications can be observed after the midship and particularly where hull converges toward the stern. An evident reduction in the iso-vorticity levels can be seen in Fig.3 and a strong reduction of the intensity of the sonar dome vortices is hence obtained ($\Delta F_4 = -4.3\%$). Fig.4 also show a more uniform flow at the propeller disk ($\Delta F_5 = -1.1\%$). This sub-obtimal configuration also shows a reduction on vertical motions ($\Delta F_2 = -5.2\%, \Delta F_3 = -2.7\%$) while only the wave resistance is slightly increased ($\Delta F_1 = +1.1\%$). For details, a complete description is reported in [6].

References

[1] Alexandrov NM, Lewis RM, Gumbert CR, Green LL, Newman PA, 2000, Optimization with variable-fidelity models applied to wing design *38-th Aerospace Sciences Meeting & Exhibit*, Reno (NE), USA, AIAA Paper 2000-0841.

[2] Alexandrov NM, Hussaini MY, (ed.), 1997, Multidisciplinary design optimization, *SIAM*, USA.

[3] Peri D., Campana E.F., 2003, Multidisciplinary Design Optimization of a Naval Surface Combatant, *Journal of Ship Research*, **47**, 1, 1-12.

[4] Peri D, Rossetti M, Campana EF, 2001, Design optimization of ship hulls via CFD techniques. *Journal of Ship Research*, **45**, 2, 140-149.

---

[1] This work was supported by the U.S. Office of Naval Research under the grant No. 000140210489, through Dr. Pat Purtell.

[5] Peri D, Campana EF, Di Mascio A, 2001, Development of CFD-based design optimization architecture, *1st MIT conference on fluid and solid mechanics*, Cambridge, MA, USA.

[6] Peri D, Campana EF, 2003, High fidelity models in Simulation-Based Design, *The 8th International Conference on Numerical Ship Hydrodynamics*, Busan, Korea.

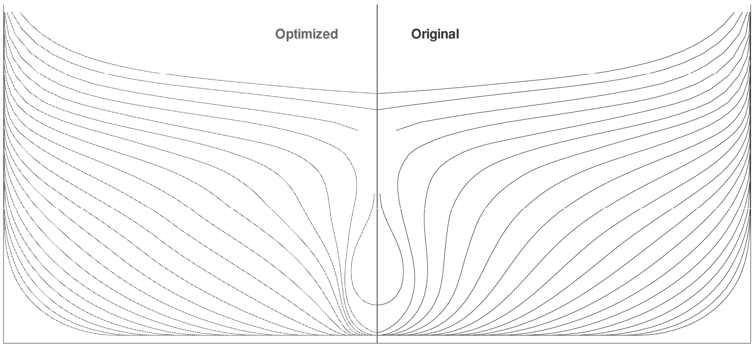

Fig.1: Original (right) and optimized geometry (left)

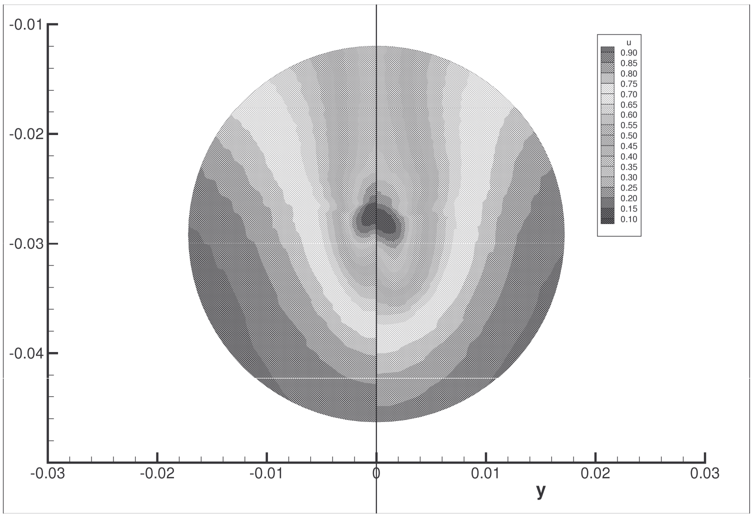

Fig.2: Wake at the propeller plane for the original (right) and optimized ship (left)

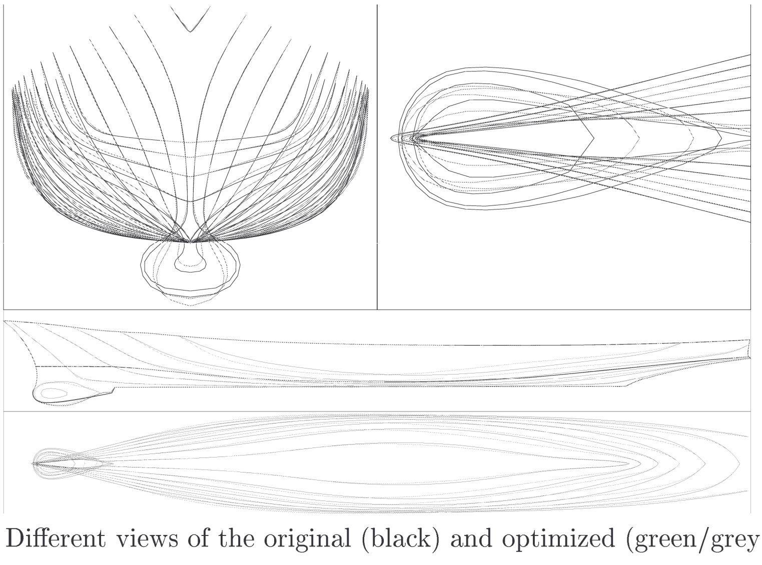

Fig.3: Different views of the original (black) and optimized (green/grey) ship

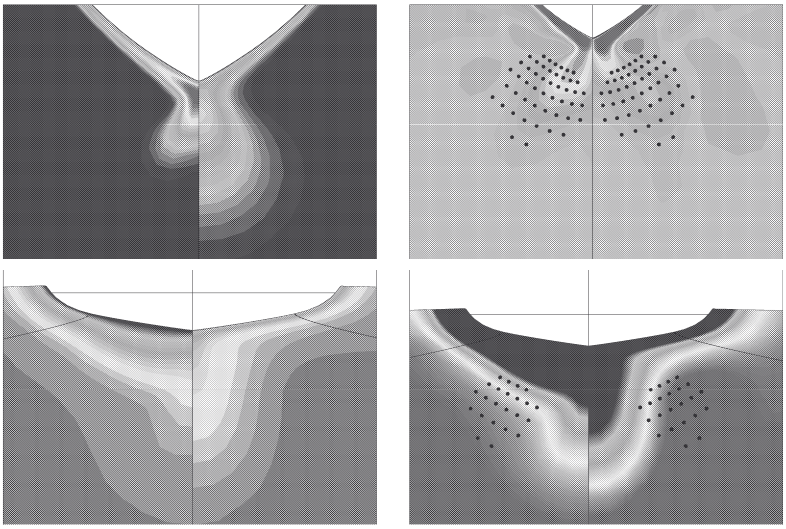

Fig.4: Optimization results on F_4, F_5. Axial vorticity downstream the bulb (top) and at propeller plane (bottom). Original (left) and optimized results with points of control region (right).

A RANS Based Prediction Method of the Ship Roll Damping with Forward Speed

Kumar B. Salui, Vladimir Shigunov, Dracos Vassalos
The Ship Stability Research Centre[†] , Universities of Glasgow and Strathclyde

Introduction

Several techniques have been applied to predict roll damping moment or its components with the presence of forward speed, including theoretical, experimental and empirical methods. One of the oldest empirical formulae is Hishida's method [2] where roll damping moment acting on a rolling ellipsoid moving at a constant velocity was predicted. His method enables prediction of damping moment due to the wave making, but not of the other components [3]. Hanaoka [4] formulated another theory for the flow field around a ship at a constant speed in an asymmetric motion such as roll, yaw and sway under the assumptions of thin and low draft to length-ratio ship. The assumptions of this theory are self-explanatory for it's limitations. Probably the most promising empirical method is Ikeda's prediction method [5]. However, the limitation of this prediction method is that it needs an adjustment for different forms of ship hull. In the case of a ship hull with appendages, the damping is calculated separately for the bare hull and appendages, and thus it cannot predict vortices at the junctions of a hull with appendages. This is another drawback of Ikeda's method.

Rapid development of computer hardware enables application of field-discretisation based methods such as finite difference or finite volume methods to solve practical problems such as ship motions in seaway. A useful literature survey of these methods can be found in [6] and [7].

The present paper demonstrates application of a RANS based technique for the simulation of flow past a rolling high-speed hard chine craft with skeg in a range of forward speeds from zero to high ($F_n=0.6$). For this study, an existing commercial solver based on an unstructured finite volume, collocated grid approach is used. The numerical results are compared well with experiments by Ikeda et al. [1].

Description of the Model

A scale model of a hard-chine craft with skeg was studied here. The description of the hull is shown in figures 1 and 2 from [1]. The fin and the bilge keel shown in figure 1 are not used in the present study.

Harmonic oscillations of the rolling hull are given by $\theta = \theta_a \sin \omega t$, where θ, t and θ_a are the instantaneous heel angle, time and the roll amplitude, respectively. The roll axis is fixed with respect to the hull as shown in figure 1. The running trim and sinkage were defined experimentally depending on the Froude number in towing tests without rolling and fixed in rolling tests to respective values shown in figure 4. The same fixed values of the trim and sinkage were used in the present calculations. The flow simulations have been done for rolling amplitude 10^0 at Froude number F_n from 0 to 0.6 in the range of non-dimensional frequency ($\hat{\omega} = \omega\sqrt{B/2g}$, where ω is the frequency of rolling and B is the beam of the ship) from 0.2 to 0.7.

Mathematical Formulation

A commercial solver used for the study is based on unstructured finite volume discretisation with collocated arrangement of flow variables. A variation of SIMPLE algorithm is used for the pressure correction. Free surface motion is modeled by a description of the water-air system as a single effective fluid with variable physical properties as density and viscosity, but with continuous velocity field. High-Resolution Interface-Capturing (HRIC) technique [8] is used for the discretisation of the equation for the volume fraction of the water. A standard *k*-ε model is employed for turbulence modeling. A brief description with relevant equations is available in [7]. Only grid generation and boundary conditions are described below.

[†] 48 North Portland Street, Glasgow, G1 1XN, United Kingdom, email: kumar.salui@na-me.ac.uk

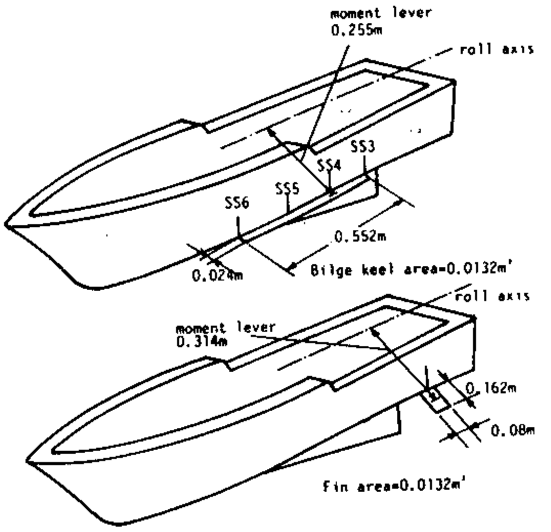

Principal particulars of the model:

length between perpendiculars 1.84 m
beam by water line 0.428 m
total draft 0.158 m
draft at midship 0.0735 m
draft at forward perpendicular 0.0437 m
draft at aft perpendicular 0.1032 m
displacement with skeg (∇) 0.0432 m^3

Figure1: Schematic view of model (left) and the model particulars (right)

Preliminary numerical tests have shown that numerical results are sensitive to the grid quality and besides, grid resolution in the boundary layer. Numerical grid was generated in two parts. The first one is an internal circular cylindrical block with the longitudinal axis coinciding with the roll axis. This cylinder is allowed to rotate with the body while the second, external block, which is a rectangular parallelepiped in shape, is fixed. The rotating cylindrical block is submerged into the fixed block using the sliding mesh technique. Grid at the bow of the hull is shown in figure 3. Grid consists of 480080 and 736000 cells in the moving and fixed parts, respectively.

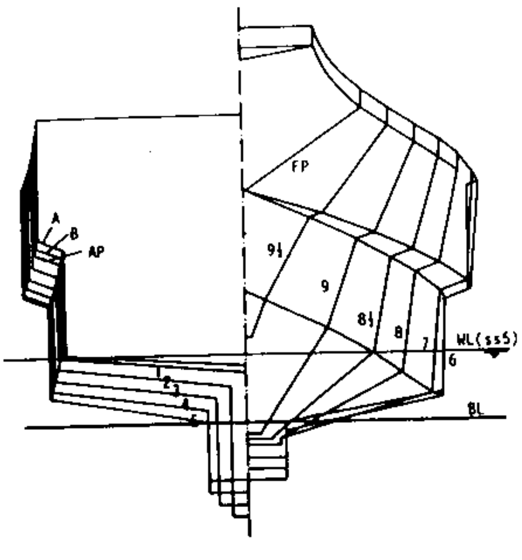

Figure 2: Body plan of the mode

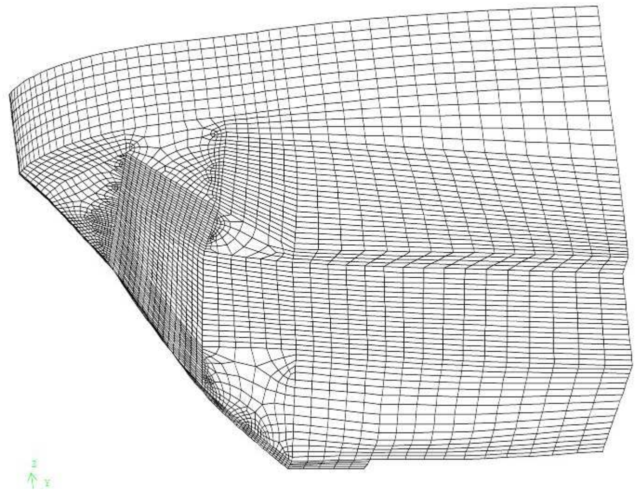

Figure 3: Grid at the bow of the model

A solution domain of one and half ship length ahead of the ship and four ship lengths at the aft of the ship is considered. The domain is 32 m wide with the model placed at the centre. The depth of water is 12 m.

The following boundary conditions are used. On the hull surface a no-slip boundary condition is applied. Hydrostatic pressure boundary condition is applied at the aft boundary of the solution domain. All other boundaries of the solution domain are considered as the inlet boundary, where the velocity prescribed is the same in magnitude as the ship speed but opposite in direction.

Calculation of the Damping Moment

The output of the solver is the total pressures and shear stresses at each of the cell faces on the hull surface. Hydrodynamic pressures (p_d) in each control volume are computed by subtracting the hydrostatic part (which is calculated with respect to the initial undisturbed free surface) from the total pressure. Finally hydrodynamic moment with respect to a point on the roll axis is evaluated using the following relationship:

$$\vec{M}(t) = -\int_s p_d \vec{r} \times \vec{n} ds + \int_s \vec{r} \times \vec{\tau} ds,$$

where $\vec{r}$, $\vec{\tau}$ and $\vec{n}$ are position vector of the centre of an elemental surface with respect to the roll centre, shear stress and outward normal to the surface, respectively, and ds is the area of the elemental surface. As the second term (moment due to shear stress) of the equation is very small compared to the first term (moment due to hydrodynamic pressure), it was neglected. Projection of the above equation on the roll axis gives the value of the moment in the roll motion as

$$M_w(t) = \int_s p_d (n_y z - n_z y) ds,$$

where n_y, n_z are the direction cosines of the normal and y, z correspond to the y- and z-components of the position vector $\vec{r}$.

The component of this moment proportional to the angular roll velocity (linear component), is evaluated by extracting the Fourier coefficient of the fundamental frequency by the analysis of the time history of the instantaneous hydrodynamic moment obtained from the above formula. This coefficient can be written as

$$B_{44} = \frac{1}{\pi \alpha_0} \int_{t-T/2}^{t+T/2} M_w(t) \cos(\omega t) dt.$$

This coefficient is non-dimensionalised in the following way:

$$\hat{B}_{44} = \frac{B_{44}}{\rho \nabla B^2} \sqrt{\frac{B}{2g}},$$

where ∇ and B represent the immersed volume and beam of the ship, respectively.

Results and Discussions

In any numerical simulation it is important to quantify the uncertainty brought by grid density and the size of the solution domain. In the present calculations, grid density and domain size independency studies were carried out for all test cases. The results are free from grid or domain size effects.

Variations of damping moment coefficients with the non-dimensional frequency at constant Froude number are shown in figure 5. From this comparison, it can be seen that at the lower Froude numbers, the accuracy of the calculated results is very good. However, there is a large deviation of the calculated results from the tests at higher Froude numbers and higher frequencies. Maximum deviation is approximately 14%.

At the zero forward speed, the non-linear nature of the damping coefficients is purely dependent on the vortex shedding, therefore the non-linear eddy component of the damping plays the most significant role. As the Froude number increases, the eddy component decreases rapidly [2]. In the absence of fins or bilge keels, at higher speeds the lift damping becomes the major component of the total damping moment, and this component is not much affected by the change of roll frequency. However, as it can be seen from figure 5, the damping moment coefficient for the hull with skeg is still non linear at the higher Froude numbers. At the high speed, it has been found that the increment of the damping moment is high with increasing frequency due to the presence of the skeg, while for the low speed the influence of appendages is much smaller.

In figure 6, the variations of roll damping coefficient are plotted against the Froude number for several constant frequencies. From these plots, it can be seen that the damping moment coefficient is increasing at a faster rate for the Froude numbers more than approximately 0.4. Up to this Froude number, the lift component increases linearly, while for greater Froude numbers it increases more rapidly in a non-linear manner. Due to this reason the total damping moment at a constant frequency is increasing at a faster rate when the Froude number is more than 0.4.

From the comparison of the numerical and experimental results in figures 5 and 6, it can be seen that the prediction by the present numerical analysis is in general good. However, at the high Froude numbers and high frequency, the deviation of the computed results from the experiments is on average larger. Improvement of grid quality can decrease this discrepancy. Here, the grid was generated using multi-block grid generation procedures, and to avoid non-matching interfaces at block boundaries, paving [8] was used. Some other type of grid topology may give better results. Besides, hydrostatic pressure boundary condition was prescribed at the aft boundary of the solution domain in the present study. Although the domain is sufficiently long, the hydrostatic boundary condition is not accurate definition especially for higher Froude numbers. Some other boundary conditions may help to compute more accurate results. Nevertheless, the method can produce quantitatively reasonable results and therefore can be used up to a certain frequency and Froude number to obtain reliable results for this type of hulls. Although the total computing time is not very small for these three-dimensional simulations, the method is still useful as it is less expensive than experiments.

Acknowledgement

The first author is thankful to Professor Ikeda and Professor Umeda for providing the hull data used in their experiments. Also it is author's pleasure to thank Professor Katayama for his helpful advice.

References

1. Y. Ikeda, N. Umeda and N Tanaka (1988) *Effect of Forward Speed on Roll Damping of a High-Speed Craft*, J. Kansai Society of Naval Architects, Japan, No. 208
2. T. Hishida (1954) *Studies of the Wave Making Resistance for the Rolling of the Ships (Report 6. The effect of motion ahead on the wave resistance for the rolling)*, J. Zosen Kiokai, 87
3. I. Watanabe (1977) *On the Effect of the Forward Velocity on the Roll Damping Moment*, Papers of Ship Research Institute, No. 51
4. T. Hanaoka (1960) *Non-Uniform Theory of Wave-Making on Low Aspect-Ratio Lifting Surface*, 10th Japan National Congress for Applied Mechanics
5. Y. Ikeda, Y. Himeno, N. Tanaka (1978) *A Prediction Method of Ship Roll Damping*, Report No. 00405, Dept. of Naval Architecture, University of Osaka Prefecture
6. T. Sarkar, D. Vassalos (2000) *A RANS Based Technique for Simulation of the Flow Near a Rolling Cylinder at the Free Surface*, J. Marine Science & Technology, Vol. 5, pp 66-77
7. K. B. Salui, T. Sarkar, D. Vassalos (2000) *An Improved Method for Determining Hydrodynamic Coefficients in Roll Motion Using CFD techniques*, Ship Technology Research, Vol. 47, No. 4
8. T. D. Blacker, M. B. Stephenson (1991) *Paving: A New Approach to Automated Quadrilateral Mesh Generation*, Int. J. for Numerical Methods in Engineering, Vol. 32, pp 811-847

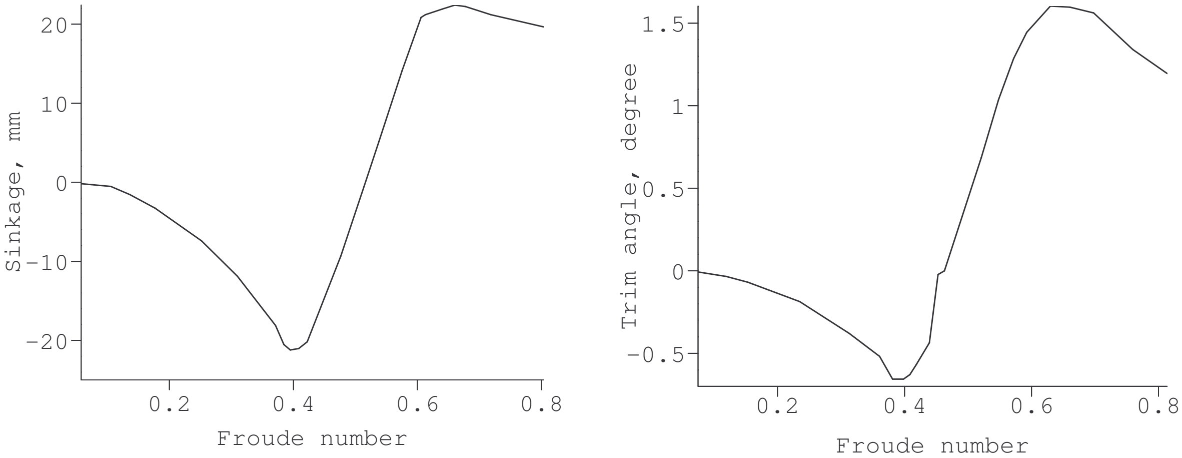

Figure 4: Vertical attitude (left) and trim angle (right) of the model

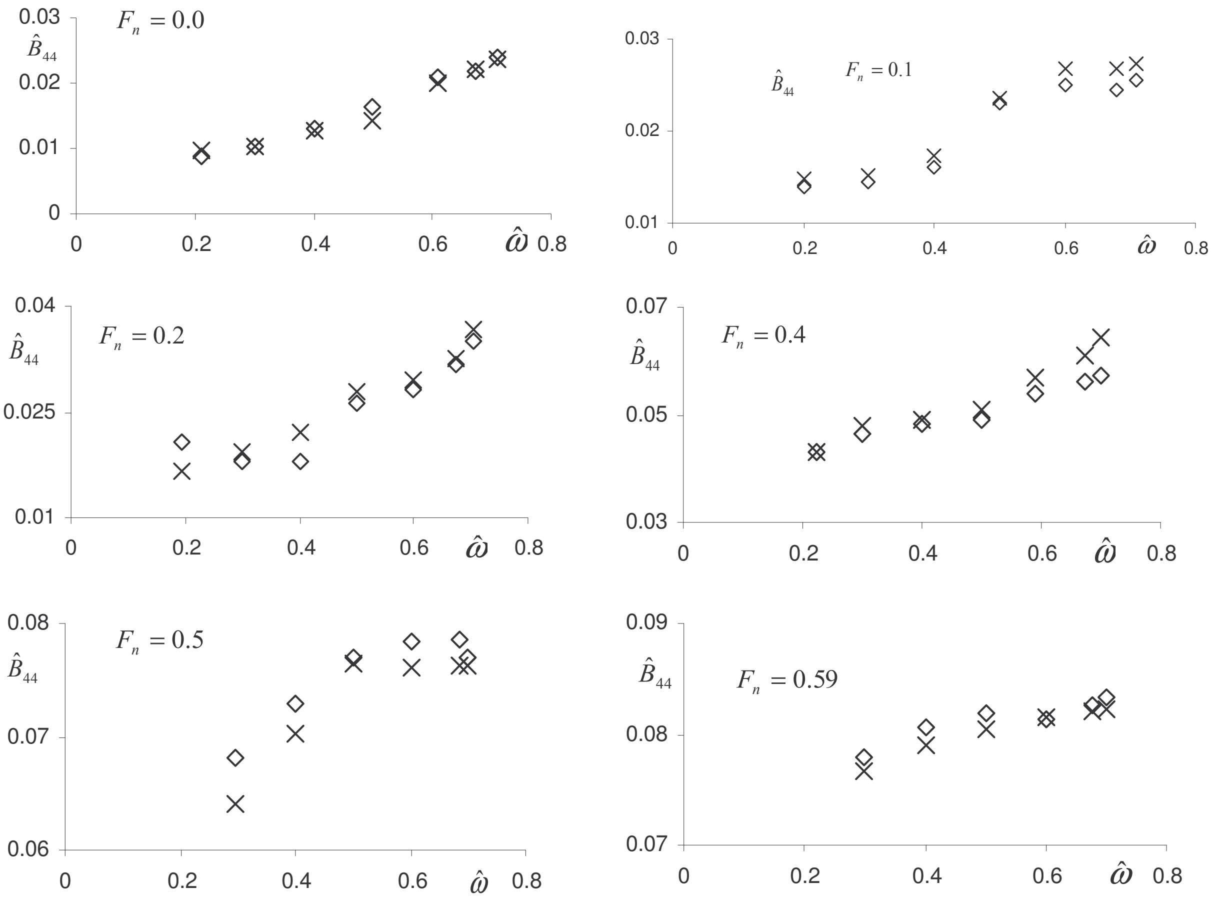

Figure 5: Damping moment coefficient depending on frequency at constant forward speed and amplitude of rolling $\theta_a = 10^0$: ◊ experiments by Ikeda et al. [1], × present calculations

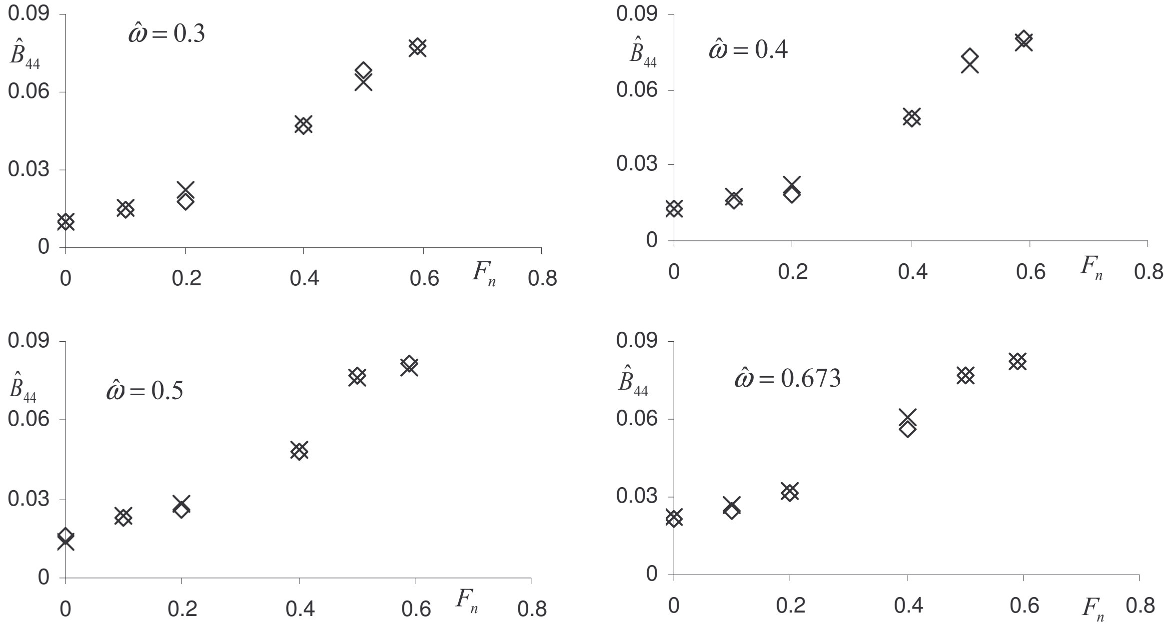

Figure 6: Damping moment coefficient for the variation of forward speed at constant frequency and amplitude of rolling $\theta_a = 10^0$: ◊ experiments by Ikeda et al. [1], × present calculations

Unsteady flow simulation around a moving body by an unstructured Navier-Stokes solver

Yohei Sato*, Takanori Hino* and Munehiko Hinatsu*

*National Maritime Research Institute, Center for CFD Research,
6-38-1,Shinkawa, Mitaka, Tokyo, 181-0004, JAPAN
E-mail: satoyoh@nmri.go.jp, hino@nmri.go.jp, hinatsu@nmri.go.jp

I. INTRODUCTION

In recent years numerous attempts have been made to develop computational methods for viscous flows around a ship and many designers become to use CFD for designing hull forms. Moreover, it is getting feasible to simulate a flow around a ship with complex appendages.

To solve a flow around a complex body, several methods have been proposed. They include a multi block method, a Chimera overlapping grid method or an unstructured grid method. In terms of grid generation, a multi block method needs many efforts and it is difficult for general users. A Chimera overlapping grid method is inaccurate in the conservation property and costs CPU time for interpolation between grids. An unstructured grid method is expected to be the most general approach.

CFD is also requested to solve a flow around a moving complex body, for example a flow around a rotating propeller, a rudder and other appendages.

The objective of this study is to develop an unsteady flow simulation method around a moving body using an unstructured grid. As the first step of validation, two-dimensional simulations are conducted and compared with experimental data.

The flapping foil experiment[1][2] was carried out by the Marine Hydrodynamics Laboratory at Massachusetts Institute of Technology (MIT). The purpose of the experiment was to determine the response of a two-dimensional hydrofoil subject to vertical gusts at high reduced frequency. A large stationary hydrofoil is mounted in the test section on the centerline of the tunnel. In the upstream, there are two small hydrofoils (NACA0025) symmetrically offset from the centerline that are driven to pitch in phase (Figure 1). Because the upstream foils flap in phase, their vortex sheets create a vertical or transverse sinusoidal gust along the centerline. Experimental data was measured near the stationary foil and on the foil itself. This experiment data is occasionally used for a validation of CFD [3][4].

A three-dimensional unsteady incompressible Navier-Stokes algorithm based on artificial compressibility was used to simulate this flapping foil problem. A comparison with the measured data for the pressures and velocities on the bounding box and the surface of the stationary foil are presented for the steady case. In addition time histories and a harmonic analysis at the same locations are examined for the unsteady case.

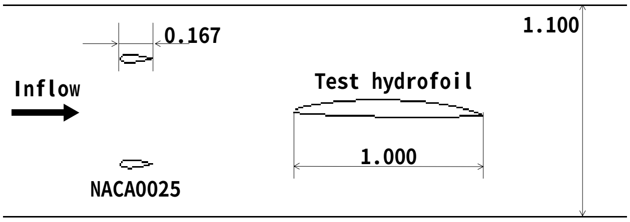

Figure 1: Experimental setup

II. NUMERICAL METHOD

In this section, we briefly summarize a numerical method used. A finite-volume method with an unstructured grid for three-dimensional Navier-Stokes equations, SURF[5], is employed.

In order to calculate a flow around flapping foils, a moving grid system is employed.

The governing equations are three-dimensional incompressible Navier-Stokes equations. In case of two-dimensional flapping foil simulation, two-dimensional analysis is sufficient. However, the objective of this study is to validate three-dimensional Navier-Stokes solver, therefore the three-dimensional Navier-Stokes equations are employed.

Spatial discretization is based on a finite-volume method. A solution domain is divided into cells. A cell shape is polyhedron: tetrahedron, hexahedron, prism or pyramid. The cell-centered layout is adopted, in which the flow variables (p,u,v,w) are defined at a center of each cell. The control volume for each cell is a cell itself.

The artificial compressibility approach proposed by Chorin [6] is employed in the present scheme to couple the velocity and pressure fields. Usually, in this approach the term $\frac{1}{\beta}\frac{\partial p}{\partial t}$ is added to the continuity equation, where β is a parameter of artificial compressibility. With this modification, however, the system of equations recovers incompressibility only at the steady state limit and transient solution does not necessarily satisfy the continuity condition. This problem can be overcome by using the dual time frames, one for physical time t and the other for pseudo time τ and the artificial compressibility is introduced in the latter frame. At each physical time step, the pseudo time integration is used to get the pressure and velocity field which satisfies the divergence free condition for velocity.

The equations to be solved have the form as follows:

$$\frac{\partial V_i q_i}{\partial t}+\frac{\partial V_i q_i^*}{\partial \tau}+\sum_{faces}\left(E-E^v\right)=0 \tag{1}$$

where

$$q_i=\frac{\int_{Vi} q^n dV}{Vi},$$

$$E=\tilde{e}S_x+\tilde{f}S_y+\tilde{g}S_z,\ E^v=e^vS_x+f^vS_y+g^vS_z,$$

$$q=\begin{bmatrix}0\\u\\v\\w\end{bmatrix},q^*=\begin{bmatrix}p\\u\\v\\w\end{bmatrix},\tilde{e}=\begin{bmatrix}\beta u\\u\left(u-u_g\right)+p\\u\left(v-v_g\right)\\u\left(w-w_g\right)\end{bmatrix},$$

$$\tilde{f}=\begin{bmatrix}\beta v\\v\left(u-u_g\right)\\v\left(v-v_g\right)+p\\w\left(w-w_g\right)\end{bmatrix},\tilde{g}=\begin{bmatrix}\beta w\\w\left(u-u_g\right)\\w\left(v-v_g\right)\\w\left(w-w_g\right)+p\end{bmatrix}$$

$$e^v=\begin{bmatrix}0\\\tau_{xx}\\\tau_{xy}\\\tau_{xz}\end{bmatrix},f^v=\begin{bmatrix}0\\\tau_{xy}\\\tau_{yy}\\\tau_{yz}\end{bmatrix},g^v=\begin{bmatrix}0\\\tau_{xz}\\\tau_{yz}\\\tau_{zz}\end{bmatrix},\tau_{ij}=\left(\frac{1}{Re}+\nu_t\right)\left(\frac{\partial u_i}{\partial x_j}+\frac{\partial u_j}{\partial x_i}\right)$$

V_i is a cell volume, S_x,S_y,S_z are area vector of each direction. $\left(u_g,v_g,w_g\right)$ are $\left(x,y,z\right)$-components of the grid velocity which is the velocity of grid movement. E and E^v are inviscid and viscous flux, respectively. $Re\left(\equiv UL/\nu\right)$ is the Reynolds number where ν is the kinematic viscosity, U and L are the reference velocity and length, respectively. ν_t is the non-dimensional kinematic eddy viscosity which is determined by the Spalart-Allmaras one equation model[7].

The inviscid fluxes are evaluated by an upwind scheme based on the flux-difference splitting of Roe [8]. The viscous fluxes are discretized by second order centered differencing [9].

Time marching of Eq. (1) is made separately for the physical time t and for the pseudo time τ. The first order accurate Euler implicit scheme is used for τ. On the other hand, three level backward differencing is used for physical time marching in order to maintain second order accuracy in time. Thus, the equation to be solved can be expressed as

$$\begin{aligned}&\frac{3V_i^{n+1}q_i^{n+1,m+1}-4V_i^nq_i^n+V_i^{n-1}q_i^{n-1}}{2\Delta t}\\&+\frac{V_i^{n+1}q_i^{*\,n+1,m+1}-V_i^{n+1}q_i^{*\,n+1,m}}{\Delta\tau}\\&+\sum_{Faces}E^{n+1,m+1}-\sum_{Faces}E^{v,n+1,m+1}=0\end{aligned} \tag{2}$$

where the superscript ^{n} denotes the time step for physical time marching and ^{m} for the pseudo time marching. Δt and $\Delta\tau$ are the physical and pseudo time increment, respectively.

At each time step, only pseudo time marches until the solutions are converged in pseudo time, i.e. $q^{*\ n+1,m+1}=q^{*\ n+1,m}$ or the continuity equation is satisfied.

III. SIMULATIONS

A. Steady State Simulations

In case of steady-state computations, the foils were fixed. Hereafter the reference length is set as chord length of the test hydrofoil. Reynolds number is 3.78x10^6 (based on the test hydrofoil chord). The turbulence trip points are set at 5% chord downstream from leading edge of each foil.

Computational grids and number of cells are shown in Figure 2 and Table 1. The position of x=0.0 is at the test-hydrofoil leading edge. The grid is composed of the combination of an unstructured grids and structured grids. The C-type structured grids are generated around the foils and the remaining area is tessellated with unstructured grid.

Three grids of different densities are used to evaluate grid dependence. The number of the fine-grid cells is four times larger than that of the medium-grid cells. The number of the medium-grid cells is also four times larger than that of the coarse-grid cells.

Table 1: Computational grids.

	Fine	Medium	Coarse
Minimum grid spacing*	5.0×10^{-7}	1.0×10^{-6}	5.0×10^{-5}
Total number of cells	72,812	19,048	5,283
Hexahedron cells	52,480	12,960	3,200
Prism cells	20,332	6,088	2,083

* Spacing in the direction of boundary layer

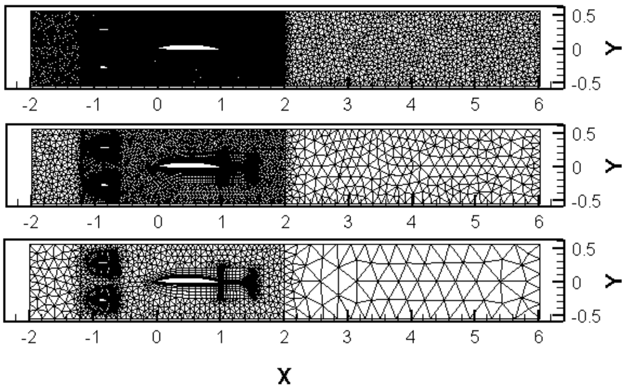

Figure 2: Computational grid. The fine grid is above, the medium grid is in the middle and the coarse grid is below.

A comparison of measured and computed surface pressure distributions of the test hydrofoil is shown in Figure 3. They agree well with one another and there is only slight grid dependence on computed results.

Velocity profiles on three sections of the test hydrofoil are shown in Figure 4. Measured data and computed results do not agree well in case of the suction side of x/c=0.972 and 1.000. Flow separation observed in the measurement is underestimated in the computations. It is presumed that the turbulence model is the cause of this disagreement. In all case of Figure 4, the fine grid solutions are better than coarse grid solutions. In the section of x/c=0.388 and other pressure side, the fine grid solution agrees reasonably well with the measured profile.

Velocity profiles and static pressure profiles on upstream and downstream sections are shown in Figure 5 and Figure 6. The upstream section is 0.259 chord length in front of the leading edge and the downstream section is 0.108 chord length downstream from the trailing edge. The measured and computed velocity profiles agree well including the test hydrofoil wake zone.

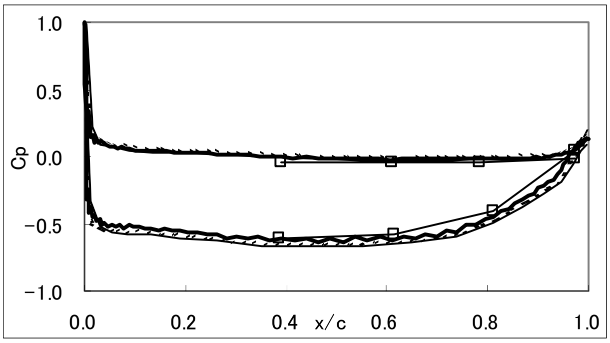

Figure 3: Steady state Cp distribution on the test hydrofoil. Hereafter, squares are measured data. Bold lines solid lines and broken lines are the results of the fine grid, medium grid and the coarse grid, respectively.

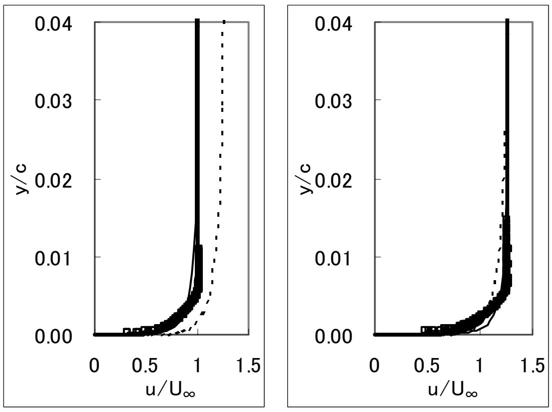

x/c=0.388 (Left: Pressure side, Right: Suction side)

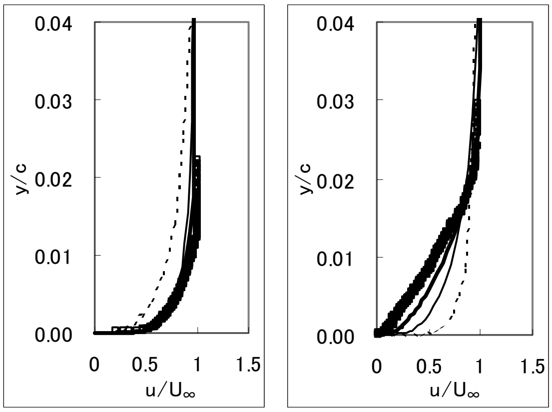

x/c=0.972 (Left: Pressure side, Right: Suction side)

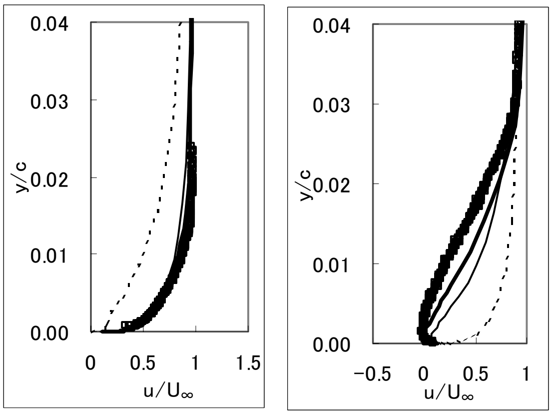

x/c=1.000 (Left: Pressure side, Right: Suction side)

Figure 4: Steady state velocity profiles.

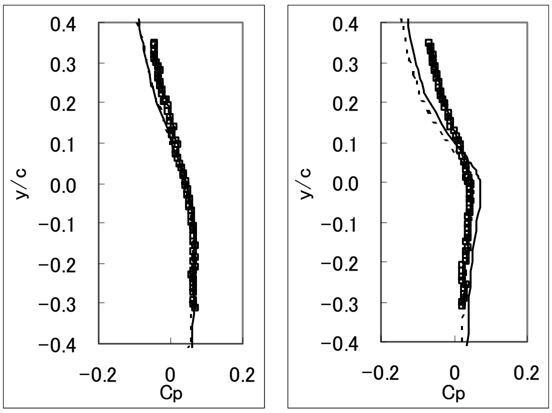

Figure 5: Steady state static pressure (Left: Upstream, Right: Downstream)

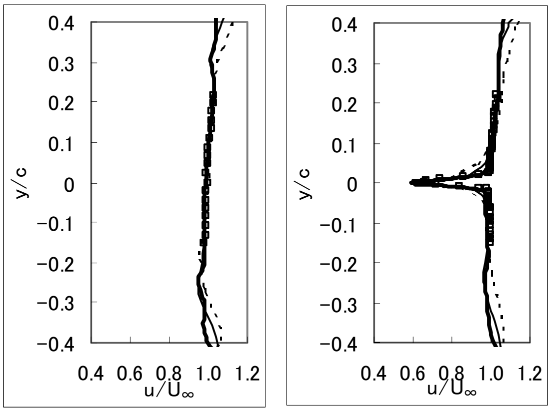

Figure 6: Steady state velocity profile (Left: Upstream, Right: Downstream)

B. Unsteady simulations

In case of unsteady simulations, the flapping foils move in pitch at a reduced frequency of 3.62 based on the half-chord of the test hydrofoil. Reynolds number is $3.78\text{x}10^{6}$ based on the stationary foil chord.

A nondimensional time step is set $8.73\text{x}10^{-3}$, which corresponds to 1/100 of the period of flapping motion. In each time step, 50 times of Newton iterations are performed.

A moving grid method is employed to simulate the flapping motion (Figure 7). The amplitude of the flapping angle is 6 degrees. Only the structured grids around the flapping foils are deformed in accordance with the flapping foil movement and the unstructured grids keep stationary. The medium grid and the coarse grid in Figure 2 are used for computation.

A comparison of measured and computed mean surface pressure distributions is shown in Figure 8. They agree well each other. Slight grid dependence is found in computed results, like steady state simulation. Figures 9 and 10 show the first-harmonic amplitude and the phase of pressure distribution on the suction side and the pressure side, respectively. The measured and computed amplitude on both sides agree reasonably well, while those of phase agree only in global trend.

The mean velocity profiles, the first-harmonic amplitude and phase on two sections of the test hydrofoil are shown in Figures 11 and 12. Similarly to the steady state simulations, the measured and computed mean velocity profiles agree well on the pressure side and suction side of x/c=0.388. In all cases, the measured and computed phases agree in the region far from the wall.

The mean static pressure profiles on the upstream and downstream sections are shown in Figure 13. The discrepancy between the measured and the computed results is nearly the same quantity as steady state cases.

A snapshot of the magnitude of velocity distribution is shown in Figure 14. The fluctuation of velocity propagates to downstream through the unstructured grid.

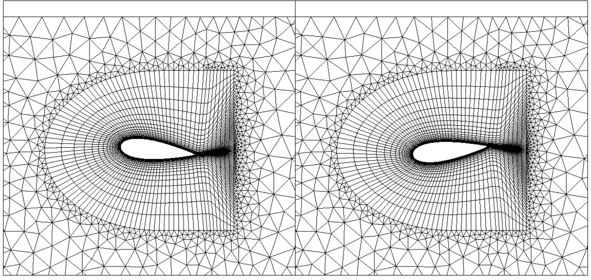

Figure 7: A moving grid method. These figures are in the case of medium grid at ±6 degrees flapping angle.

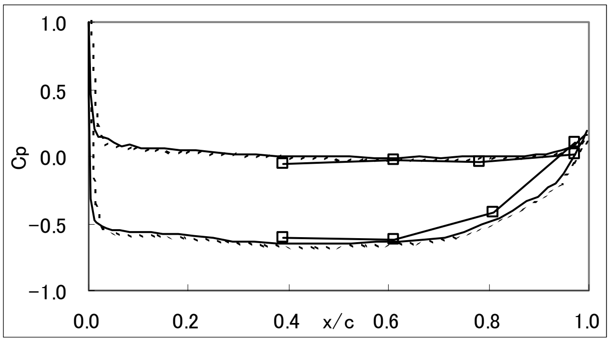

Figure 8: The mean Cp distribution on the test hydrofoil. Hereafter, squares are measured data. Solid lines and broken lines are the results of the medium grid and the coarse grid, respectively.

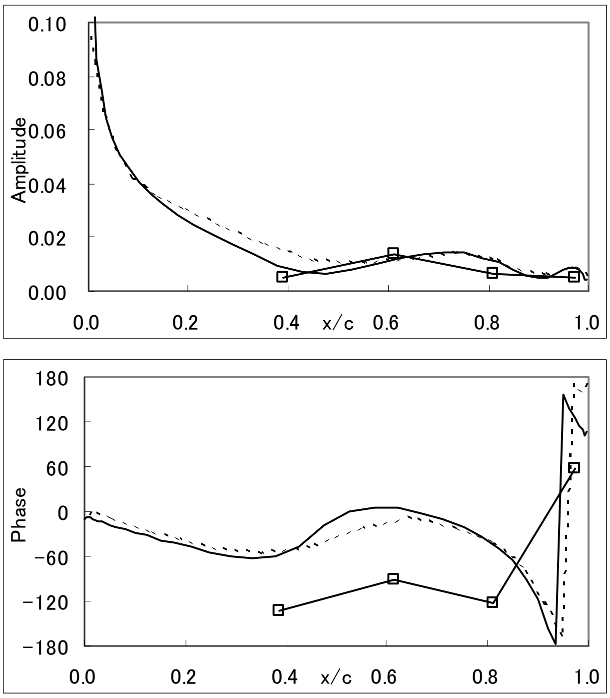

Figure 9: The amplitude and phase of Cp on Suction side

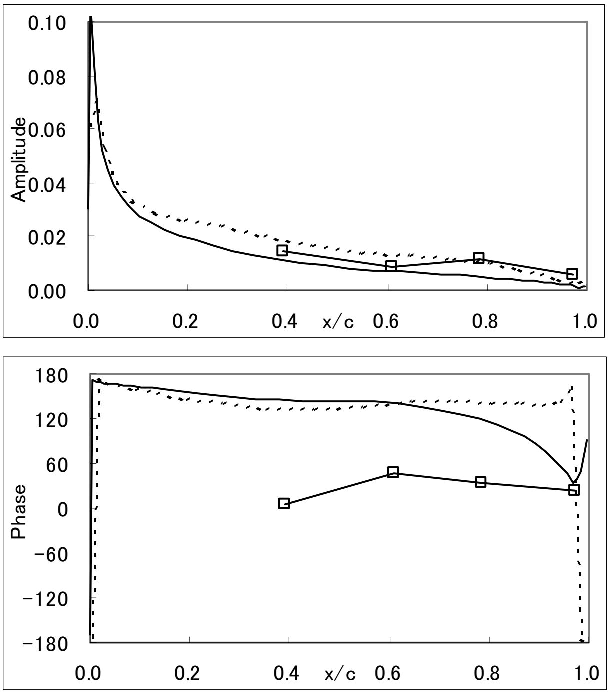

Figure 10: The amplitude and phase of Cp on Pressure side

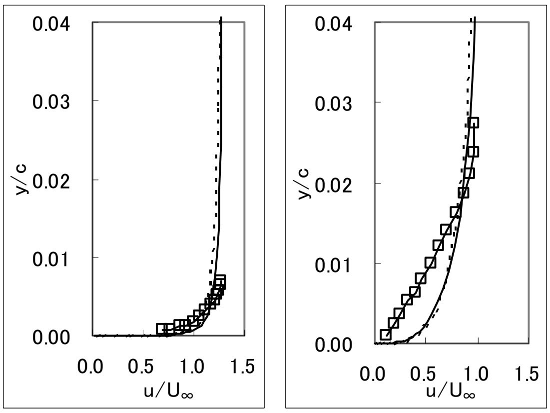

Suction side (Left: x/c=0.388, Right: x/c=0.972)

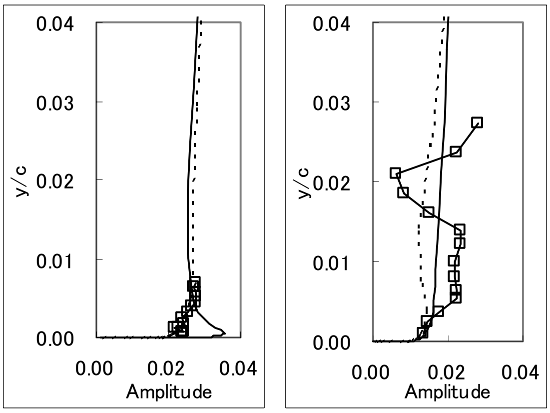

Suction side (Left: x/c=0.388, Right: x/c=0.972)

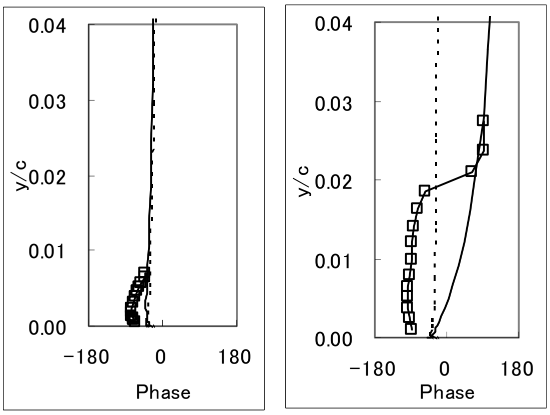

Suction side (Left: x/c=0.388, Right: x/c=0.972)

Figure 11: Mean velocity, amplitude and phase on suction side.

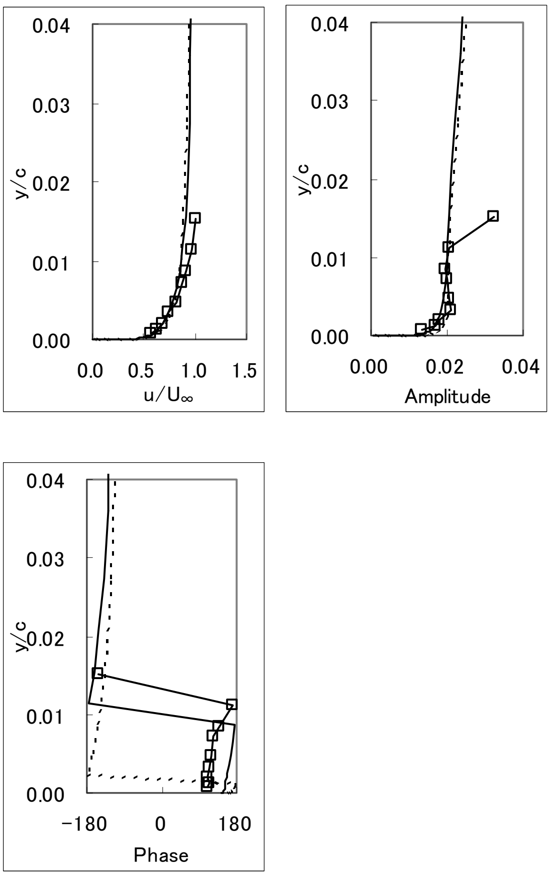

Figure 12: Mean velocity, amplitude and phase on pressure side. (x/c=0.972)

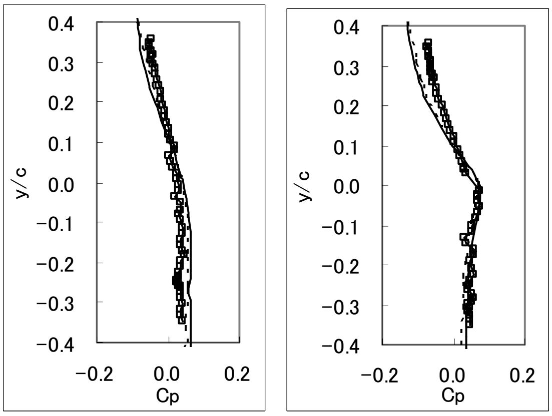

Figure 13: Mean static pressure (Left: Upstream, Right: Downstream)

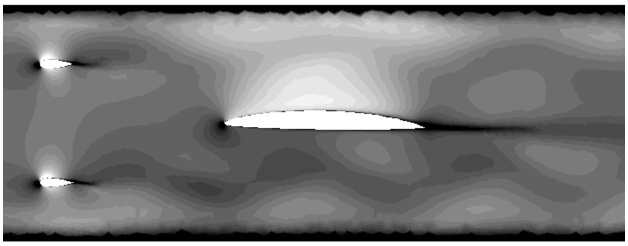

Figure 14: Unsteady velocity $|\mathbf{u}|$ distribution. (Medium grid)

IV. CONCLUSIONS

An unsteady incompressible Navier-Stokes equation solver based on the artificial compressibility hypothesis has been developed. Moving grid method is employed to simulate the flapping motion.

In steady state simulation, three grids of different densities are used to evaluate the grid dependence and the finest grid gives the best results.

In unsteady simulation, two grids of different densities, medium and coarse grids, are used. Computed mean velocity and first-harmonic amplitude agree well with the measured results. The disagreement of the phase is open as the future study.

REFERENCES

[1] J.Q.Rice, "Investigation of A Two Dimensional Hydrofoil in Steady and Unsteady Flows," M.S. Thesis, Massachusetts Institute of Technology, June 1991
[2] P.M.Delpero, "Investigation of Flows around a Two Dimensional Hydrofoil Suject to A High Reduced Frequency Gust Loading," M.S. thesis, Massachusetts Institute of Technology, February 1992
[3] L.K.Taylor, et al.,"Time Accurate Incompressible Navier-Stokes Simulations of the Flapping Foil Experiment," Proc. 6th Inter. Conf. on Numerical Ship Hydrodynamics, Iowa, 1993, pp.13_11-18
[4] E.Paterson and F.Stern," Computation of Unsteady Viscous Flown with Application to the MIT Flapping-Foil Experiment," Proc. 6th Inter. Conf. on Numerical Ship Hydrodynamics, Iowa, 1993, pp.13_5-10
[5] T.Hino, "A 3D Unstructured Grid Method for Incompressible Viscous Flows," J. Soc. of Naval Archit. Japan, Vol 63, 1997,pp.455-459
[6] A.J.Chorin, "A Numerical Method for Solving Incompressible Viscous Flow Problems," J. Comput. Pys., Vol.2, 1967, pp.12-26
[7] P.R.Spalart, et al., "A One-Equation Turbulence Model for Aerodynamic Flows", La Recherche Aèrospatiale, No.1, 1994, pp.5-21
[8] P.L.Roe, "Characteristic-based scheme for the euler equations," Ann. Rev. Fluid Mech., Vol.18, 1986, pp.337-365
[9] T. Hino, "Navier-Stokes Computations of Ship Flows on Unstructured Grids," Proc. of the 22nd Symp. on Naval Hydro., 1998, pp.463-475

Towards an Adaptive Transient Cartesian Grid Method with VoF for Floating Bodies

Daniel Schmode, d.schmode@tu-harburg.de
Gerhard Jensen, g.jensen@tu-harburg.de
AB 3-13 of TU Hamburg-Harburg, Lämmersieth 90, 22305 Hamburg

1 Introduction

Prediction of ship-motions is important to improve seakeeping and maneuvering abilities. State of the art in simulation of ship motions are strip-methods based on potential theory with empirical corrections for the viscous effects. In the last years results of RANS computations for seakeeping and maneuvering were presented by various authors. One approach presented e.g. by Cura uses a static grid which is moved with the body. Special grids which had to be fine in a wide area of possible free-surface (FS) positions, Fig.1, are required. This yields too large cell numbers and large computational effort. An alternative approach is the moving grid technique [3], where the grid is warped according to the motion of the body, Fig.2. For large motions, the cells possibly deform strongly which may causes large discretization errors. A relatively new approach is the overlapping grid technique. Here a foreground-grid which is fine near the body and a background-grid which is fine in the area of the FS are used. The foreground-grid moves with the body and the background-grid is fixed, Fig.4. In the overlapping area the values are interpolated from one grid to the other and back. This technique seems to be promising, even though the conservation of mass is not trivial. But again, a lot of cells are wasted in the area of possible free-surface positions. Other approaches use sliding interface technique, Fig.3, [3]. To allow rotation the inner grid has to be a cylinder in 2d and a sphere in 3d. Thus grid generation is difficult.

We outline here another approach which attempts to avoid these problems. We use a Cartesian grid method (CGM) with immersed boundaries. The relatively coarse initial grid will be automatically refined near the floating body to resolve boundary-layer effects sufficiently and near the free surface to keep numerical diffusion of the two phases low. The grid will be adapted automatically as follows: When the body and the FS move during the computation the grid will be refined in regions where the body and the FS move to, and “coarsened again” in areas where the higher resolution is no longer required. The advantage of this procedure is, that in every time-step during the computation the grid is fine just where it is needed (Fig.5). This keeps the number of cells low and saves computation time.

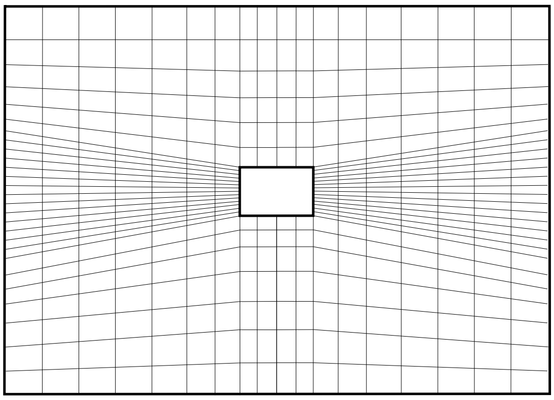

Figure 1: Example for static grid technique

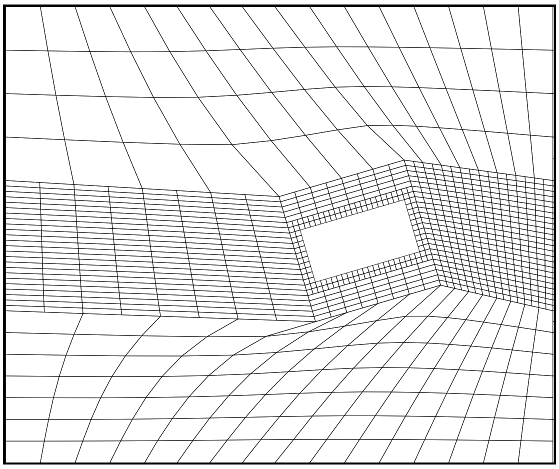

Figure 2: Example for moving grid technique

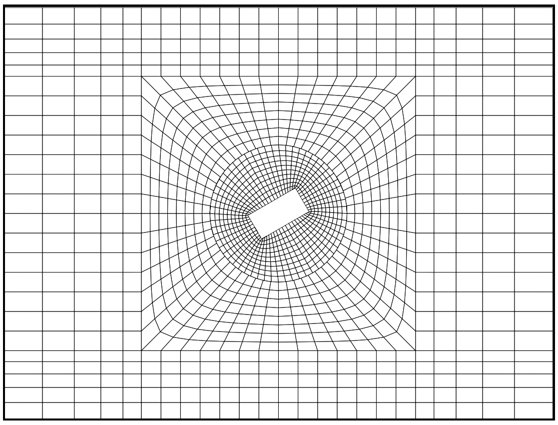

Figure 3: Example for sliding interface technique

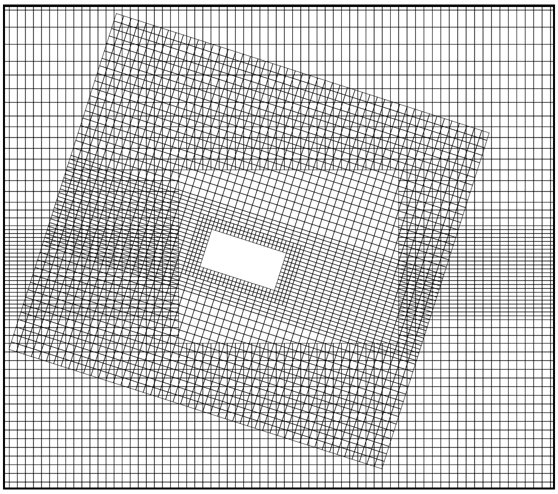

Figure 4: Example for overlapping grid technique

2 Cartesian grid methods

In literature a lot of different Cartesian grid methods were presented. In aeronautical context CGM's were developed and successfully used in the last decade, [1],[6]. These methods are often optimized for compressible flows and do not treat free surfaces.

Dommermuth, [2], and Sussmann, [4], presented different CGM computations with free surface for ships with breaking bow waves. They used a so-called body-force technique to model the body boundary-condition. First results show good agreement in the bow-region, but some numerical problems were reported.

Here the approach presented by Ye et al. [7], is pursued. Ye developed an algorithm which uses trapezoidal cells near the body. The basic principle is simple. Cells cut by the body were treated as follows: if the cell-center is outside the body, the part inside the body is discarded, Fig.6a. If the cell center lies inside the body the cell is absorbed by the neighbor (Fig.6b). Very small cells requiring small time-steps can be avoided that way.

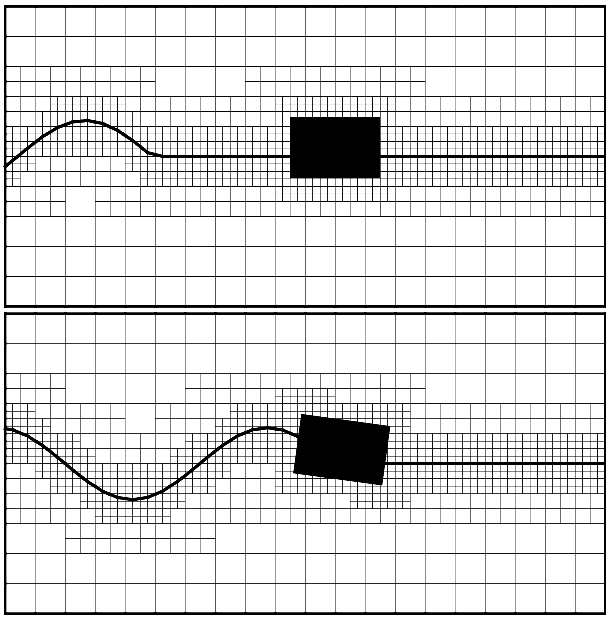

Figure 5: Principle of transient adaptive CGM

Fig.6c shows a special case. Cell no.3 is cut and the east neighbor is absorbed by the cell no.1. In this case the cell no.1 has two west neighbors (no.2 and no.3). This configuration leads to an unstructured grid. Thus an appropriate data structure is required (see below).

Nevertheless approximations in these cases are difficult. Ye reports that he could achieve second-order approximation by using a polynomial interpolation for the trapezoidal cells near the body. This is desirable because important features of the flow occur especially in this region.

Fig. 7 shows a cut-cell configuration for the a simple geometry.

3 Transient adaptive grid technique

Generally, adaptive grid technique means that the solver automatically makes local refinements depending on some refinement criteria (e.g. truncation error). For steady computations, this is relatively simple and presented by many authors. For transient computations the flow field is changing and there appear regions where the grid resolution is higher than necessary. To avoid waste of computation time the grid should be "coarsened" there. Thus a special coarsening procedure is necessary.

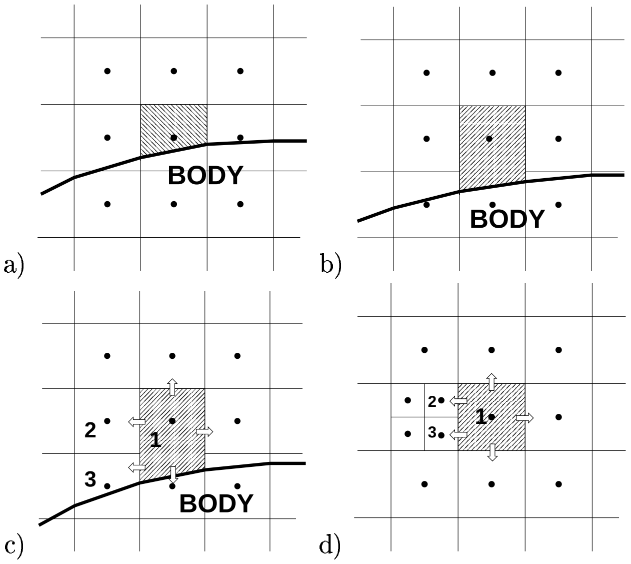

Figure 6: Cut-Cell-Algorithem

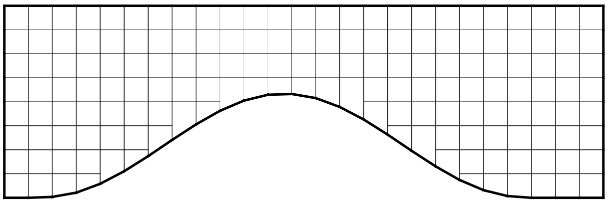

Figure 7: Cut-cell-configuration for bottom bump

4 Data structure

This approach leads to unstructured grids. Some authors propose a quad-tree or oct-tree structure. The advantage of this data structure is a lower memory consumption. The disadvantage is the higher computational effort. Every time the neighbor is demanded it has to be searched by a more or less costly procedure.

Here a data structure where every cell has pointers indicating the neighbor cells is chosen. This requires more memory but saves computation time. We believe this is a good choice because for time depending problems memory is often not the bottle neck, but computation time limits the possible resolution.

5 Numerical techniques

We use a finite-volume discretization with co-located arrangement to solve the Reynolds-Averaged Navier-Stokes Equations (RANS). The Midpoint rule for volume and surface integrals is a natural choice. Face center values are approximated by a blending of upwind and central differencing scheme using deferred correction. For trapezoidal cells a special treatment is used. Mass and momentum equation are coupled by the SIMPLE algorithm. The Implicit Euler scheme is used for time integration. The free surface is treated by the Volume-of-Fluid technique.

Local refinement and the cut-cell algorithm lead to unstructured grids. This requires a special data-structure and appropriate solvers. Conjugate-Gradient algorithms are well proven for unstructured grids. A CG for pressure correction and an Bi-CG-stabilized for the other equations is used here.

The k-ε-turbulence model is implemented.

All methods used here are described more detailed in [5].

6 First results

A classic test case for free-surface flows is the dam-break. Fig.8 shows the computation of the breaking dam problem with an adaptive CGM with refinement and coarsening. Here the cells near the free surface were refined. Other refinement criteria such as the truncation error are possible.

Fig.9 shows a computation for a bottom bump with the cut-cell algorithm. Pressure and velocity vectors are plotted. Pressure distribution and velocity field seem to be realistic.

7 Next steps

After intensive testing and improving the cut-cell-algorithm the next steps could be as follows:

- couple cut-cell-algorithm with VoF method
- compute forces on floating bodies
- implement equations of motion
- validation
- testing and optimizing
- implement multi grid technique
- if results are promising: upgrade to 3D ...

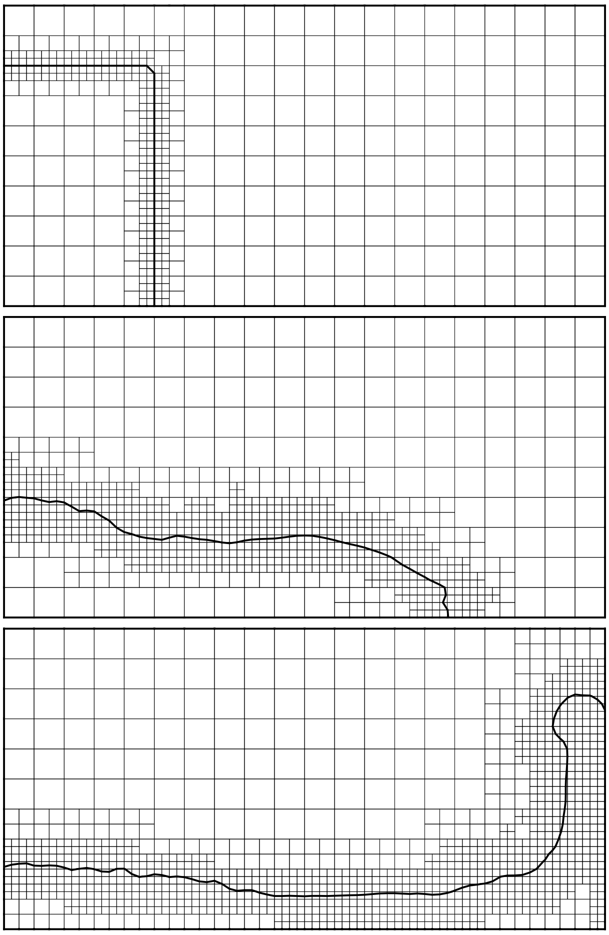

Figure 8: Dam break computed with transient adaptive CGM

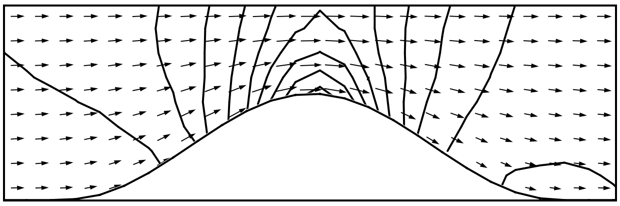

Figure 9: Bottom-bump with cut-cell-algorithm

References

[1] F. DEISTER & E.H. HIRSCHEL (1999)
Adaptive Cartesian/Prism Grid Generation and Solutions for Arbitrary Geometries
AIAA 99-0782

[2] D.G. DOMMERMUTH, G.E. INNIS, T. LUTH, E.A. NOVIKOV, E. SCHLAGETER, J.C. TALCOTT (1998)
Numerical Simulation of Bow Waves
ONR 1998

[3] I. HADZIC, Y.XING, M. PERIC (2002)
Simulation turbulenter Strömung und strömungsbedingter Bewegung schwimmender Körper
TUHH-Report 618

[4] M. SUSSMANN, G. DOMMERMUTH (2000)
The numerical Simulation of Ship Waves using Carthesian Grid Methods
ONR 2000

[5] J.H. FERZIGER, M. PERIC (1997)
Computational Methods for Fluid Dynamics
Springer

[6] Z.T. WANG, R.F. CPHEN, N. HARIHARAN, A.J. PRZEKWAS (1999)
A 2^N Tree Based Automated Viscous Cartesian Grid Methodology for Feature Capturing
AIAA 99-3300

[7] T. YE, R.MITTAL, H.S. UDAYKUMAR, W. SHYY (1999)
An Accurate Cartesian Grid Method for Viscous Incompressible Flows with Complex Immersed Boundaries
J. Comp. Physics 156, pp.209-240

Viscous-Flow Computations at Full-Scale Ship Reynolds Numbers Using the RANS Solver FINFLO

Juha Schweighofer[1]

Ship Laboratory, Helsinki University of Technology, Espoo, Finland

1 Introduction

Numerical investigations of turbulent free-surface flows are usually carried out at the Reynolds number of a model-scale ship. The results obtained must be scaled to full scale, which might cause errors in the case of new vessel types where the scaling mechanisms are not known. Computations of full-scale ships are attractive as no scaling is necessary, and the allowances may be reduced. The shape of the hull and the propeller may be optimized with respect to the proper flow around the ship. Additionally, computations of full-scale ships will serve as supplement to model testing as more insight in the flow field and the scaling mechanisms is obtained. Existing extrapolation techniques regarding the evaluation of the final power of a ship, e.g. the ITTC-57 or the ITTC-78 extrapolation methods, and novel ones may be investigated with respect to novel ship types.

Computations of turbulent flows solving the RaNS equations at full-scale ship Reynolds numbers are presented in the following references: *Ju and Patel (1991,1994), Tzabiras (1992,1993), Ishikawa (1994), Schmitt (1997), Eca and Hoekstra (1997,2000), Schweighofer (1997,2002,2003a,2003b), Dolphin (1997), 6 from Larsson et al. (2000), Chen et al. (2001), Starke (2001), Chao (2001).*

Recently, at full-scale ship Reynolds numbers, turbulent free-surface flows have been computed using the moving grid-technique without the use of wall functions by *Schweighofer (2002,2003a,2003b).*

Based on the given references, it may be concluded that, nowadays, full-scale computations of turbulent ship flows are possible to a certain degree. Full-scale RaNS computations of ship flows taking into account the entire physics around a ship, e.g. the hull roughness, the entire boundary layer, the free surface, the propeller and appendages, and sinkage and trim have not been presented yet. Nevertheless, a big step forward is done in order to reach this final goal. In the European-Union project, EFFORT, *Verkuyl and Raven (2003)*, several existing ships are being computed at model- and full-scale ship Reynolds numbers. Features as the turbulent boundary layer, the free surface, the propeller-hull interaction, appendages and complex geometries are taken into account. A very sorrowful verification and validation of the computed results is made possible by the model- and full-scale measurements conducted within this project.

The recent publications and the results presented in this abstract indicate that numerical difficulties in association with full-scale computations of ships may be overcome. With respect to numerical difficulties, full-scale computations of ships may be carried out with confidence. Nevertheless, the validation of the obtained results remains still a problem. Experimental results for such high Reynolds numbers are very rare or difficult to obtain, and the validation issues are often a combination of several pyhsical phenomena demanding also several models. E.g. at model scale the validation of the resistance is relatively simple as one has to take into account only the proper modelling of the turbulence and the free surface. At full scale, the resistance cannot be measured. Either the thrust or the power of a ship is known. When evaluating the thrust numerically, the results are affected by the used turbulence model, the free-surface model, the hull roughness, and the propeller. Due to the larger amount of

---

[1] Correspondence to: Ship Laboratory, Helsinki University of Technology, Tietotie 1A, FIN 02015 Espoo, Finland, e-mail: juhaschw@nefer.hut.fi, phone: +358 9 451 3503, fax: +358 9 451 4173

models needed at full scale, it is more difficult to evaluate which one is working properly and which one is causing errors.

2 Numerical Method

The computations used the RANSE solver FINFLO. The Reynolds-averaged Navier-Stokes (RANS) equations are iteratively solved by a cell-centered finite-volume method until the steady state is reached. An upwind-type spatial discretization of third-order accuracy without flux limitation is applied to the approximation of the convective terms. The viscous fluxes are evaluated according to a thin-layer approximation being activated in all coordinate directions exept in the case of the flat plate where it is activated only in the cross direction of the flow. The central differencing scheme is used for the calculation of the velocities at the cell surfaces needed for the evaluation of the viscous fluxes. The solution of the discretized equations is obtained using a diagonally dominant alternating direction implicit (DDADI) time integration method with time stepping adjusted depending on a parameter based on local velocities and cell sizes. No wall functions are used. The boundary layer is resolved till the wall. The free surface is evaluated by a moving-grid technique.

3 Results

Flat Plate

A comprehensive list of references and description of the respective investigation and is given in *Schweighofer (1997).*

The computations are carried out using the FINFLO version, FINF2D, for compressible, two-dimensional turbulent flows, *Hoffreń and Siikonen (1992).* The convective fluxes are evaluated by Roe's method.

The Reynolds number of the computations is $R_n = U_\infty \cdot L_{pp}/\nu = 1.296 \times 10^9$. $U_\infty = 66.948$ m/s is the free stream velocity, $L_{pp} = 129.6$ m is the reference length, and ν is the free-stream kinematic viscosity. The Mach number is 0.2. The free-stream turbulence level and the free-stream turbulent viscosity referred to the molecular viscosity are 0.005. The applied turbulence models are the Cebeci-Smith, the Baldwin-Lomax, Menter's k-ω SST, and Chien's low Reynolds number k-ϵ turbulence models. The nondimensional distance of the first node from the wall, y^+, is between 0.45 and 1.7.

The best overall performance is obtained with Menter's SST turbulence model. With respect to the skin friction, Menter's SST, the Cebeci-Smith and the Baldwin-Lomax models give a very good accuracy of about two percent (Table 1) compared with the semi-empirical Engineering Scienes Data (ESD), which are based on measurements over a large range of Reynolds numbers, *Royal Aeronautical Society (1968).* With respect to the evaluation of the skin friction, Chien's turbulence model gives a little poorer result with an accuracy of about 7 percent.

Two-Dimensional Transom Waves

Two-dimensional transom waves behind the model, Ile, (Fig. 1, left), are evaluated in *Schweighofer (2003 a).*

The computations are carried out using the FINFLO version, FINFLO SHIP, for incompressible, three-dimensional turbulent flows. A comprehensive list of references is given in *Schweighofer (2003 a).* Incompressibility of the flow is considered by an artificial compressibility approach. The convective fluxes are evaluated by incompressible flux-difference splitting. The computations are performed using Chien's low Reynolds number k-ϵ turbulence model.

The model is assumed to be infinitely wide in the y-direction (Fig. 1, left). The shape of the bow is a circle segment with radius R and the bottom is flat. The transom is located at the origin of the global Cartesian coordinate system. At the bow, the formation of the bow wave is suppressed. At the transom, the wave height of the free surface is set equal to the draught T. Behind the transom, the free surface may be deformed arbitrarily. The geometrical dimensions of the investigated model are the length overall, $L = 80.00$ m, the length between the perpendiculars, $L_{pp} = 61.16$ m, $R = 58.00$ m, and $T = 4.00$ m. The scale is 1:40.

The computations are carried out at $F_{nT} = U_\infty/(\sqrt{gT}) = 2.8$, and $R_n = 3.732\times10^6$ and 9.442×10^8. $g = 9.81$ m/s^2 is the gravitational constant. At model scale, the initial values of the turbulence level and the nondimensional turbulence coefficient are set to 0.02 and 10.00 in the computational domain and to 0.001 and 0.01 at the outer boundaries (sides 1 and 6). At full scale, the same values are applied but the nondimensional turbulence coefficient is set to 16.5 at the outer boundaries. The turbulence coefficients are made nondimensional with the free-stream molecular viscosity. At model scale, almost everywhere at the wall, $y^+ \approx 0.7$. At full scale, $y^+ \approx 2$.

Using solutions with different free-surface boundary conditions and solutions of the Euler equations, it may be concluded that the wave profiles at model and full scale should be almost the same for this case. This phenomena is reproduced very well in Fig. 2, left. Therefore, the free surface is computed successfully at full scale with the moving grid technique. At full scale, the total resistance coefficient is compared with the one obtained from the computed value at model scale by extrapolation with the ITTC-78 method (Table 1). The pressure resistance coefficient remains almost constant. The form factor is obtained from the computed skin friction resistance coefficient and the ITTC-57 model-ship correlation line at model scale. At full scale, the deviation of the resistance coefficient from the expected value is less than two percent. Therefore, the scaling is reproduced very well. The comparison of the computed turbulent viscosity with the one within the boundary layer of a respective flat plate gives similar magnitudes.

Series 60

The computations are carried out using the FINFLO version, FINFLO SHIP, for incompressible, three-dimensional turbulent flows with Chien's low Reynolds number k-ϵ turbulence model. The free surface is evaluated using the inviscid mirror free-surface boundary conditions, *Schweighofer (2003a)*.

The geometry of the ship is given in Fig. 1, right. The length between the perpendiculars, $L_{pp} = 121.92$ m. $F_{n_{Lpp}} = U_\infty/(\sqrt{gL_{pp}}) = 0.316$, and $R_n = 1.170 \times 10^9$. The initial and free-stream values of the turbulence level and the nondimensional turbulence coefficient are set to 0.000158 and 0.01, respectively. The nondimensional distance of the first node from the wall, y^+, is about 2.2.

In Fig. 2, right, the computed wave profile is compared with the model-scale measurements of Toda and Longo, *Gao (2002)*, and the potential flow computation of *Wyatt (2002)*. Due to the high Froude number, viscosity effects on the wave profile are assumed to be of minor significance. This is confirmed by the result of Wyatt, which agrees very well with the measurements. Therefore, at full scale, the wave profile is expected to be very close to the measurements and the potential-flow result, particularly in the foreship region. The computed wave profile (FINFLO SHIP) is reproduced very well. Only at the stern, it is higher and steeper than the measured ones, and it deviates clearly from the potential flow result as consequence of the influence of the viscosity.

In Table 1, the computed total resistance coefficient is compared with the measurement of *Kim and Jenkins (1981)* extrapolated to full scale using the ITTC-57 method. The agreement of the computed result with the extrapolated experimental one is very good. The deviation of the computed result from the extrapolated one is less than 4 percent. The measured value of Kim and Jenkins is 4.6×10^{-3} for the Reynolds number $R_n = 1.619 \times 10^7$. The ITTC-57 extrapolation method is based on ships of similar form as the one of the Series 60 ship. The respective correlation allowance is 0.4×10^{-3}, *Guldhammer and Harvald (1974)*. The respective value for a rough flat plate is approximately the same, *Schlichting (1979)*. Therefore, no scaling effects are included in the correlation allowance, and the measured total resistance coefficient extrapolated to full scale by the ITTC-57 extrapolation method may be assumed as the resistance of the smooth full-scale ship.

With respect to the computation of turbulent free-surface flows around ships at full-scale ship Reynolds numbers using the moving-grid technique and no wall-functions, the presented results are very encouraging.

Acknowledgement

The work with respect to the computation of the Series 60 ship is a part of the European-Union project, EFFORT - European Full-Scale Flow Research and Technology. The financial support is gratefully acknowledged.

References

CHAO, K.Y. 2001. Numerical Propulsion Tests, *Ship Technology Research - Schiffstechnik*, No. 48, pp. 51-55.

CHEN, Y.J., KOUH, J.S. AND CHAU, S.W. 2001. Computation of Free-Surface Ship Flow at Full-Scale and Model-Scale Reynolds Number Using VOF Method, *Fourth Numerical Towing Tank Symposium*, Hamburg, Germany.

DOLPHIN, G.W. 1997. Evaluation of Computational Fluid Dynamics for a Flat Plate and Axisymmetric Body from Model- to Full-Scale Reynolds Numbers, Master's Thesis, University of Iowa, Iowa City, IA.

ECA, L. AND HOEKSTRA, M. 1997. Numerical Calculations of Ship Stern Flows at Full-Scale Reynolds Numbers, *Twentyfirst Symposium on Naval Hydrodynamics*, National Research Council, pp. 377-391.

ECA, L. AND HOEKSTRA, M. 2000. Numerical Prediction of Scale Effects in Ship Stern Flows with Eddy-Viscosity Turbulence Models, *Twentythird Symposium on Naval Hydrodynamics*, National Research Council, pp. 553-568.

GAO, Q.X. 2002. Numerical Simulation of Free Surface Flow around Ship Hull, *Journal of Ship Mechanics*, Volume 6, Number 3, pp.1-13.

GULDHAMMER, H.E. AND HARVALD, S.A. 1974. Ship Resistance - Effect of Form and Principal Dimensions (Revised), Akademisk Forlag, Copenhagen.

HOFFREŃ, J. AND SIIKONEN, T. 1992. FINF2A: A Multi-Block Navier-Stokes Solver for Steady Two-Dimensional and Axisymmetric Flows, Report B-38, Laboratory of Aerodynamics, Helsinki University of Technology.

ISHIKAWA, S. 1994. Application of CFD to the Estimation of Ship's Viscous Resistance - A Series of Full Hull Forms, Transactions of the West-Japan Society of Naval Architects, No. 87.

JU, S. AND PATEL, V. 1991. Stern Flows at Full-Scale Reynolds Numbers, *Journal of Ship Research*, Volume 35, No. 2, pp. 101-113.

JU, S. AND PATEL, V. 1994. A Numerical Approach for Predicting the Total Resistance and Nominal Wakes of Full-Scale Tankers, *Nineteenth Symposium on Naval Hydrodynamics*, National Research Council, pp. 371-387.

KIM, Y-H. AND JENKINS, D. 1981. Trim and Sinkage Effects on Wave Resistance with Series 60, $C_B = 0.6$, DTNSRDC Report/PSD-1013-01.

LARSSON, L., STERN, F. AND BERTRAM, V. 2000. Gothenburg 2000 - A Workshop on Numerical Ship Hydrodynamics, Department of Naval Architecture and Ocean Engineering, Chalmers University of Technology, Sweden.

ROYAL AERONAUTICAL SOCIETY. 1968. The Compressible Two-Dimensional Turbulent Boundary Layer, Both with and without Heat Transfer, on a Smooth Flat Plate, with Application to Wedges, Cylinders and Cones, Engineering Sciences Data item Number 68020 with amendments A to C March 1988, Engineering Sciences Data Unit, London.

SCHLICHTING, H. 1979. Boundary Layer Theory, 7^{th} edition, McGraw-Hill, New York.

SCHMITT, H. 1997. Advances in Fluid Dynamics - Flows at Large Reynolds Numbers, Computational Mechanics Publications, pp. 251-290.

SCHWEIGHOFER, J. 1997. Evaluation of the Fully Turbulent Flow over a Flat Plate for a Large Range of Reynolds Numbers, Master's Thesis, Report M-226, Ship Laboratory, Helsinki University of Technology.

SCHWEIGHOFER, J. 2002. Investigation of Two-Dimensional Transom Waves Using Inviscid and Viscous Free-Surface Boundary Conditions at Model- and Full-Scale Ship Reynolds Numbers. *5th Numerical Towing Tank Symposium*, Pornichet, France.

SCHWEIGHOFER, J. 2003a. Investigation of Two-Dimensional Transom Waves Using Inviscid and Viscous Free-Surface Boundary Conditions at Model- and Full-Scale Ship Reynolds Numbers. Dissertation, Report M-281, Ship Laboratory, Helsinki University of Technology.

SCHWEIGHOFER, J. 2003b. Viscous-Flow Computations at Full-Scale Ship Reynolds Numbers, *Maritime Research News*, Volume 17, Number 1.

STARKE, B. 2001. A Validation Study of Wake-Field Predictions at Model and Full Scale Reynolds Numbers, *Fourth Numerical Towing Tank Symposium*, Hamburg, Germany.

TZABIRAS, G.D. 1992. A Numerical Investigation of the Reynolds Scale Effect on the Resistance of Bodies of Revolution, *Ship Technology Research - Schiffstechnik*, Volume 39, No. 1, pp. 28-44.

TZABIRAS, G.D. 1993. Resistance and Self-Propulsion Numerical Experiments on Two Tankers at Model and Full Scale, *Ship Technology Research - Schiffstechnik*, Volume 40, No. 1, pp. 20-38.

VERKUYL, J.-B. AND RAVEN, H.C. January 2003. Joint EFFORT for Validation of Full-Scale Viscous-Flow Predictions, *The Naval Architect*.

WYATT, D.C. 2000. Development and Assessment of a Nonlinear Wave Prediction Methodology for Surface Vessels, *Journal of Ship Research*, Volume 44, Number 2, pp. 96-107.

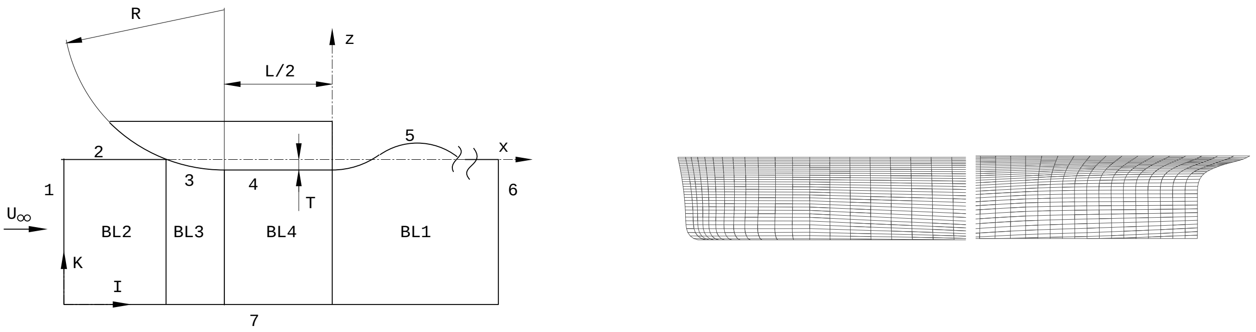

Fig.1: Computed cases at full-scale ship Reynolds numbers. **Left:** Two-dimensional transom waves of the model, Ile. $R_n = 3.732 \times 10^6$ and 9.442×10^8. **Right:** Series 60 ship. $R_n = 1.170 \times 10^9$.

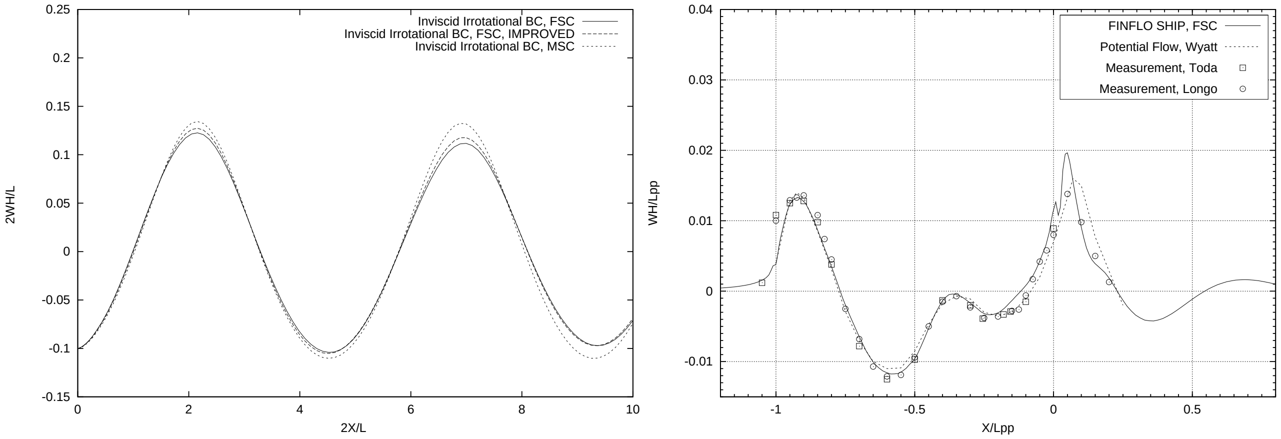

Fig.2: Computed wave profiles at full-scale ship Reynolds numbers. **Left:** Two-dimensional transom waves of the model, Ile. $R_n = 3.732 \times 10^6$ (MSC) and 9.442×10^8 (FSC). $F_{nT} = 2.8$. **Right:** Series 60 ship. $R_n = 1.170 \times 10^9$. $F_{n_{Lpp}} = 0.316$.

Table 1: Computed total resistance cofficients compared with experiment (ESD), extrapolation with the ITTC-78 method, and extrapolation of the measurement of *Kim and Jenkins (1981)* with the ITTC-57 method for full-scale ship Reynolds numbers.

Case	$C_T \times 10^3$	ΔC_T [%]
Flat plate, Cebeci-Smith	1.465	-2.3
Flat plate, Baldwin-Lomax	1.473	-1.8
Flat plate, k-ω SST	1.479	-1.4
Flat plate, k-ϵ, Chien	1.606	7.1
2-D transom waves	8.192	-1.5
Extrap. ITTC-78	8.317	
Series 60	3.463	3.9
Kim and Jenkins (1981), extrap. ITTC-57	3.331	

Hydrofoil Performance Close to the Free Water Surface

Mohammad S. Seif, Hamid Saddathosseini, Maysam Mousaviraad
Mechanical Engineering Department, Sharif University of Technology
Tehran, Iran, P.O. Box: 11365-9567, seif@sharif.edu

Introduction

A moving hydrofoil close to the water surface creates waves. These waves may have steady or unsteady forms, resulting in steady or unsteady forces on the hydrofoil. In the unsteady case, waves grow to the point of wave breaking in certain conditions. There is not any analytical solution for this case and numerical modeling is the only tool (besides model tests) to investigate the hydrofoil performance.

For the steady case, *Vladimirov (1937)* presented a method based on potential flow. Then *Kotchin (1951), Wadlin et al. (1955)* and *Ducane (1972)* added the image technique to the method and analyzed steady motion of hydrofoil. *Sutherland (1951)* and *Payne (1996)* used concept of added mass to discuss the effects of free surface on hydrofoil performance. For the unsteady case, *Duncan (1983)* investigated wave breaking due to a moving hydrofoil close to free surface. *Azcueta et al. (2000)* studied the issue using CFD modeling. They pointed out that the wave breaking changes the lift force of hydrofoil considerably.

We modeled the flow using the commercial RANSE solver Fluent, including the effects of surface tension, turbulence, and free-surface deformation. We simulated both cases with and without wave breaking. The free surface is determined using a surface capturing technique, namely a volume of fluid (VoF) approach. Very fine grids are necessary in free surface region to get acceptable results for free surface position. We used 200,000 cells in our 2-d simulations. The time steps of 0.0001 seconds resulted in typical CPU times of 50 hours.

Approximate Formulas

In steady motion of a hydrofoil, low pressure on the upper face and high pressure on the mower face are created resulting in a lift force. Near the free surface, the waves are created and the pressure distribution changes, reducing the lift force (compared to the infinite depth case). Different formulas have been developed to estimate lift force near the free surface. Several parameters influence hydrofoil performance in this condition: hydrofoil geometry, cavitation, viscosity, angle of attack α, depth to chord ratio *h/c* (*h* is the height of the leading edge of the foil from calm surface; *c* the chord length), etc. These formulas assume generally some simplifications. The fluid is usually considered inviscid and incompressible, neglecting cavitation. C_L is the lift coefficient near the free surface, C_{Lmax} the lift coefficient for infinite submergence depth at given angle of attack, C_{L0} the lift coefficient for infinite submergence and α=0°. The Wadlin formula, *Wadlin et al. (1955),* estimates the lift force as follows:

$$\frac{C_L}{C_{L.\max}} = k \qquad \text{with} \qquad k = \frac{16\left(\frac{h}{c}\right)^2 + 1}{16\left(\frac{h}{c}\right)^2 + 2} \qquad C_{L\max} = 2\pi\alpha + C_{L_0}$$

k<1 always, thus the lift coefficient close to free surface is less than for the infinite-depth case. The Wadlin formula cannot be employed for high speeds or low *h/c* values, because wave breaking will occur and the flow will be unsteady. In these cases, numerical modeling is necessary.

Numerical Results

The simulation solves the two-phase flow in water and air in a grid covering both domains, Fig.1. The grid is unstructured with triangular cells near the foil and quadrilateral cells in the remaining area. To investigate the accuracy of the model, we simulated a NACA0012 foil for with α=5° and c=203mm. The results agree well with experimental data of *Vladimirov (1937)* for h=210mm, Fig.2. In this condition, surface waves are regular (steady) with very small amplitude. The CFD results predict the k values more accurately than the Wadlin formula, Fig.3. CFD considers also the actual geometry which is not possible in the Wadlin formula. Fig.4 shows CFD results for different hydrofoils sections demonstrating how results depend on section type. In general, k is not estimated well for unsymmetrical sections, but well for symmetric sections. Fig.5 shows the effect of changes in attack angle. For small attack angles, k is estimated with good accuracy. For higher angles, the accuracy decreases.

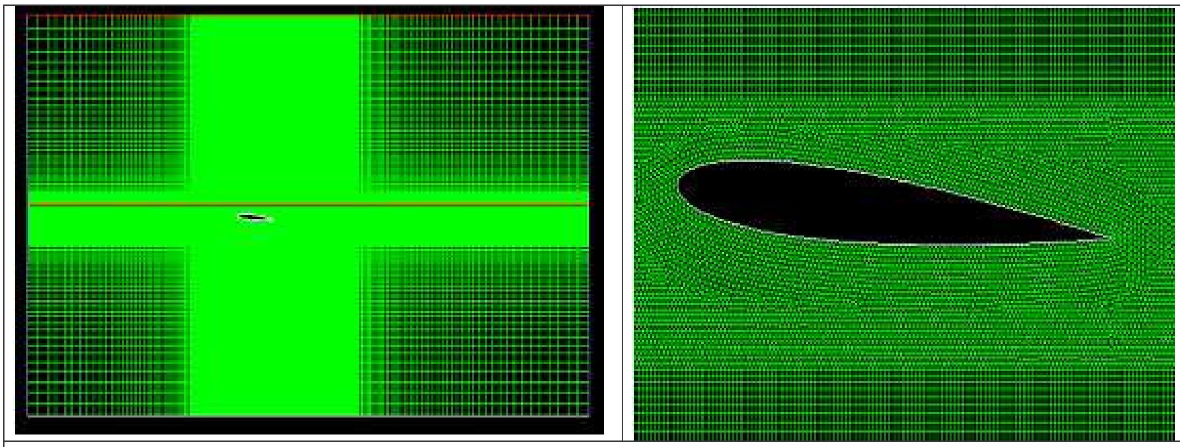

Fig.1: Grid around foil covering water and air

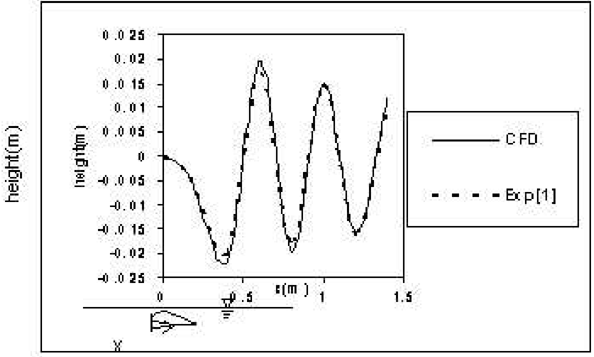

Fig.2: Water surface deformation for steady case

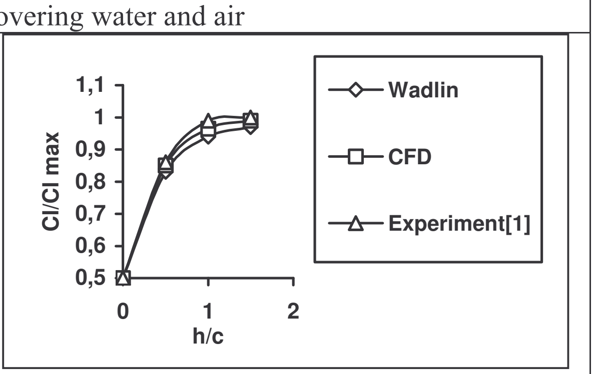

Fig.3: Comparison of different methods

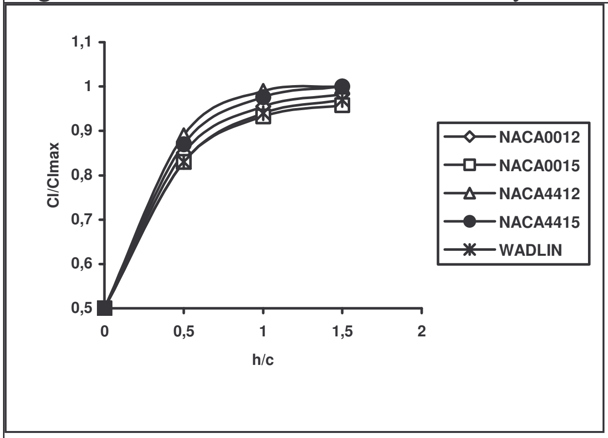

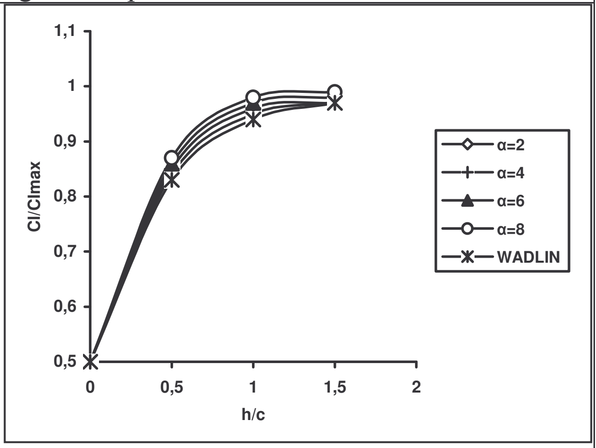

Fig.4: Effect of section geometry

Fig.5: Effect of angle of attack

For higher angles of attack or higher speeds, the flow may become unsteady. A simulation was carried out for this case: NACA0012 section at α=5°, *h/c*=0.5 (*c*=203mm), speed of 5.1m/s. The flow becomes unsteady due to the wave breaking. Fig.6 shows how the variation of the free surface causes considerable changes in the lift coefficient. Fig.7 shows that the code is capable to reproduce complex breaking waves in this case.

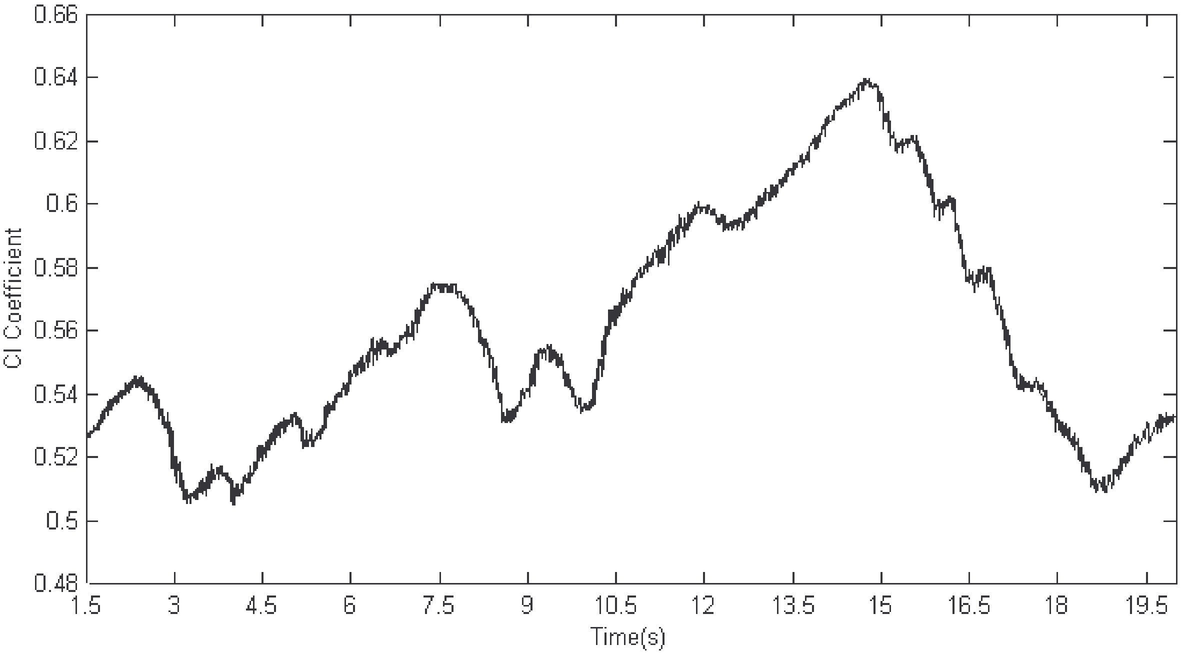

Fig.6: Lift coefficient variations for case involving wave breaking

References

AZCUETA, R.; MUZAFERIJA, S.; PERIC, M.; YOO, S.D. (2000), *Computation of flows around hydrofoils under the free surface*, TU Hamburg-Harburg report

PAYNE, P.R. (1996), *A new type of hydrofoil*, Small Craft Marine Engineering Resistance and Propulsion Symposium, Ann Arbor

DUNCAN, J.H. (1983), *The breaking and non-breaking wave resistance of a two-dimensional hydrofoil*, J. Fluid Mech. 126, pp.507-520

WADLIN, K.L.; SHUFORD, C.L.; McGEHEE, J.R. (1955), *Theoretical and experimental investigation of the lift and drag characteristics of hydrofoils at sub critical and supercritical speeds*, NACA Report No.1232

DUCANE, P. (1972), *High speed small craft*, Principles of Hydrofoils, chapter III. John DeGraff, Inc. Tuckahoe, NY

KOTCHIN, N.E. (1951), *On the motion of profiles of any from below the surface of a heavy fluid*, SNAME T& R Bulletin No. 1-8

SUTHERLAND, W.H., 1951. Exploratory model tests for engineering design of a hydrofoil vessel. Stevens Institute of Technology, ETT Report No.407

VLADIMIROV, A.N. (1937), *Approximate hydrodynamic design of a finite span hydrofoil*, NACA TM – 1341, June 1955

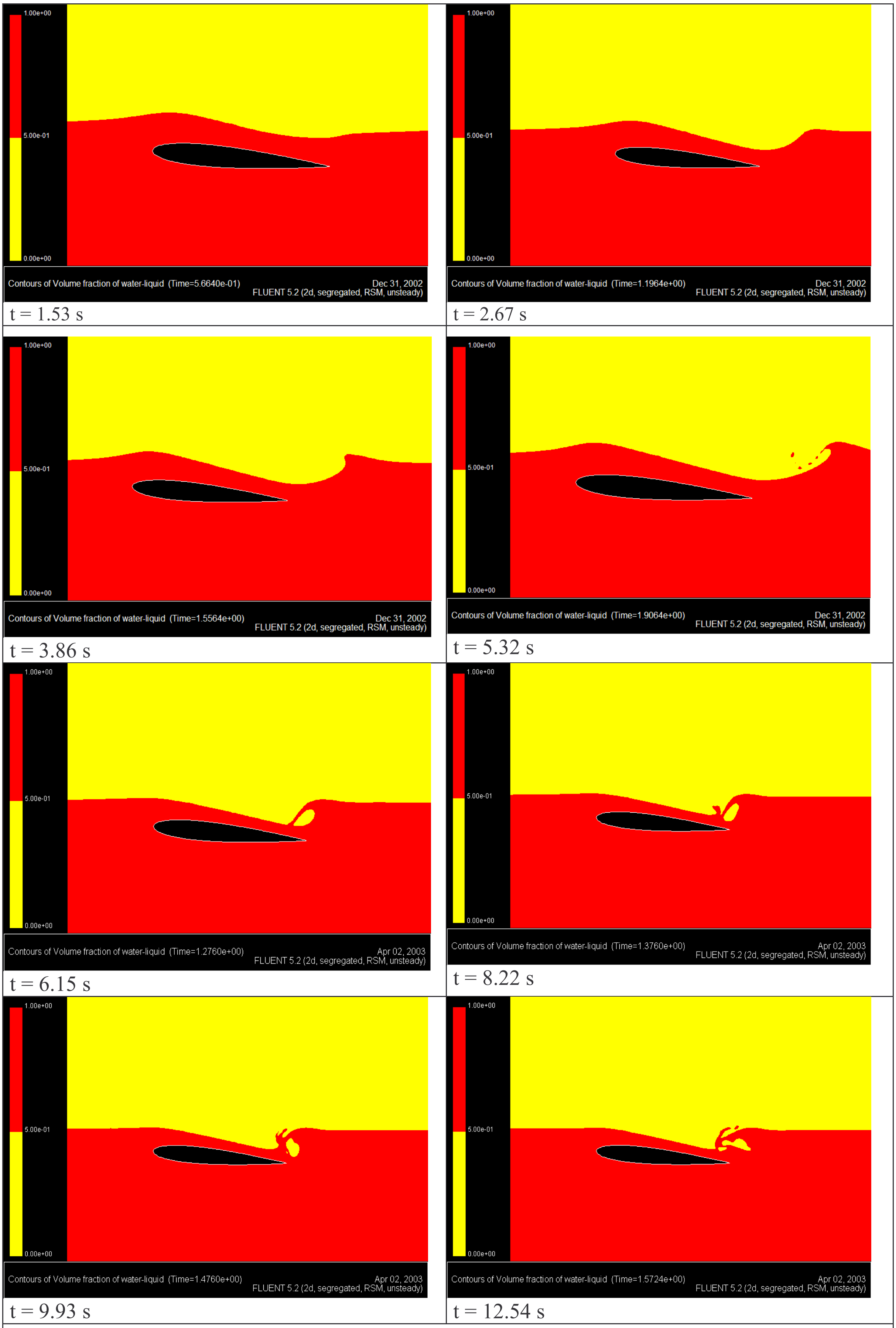

t = 1.53 s

t = 2.67 s

t = 3.86 s

t = 5.32 s

t = 6.15 s

t = 8.22 s

t = 9.93 s

t = 12.54 s

Fig.7 : Wave breaking for NACA 0012 section at 0.8 m/s

RANS CFD for Marine Propulsors: A Rolls-Royce Perspective

Gregory J. Seil – Rolls-Royce Plc, gregory.seil@rolls-royce.com

1.0 Introduction

Over the last ten years, tremendous progress has been made in the development and application of RANS CFD technology to marine propulsors. During the author's PhD studies in waterjet inlet hydrodynamics, which he commenced in early 1994, he used a commercially-available single-block structured CFD code to solve the flow on meshes produced by his own mesh generation program written in Fortran for parameterized rapid meshing [1]. "Large" meshes (see Fig. 1) of between 100000-250000 cells were used in a typical analysis which was run on a single processor Unix workstation. Contrast this with today, where complex multi-million cell meshes, generated from CAD geometry using sophisticated and yet user-friendly meshing tools, are run in parallel on Linux clusters using unstructured solvers and the evolution of the technology becomes evident.

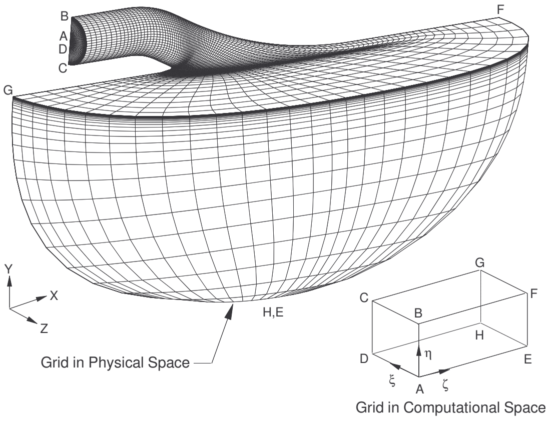

Fig. 1 Mesh of waterjet inlet, mid-1990s [1]

Over the last five years RANS CFD has become an integral part of marine propulsor development at Rolls-Royce. RANS CFD has been applied to the study of waterjet components, high-skew propellers and podded propulsors. Studies to date have focused on the development and experimental validation of CFD methods as the basis for developing CFD capability within the company, as well as contributing to product development. The challenge for a company like Rolls-Royce is to consider how, not only to use CFD to create the greatest impact on the company at present, but also to anticipate the potential of the technology and plan accordingly, in order to use the technology strategically in the future.

An overview of the some of the highlights of the RANS CFD work carried out at Rolls-Royce during the last 5 years is presented in Chapter 2 including: the calculation of free-surface flows in waterjet steering and reversing units, open-water calculations of a high-skew propeller and calculations of an electric pod unit. In Chapter 3 the future of RANS CFD development for marine propulsor applications at Rolls-Royce is discussed.

2.0 Examples of the Application of RANS CFD at Rolls-Royce

2.1 Waterjet Steering and Reversing Unit

In 2000, CFD methods for calculating the single-phase and two-phase (water and air) flow in a waterjet steering and reversing unit (SRU) were developed during the course of the development of a new SRU for the Kamewa Size 200 waterjet. The Kamewa Waterjets Size 200 waterjet pump and SRU is shown in Fig. 2. At Kamewa, the "size" of the waterjet is a measure of the pump inlet diameter in centimeters.

Fig. 2 Kamewa Waterjets Size 200 steering and reversing unit

The key motivation behind the development of the new SRU was weight and size minimization, relative to the standard design. Structural loading and required actuator forces were therefore key design issues. A model of the Size 200 SRU shown in Fig. 3 was therefore built and comprehensively tested at the Rolls-Royce Hydrodynamic Research Centre (RRHRC) in Kristinehamn, Sweden, using the waterjet test unit (WTU) described by Aartojärvi and Häger [2]. The WTU contains a complete waterjet geometry including the inlet duct, a Size 20 waterjet pump and the possibility of mounting an SRU. The waterjet pump is driven by electric motors through a flywheel and shaft line. The WTU was mounted in the T31 free-surface cavitation tunnel at the RRHRC.

The model SRU was instrumented with the following:

- A six component dynamometer measuring the total forces and moments acting on the SRU.
- Force transducers measuring the forces at hinge points.
- Strain gauges measuring the elastic strain in the linkage arm between the steering nozzle and the lower reversing bucket, allowing forces to be determined.
- Static pressure tappings for measuring the static pressure distribution over the surface of the steering nozzle and reversing bucket.

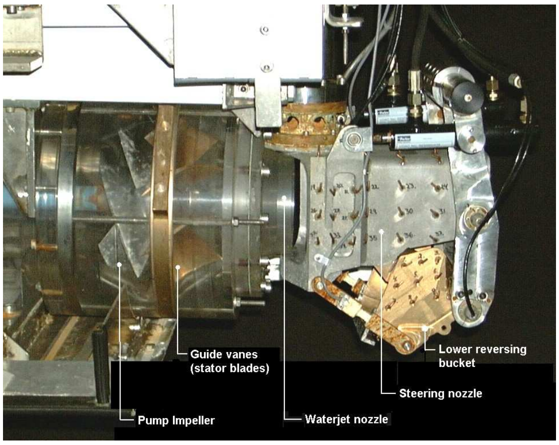

Fig. 3 Model steering and reversing unit mounted on WTU

Both single-phase and two-phase (water and air) volume of fluid (VOF) calculations were made for a number of SRU operating configurations and conditions using Fluent 5.3. The RANS equations were solved, with Standard k-ε modeling and wall functions on hybrid meshes of tetrahedral, hexahedral and pyramid cells. The CFD results were found to be in good agreement with the experimentally-measured pressure and force data. For the VOF calculations the interface between the phases was tracked using Fluent's "implicit" interface tracking scheme. More details of the single-phase validation work can be found in [3].

Fig. 4 shows the development of the free-surface on the centreplane of the SRU for full reverse, with a steering angle of 0°. Note that in the CFD model, the water exhausts into an air-filled volume as the geometry of the experimental configuration has not been modeled. In the computational model, only the geometry of the waterjet nozzle and SRU was modelled. Significant smearing of the interface between the water and air phases is evident from Fig. 4, particularly on the jet emerging from the lower reversing bucket. This may be attributed to numerical diffusion associated with relatively large cells in the vicinity of the interface. The calculation was started with an initial mesh of 1335897 cells and with solution adaption the final mesh size was 2324199 cells. Clearly further solution adaption would be needed for improved interface resolution.

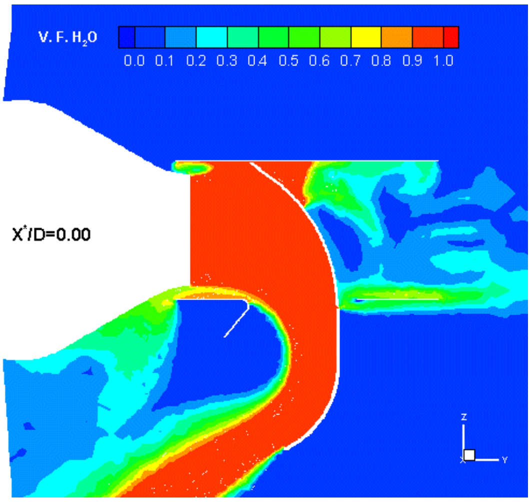

Fig. 4 Example of calculated free-surface flow on centreplane of SRU for full reverse

2.2 High-Skew Propeller

In early 2001, Rolls-Royce embarked on a relatively comprehensive combined CFD and experimental study of Propeller 734-b, a propeller from the Kamewa high-skew series. The objectives of the study were:

- Development of a set of in-house experimental reference data for validating CFD methods.
- Experimental validation of calculated propeller curves over the complete range of advance numbers tested.
- Laser-Doppler Anemometry (LDA) measurements of the propeller slipstream at several axial locations downstream of the propeller for one advance number.
- Comparison of RANS CFD results with the results of in-house potential flow codes.
- Enhanced understanding of flow physics.

Propeller diameter	250 mm
Hub diameter	75 mm
Number of blades	4
Expanded blade area ratio	0.603
Design pitch ratio at 0.7R	1.2
Projected skew angle	48°

Table 1: Propeller data for 734-b at model-scale

Details of the propeller geometry are given above in Table 1.

A structured mesh of 2075275 hexahedral cells was generated using the commercially-available mesh generation software Gridgen by Pointwise Inc.. This mesh size is clearly large and may be attributed to the following:

- Modelling of the hub geometry.
- The need to resolve the downstream slipstream and keep cell aspect ratios within reasonable values.
- The radial extents of the flow domain, including resolution of boundary layers on the cylindrical representation of the tunnel walls.

The basic mesh topology is of an H-type with conformal periodic boundaries (axially and radially matching nodes on opposite periodic boundaries). The surface mesh on the propeller blade, hub and shaft fairing can be seen from Fig. 5. Extensive use was made of Gridgen's elliptic solver capability in order to reduce cell skewness both on the blade and in the volume mesh. Even with elliptic smoothing of the mesh, there was still significant cell skewness present in the volume mesh, due to the relatively low pitch angles near the blade tip.

Fluent 6.0, was used to solve the RANS equations using RNG k-ε turbulence modeling with swirl modification and Two-layer Nonequilibrium wall functions. The QUICK scheme was used for convective differencing.

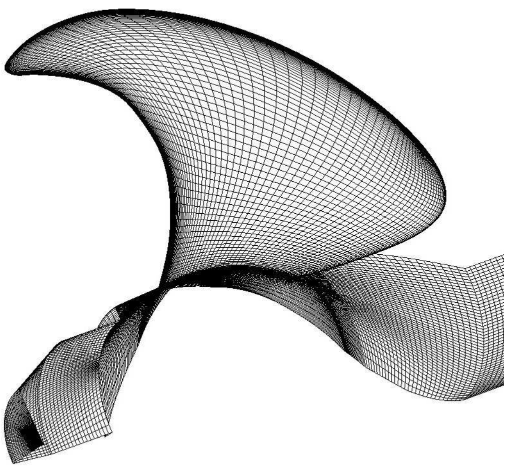

Fig. 5 RANS surface mesh of propeller 734-b

The calculated propeller curves (K_T, $10K_Q$, η), under open-water conditions, are compared with experimental measurements in Fig. 6. Also compared are the results from the potential flow codes MPUF 3a v2.0 (Vortex Lattice Method) and PropCav v2.0 (Boundary Element Method).

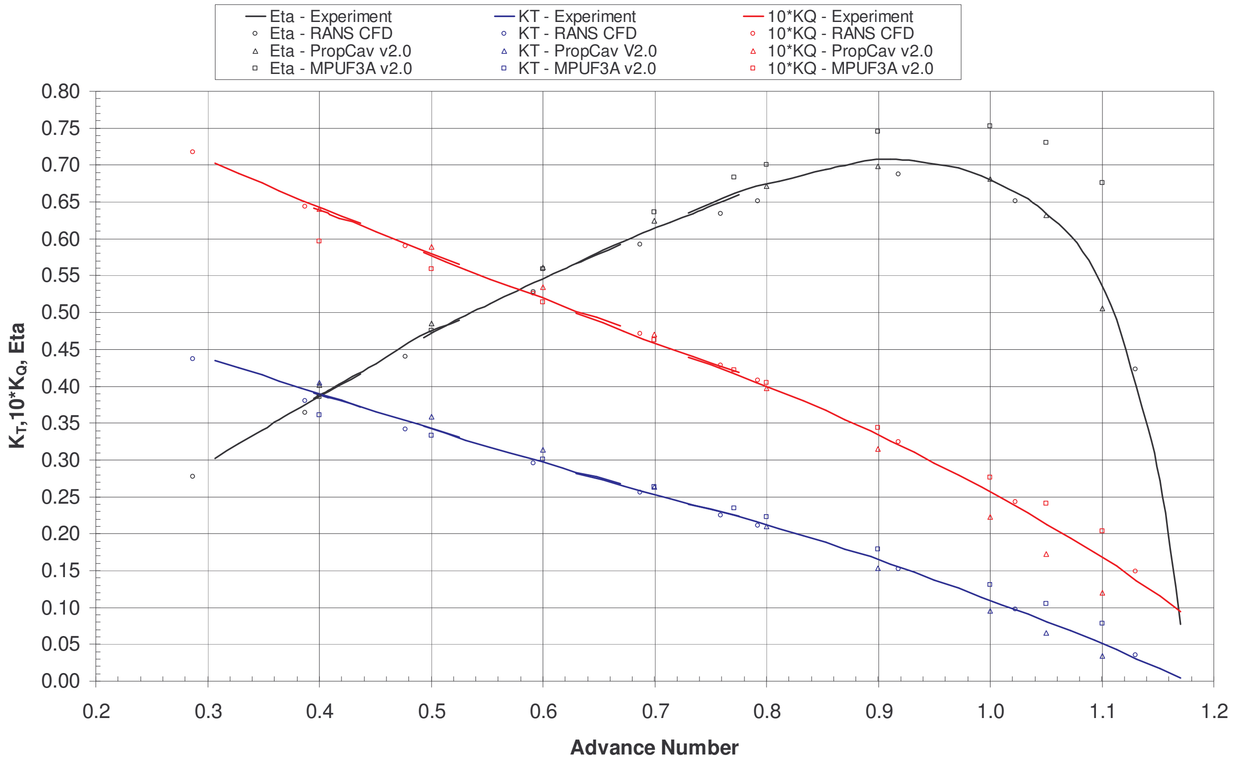

Fig. 6 Comparison of calculated and measured propeller diagram

Fig. 6 clearly shows that the RANS calculations yield results in closest agreement with experimental data for thrust and torque. The agreement between the measured thrust and torque and the values calculated by the three numerical methods deteriorates at both high and low J values. This deterioration is most marked for the Boundary Element Method (BEM) and Vortex Lattice methods (VLM), with the RANS results still remaining in relatively good agreement with the experimental measurements

The RANS and the BEM results consistently follow the curve of measured open-water efficiency over the range of J examined. Although the results yielded by the BEM and RANS methods are close, the BEM produces closer agreement with the experimental data except at the highest and lowest values of J calculated.

Extensive LDA measurements (using a Dantec 300 mW FVA differential Doppler backward scatter system) were made for an advance number of 0.77 at five axial locations, one upstream (0.20D) and four downstream of the propeller (-0.12D, -0.20D, -0.58D and -0.95D). At each axial location, axial, radial and circumferential velocity measurements were made at one degree intervals over several radii in the range of 0.5R to 1.1R, where R is the propeller radius. At each of the measurement locations downstream of the propeller, the slipstream calculated using CFD was validated against experimental measurements, as shown for example in Fig. 7. From this figure, the calculated slipstream can be seen to be in good agreement with the experimental measurements, although evidence of damping and phase shift of slipstream peaks and troughs is evident. More details of the work can be found in [4].

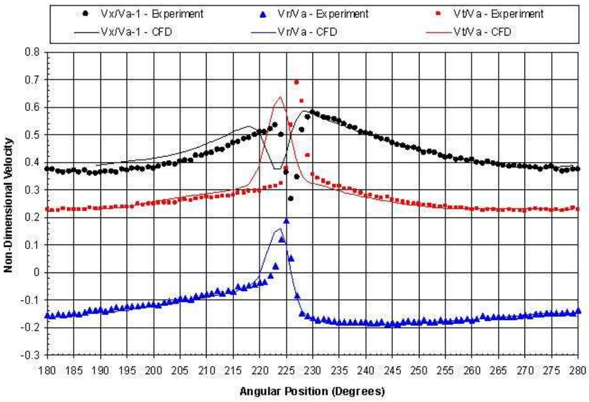

Fig.7 Slipstream validation, x/D=-0.12, r/D=0.7, J=0.77

2.3 Electric Pod Propulsor

In 2001, work commenced on a RANS CFD methods development programme with the objective of developing the capability to perform accurate quasi-steady and sliding mesh calculations of electric pod units. Previous work at Rolls-Royce had focused on using an actuator disc approach to model the effect of the propeller on the flow around the pod body and was therefore limited in its capability.

Structured meshes of close to 3 million cells have been generated using Gridgen for the purposes of analysis. The surface mesh on an electric pod unit is shown in Fig. 7.

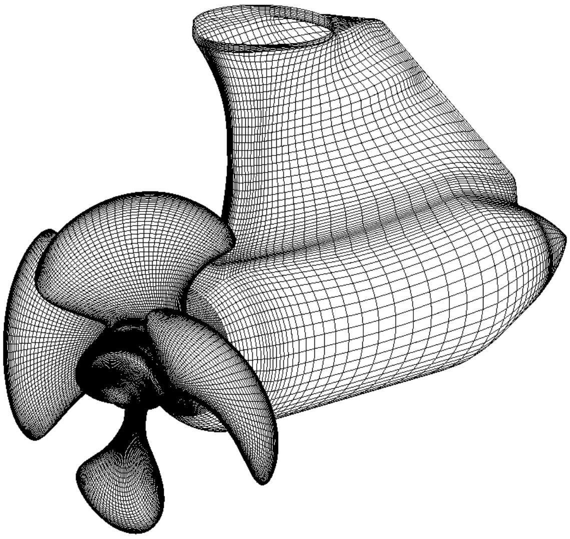

Fig. 7 Surface mesh of pod unit

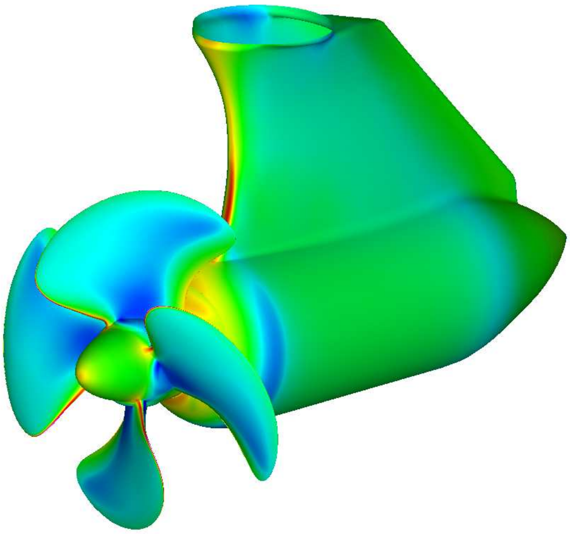

Fig. 8 Example of calculated pressure distribution on pod unit

Fluent 6.0 and Fluent 6.1 have both been used to solve the RANS equations using the RNG k-ε turbulenceb modeling with swirl modification and Two-layer Nonequilibrium wall functions. The QUICK scheme was used for convective differencing. An example of the calculated pressure distribution on the surface of the pod is shown in Fig. 8.

3.0 The Future of RANS CFD for Marine Propulsor Applications at Rolls-Royce

There are two primary sets of challenges that lie ahead for us at Rolls-Royce. The first is the continued development of a world-class network of hydrodynamicists, CFD specialists and engineers both within the company and externally via University Technology Centres, consultants and hardware and software partners. This helps us to keep abreast of the latest developments in hydrodynamics, computer hardware, software, RANS CFD applications and of course what our competitors are doing. This is one of the reasons why we seek to actively participate in conferences and symposia – in order to keep up to date with technology and to build relationships. Another reason we like conferences is that they are generally fun and interesting!

The second challenge is to exploit the continuing rapid growth in computing power for: 1) a reduction of existing CFD analysis cycle times, 2) a greater integration of CFD into the product development process, 3) more detailed and complex modeling, such as CFD analysis of integrated propulsor/hull configurations and cavitation and 4) multidisciplinary analysis and optimization

3.1 Reduction of CFD Analysis Cycle Time

As computing power continues to increase and the cost of computing continues to decrease, larger meshes can be solved in a given time. The challenge is to therefore to make use of large unstructured meshes that can be generated rapidly in order to significantly shorten the CFD analysis cycle. For parametric studies of simple geometries, where large numbers of calculations are required, the CFD analysis cycle time may be reduced through the semi-automation or full automation of the meshing process. Waterjet pump blading is an excellent example of this. The meshing of blade rows in waterjet pumps has been automated via the use of the PADRAM (Parametric Design and Rapid Meshing) code developed by Civil Aeroapace [5]. This allows a mesh to be generated by the user in minutes, or fully automatically as part of an optimization code.

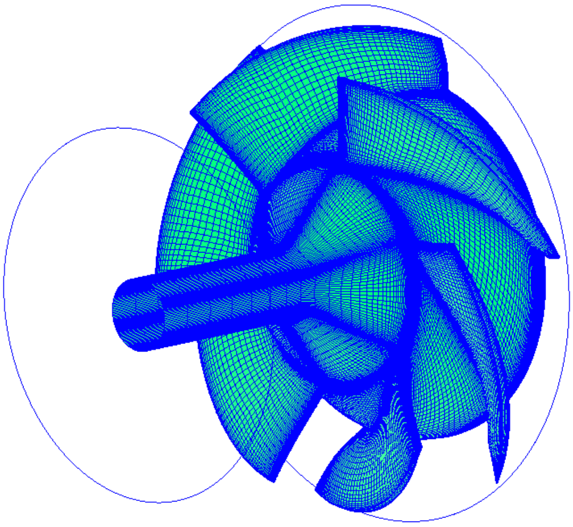

Fig. 9 Mesh of waterjet impeller mesh produced by PADRAM [5]

3.2 Greater Integration of CFD into the Product Development Process

In order to realize the full potential of CFD, it is necessary to integrate CFD more closely into the product development cycle, so that information flows smoothly and efficiently from CAD, to CFD and then to FEM, or between CFD and FEM (for fluid structural simulations). While this is obvious, the challenge also lies in effective project management of CFD within a company, whether by virtue of projects related to integration of CFD into the product development process, or by management of CFD on existing projects. The latter is only straightforward if a particular generic configuration has been studied before, for example quasi-steady blading calculations, where meshing, calculation and postprocessing times are known from previous experience.

Ideally, the study of new configurations should be undertaken as part of “methods development” and is more of a research-related activity, rather than part of product development. If for some reason methods development is undertaken as part of a product development project, it should be considered as a peripheral activity, and not as task on which the ultimate success of the project, in terms of timeframe depends; that is it should not be a task lying on the critical path of the project. Proper methods development will include an experimental validation component, allowing an assessment to be made of the reliability of the CFD model and the lessons learnt can be used as the basis for incorporating CFD into the product development cycle.

For CFD projects that are outsourced, a company must act as an "intelligent buyer" of services and this requires appropriately trained in-house staff who have knowledge of both project management and a the technology itself.

For a medium-sized company of several hundred employees covering a wide range of different products, a CFD group of three people represents, in the author's view, a critical-mass for effective operation. In terms of value-added to the business this will depend on an intelligent and well-thought out portfolio of projects.

3.3 CFD Analysis of Integrated Propulsor/Hull Integration

The challenge for Rolls-Royce is to move beyond RANS CFD analysis of isolated propulsors and consider integrated propulsor/hull configurations as part of the product development process. This includes not only propeller/hull, but also waterjet/hull and pod/hull configurations. In other words, to move forward by extending the complexity or our analysis and look for synergies in designing the hull and propulsor together in an integrated manner. This includes examining design, off-design and manoeuvring conditions in line with the operating spectrum of the vessel and weighting the relative importance of each condition to a successful overall design. These analyses will inevitably be computationally demanding since they will include the full geometry of the hull and the propulsor(s), calculated in a time-dependent manner.

3.4 Multidisciplinary Analysis and Optimisation

Another challenge for realizing the full potential of CFD in a company is to integrate CFD hydrodynamic analysis into a multidisciplinary environment incorporating structural, thermal and acoustic analysis during the product development process; in other words, to develop the analysis model in an integrated and multidisciplinary manner. This demands an engineer with not only a thorough knowledge of hydrodynamics and CFD but also with a broader knowledge and grasp of other areas such as structural mechanics, acoustics and project management. For large companies the danger in this regard is over-specialisation of skills and lack of a broader understanding or knowledge of key engineering disciplines. For a smaller company the reverse may be the case: good general technical knowledge, but lack of technical depth in key areas.

Rolls-Royce Civil Aerospace has successfully incorporated CFD into optimization routines for the optimization of blading and endwall components for gas turbine engines. The challenge is to do the same for marine components, initially for single and multi-objective hydrodynamic optimization and then for multi-objective and multidisciplinary optimization. The power of such methods does not of itself lie in the finding the "optimum" design, but in understanding what an improved component design may look like and the underlying reasons why.

References

1. Seil, G. J. *Computational Fluid Dynamics Investigation and Optimisation of Marine Waterjet Propulsion Unit Inlet Design*, PhD Thesis, Department of Mechanical and Manufacturing Engineering, The University of New South Wales, 1997.

2. Aartojärvi, R. and Häger, C. (2001), "Tansient Loads on Waterjets Resulting from Air Ingetion", Paper No. 4, *Proc. RINA International Conference - Waterjet Propulsion III*, Gothenburg, Sweden, 20-21 Feb. 2001.

3 Seil, G. J. (2001) "Experimental Validation of the Calculated Flow in a Waterjet Steering and Reversing Unit", *Proceedings of the Sixth International Conference on Fast Sea Transportation (FAST2001)*, Southampton, England

4. Seil, G. J., Lundberg, J. and Pettersson, G. (2003) "CFD Calculation and Validation of a Kamewa High-Skew Marine Propeller", *Proceedings of CFD 2003: Computational Fluid Dynamics Technology in Ship Hydrodynamics*, The Royal Institution Institution of Naval Architects, London, England, 6-7 February 2003.

5. Shahpar, S. and Lapworth, L. (2003), "PADRAM: Parametric Design and Rapid Meshing for Turbomachinery Optimisation", GT2003-38698, Proc. of IGTI: ASME Turbo Expo, Atlanta, Georgia, June 16-19, 2003.

Disclaimer: The views expressed in this paper are the author's and do not necessarily reflect the views of senior management at Rolls-Royce.

Calculation of Fire Development and Smoke Propagation in Ship Compartments

Vladimir Shigunov, *Universities of Strathclyde and Glasgow*[1]

Abstract. A numerical method is proposed for calculation of fire development and transport of combustion products and heat in ship compartments. The method is based on numerical integration in time of differential equations stating conservation of mass, energy and chemical species and includes convective mass and heat transfer, radiative energy exchange and heat conduction through walls. The method is validated against model tests and applied to a vehicle deck of a roro ship.

Introduction

The method of investigation is based on numerical simulation in time of the development of fire and transport of heat and combustion products in connected compartments. Aiming at computationally cheap solutions, the method uses coarse numerical grid in space (one control volume for one room) and time (time steps about 1 s). Such approaches (see for instance [1] and [2]) are referred to as zonal models. Compared to existing codes, the treatment of walls is improved here.

Description of the Method

Governing Equations. Gas in a compartment is assumed to consist of two layers with a horizontal interface between them. The upper layer is fed by fires with combustion products and heat. Additionally, fire plumes pump gas from the lower into the upper layer. This method produces two distinctly separated gas volumes, the upper hot gas volume, containing combustion products, and colder lower layer with ambient (if mixing is neglected) contents. Although simplified, the model reflects well experimental evidence about temperature and species distribution in compartments.

For each gas layer, a set of ordinary differential equations is written following from the conservation of mass and energy. Numerical integration of the differential equations provides time histories of temperature, volume, density, composition of the gas etc. in each gas layer in each room.

Mass Conservation. Mass conservation equation is solved for each gas layer γ ($\gamma = u$ or l for upper or lower gas layer, respectively) in the form

$$dm_\gamma/dt = \dot{m}_\gamma, \tag{1}$$

where the left-hand side will be integrated in time t, and $\dot{m}_\gamma$ represents sources of mass including

- for the upper gas layer: products of combustion from fire, mass entrained in the fire plume from the lower layer and mass fluxes through vents such as windows, doors, ducts and fans, and
- for the lower gas layer: mass loss due to the entrainment in the fire plume (equal and opposite to the term for the upper layer) and mass transfer through vents.

Momentum Transport. The velocities on the solid boundaries of a control volume are zero; if the vents are small compared to the room size, the average velocity in the control volume is small and momentum transport inside a compartment can be neglected as it was done here.

Energy Transfer. The energy conservation equation is solved in the form

$$dU_\gamma/dt + p_0 dV_\gamma/dt = \dot{h}_\gamma, \tag{2}$$

where $U_\gamma = c_v m_\gamma T_\gamma$ is the internal energy of the gas layer γ, V_γ is its volume, p_0 is a characteristic pressure in the compartment, and $\dot{h}_\gamma$ represents all heat sources. Energy is transferred through convection, conduction and radiation.

---

[1] Colville Building, 48 North Portland str., Glasgow, G1 1XN, United Kingdom; vladimir.shigunov@strath.ac.uk

Convective Transport. Convective transport of energy includes terms similar to mass sources: convective part of the heat of combustion from fires (for the upper layer), heat pumped by the fire plume from the lower into the upper layer and heat flux through vents.

An additional term arises due to the convective heat exchange between the gas and adjacent solid walls of the enclosure.

Heat Conduction. Walls between adjacent rooms or between a room and the ambient atmosphere are subdivided into an arbitrary number of segments. For each wall segment, the normal heat conduction through wall is calculated by finite-difference discretisation of a heat conduction equation.

The heat flux from the wall segment into the two adjacent compartments, including radiative and convective parts, serves as boundary conditions for the heat conduction problem; the solution of the latter, namely the temperatures of the two segment surfaces, serves as boundary conditions for the calculation of convective and radiative heat transfer.

Walls included in the model so far encounter a single material wall, a double wall (two plates with air between; the air transfers convective and radiative heat) and a triple-layer wall (e. g. two plates with insulation between); the layers of materials can be treated as either thermally thin (uniform temperature throughout the layer) or thermally thick.

To enable easy keeping of and referencing to the wall segments, an arrangement similar to the sell-face based connectivity structure used in unstructured grids in numerical fluid dynamics is employed.

Radiative Heat Transfer. Surfaces of wall segments are considered as surface panels in the calculations of the radiative heat exchange. Radiative heat transfer is considered between different surface panels, between surface panels and gas layers and between gas layers. If there are fires in the compartment, additional radiative heat fluxes from the fires are added to surface panels and gas layers.

Species Transport. The following species are considered:

- fuel components, i. e. the species contained in the pyrolisate such as carbon, hydrogen and oxygen
- ambient air components such as oxygen, carbon dyoxide, water and inert species (nitrogen)
- combustion products such as unburned fuel, carbon di- and monoxide, water, soot, hydrogen cyanide and hydrogen chloride

A total of eight conservation equations of species are solved, for oxygen, carbon dioxide, carbon monoxide, soot, unburned fuel, hydrogen cyanide, hydrogen chloride and water; conservation of inert species follows from mass conservation. Species are transported by convective fluxes similarly to the mass transport, by vents and fire plumes, and are produced or consumed in combustion.

Fire. The burning rate is prescribed as the heat release rate from a fire under free burning conditions, i. e. under unlimited oxygen supply. This heat release rate can be defined experimentally and found in textbooks for standard items of furniture, linings, pools of fuel etc.

Actual burning rate is calculated considering the actual ventilation conditions and fire geometry. This heat release rate is separated into the radiation and convection parts according to a user-prescribed percentage. It is assumed that the radiative part is transferred uniformly in all directions, while the convective part contributes only to the upper gas layer through the fire plume.

The fuel composition is specified by mass ratios of components such as hydrogen and oxygen to carbon of the fuel. Such products of combustion as hydrogen chloride and hydrogen cyanide are also specified as components of the fuel by respective mass ratios.

The production properties of fires are described again as branching ratios for carbon monoxide and soot, depending on the fuel type, fire geometry and ventilation conditions. These branching ratios can be either prescribed or calculated using empirical correlations.

Vent Flows. Mass flow rates through vents are calculated by integration over the vent area of

Bernoulli's equation for a streamline, taking into account hydrostatic pressure distribution in the adjacent gas layers. The calculated mass, heat and species fluxes through the vent are redistributed between the gas layers of the adjacent compartments, assuming that the mass flux originating in the lower or upper layer must terminate in the lower or upper layer, respectively, of another compartment due to buoyancy; mixing effects at the interfaces of the fluxes have been neglected so far.

If a fan is placed inside a vent such as a duct, an additional head from the fan is included.

One of the issues defining the overall efficiency of the method is the calculation of the characteristic pressures p_0 in connected compartments. Rise of the pressure in one of the compartments due to a fire gives rise to mass and heat outflow, and in turn to decrease of the pressure. The characteristic time of equalizing pressures in connected compartments is very small, therefore pressure solution procedure needs some care. In the present method, pressures were found from a system of equations similar to a discretised Poisson's equation in incompressible flow solvers. The matrix of coefficients on the left-hand side of the system was calculated approximately, using complex differencing.

Calculations

One of the main sources of fire hazard onboard roro ferries is a vehicle deck. The fire load due to burning of a vehicle or a pool of fuel may be very high, but if the access of oxygen is limited, the fire may self-extinguish in a short time. On the other hand, under good ventilation conditions (e. g. open loading gate) the fire can develop and propagate to other vehicles. It is therefore important to be able to predict the influence of different ventilation conditions on possible fire development.

Validation. Experiments were performed at the Swedish National Testing and Research Institute [3] with two scale models of a vehicle deck to study the influence of ventilation conditions and water spray fire-damping system on fire development; only the tests with a small scale model without sprinklers are considered in the calculations in this paper. The model was fitted with a ventilation fan, exhaust ventilation shaft, loading gate, two windows and scuppers for drainage of the water from the spray system.

A wood crib was used as a fire source. The measured free-burning heat release rate for fully developed fire was about 400 kW, which corresponds to about 70 MW in full scale.

In the present work, calculations were done for the cases 4 (ventilation shaft and scuppers open), 5 (ventilation fan on, ventilation shaft and scuppers open), 6 (two windows open) and 9 (loading gate and scuppers open); numbers correspond to numbers of tests in [3].

Prescribed Heat Release Rate. Firstly, a common approach was used, where the time histories of heat release rate were prescribed according to the measurements. The prescribed experimental heat release rate time histories are shown on the right-hand plots in Fig. 3. Results of calculations are shown on the left-hand plots in Figures 1 (the temperature of the upper gas layer) and 2 (mass fraction of oxygen in the upper layer). Measured temperature at the point 0.475 m above the floor and 3 m from fire and oxygen concentration (0.475 and 5.4 m, respectively) are shown for comparison on the right-hand plots in these figures.

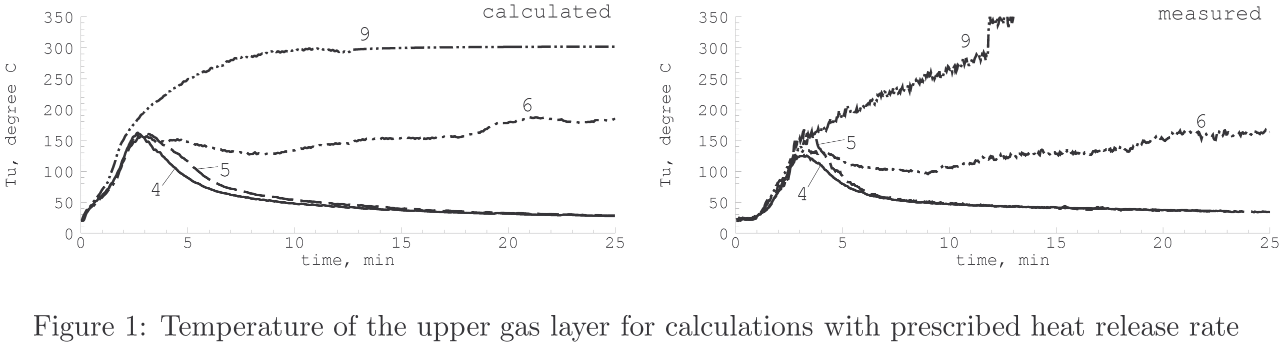

Figure 1: Temperature of the upper gas layer for calculations with prescribed heat release rate

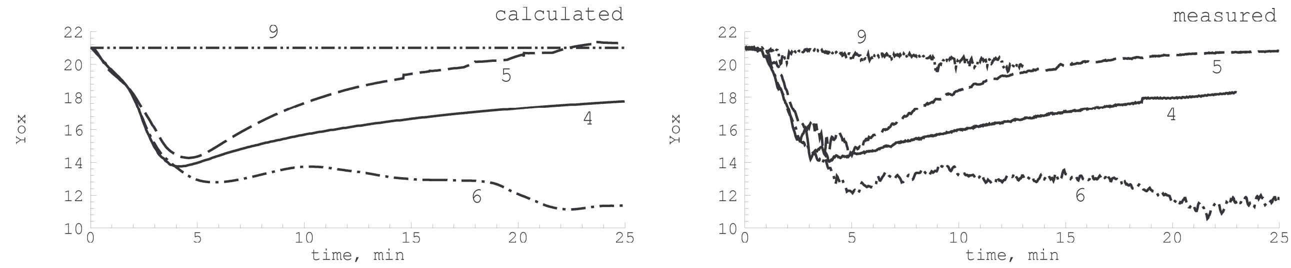

Figure 2: Oxygen mass fraction in the upper layer for calculations with prescribed heat release rate

Calculated Heat Release Rate. With the approach used in the previous paragraph, the heat release rate under different burning and ventilation conditions must be prescribed. It would be more useful to use only the heat release rate under free-burning conditions with appropriate corrections. In the next set of results, the heat release rate from unlimited fire (taken from test 9) was prescribed. It was resricted by the available oxygen and besides, the finite height of the fire source was taken into account, so that its part in the upper, contaminated gas layer was excluded from the burning region, and the position of the fire (varying in time) was taken at the middle of the burning height.

Calculated heat release rate is compared with measurements in Fig. 3. The left-hand plot shows calculated results, the right measurements. Calculated temperatures and oxygen mass fractions for the upper gas layer are shown in figures 4 and 5, respectively.

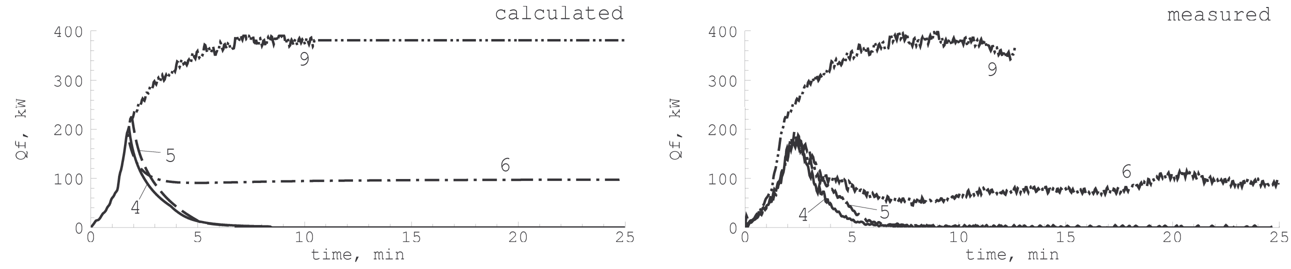

Figure 3: Comparison of calculated (left plot) and measured (right) heat release rate from fire

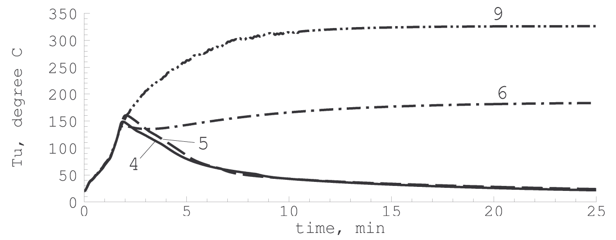

Figure 4: Calculated temperature of the upper gas layer for calculated heat release rate

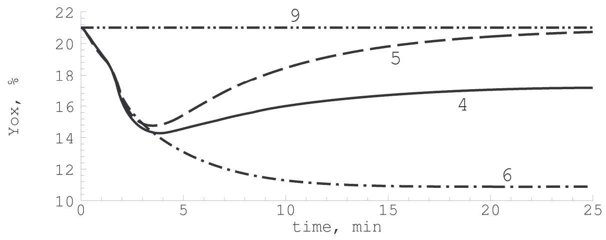

Figure 5: Calculated mass fraction of oxygen in the upper layer for calculated heat release rate

Application. Full-scale calculations for a generic vehicle deck of a roro ship were performed. Fig. 6 shows a plan view of the deck. The vehicle deck is a box of dimensions 200 by 30 by 6 m (length, breadth and height, respectively) with double sides, a central casing and a forepeak space. The double sides and the central casing are considered as double steel plates with 3 m thickness air layer between them (`d` in Fig. 6); all other walls, as well as the floor and ceiling are single steel plates (`s`). The loading gate is considered to be the entire stern wall.

In the calculations, the deck is subdivided into three “rooms” A, B and C corresponding through vents shown with dashed lines (`v`). The fire placed in part A produces free burning heat release rate shown on the upper right-hand plot in Fig. 7, with maximum of 70 MW[2] for fully developed fire.

Two cases were considered, one with closed compartment and another with open loading gate. In Fig. 7, the upper plots show time histories of heat release rate from fire, the middle temperatures and the lower mass fraction of oxygen in the upper gas layer, separately for “rooms” A, B and C.

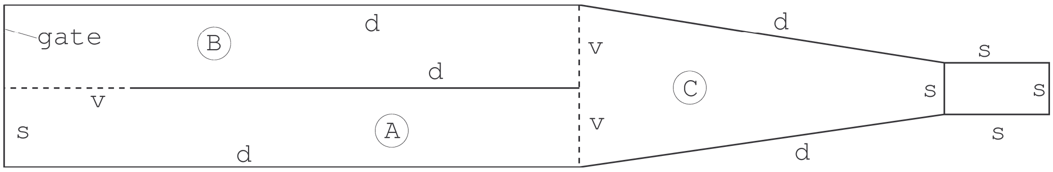

Figure 6: Plan view of a full-scale vehicle deck

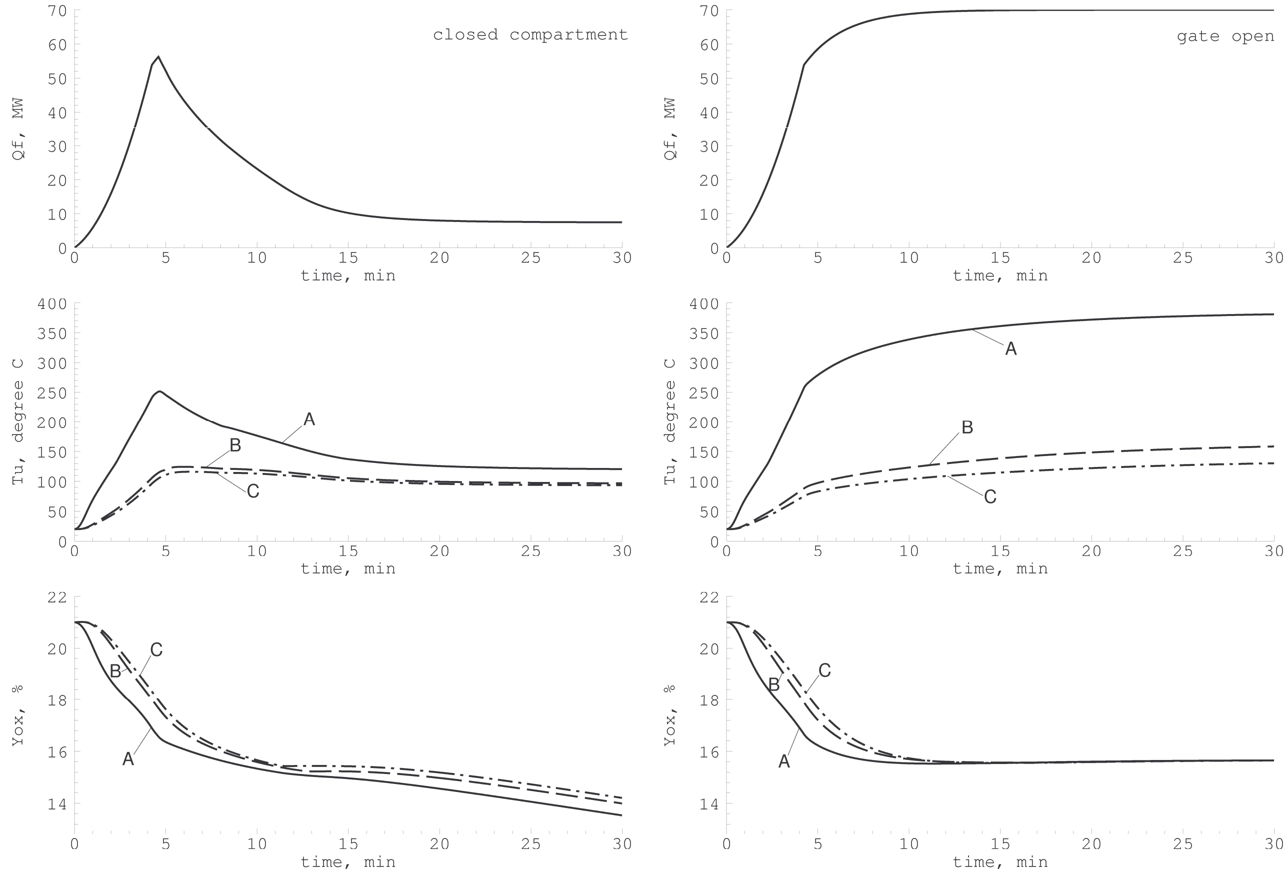

Figure 7: Results of calculations of the heat release rate (upper plots), temperature (middle) and mass fraction of oxygen (lower) for the upper gas layer, for closed deck (left plots) and deck with open loading gate (right), separately for “rooms” A (solid lines), B (dashed) and C (dash-dotted); for the vehicle deck shown in Fig. 6

Computational Time. Computing time grows with increasing number of rooms and depends significantly on the stiffness of the pressure solution problem. The minimum computing time corresponds to concealed compartments; slightly more for compartments with large vents. The largest computing

---

[2] According to [3] and references therein, a standard car burns with a heat release rate of up to 5 MW, a small truck up to 15 MW and large heavy vehicles 45 to 120 MW under good ventilation conditions

time is needed for compartments with small orifices. In the examples considered in the present paper, computing time was 0.1 to 0.4 seconds on a Pentium II computer for one real-time second.

Conclusion

The calculation method presented provides results of acceptable accuracy for fire safety assessment and is cheap regarding computational time required, which is essential for parametric studies in ship design. Especially useful the method would be when combined with evacuation simulation.

The underlying idea of using very coarse grids does not allow the investigation of scenarios with strong influence of diffusion (diffusion-driven mass exchange) or mixing (multiphase applications, e. g. for fire damping systems) where the method must use empirical correlations derived from tests or calculations with much finer grids.

Even remaining on the present level of approximation, there are some questions for further exploration, for example

- Is the simulation of the normal heat conduction through walls enough for ship design applications or the longitudinal heat transfer along plates, beams etc. must also be included. To be able to include longitudinal heat conduction, the structure of the code must be more complex.

- For high compartments such as staircases, the assumption of uniform density of the lower gas layer, neglecting the stratification due to the gravity, may lead to wrong results. If the buoyancy of the combustion products is not sufficient to reach the ceiling, the hot gas layer will form at some intermediate height. This problem can be solved by subdivision of the height of the compartment into more than two gas layers.

- For rooms with large horizontal dimensions such as cargo decks and corridors, the assumption of horizontal interface between gas layers over-estimates the speed of propagation of convective heat and combustion products from fire. Accuracy can be improved by further subdivision of such compartments by vertical vents into smaller, but still large control volumes. Since such “rooms” are no more restricted by solid boundaries from all sides, the average flow velocities inside the control volumes cannot be neglected, which requires the incorporation of momentum transport into the model.

References

[1] *Jones, W. W., Forney, G. P., Peacock, R. D. and Reneke, P. A.* (2000) A technical reference for CFAST: An engineering tool for estimating fire and smoke transport, *Technical Note 1431,* National Institute of Standards and Technology, Galthersburg, MD

[2] *Wade, C. A.* (2002) BRANZFIRE, Technical reference guide, *Study Report No. 92,* Building Research Association of New Zealand, Judgeford, Porirua City, New Zealand

[3] *Larsson, I., Ingason, H. and Arvidson, M.* (2002) Model scale fire tests on a vehicle deck on board a ship, *SP Report 2002:05,* Swedish National Testing and Research Institute, Fire Technology

Simulation of Cavitating Flows around Propellers with a RANSE-code

Heinrich Streckwall
Hamburg Ship Model Basin (HSVA),
Hamburg, Germany
streckwall@hsva.de

Ole Hympendahl
Technical University Hamburg-Harburg,
Hamburg, Germany
o.hympendahl@tu-harburg.de

1 Introduction

The prediction of cavitation at propellers and rudders is of great importance because noise and vibrations and often also erosion damages occur at modern propellers, partly due to the increasing loads of recent propeller designs.

Model tests are carried out for a great number of ships, but are quite expensive, particularly when several versions are investigated. For numerical simulations vortex-lattice- and panel-methods are being used. They are fast but often limited to some kinds of cavitation, for example it is impossible to simulate tip and hub vortex cavitation. Over the last few years it is possible to simulate cavitation with RANSE-methods. This paper presents RANSE-calculations of propellers in a cavitating flow.

2 The numerical method

For the simulations of the cavitating flow the RANSE-code COMET has been used. A cavitation module has been developed for this software following the PhD-thesis of J. Sauer [1]. The modelling of the cavitation consists of three steps:

1. Seed distribution
2. convection of vapour bubbles
3. description of bubble growths and collapse

In a real fluid a distribution of cavitation seeds exists, which can be particles or small vapour bubbles. In the model these are simplified to a single seed type 'micro-bubble' with an average radius and an average number.

Cavitation is modelled as a two phase flow, containing the phases water and vapour. The transport of vapour can be treated with Volume of Fluid (VoF) methods, using the vapour fraction C_V.

$$C_V = \frac{\text{Vapour volume}\, V_V}{\text{Standard volume}\, V} \tag{1}$$

An additional transport equation for the vapour fraction is solved.

$$\frac{\mathrm{d}C_V}{\mathrm{d}t} + C_V \nabla \cdot \vec{\mathbf{v}} = \frac{\partial C_V}{\partial t} + \nabla \cdot (C_V \vec{\mathbf{v}}) \tag{2}$$

Compared to standard-VoF applications it is extended by a source term for the creation and destruction of vapour volume. According to bubble dynamics, growth and collapse of vapour bubbles can be described by the Rayleigh-Plesset-Equation.

$$R\frac{\mathrm{d}^2R}{\mathrm{d}t^2} + \frac{3}{2}\left(\frac{\mathrm{d}R}{\mathrm{d}t}\right)^2 = \frac{p_{sat}\,(T) - p_\infty}{\rho_l} - \frac{2\tau_o\,(T)}{\rho_l R} - 4\frac{\mu_l}{\rho_l R}\frac{\mathrm{d}R}{\mathrm{d}t} \tag{3}$$

R	Bubble radius
p_{sat}	Pressure of saturation
ρ_l	Density of liquid
$\tau_o(T)$	Surface tension
μ_l	Viscosity of liquid

The influences of inertia, viscosity and surface tension are neglected. This leads to the equation of Rayleigh.

$$\left(\frac{\mathrm{d}R}{\mathrm{d}t}\right)^2_{Ray} = \frac{2}{3}\frac{p_{sat} - p_\infty}{\rho_l} \tag{4}$$

The Rayleigh equation is used in the method because its numerical solution is much simpler.

3 Calculations in an homogenous flow

Two propellers have been investigated: The propeller of a recent RoRo-ship and the older Propeller of the container-vessel 'Sydney-Express'. A cylindrical section of the former has been investigated at first in a two-dimensional calculation.

3.1 Two-dimensional calculation

A section of one blade at 80 % of the propeller radius is investigated. The profile used in the simulation is not exactly equivalent to the section of the propeller blade but geometrically distorted so as to reach the same pressure distribution as in three-dimensional case at the same radius, calculated with a panel method.

There are no model tests available of this propeller in an homogenous flow, but the form and extent of the calculated cavity seem realistic.

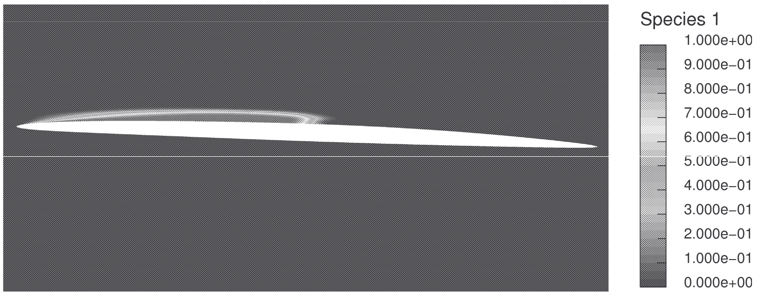

Figure 1: Vapour volume fraction in two-dimensional calculation, $J = \frac{v_A}{nD} = 0.8$, $\sigma = \frac{p_{sys} - p_{sat}}{\frac{1}{2}\rho_l U^2} = 0.35$

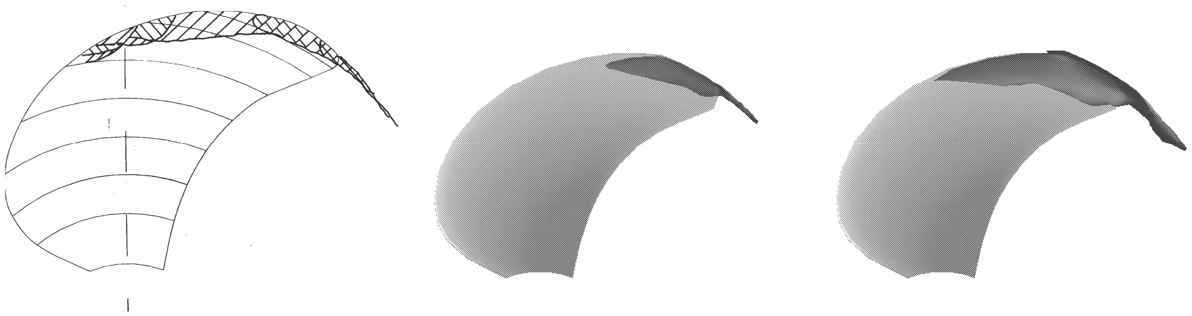

Figure 2: Left: Model test result (source: [4]), middle / right: Calculated Cavity at the propeller of the RoRo-vessel, visualised by iso-surface of vapour volume fraction C_V of 0.5 resp. 0.05. $J = 0.8$, $\sigma_n = \frac{p - p_{sat}}{\frac{\rho_l}{2}(\pi n D)^2} = 0.25$

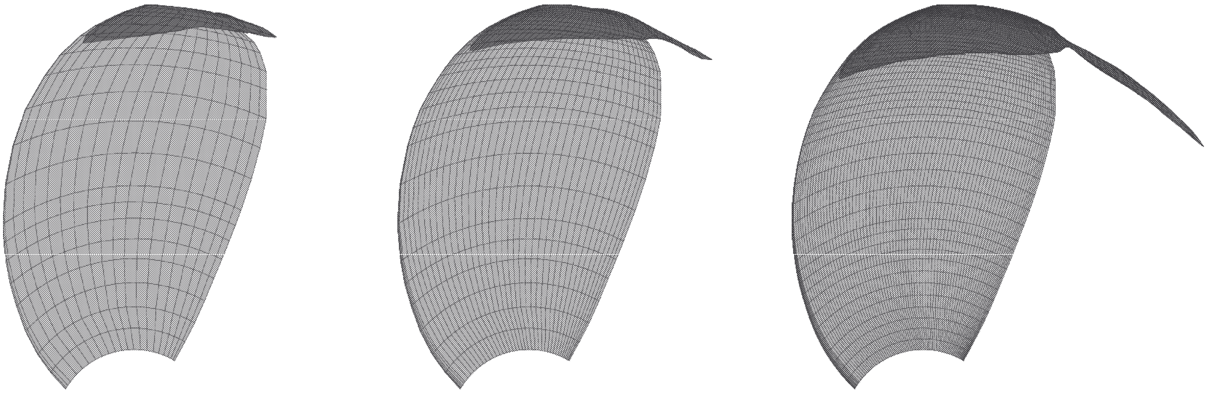

Figure 3: Propeller of ‘Sydney-Express’. Left: Coarse grid, middle: Partially refined grid, right: Refined grid. Dark gray: Cavitation, Iso-surface at $C_V = 0.5$. $\sigma_n = \frac{p - p_{sat}}{\frac{\rho_l}{2}(\pi n D)^2} = 0.185$, Thrust coefficient $k_T = 0.243$.

3.2 Three-dimensional investigations

The propeller of the RoRo-vessel is investigated in an homogenous flow. The grid of one blade consists of approximately 117000 cells, the influence of the other three blades is taken into consideration by cyclic boundaries. Rotation is realized by a rotating coordinate system. The inflow and rotational velocities are chosen similar to the local velocities in the ship’s wake at a position of 200 degrees.

Figure 2 shows the results of the calculation compared to a result of a model test in the cavitation tunnel HYKAT of HSVA behind the ship model. Velocities in this position should be similar to the conditions in the simulation. For the representation of the cavity two criteria have been chosen: vapour volume fractions (C_V) of 0.5 and 0.05. The simulation results in a stationary cavity with tip vortex. With a vapour volume fraction of 0.5 the cavitation at the trailing edge, including the tip vortex, is represented quite well. At the leading edge there is less cavitation than observed in the model test. This area is represented better with a criterion of $C_V = 0.5$.

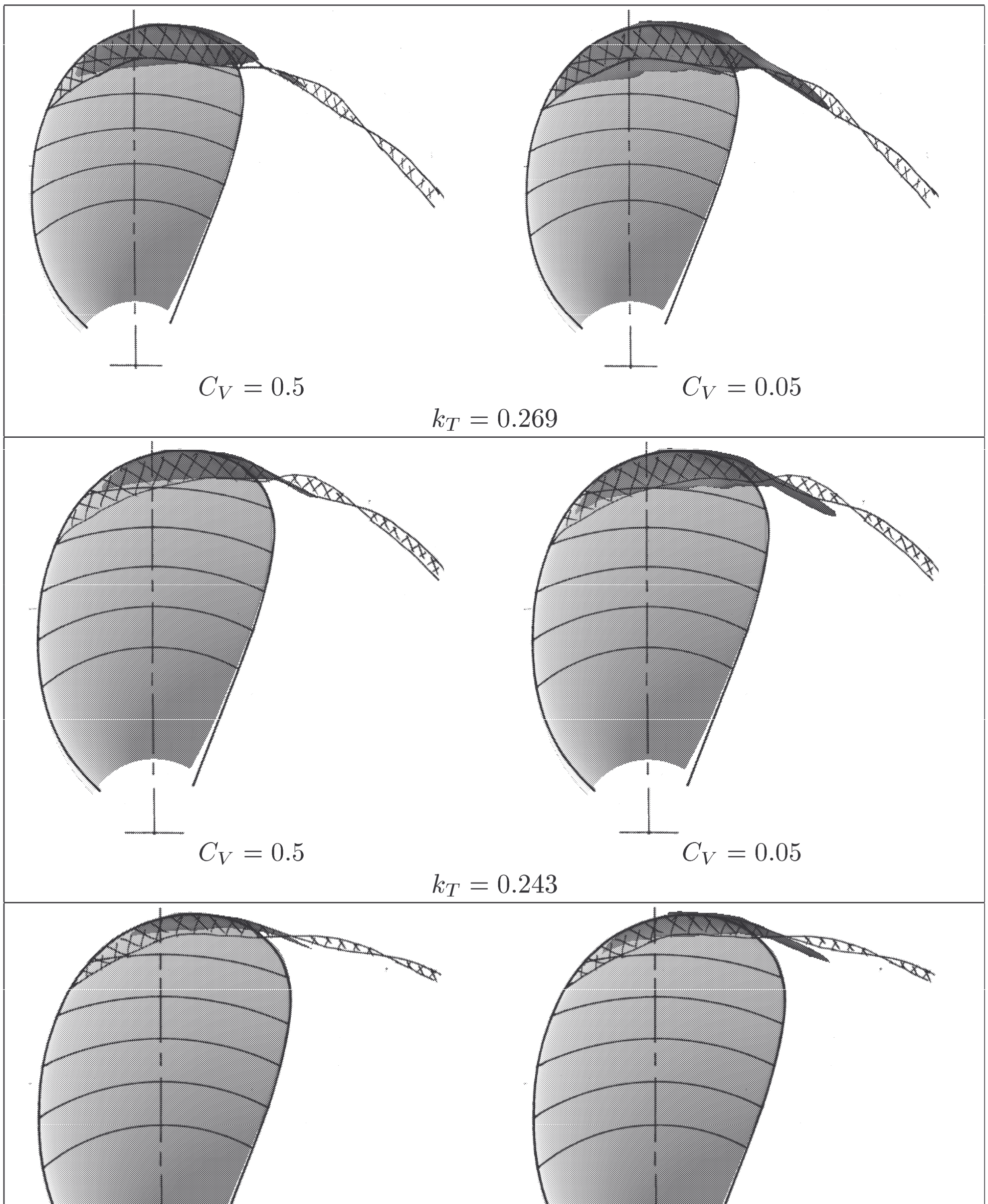

Figure 4: Comparison of simulation and experiment, grid of approx. 100000 cells. Sketch: Observation from experiment, dark gray: Cavity according to Calculation, iso-surface of $C_V = 0.5$ resp. 0.05. $\sigma_n = 0.185$

3.3 Simulations with the propeller of the 'Sydney-Express'

No model test results in homogenous flow are available of the Propeller of the RoRo-ship. For this reason investigations are continued using the propeller of the container-vessel 'Sydney-Express'. This propeller could be used for model test in the large cavitation tunnel of HSVA. No wire mesh has been used for the generation of a wake field. Three different loads have been investigated.

For the simulation, three different grids have been prepared, of 36000, 100000 and 650000 cells. Figure 3 shows the different grids and the simulation results. It is visible, that the cavity is calculated too small using the coarser grids. Nevertheless the medium grid is used for further calculations, because the calculation time was 38 hours using the medium grid, while it was twelve days using the fine grid.

Figure 4 shows the calculation results for the three

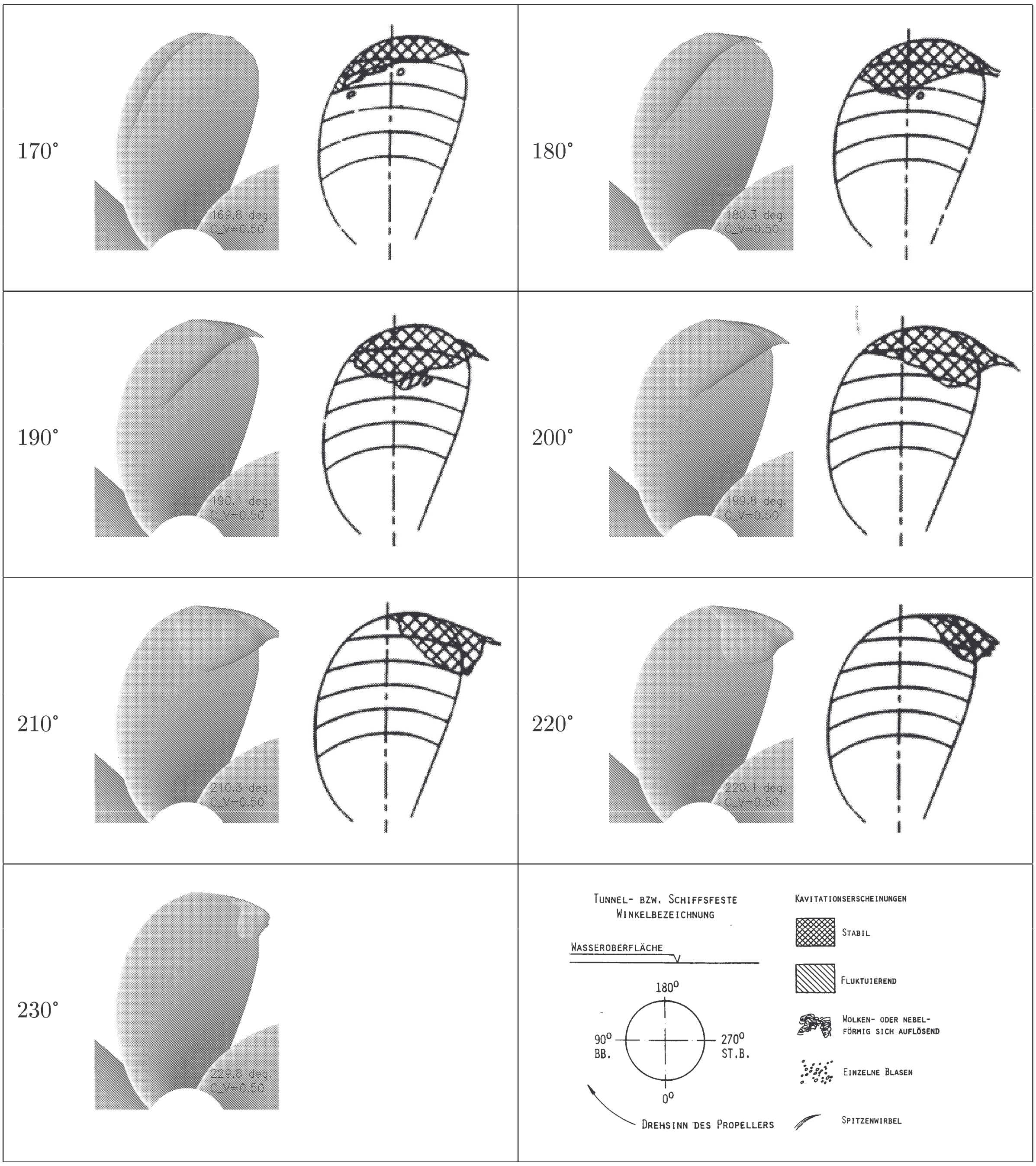

Figure 5: Propeller cavitation in axial wake field. Left: Simulation, right: experiment (source: [5]). $k_T = 0.179$, $C_V = 0.5$, $\sigma_n = 0.185$.

different loads, compared with the results of the model test. In all cases calculation and model test showed a stationary cavity, consisting of sheet cavitation on the outer radii and a cavitating tip vortex. As above, two criteria for the representation of the cavity are plotted. The form and extended is generally well met, but using the criterion of $C_V = 0.5$ the cavity is too small near the leading edge. With $C_V = 0.05$ it is too large near the trailing edge. For the lowest load the simulation shows a smaller cavity than the model test.

4 Simulation in axial ship's wake field

Another simulation with the propeller of the 'Sydney-Express' has been examined, using the axial wake field of the ship as inflow boundary condition. The tangential component of the wake has been neglected. In this calculation the whole propeller must be modelled.

Figure 5 shows the calculation results compared to results of model tests carried out in the medium sized

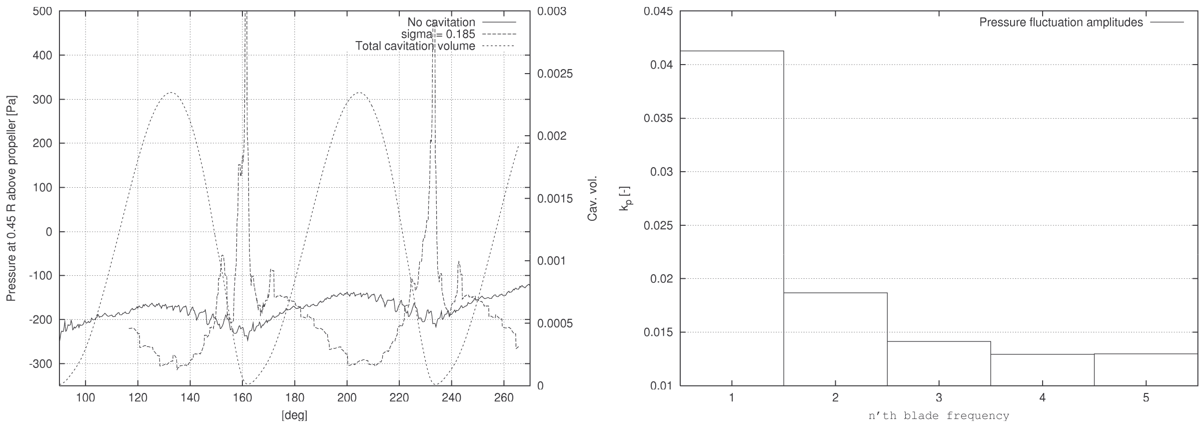

Figure 6: Left: Pressure above Propeller plotted above angular position of one blade. For comparison the total vapour volume is also plotted. Right: Normalised pressure fluctuation amplitude $k_p = \frac{\hat{p}}{\rho_l n^2 D^2}$, received from calculated pressure development. $\sigma_n = 0.185$

cavitation tunnel of HSVA. For the generation of the wake in the tunnel a wire mesh has been employed, so that there is no tangential velocity component as in the calculation.

The extent and form of the simulated cavity is very similar to the one observed in the model test. At the position of 170°the calculated cavity reaches further to the hub. The development of the cavity is a little late compared to the model tests. This delay may be explained by the fact that the wake is given at the inlet boundary 20% of the propeller radius in front of the propeller and not in the position of the propeller.

During the numerical simulation of the propeller in the ship's wake, the pressure fluctuations above the propeller have been recorded. Figure 6 shows the pressure at the monitoring location approximately 45 % of the radius outside the propeller disc. For comparison the pressure from a calculation without cavitation is also plotted. The third graph shows the total vapour volume. There are strong peaks visible at the moments when the cavity collapses. The normalised pressure fluctuation amplitudes are shown in the figure to the right. The value of 0.041 for the blade frequency is of the same order as values received from model tests as well as full scale measurements. An exact comparison is not possible because of different tunnel geometries between model tests and numerical simulation.

5 Criteria for the graphical representation of the calculated cavity

In figures 2, 3, 4 and 5 the cavity is represented by an iso-surface for the vapour volume fraction. As a first attempt a criterion of $C_V = 0.5$ as in free surface calculations is used. As visible above this leads to cavities which are too small near the leading edge. One possible explanation is, that the cavity is still very thin here and the grid is too coarse for a correct resolution of this thin sheet.

Another possibility would be to use another criterion. The vapour volume fraction C_V is analytically connected to the bubble radius R:

$$C_V = \frac{n_0 \cdot \frac{4}{3}\pi R^3}{1 + n_0 \cdot \frac{4}{3}\pi R^3} \tag{5}$$

$$\begin{aligned} R & \quad \text{bubble radius} \\ n_0 & = \frac{\text{Number of cavitation seeds}}{\text{Standard Volume}} \end{aligned}$$

A vapour volume fraction of 0.5 corresponds to a bubble radius of 1.34 mm, based on a number of seeds of $n_0 = 10^6$, while a $C_V = 0.05$ corresponds to $R = 0.5$ mm. A closer look at model tests is necessary to find out which size is taken into account in the model tests. Lindenau [2, 3] suggests using different criteria for different kinds of cavitation.

6 Conclusions

The cavitating flow around two propellers in an homogenous velocity field has successfully been simulated using RANSE-methods. The results, in general, show a good correspondence to model tests. Also, a calculation in a ship's wake field shows similar cavitation behaviour as observed in a model test.

Due to the necessarily small time step, calculation times were quite large. Parallel computing, which was not possible when these calculations were carried out, but is now available, will be a great advantage.

Further investigations are necessary to find a reliable iso-surface criterion for the graphical representation of the cavity.

Also, the correspondence of the fluid quality (gas content, seed distribution), and the initial conditions of the numerical model (concentration and radius of cavitation seeds) has to be subject of further investigations.

References

[1] J. Sauer, *Instationär kavitierende Strömungen – Ein neues Modell, basierend auf Front Capturing (VoF) und Blasendynamik*, PhD-Thesis, University of Karlsruhe, 2000

[2] O. Lindenau, V. Bertram, *RANSE Simulation of Cavitating Flow at a Foil*, Ship Technology Research 50/2003, pages 51-65

[3] O. Lindenau, H. Streckwall, V. Bertram, *RANSE Simulations for Cavitating Hydrofoils*, Proceedings of 5th Numerical Towing Tank Symposium (NuTTS), Pornichet, France, 2002

[4] H. Streckwall, *Berechnung 3-dimensionaler Kavitationserscheinungen mit Finite-Volumen-Methoden*, HSVA-Report No. 1655, 2003

[5] H. Tanger, *Einfluß des Gasgehaltes auf Kavitation und propellererregte Druckschwankengen*, HSVA-Report No. 1580 Part 3, 1993

Adaptive Multigrid for the Incompressible Navier Stokes Equations

Sofia Werner[1], Björn Regnström[2], Lars Larsson[3]

[1] Graduate Student, Dept. of Naval Architecture, Chalmers University of Technology, Sweden,
sw@na.chalmers.se
[2] Research Engineer, Dept. of Naval Architecture, Chalmers University of Technology and
Flowtech International AB, Sweden
[3] Professor, Dept. of Naval Architecture, Chalmers University of Technology, Sweden

Abstract

The first steps toward the implementation of an adaptive multigrid (AMG) method for the flow code Chapman are described. The recursive adaptation procedure creates a set of aligned refined grids of several refinement levels. A velocity gradient adaptation criteria is used to locate the under-resolved areas. The AMG method is applied to a 2D laminar test case and evaluated using a grid convergence study. The adapted grid is shown to be more efficient in terms of grid points and computational time compared to a uniform grid.

1 Introduction

The new flow solver Chapman is currently under development by Flowtech International AB and Chalmers University of Technology. Chapman is a structured multigrid solver intended to run large simulations of ship hulls on ordinary work stations. In order to manage that task with a satisfactory accuracy an adaptive mesh refinement procedure compatible with the multigrid solver needs be implemented. The present paper describes the first attempts to develop this adapted multigrid (AMG) technique for Chapman.

The refinement criterion investigated here is a velocity gradient based criterion based on the Theory of Smallest Length Scale [3][4]. In regions where the criterion is fulfilled new refined subgrids are created. Together with the existing grids they form a grid hierarchy of several refinement levels. This approach enables us to benefit from the multigrid algorithm already implemented in Chapman. The AMG method is evaluated using a formal grid convergence study of the adapted grid structure for a simple 2D test case. The goal is to verify that the solution on the adapted grid approaches the same values as a uniform grid by using less grid points and computational time.

2 Flow code

2.1 Solver

The incompressible RANS equations are solved on structured overlapping grids in a coupled system using a finite volume discretization. The viscous fluxes are discretized with a central differencing scheme, while an upwind scheme based on Roe flux splitting [6] is used for the non-viscous fluxes. This discretization is formally first order. A minmod-limited flux correction increases the accuracy to second order. The second order correction is not used for the calculations in the present work. Pseudo-time stepping with Euler backward differencing is used to reach a steady state solution.

The discretized and linearized equations are solved with a Non-Aligned Multigrid method using the Full Approximation Storage technique. A V-cycle starts at the finest level, smoothings are carried out and defect corrections are calculated for the next level until the coarsest grid is reached. At this level the equations are solved to machine accuracy. Instead of prolongating the coarse grid solution directly back to the fine grid a sweep is made through all levels, whereby a coarse grid correction is computed at each level. The smoothing is carried out using the block Jacobi method.

2.2 Grid structure

The flow domain outside the ship surface is represented by a number of overlapping base grids. The base grids are either Cartesian (background grid) or curvilinear (bodyfitted grids). Each base grid contains a hierarchy of refined subgrids taking part in the multigrid algorithm. A subgrid is always aligned and shares the mapping function with its base grid.

3 Adaptation technique

3.1 Development strategy

The goal of the present efforts is to develop an adaptation procedure for the grid structure described above. Since the target geometry is fairly simple, a suitable division of the domain into base grids can be done manually based on experience; there are no reasons to automate this process. The purpose of the automatic adaptation procedure is to find suitable grid densities of the grids **within** the prescribed base grids. Hence, the adaptation procedure needs only to consider one base grid at a time. The work toward a satisfactory adaptation techniques can therefore be carried out on a single mapping test case.

3.2 Adaptive grid structure

Our AMG approach is based on the nested grid scheme first described by Berger and Oliger [2]. The adaptation procedure produces a set of aligned grids of increasing refinement levels. The coarsest grids cover the whole domain while subgrids of larger grid density are placed over regions that require higher resolution. By forcing the subgrids to be aligned with the underlying base grid, a inexpensive interpolation scheme can be employed for the grid-to-grid communication. Each level in the grid hierarchy represents a refinement ratio increment of 1 compared to the level below. The increment can be in one or several directions. Each subgrid is completely embedded within its parent grid. For reasons related to the multigrid procedure, one subgrid is not permitted to overlap other grids on the same refinement level.

The grid points that are covered by finer grids are not omitted from the calculations. This gives a double coverage of some areas, which may seem not to be the best way to economize with grid points. However, by taking part in the multigrid algorithm, the coarser grids efficiently take care of the long wave length errors which speeds up the over-all convergence. This advantage would be lost if grid points were omitted from the low level grids.

3.3 Refinement criterion

Several refinement criteria are planned to be tested for the AMG procedure of Chapman. The present work treats a velocity gradient type of criterion based on the Theory of the Smallest Length Scale by Reyna et.al. [3]. According to this theory, the discretized Navier-Stokes equations are accurately resolved if the cell size is smaller than the square root of the viscosity divided by the largest local velocity gradient. The theory is developed using Fourier analysis for the purpose of investigating the numerical stability of Navier-Stokes solutions. Since the smallest length scale defines the smallest features of the flow and marks the limit between resolved and under-resolved flow, Reyna et.at. suggest that it may be used as a refinement criterion, even though it is not applied as such in their own work.

In the test case presented here the grid is refined if

$$\frac{h_i}{\lambda_i} > 1, \tag{1}$$

where h_i is the cell size in the direction i and

$$\lambda_i = \sqrt{\frac{\nu}{|\partial_i(\mathbf{u})|}}. \tag{2}$$

This is equivalent to a viscosity dependent tolerance in a velocity gradient type of adaptation criterion.

For a turbulent flow, this refinement criterion corresponds to resolving the Kolmogorov scales, which will require grid densities far too high for practical applications. Future investigations will examine whether the Smallest Length Scale criterion can be combined with the turbulence models used in Chapman to obtain a suitable criterion for the turbulent flow. The possibility of detecting under-resolved turbulent flow by using the effective viscosity in the expression 2 has been studied in [7].

3.4 Adaptation procedure

The adaptation cycle starts by advancing the solution a number of multigrid cycles on two or more levels of coarse base grids, each covering the whole domain. The adaptation criterion is calculated in each cell of the finest base grid. Every cell that satisfies the refinement criteria in both the x- and y-directions is flagged and the flagged cells are grouped in suitable rectangular areas. The same thing is done for the cells that fulfill the criteria in x but not in y, and the other way around. New refined subgrids are created in the obtained areas, and data from the parent grid are interpolated to the subgrids. The adaptation criterion is calculated on the new subgrids based on the interpolated data, and the refinement process continues recursively with the new subgrids as parent grids. Several parameters control the process, e.g. minimum size of a subgrid, ratio of unflagged/flagged cells to be tolerated without trying to divide an area into two areas etc.

The multigrid solver can now be applied to the new grid structure. After a number of multigrid cycles the adaptation criterion is evaluated again, and if necessary, the adaptation cycle is re-started. The new subgrids will then copy data from old subgrids of the same level if possible, and otherwise from levels below, after which the old subgrids will be deleted. In this way, there is no need for a coarsening algorithm. If a region of high active flow moves or changes its shape, the old out of date subgrids will be replaced by new updated subgrids.

4 Test case

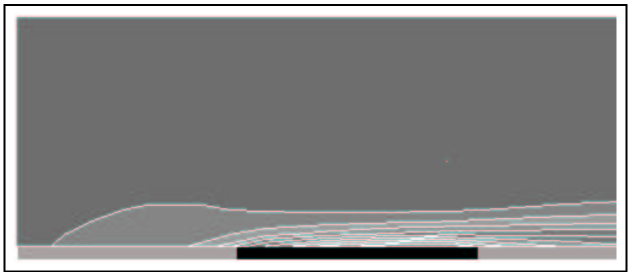

Figure 1: Part of the x-velocity field. Plate shown in black.

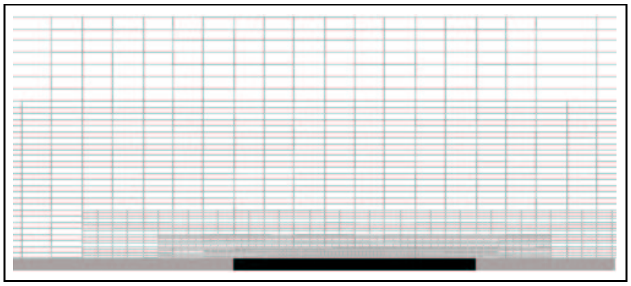

Figure 2: Part of the adapted grid structure. Plate shown in black.

Our first test case considers the laminar flow past a 2D flat plate, including the entrance effect and the wake. This test case is simple enough to allow a large number of simulations with modest resources. Large velocity gradients in both the x- and y-directions make the flow field complex enough for serving as a suitable test of the AMG method.

The adaptation is applied to a uniform Cartesian grid. For the current test case it would be reasonable to use a stretched base grid. However, for the purpose of developing the AMG technique the uniform base grid is sufficient as a first attempt. Later work will deal with adaptation of stretched base grids.

We define a computational coordinate system with the origin at the plate leading edge and the x-axis in the direction of the inflow. The computational domain reaches from 1.5 plate lengths upstream of the leading edge to 2.5 plate lengths downstream of the trailing edge. The domain height is two plate lengths, about 8 times the boundary layer thickness. The inflow profile is a uniform velocity profile of magnitude 1 in the x-direction. The slip condition is applied on all edges parallel to the plate except from at the plate surface, where the no-slip condition is used. A homogeneous Neumann condition for the velocity and a Dirichlet condition for the pressure are used at the outflow plane.

The solution on the adapted grid is compared to the original solution using one local and one integrated parameter, namely the x-velocity at a fixed point in the boundary layer $(\frac{L}{2}, \frac{L}{40})$ and the total skin friction coefficient C_f. The point velocity is found by a fourth order polynomial interpolation between cell centers. The skin friction coefficient C_f is calculated by

$$C_f = \frac{\int_0^L \mu \frac{\partial u}{\partial y}|_{y=0} \mathrm{d}x}{\frac{1}{2}\rho u_\infty^2} \tag{3}$$

where the integration is approximated using the trapezoidal rule and the velocity gradient at the wall by a first order upwind scheme.

Figure 1 shows the x-velocity field at Reynolds number 400, which is the flow case used for all calculations presented in the following sections. For this Reynolds number, the pressure is not constant with y in the boundary layer at any x-position. Also, the free stream velocity above the plate exceeds the inflow velocity due to the finite domain height. For those reasons, the flow field cannot be regarded as a Blasius boundary layer and therefore, analytical values cannot be used as a reference.

The base grid consists of one 20x40 and one 40x80 grid that both cover the whole domain. The solution is advanced one multigrid cycle on the base grids before the adaptation procedure is applied. (Tests have shown that one multigrid cycle is sufficient for establishing converged values of the adap-

N_{loc}*	h	C_f	p	$u(\frac{L}{2},\frac{L}{40})$	p
1455	4	0,03412	-	0,3075	-
5788	*2*	*0,03438*	-	*0,2980*	-
13047	1,33	0,03436	nan	0,2958	1,62
23152	1	0,03435	0,96	0,2951	2,036
∞	0	0,03432		0.2941	

*)Number of cells on the locally finest level

Table 1: Result of *adapted grid* and its refined/coarsened clones.

N_{loc}	h	C_f	p	$u(\frac{L}{2},\frac{L}{40})$	p
800	16	0,03656	-		-
3200	8	0,03607	-	0,3484	-
7200	5,33	0,03567	nan	0,3253	-
12800	4	0,03541	0,24	0,3145	1,16
51200	2	0,03492	0,52	0,3011	1,43
204800	1	0,03462	0,70		
∞	0	0,03414		0.2933	

Table 2: Grid convergence of uniform grid

tation criterion. Advancing the base grids further will result in exactly the same adapted grid structure.) The simulation continues with repeated multigrid cycles on the adapted grid structure until convergence is reached. For this simple test case there is no need to re-run the adaptation cycle. A part of the adapted grid structure is shown in Figure 2.

5 Evaluation of the adaptive method

5.1 Accuracy and storage efficiency

The importance of formal convergence studies for verification of CFD results has been expressed by several authors, for example in the ITTC Guidelines [1]. We believe that this is also important for adapted grids, especially in the development phase. We will in the following use the verification method due to Eca and Hoekstra [5] to investigate the adapted grid from the test case described above. A set of geometrically similar grids is obtained by refining or coarsening the adapted grid hierarchy with a refinement factor of r, while keeping the relative size, placement and order of the subgrids fixed. Two refined and one coarsened clone of the adapted grid are created. Solutions are obtained on the refined grid hierarchies with multigrid cycles until convergence is reached. The result is given in Table 1, where the order of accuracy p and the extrapolated zero cell size solutions are calculated using the curve fit approach [5] applied to 3 grids at a time (equivalent to the Richardson Extrapolation.) The reference cell size h in the tables represents the inverted refinement factor with respect to the finest grid in each series. For comparison, a grid convergence study of a uniform grid is presented in Table 2.

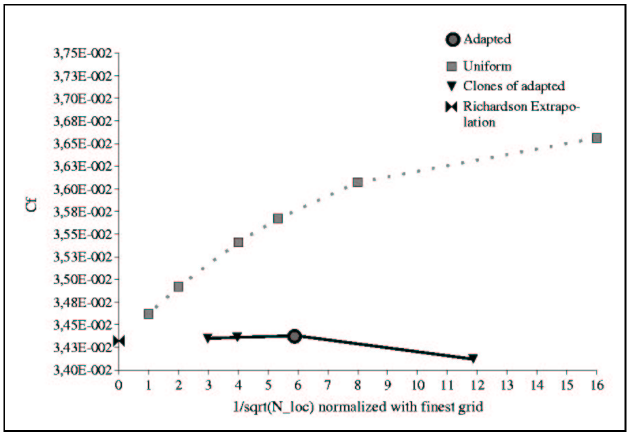

Figure 3: Frictional resistance coefficient versus the inverse square root of the number of cells on the locally finest level, normalized against the finest grid

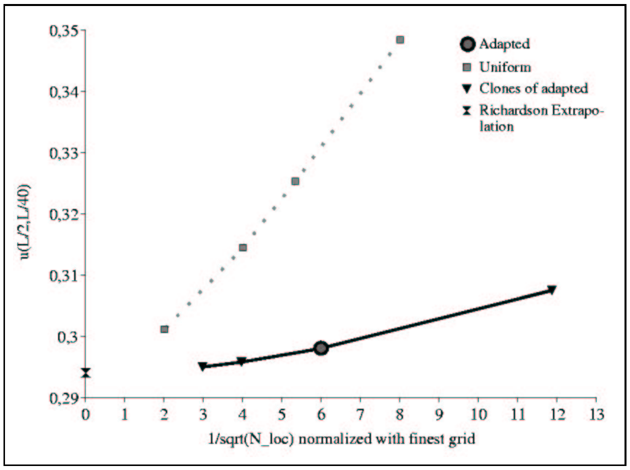

Figure 4: x-velocity at $\frac{L}{2},\frac{L}{40}$ versus the inverse square root of the number of cells on the locally finest level, normalized against the finest grid

Figure 3 and 4 compare the results of the two grid series with respect to the cost of grid points. The solutions are plotted against the inverse square root of N_{loc}, the number of cells on the locally finest level, normalized against the finest grid. The coarser cells hidden under the fine layers are not counted since their purpose is to speed up the multigrid convergence, they will not contribute to the accuracy of the solution.

These tables and graphs show that the solutions on the adapted grid tend toward the same solution as on the uniformly refined grid. Furthermore, they show that for the same amount of grid points, the adaptive grid solution is closer to the extrapolated zero cell size solution.

In spite of the fact that the solver is formally first order for the current calculations, the order of accuracy p is as high as 2 for the point velocity values. This can be explained by the fact that the viscous terms are discretized by a second order scheme. For the current low Reynolds number test case, the viscous terms dominate the convective terms, discretized by a first order scheme, and this increases the order of accuracy.

For the C_f values, however, the order of accuracy is only approaching 1, and for the uniform grid p is considerably lower then 1. The suspicion that this is due to the numerical integration did not prove to hold. Employing a second order Simpson integration did not change the result noticeably. The cause of the low accuracy is probably the linear approximation of the velocity derivative at the wall, though this has not yet been verified numerically. The reason why the values of C_f are far from the asymptotic range (p far from 1) for the uniform grid is probably that the flow close to the wall is so under-resolved that the derivative is taken in the non-linear part of the velocity profile. This points out the secondary effect of the adaptation. Refining the grid where the velocity gradients are large will increase the accuracy of the post-processing calculations, i.e. approximations of derivatives and integrals.

5.2 Computational time

In the previous section we investigated how the solution error depends and the number of grid points on the locally finest level. Of the same importance is the dependency of the computational time. Figure 5 shows the error, relative to the extrapolated zero cell size solution, as a function of computational time. The uniform grid series in this plot is obtained by repeatably adding refined multigrid levels to a uniform base grids. Hence, those grids contain enough levels to ensure a fast convergence. Still, the adapted grid displays a faster convergence for a given error.

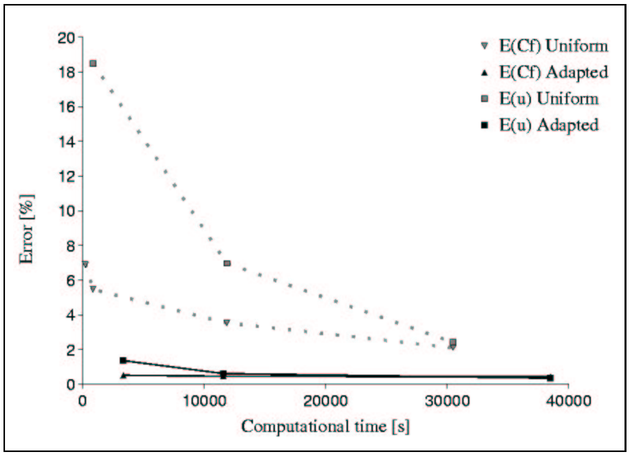

Figure 5: Error % relative to extrapolated solution versus computational time.

5.3 Tuning the adaptation parameters

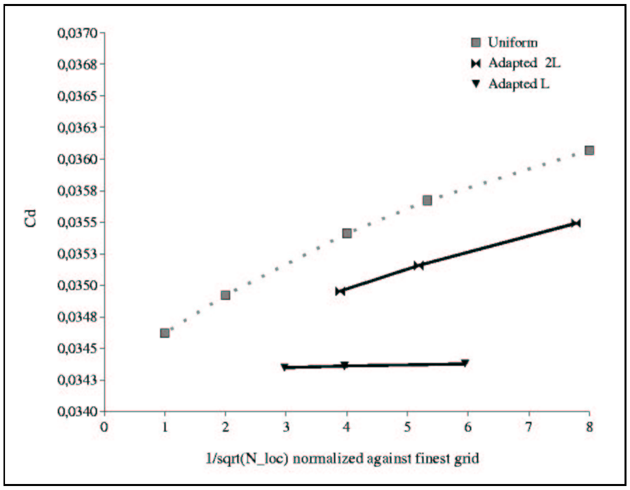

Figure 6: Comparing adaptation criteria

The verification technique illustrated above can be used in the development phase of the AMG method, for example when tuning the magnitude of the criterion and the parameters that govern the process, or when comparing alternative types of adaptation criteria. With a verification study we can not only find out which alternative is close enough to "the right" solution with least effort, we can also verify that this solution is approached with a certain order of accuracy, which should increase the confidence in the result.

As an example Figure 6 compares the adaptation criterion λ used above with the criterion set to 2λ, where the latter is clearly inferior.

6 Conclusions

The first efforts of developing an adaptive multigrid (AMG) technique for the flow code Chapman are described. The goal of this work is to reach the same accuracy as a uniform grid using fewer grid points and less computational time. The AMG technique is applied to a 2D test case consisting of the laminar boundary layer of a flat plate. The result is evaluated using formal grid convergence studies of the original and the adapted grid structure. The work results in the following conclusions:

- The solutions on the two grid types approach the same extrapolated zero cell size values. The adapted grid solutions are closer to this value for the same amount of cells on the locally finest level. Hence, the adaptation is successful in terms of grid points savings.
- The error relative to the extrapolated solution is smaller for the adapted grid than for the uniform for the same computational time.
- The Theory of the Smallest Length Scale has been applied as refinement criterion. For the present laminar test case, this criterion gives reasonable grids. Whether this theory can be useful for turbulent cases still needs to be investigated.
- Applied to adapted grids, formal verification methods can be used for evaluating the success of an adaptive method and for tuning the technique.

7 Further work

The work described here comprises the first steps toward a well functioning AMR for Chapman. The next phase in the development will include investigations of different types of adaptation criteria suitable for turbulent flow. Moreover, a great deal of work remains to make the AMR procedure applicable to 3D, stretched and curvilinear grids.

References

[1] 22nd International Towing Tank Conference. *ITTC - Quality Manual*, 1999.

[2] Oliger J. Berger M.J. Adaptive mesh refinement for hyperbolic partial differential equations. *Journal of Computational Physics*, 53:484–512, 1983.

[3] Reyna L.G. Henshaw W.D., Kreiss H.O. On the smallest scale for the incompressible navier-stokes equations. *Theoretical and Computational Fluid Dynamics*, 1:65–95, 1989.

[4] Reyna L.G. Henshaw W.D., Kreiss H.O. Smallest scale estimates for the navier-stokes equations for incompressible fluids. *Arch.Rational Mech. Anal.*, 112:21–44, 1990.

[5] Eca L. Hoekstra M. On the application of verification procedures in computational fluid dynamics. In *2nd MARNET-CFD Meeting Copenhagen*, 2000.

[6] Roe P.L. Approximate riemann solvers, parameter vectors and difference schemes. *J. Comp. Phys.*, 43:357–372, 1981.

[7] Svennberg U.S. *On Turbulence Modelling for Bilge Vortices.* PhD thesis, Chalmers University of Technology, 2000.

Towards accurate wake predictions of twin-screw ships with an open-shaft stern configuration.

Jaap Windt
Maritime Research Institute Netherlands (MARIN), P.O. Box 28, 6700 AA Wageningen, Netherlands.
e-mail: j.windt@marin.nl

Nomenclature

U_∞ : Axial free stream velocity.
W_s : Transverse velocity at the wall.
u, v, w : Cartesian velocity components.
p : Pressure.
x, y, z : Cartesian co-ordinates.
ξ, η, ζ : Curvilinear co-ordinates.
D : Cylinder or shaft diameter.
$\overline{x}$: Node on cylinder.
$\overline{r}$: Direction vector cylinder centreline.
$\overline{z}$: Node on cylinder centreline.

1. Introduction

Many twin-screw ships have a so-called open-shaft stern configuration. While in most cases the hull has a geometrically simple shape, the protruding shafts, bossing and supporting struts make the over-all geometry complex. This geometrical complexity and possibly the shaft rotation cause the behaviour of the flow near the shafts and brackets to be complicated as well, and it is a challenge to be able to make reliable numerical flow predictions.

As a first step in establishing this capability at MARIN, using the PARNASSOS code (see [1]), we have considered the calculation of the viscous flow around an inclined non-rotating cylinder protruding from a flat plate. In 1997, Pinard [2] investigated this kind of flow experimentally. In 2001, Hally [3] predicted the flow using a viscous flow solver and compared the calculations with the experiments; the agreement between numerical and experimental data was found to be good. As a second step we studied the same case but now with the cylinder rotating about its axis. Finding serious difficulties, we reduced the complexity of the case by considering the flow along a rotating (around its axis) cylinder aligned with the main flow. The flow along the rotating cylinder was investigated experimentally by Lohmann [4] in 1976 and investigated numerically in 1982 [5].

The inclined cylinder test case is used to investigate the possibility to incorporate the shaft in real ship calculations when applying the same kind of grid topology, i.e. an O-H type, that is usually being applied at MARIN. The flow around the flow aligned rotating cylinder is used to test the implementation of the new boundary condition in the PARNASSOS code, to investigate the necessary grid density in case of rotation and to reveal imperfections of turbulence modelling.

2. Test cases

2.1 Inclined cylinder protruding from a flat plate

Numerical set-up

The experiments by Pinard have been performed in a circulating water tunnel. The roof of the tunnel test section represented the flat plate. The cylinder protruded from the tunnel wall and was fixed to the bottom of the test section further downstream. Three different cylinder inclination angles (5, 8 and 12-degrees) have been used and three different incident boundary layer thicknesses have been imposed. This gives a total of nine experimental configurations.

In the numerical simulations we focus on only one experimental set-up, viz. the cylinder protruding from the flat plate at an inclination angle of 8 degrees, with an incident boundary layer thickness at plane P1 roughly equal to 3.2D. Figure 1 gives an impression of the set-up as used in the calculations.

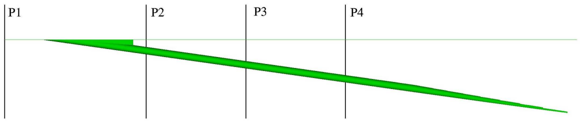

Figure 1: Numerical set-up and measurement planes.

The planes P1 to P4 represent the measurement planes. The cylinder protrudes from the plate and is extended beyond the last measurement station P4 where the cylinder diameter is gradually reduced until it vanishes.

Grid topology

While Hally adopted an O-type grid around the cylinder, which was highly sheared because it was fitted to the plate as well, we operate with a grid topology similar to what we presumably would use for a real ship case, i.e. an O-H type grid. The single-block grid can be described by curvilinear co-ordinates, ξ, η and ζ running roughly in streamwise, wall-normal and girthwise direction respectively. In principle this grid topology is capable of capturing the geometry of the ship including the shaft, although the grid does not fit to the cylinder as nicely as in Hally's grid. Important to realise is that the diameter of the shaft is quite small compared to the ship's main dimensions. So, a very fine grid may be needed to resolve the flow phenomena close to the shaft. To investigate the influence of the grid resolution and to get experience with grid generation for typical hull+shaft geometries, we decided to calculate the flow around the inclined cylinder on three grids of varying density.

The computational domain is defined as follows: the width of the flat plate is equal to half the width of the tunnel roof;

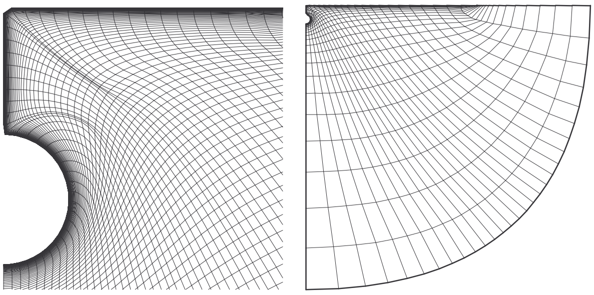

Figure 2: O-grid around cylinder and flat plate.

the total width of the domain is approximately 30 cylinder diameters; the inlet of the computational domain is located at plane P1, at which the incident boundary layer was measured; behind the cylinder the computational domain is extended in downstream direction over approximately 50 cylinder diameters. The $\eta = 0$ plane models the flat plate, symmetry plane and cylinder. Hence an O-grid is created running around the cylinder and along the flat plate. In streamwise direction an H-grid topology is applied. A representative ξ =constant plane is plotted in Figure 2.

Close to the flat plate, the geometry of the cylinder is slightly modified. It was impossible to use an O-type grid near the junction of the flat plate and the "trailing edge" of the cylinder because of unacceptable local grid properties. The figure at the right shows several sections of the cylinder-plate configuration close to the junction.

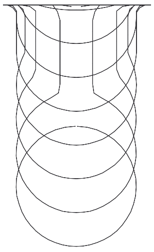

The finest grid is generated by elliptic grid generation methods. From this grid two coarser grids are extracted (each 2nd or 4th grid node is used in all three directions) which will be denoted as medium and coarse. The grids consist of 145x161x113, 73x81x57 and 37x41x29 nodes, with 20, 10 and 5 cells on half the cylinder circumference respectively.

Boundary conditions

Inlet plane: fixed velocity components u, v and w, i.e. a boundary layer profile with boundary layer thickness equal to 3.2D in conformance with the measurements. Outlet plane: first ξ-derivative of pressure equal to zero. Cylinder and flat plate: no-slip condition $\partial p / \partial \eta = 0$ and $u = v = w = 0$ or W_s / U_∞ fixed. The transverse velocity vector at node $\overline{x}$ can be written as:

$$W_s = \frac{(\overline{x} - \overline{v}) \times \overline{r}}{\| (\overline{x} - \overline{v}) \times \overline{r} \|} \quad with \quad \overline{v} = \overline{z} + \lambda \overline{r}, \; \lambda = \frac{\overline{r} \cdot (\overline{x} - \overline{z})}{\overline{r} \cdot \overline{r}}$$

Outer boundary: fixed pressure and tangential velocity components (from potential flow solution). At the remaining boundaries symmetry conditions are imposed.

The size of the computational domain is deliberately chosen to be rather large. Therefore the influence of the size of the domain on the computational results is not considered in this paper.

2.2 Flow aligned rotating cylinder

Numerical set-up

The experiments of Lohmann consisted of measurements of the boundary layer along a circular cylinder in an external flow parallel to its axis and with a rotating segment of the cylinder downstream. The incident boundary layer thickness, $x / D = -0.0474$ upstream of the rotating section, is approximately 15% of the cylinder radius. Initially a two-dimensional boundary layer develops along the cylinder. At the rotating section the boundary layer becomes three-dimensional due to the transverse shear forces. Three different values of the surface-to-free-stream velocity ratio $W_s / U_\infty = 0$, 1.45 and 2.2 have been investigated. The experiments without surface rotation are performed to measure the reference boundary layer thickness. All of the measurements were obtained at a free stream velocity $U_\infty = 16.8$ m/s at $\mathrm{Re} = 2.9 \times 10^5$ based on the free stream velocity and cylinder diameter.

The calculations are performed with and without surface rotation, however $W_s / U_\infty = 1.45$ only. With this simulation we investigate discretisation errors due to for example grid topology. The flow has to be axi-symmetric so any deviation from symmetry will be due to an asymmetric grid topology or discretisation. Moreover the simulation is used to investigate the necessary grid density and to reveal imperfections of turbulence modelling.

Grid topology

At first we used a grid topology nearly similar to the inclined cylinder case. However because no flat plate is present, this means a C-grid around the cylinder and along the vertical symmetry plane. With this kind of topology two blocks model the computational domain only.

The computational domain is defined as follows: the cylinder is placed 2.5 cylinder diameters below the horizontal symmetry plane to avoid influence of the symmetry conditions on the flow close to the cylinder; the inlet and outlet planes are located at $x / D = -0.568$ and $x / D = 2.5$ from the upstream end of the rotating section respectively; the outer boundary is located at approximately 5 cylinder diameters from the cylinder axis.

The grid node distribution in main stream direction is equidistant with 28 nodes on the rotating part and 49 nodes in total. In wall normal and girthwise direction 81 and 24 nodes are used respectively. 11 nodes are used on half the cylinder circumference. A second grid is generated with a different grid node distribution in girthwise direction. Grid nodes are highly clustered at the top section of the cylinder: 121 grid nodes are used with 61 nodes on half the cylinder circumference.

Driven by the numerical results obtained with this kind of grids, which will be discussed later on, a second grid topology is applied. An O-grid around the cylinder is

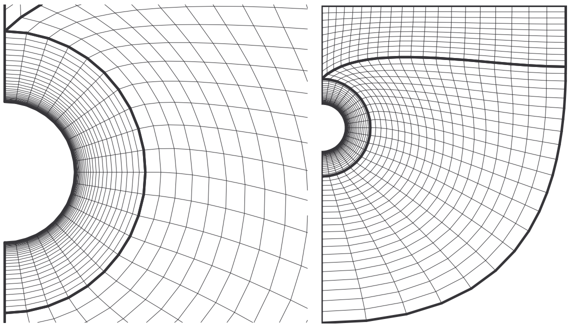

Figure 3: O-grid embedded in C-grid.

embedded in the C-grid as plotted in Figure 3. Because the grid is symmetric only three blocks have been plotted. With this kind of topology six blocks model the computational domain. The O-grid around the cylinder contains 21 nodes on half the cylinder circumference, 61 nodes in wall normal direction and 49 nodes in main stream direction, i.e. a 49x61x21 grid. To examine the grid dependency several other grids have been generated: 25x61x21, 97x61x21, 49x61x11 and 49x121x21.

Boundary conditions

Inlet plane: fixed velocity components u, v and w. The boundary layer thickness is such that at $x/D = -0.0474$ the boundary layer thickness (defined by 99% of the free stream velocity) is equal to the measurements. Outlet plane: first ξ-derivative of pressure equal to zero. Cylinder wall: no-slip conditions $\partial p / \partial \eta = 0$ and $u = v = w = 0$ or W_s / U_∞ fixed. Outer boundary: $p = 0$, $u / U_\infty = 1$ and $W_s / U_\infty = 0$. At the remaining boundaries symmetry conditions are imposed.

3. Results

3.1 Inclined cylinder protruding from a flat plate

The coarse, medium and fine grid are used now to simulate the flow around the cylinder. Menter's one equation turbulence model, including the Dacles-Mariani correction (c_{vor}=4, see [1] and [6]), is used to calculate the turbulent viscosity. The governing equations are integrated down to the wall (no wall functions used). The Reynolds number, based on the cylinder diameter (D=0.033 m) is equal to 1.8×10^5. The incident boundary layer thickness is equal to 3.2D.

The maximum y^+ value for the medium and fine grid is below 1.0. For the coarse grid the maximum y^+ value is below 1.5. All solutions are converged until changes in the pressure coefficient and in the velocity components are below 5.0×10^{-7}. Scaled residuals have been reduced by seven orders of magnitude. The maximum change in the turbulent viscosity is below 1.0×10^{-2} times the laminar viscosity. This means that iterative errors are far below grid convergence errors.
The discussion of the results will be focused on the following aspects:

- Pressure on the cylinder
- Limiting streamlines on the cylinder
- Three-dimensional streamlines of the flow
- Axial and transverse velocity fields at 3 planes in space

Pressure on the cylinder

The calculated pressure coefficient on the cylinder for the coarse, medium and fine grid show that the solution is clearly grid dependent, especially close to the flat plate. This is mainly due to the fact that there is no grid line at the junction of the flat plate at the “trailing edge” of the cylinder. This means that the position of the trailing edge changes, hence the coarse grid geometry is quite different from the medium grid geometry. Further away from the plate, where the flow tends to become independent of the co-ordinate running along the cylinder, the differences between the medium and fine grid solution are quite small. Still, the minimum pressure on the side of the cylinder and the pressure recovery at the "trailing edge" change between medium and fine grid. So, considering the present results, it seems that for an accurate prediction of the pressure on the cylinder at least 20 cells on half the cylinder circumference have to be used.

Limiting streamlines

Next we consider the limiting streamlines on the cylinder, plotted in Figure 4. The streamlines converge at the upper (downstream) side of the cylinder, indicating the formation of a vortex pair. The limiting streamlines obtained with the medium and the fine grid are very similar. Especially further away from the flat plate no significant differences can be distinguished between the medium and fine grid solution. Close to the flat plate the differences are somewhat larger. This is as expected, considering the numerical geometry in this region.

Three dimensional streamlines

Examining three-dimensional streamlines around the cylinder shows that the solutions are evidently grid dependent, but then it is well known that streamline tracing is notoriously sensitive in this regard. At least encouraging is that the solutions converge in the sense that the differences between fine and medium grid are much smaller than between medium and coarse grid. Not surprisingly, the streamlines close to the plate show the most significant grid effect.

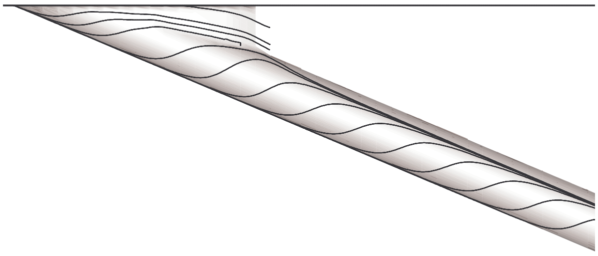

Figure 4: Limiting streamlines on the cylinder. Fine grid solution.

The experiments by Pinard showed a flow pattern as predicted by the fine grid calculation. The flow is locally aligned with the cylinder as indicated by the fine grid solution.

Axial and transverse velocity field

The numerical solutions of the axial and transverse velocity field in three x-constant planes have been compared to the experiments. It is found that for a fairly accurate prediction of the flow field, i.e. considering the discretisation errors, the medium grid is dense enough. Nevertheless, the fine grid solution is smoother than the medium grid solution. Also contour plots of the velocity component in the z-direction show that a grid independent solution is not yet obtained.

Figure 5 plots the axial velocity in plane P3 obtained from the measurements by Pinard versus the calculated velocity obtained with the finest grid density. Figure 6 plots the corresponding vertical velocity component. The horizontal velocity component is plotted for the calculations as well. The numerical solution is interpolated on the measurement points hence the solution is much smoother than indicated by the figures. The agreement of the PARNASSOS results with the experiments by Pinard is satisfactory, even if certain discrepancies can be pointed out. But, first of all, the incident boundary layer, as found by experiment, has a quite different shape compared to the boundary layer imposed in the calculations. It might be worthwhile therefore to impose directly the experimental boundary layer profile in order to exclude this source of discrepancies. Secondly, the geometry of the cylinder has been modified close the flat plate. This influences the accuracy of the predicted axial velocity behind the cylinder close to this region. Moreover, even the applied (modified) geometry can be captured more accurately by locating a grid line at the end of the cylinder shape close to the flat plate. Finally, the experimental data are not perfectly symmetric due to an a-symmetric geometry, experimental inaccuracy or instationarity of the flow. Of course also the influence of turbulence modelling may be important.

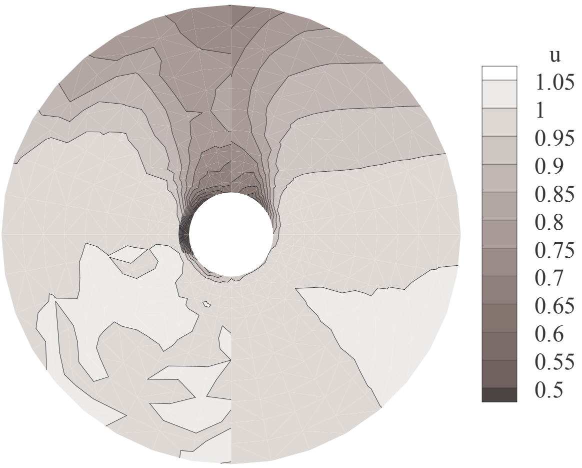

Figure 5: Axial velocity field at plane P3. Left side of the figure: measurements. Right side of the figure: fine grid solution.

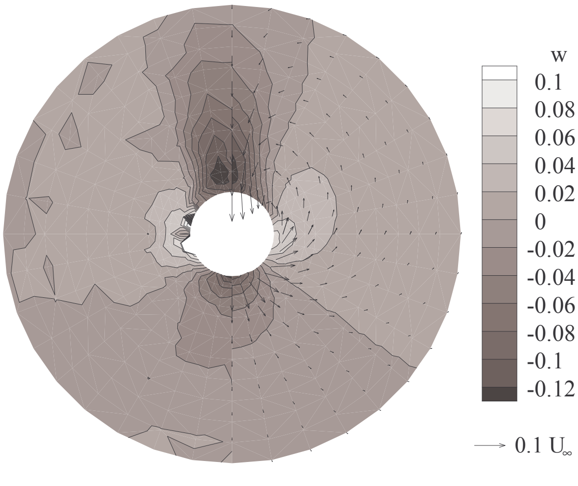

Figure 6: Vertical velocity component at plane P3. Left side of the figure: measurements. Right side of the figure: fine grid solution.

Hally has pointed out that the uncertainty in Pinard's experimental data is substantial and he has even suggested certain corrections. We have compared here with the original experimental data, but it is true that the correspondence between our and Hally's numerical results is much better than the correspondence with the measurements. Where Hally concludes that his code possibly "somewhat underpredicts the recirculation in the wake of the cylinder while it is embedded in the boundary layer, but overpredicts it once the cylinder is fully clear of the boundary layer", the same conclusion would hold for our results as well.

3.2 Inclined partly rotating cylinder protruding from a flat plate

As a first exercise to test the implementation of the surface rotation boundary condition the inclined cylinder with medium grid density is used. Part of the cylinder is rotating from just after the junction to approximately 8 cylinder diameters behind x-constant plane P4. The surface-to-free-stream velocity ratio W_s / U_∞ is equal to one. This is a typical shaft rotation speed for ships.

The numerical solution contained non-physical flow phenomena related to rotation of the cylinder. They were caused by large discretisation errors due to the specific grid topology. At the upper part of the cylinder cell sizes in girthwise direction are much too large to capture the gradient well in that region. Therefore we decided to examine this numerical effect and the surface rotation implementation by an even simpler test case, that is the rotating cylinder aligned with the flow. This case clearly shows these errors because the resulting flow has to be axi-symmetric.

3.3 Flow aligned rotating cylinder

Menter's one equation turbulence model, including the Dacles-Mariani correction, is used to solve the turbulent viscosity. The Reynolds number, based on the cylinder diameter (D=0.268 m) is equal to 2.9×10^5. The surface-to-free-stream velocity ratio is equal to $W_s / U_\infty = 0.0$ and 1.45. The maximum y^+ value for all cases is below 0.5 and all solutions are converged until changes in the pressure

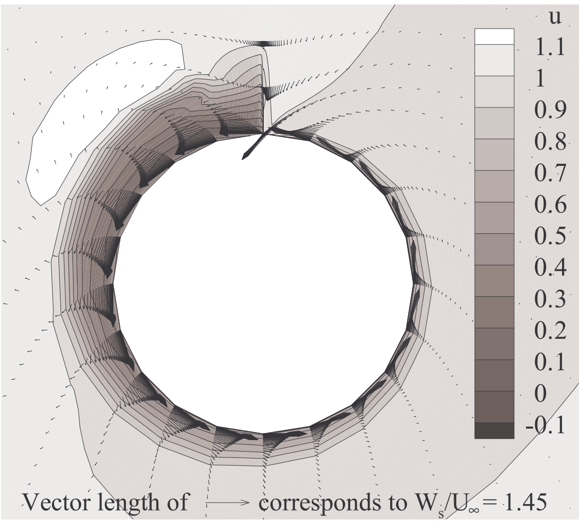

Figure 7: Axial and transverse velocity field. C-grid.

coefficient and in the velocity components are below 5×10^{-8}. Scaled residuals have been reduced by at least eight orders of magnitude. The maximum change in the turbulent viscosity is below 1×10^{-5} times the laminar viscosity.

At first, the C grid is used with an equidistant grid node distribution on the cylinder circumference. Figure 7 plots the axial and transverse velocity field approximately one cylinder diameter downstream of the upstream end of the rotating section. At the wall the surface speed is imposed but the solution is not axi-symmetric due to the too large cell sizes just above the cylinder. In girthwise direction the stepsize is much too large to capture the gradients of the boundary layer. Just above the cylinder the left and right side of the domain are connected via the j=1 & k=11…24 line. The node j=1 & k=11 is located on the cylinder surface. The node above, j=1 & k=12, is the first node above the cylinder in which the continuity and momentum equations are solved. This node is already far outside the boundary layer and hence the effect of it is that nearly no mass and momentum is transported in circumferential direction in the region just above the cylinder.

Stretching the grid towards the top section of the cylinder can solve this lack of resolution, however as a result a Navier-Stokes grid runs from the top section of the cylinder to the outer boundary. This increases the number of grid cells significantly. We found that it was not possible, at least not easy, to converge the flow solver with a cell size in girthwise direction at the top section equal to the cell size in wall normal direction. With a local cell size 100 times larger then the cell size in wall normal direction the solution improves definitely but is still not exactly axi-symmetric. But even for a properly stretched grid the solution in the top section of the cylinder will be not very accurate because of the discontinuous change of the direction of the grid lines. Whether or not the discretisation errors will then only spoil the solution locally is not clear in advance.

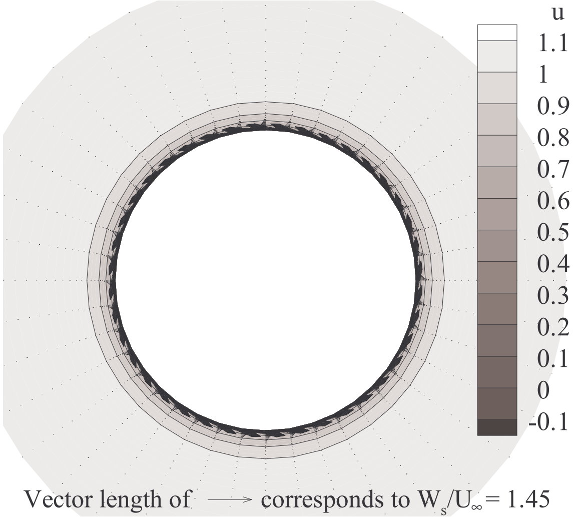

Figure 8: Axial and transverse velocity field. O-grid embedded in C-grid.

A much better solution can be obtained with the O-grid embedded in the C-grid. This gives an axi-symmetric solution as plotted in Figure 8. Moreover the convergence behaviour of the solver has improved significantly.

Now we have a more reliable solution, we can compare it with the measurements. Figure 9 plots the transverse velocity profiles in the bounder layer on the cylinder at $x/D = 0.09$, $x/D = 0.28$, $x/D = 0.47$, $x/D = 0.76$, $x/D = 1.23$ and $x/D = 1.52$ downstream of the upstream end of the rotating section. The reference length δ is the local boundary layer thickness in the absence of surface rotation. Symbols represent the experiments by Lohmann and dotted, dashed and solid lines represent our calculations. The calculations show a fairly

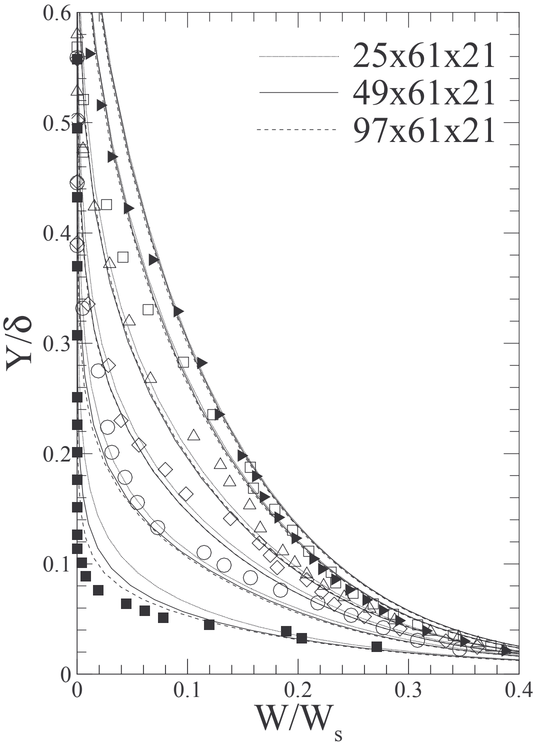

Figure 9: Transverse velocity profiles in the boundary layer on the rotating surface.

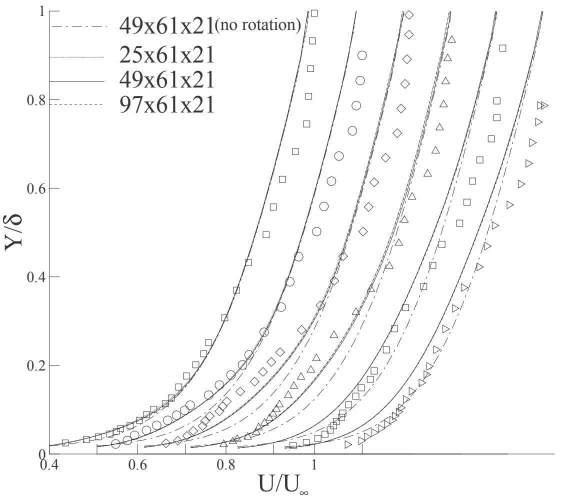

Figure 10: Axial velocity profiles in the boundary layer on the rotating surface.

good agreement with the measurements especially for the transverse velocity field.

The axial velocity profiles plotted in Figure 10, are in less good agreement with the measurements. The main characteristics however are predicted well. The experiments show a deceleration of the mean axial velocity on the first part of the rotating section that is predicted as well. Secondly the experiments show that the influence of rotation shifts from the rotating surface to the outer boundary region from the start of the rotating section to downstream respectively. The same trend can be found in the calculations. However the experiments show an acceleration of the mean axial velocity on the second part of the rotating section. This is not predicted by our calculations and is most likely due to imperfections of turbulence modelling. These numerical results are consistent with numerical analysis reported by Aguilar and Pierce [7]. The main discrepancy with the measurements however, is caused by the incident boundary layer profile that differs from the measured profile. In the calculations only the boundary layer thickness is tuned with the experiments.

In both figures some results of the grid refinement study are plotted as well. Grid refinement in wall-normal direction and grid coarsening in girthwise direction (not plotted) show, as expected, no significant influence on the solution. Also grid refinement in streamwise direction has no influence on the predicted axial velocity field. The predicted transverse velocity however is not yet grid independent. It shows that just behind the discontinuous change in the boundary condition (no-rotation to rotation), the solution is still improving by grid refinement in streamwise direction. However the solution 1.5 cylinder diameters downstream is hardly influenced. This is similar to numerical results presented at [5]: the effects may be expected to remain local.

4 Conclusions and future work

The aim of this study is to investigate the possibility to predict the wake of a shaft by PARNASSOS using the O-H grid topology. The results show that, considering discretisation errors, a fairly accurate prediction of the wake can be obtained using 10 cells on half the shaft circumference. The main features of the flow field are predicted quite well and finer grids only lead to minor changes in the flow field; it is mainly smoother. Of course, for accurate predictions of details of the flow close to the shaft, at least 20 cells on half the shaft circumference seem to be necessary. Further confidence in the quality of the results is obtained from the comparison with data obtained with another numerical simulation code. The differences found between measurements and computations might be further elucidated by studying the influence of the inflow boundary conditions.

For a non-covered, open shaft, the O-H grid topology is inappropriate because it leads to large discretisation errors. These errors only spoil the solution locally for the non-rotating case because the flow is symmetric along the vertical axis. But because the cylinder is not rotating and hence the velocities are zero at the wall, it is expected that even for a-symmetric inflow to the shaft the O-H grid topology can give fairly accurate flow predictions. The discretisation errors for the rotating case have been investigated by predicting the flow on a flow aligned rotating cylinder. It shows that this kind of flow can be predicted much better by using an O-type of grid around the cylinder embedded in a C-grid.

In the future we will use a better grid topology to predict the flow around the inclined, partly rotating cylinder properly. Combined with the present results this all leads to grid topology and grid density guidelines to assure accurate flow predictions of the wake field behind open-shaft stern configurations.

References

[1] M. Hoekstra. Numerical Simulation of Ship Stern Flows with a Space-Marching Navier-Stokes Method. PhD thesis, Delft University, 1999.

[2] J.C. Pinard. Etude expérimentale et numérique du sillage en amont d'une hélice. Ph.D. thesis. Ecole Doctorale Sciences pour l'Ingénieur de Nantes. Oktober 1997.

[3] D. Hally. Flow past an inclined cylinder protruding from a flat plate: comparison of numerical predictions with experiment. Technical Report. DREA ECR 2000-168. May 2001.

[4] R.P. Lohmann. The response of a developed turbulent boundary layer to local transverse surface motion. Journal of Fluid Engineering, September 1976, pp. 354.

[5] B. van den Berg, D.A. Humphreys, E. Krause and J.P.F. Lindhout. Three-Dimensional Turbulent Boundary Layers - Calculations and Experiments. Notes on Numerical Fluid Mechanics. Vol 19, 1988, pp. 92-120.

[6] J. Dacles-Mariani, G.G. Zilliac, J.S. Chow and J.S. Bradshaw. Numerical/experimental study of a wingtip vortex in the near field. AIAA Journal, Vol. 33, September 1995, pp. 1561-1568.

[7] F. Aguilar and F.J. Pierce. Numerical Analysis of Turbulent Flow Along an Abruptly Rotated Cylinder.

Hybrid RANSE-Potential Flow Approach to Damaged Ship in Seaways

Peter Woodburn[1], Paul Gallagher[1], Luca Letizia[1,2]

1. Basis of the Model

In the context of damaged stability regulations for ships, the simulation of damaged ships is of interest. So far, simulations for a damaged ship in seaways were based typically on potential flow methods assuming flat water surface in the damaged room or some hydraulic bore form. We present here a hybrid approach allowing more realistic simulations.

The coupled model consists of a 6 degree of freedom (6DOF) ship dynamics model for the vessel motions, coupled to a moving grid CFD model for the floodwater dynamics. The ship dynamics program calculates the position of the vessel under the action of forces of the waves on the outside of the hull and the floodwater inside the hull, and also calculates the height of the water surface at the damage. The position of the vessel and the height of the water surface at the damage are passed to the CFD program. The computational grid used in the CFD program adapts to the vessel motions. The dynamics of the floodwater and the loads on the vessel due to the floodwater are calculated and passed back to the ship dynamics model. All the relevant physics are therefore simulated directly rather than through the use of conventional empirical models. The two programs run alternately, waiting between run periods for the other program to complete its calculation at each time step. The coupling is explicit, which places restrictions on the maximum time step that may be used to ensure stability. However, in practice other factors in the CFD calculation restrict the time step to smaller values than those required by the explicit coupling.

1.1. Ship dynamics model NEREID

The ship dynamics program NEREID is a 6 degree of freedom (6DOF) model, developed at WSA, building on the theory behind the code CASSANDRA, originally developed at the University of Strathclyde Ship Stability Research Centre (SSRC) [1]. Like CASSANDRA, NEREID also uses a 3D panel method to calculate and integrate the hydrodynamic pressure over the surface of the hull, taking into account the slowly varying characteristics of the forces and moments thus derived due to the change of the mean underwater geometry of a ship during the flooding process.

The dynamic model adopted takes into account radiation damping by means of convolution integrals and also features linearised viscous damping [3], non-linear restoring forces and moments and second order wave forcing terms. The number of degrees of freedom of the vessel can be limited by restraining displacements and/or rotations in any chosen direction. The hydrodynamic coefficients and first order wave forces are determined beforehand by means of a linear diffraction/radiation code (AQWA-LINE) and generally stay constant throughout the simulation. If the need arises, the variation of these terms with the vessel low frequency motion - heel, trim and draught - can be allowed, although usually only large variations of attitude of a typical RoRo vessel induce a significant change of the first order wave excitation and hydrodynamic coefficients.

The non-linear buoyancy terms are an essential feature of a model, which tries to deal with substantial changes of a vessel's displacement during a simulation. These terms are calculated by integrating the instantaneous underwater volume of the hull, up to the mean water line. This approach is consistent with the assumptions made for the evaluation of the first order wave forces. Second order wave drift forces vary slowly in time and both first and second order excitation take into account the effect of the vessel's drift motion on encountered frequency.

Lastly, the wave elevation at the damage is passed to the CFD code to provide the appropriate external water elevation, modified for wave diffraction effects as described later.

1.2. CFD Model

The extent of the domain used in the CFD calculation is shown in Fig.1, superimposed for the purposes of illustration on a simple representation of the vessel. The domain consists of all floodable internal compartments, together with an area of sea immediately adjacent to the damage. At the damage, the external free surface is assumed to behave as a simple water column. Its height follows the external wave elevation time history, adjusted for reflection/diffraction effects. The wave profile imposed can be monochromatic or irregular, and, importantly, the same wave elevation time history can be used for a series of tests which allows the effect of different parameters to be tested under exactly the same wave conditions. For this research, CFD model of choice was the CFX4 code.

To commence the simulation process, the ship dynamics code is started from an approximate equilibrium position and the wave amplitude is increased linearly over the first 20s. At 60s the

---

[1] Fluid Mechanics Dept, WS Atkins Consultants Ltd
[2] Safety at Sea Ltd, l.letizia@safety-at-sea.co.uk

damage is ‘opened’ and the CFD code is started, allowing flooding simulation to begin.

As the simulation proceeds, fluid pressures calculated by the CFD model acting on the internal structure are integrated to provide the forces and moments due to internal floodwater movement.

The loads and displacements are transferred between the programs, and the simulation is continued until either a specified time is reached, or the vessel capsizes. Motions in all 6 D.O.F., the wave profile, and the floodwater distribution within the vessel are recorded at each time step, which provides a large volume of data for each individual case. These comprehensive data sets provide much data for investigation of the physics underlying the dynamics and capsize.

The purpose of modelling the region of sea outside the damage is not to provide an exact representation of the water surface within this region. Rather, it is to provide the correct height of water at the damage as a boundary condition for the flooding of the vessel. This approach is taken because the computational cost of simulating the entire sea surface around the vessel is both prohibitively expensive and inefficient when the requirement is only to provide the boundary conditions for the flooding process. The strategy for achieving this is to attain a target height of water at a short distance outside the damage (a distance at which the influence of the damage on the water surface is negligible). This target water height is provided by the ship dynamics program (based on the relative motion for this location) and includes the effects of wave reflection from the hull. Some local effects due to the hull and flooding through the damage are calculated as near field deflections of this target height as part of the CFD solution. This means that a local depression of the water surface through the damage as water flows into the vessel is simulated.

Fig.2 shows a view of the vehicle deck in the CFD model looking aft at one instant during a flooding simulation. The forward bulkhead of the vehicle deck has been removed. At this time the whole vehicle deck was submerged beneath the floodwater, and the waves caused by water flooding onto the deck can be seen. The damage and the external water surface outside the damage are clear. The vessel is heeled towards the damage, though the movement of the floodwater means that it is deeper on the side of the deck furthest from the damage at this instant.

There are some aspects of wave dynamics, such as the external orbital motions of the water particles, which are ignored in this approach. It is assumed that these effects are secondary, since the presence of the vessel hull reduces the horizontal components of these motions significantly. Further work is being carried out to verify this but early results described below show support for this assumption.

2. Testing the Numerical Model

The two models used to form the coupled model, NEREID and CFX4, have individually undergone extensive testing and validation [2]. Indeed, this was one of the motivations for developing a coupled model rather than a single, dedicated model, in that only the specific coupled aspects of the model would require testing.

Tests of the numerical model were carried out for a series of cases which isolated particular components of the overall dynamic behaviour, with the key objective being to ensure that the model was consistent with all the component physics, as well as allowing rapid identification of errors. The particular scenarios studied included:

- Sloshing at known frequencies and amplitudes in closed tanks.
- Roll-decay, regular and irregular wave behaviour for an intact vessel.
- Roll decay tests of coupled ship dynamics – closed tank sloshing models.

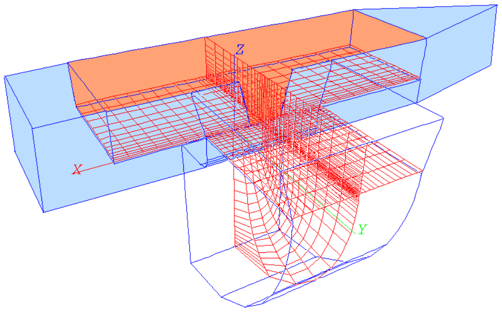

Fig.1. A simplified view of the domain and grid used in the CFD calculation superimposed on a representation of the vessel. In this case only the vehicle deck is open to flooding through the damage.

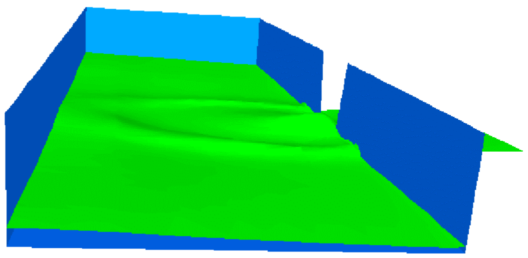

Fig.2. View of the vehicle deck in the CFD model looking aft at one instant during a simulation. The forward bulkhead of the vehicle deck has been removed. At this time the whole vehicle deck was submerged beneath the floodwater.

- Regular wave forcing of vessels with closed tanks.

- Regular and irregular wave flooding into compartments in vessels fixed in space.

In all these cases, the numerical model demonstrated consistency with the experimental data [2,4,5].

2.1. Sloshing simulations

Simulation of the dynamics of the floodwater on deck can be isolated in simulations of sloshing in a closed tank. For these tests, the geometrical data and the test conditions were similar to those reported by Armenio and La Rocca [4,5].

Forced oscillation tests, which tested the CFD modeling of floodwater flowing around a moving tank, were carried out at a frequency of 3 rads^{-1}. The non-dimensional wave height at the sides, (with respect to the tank breadth) in the simulation was 0.62, which compared favorably with that measured by Armenio and La Rocca, which was in the range 0.65-0.7.

The coupled model was applied to the case of a model fishing vessel with a large closed container, partially filled with water, on board [5]. The vessel was initially displaced from its equilibrium position in roll, and the resulting roll motion was compared with that observed in the experiments. The computed results for roll natural periods (in seconds) compared with those derived from experiment are shown in Table 1.

Table 1: Comparison of roll periods (s) in roll decay tests.

Depth/Breadth	Present	Armenio et al.
0.15	1.90 s	1.84 s
0.10	2.05 s	1.98 s

Fig.3 shows the forced roll response from the same fishing vessel with a partially filled tank when subjected to a range of forcing frequencies (ω) in both experimental and numerical tests. The external wave slope was restricted to 1/100 so as to give results which were as close to linear as possible.

The results from the numerical model compared reasonably well with the experimental data, particularly given the need to estimate some of the key hydrodynamic coefficients in the roll equation of motion used. The main differences appeared around the peak of the response in roll, where damping, and in particular the degree of additional viscous damping, is a critical parameter, and was not available for this vessel.

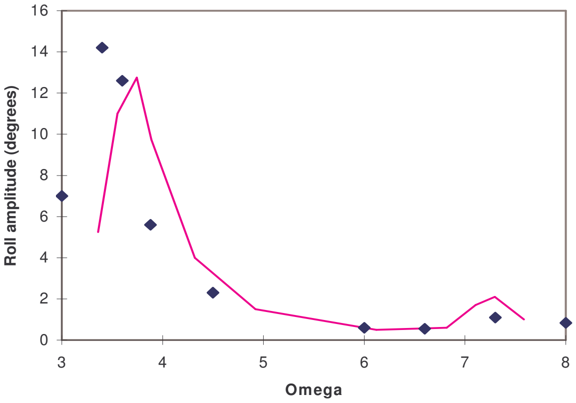

Fig.3: Roll amplitude versus frequency for ship model for d/B = 0.25; ◆: Present results, line: Armenio and La Rocca experimental results.

2.2. Ship fixed flooding tests 1

Simulations were carried out of a damaged Ro-Ro in which the ship was held fixed and subjected to flooding through a damage opening, in a repetition of an experiment carried out at the University of Strathclyde [2]. The prescribed water elevation time history was derived directly from the experimentally measured water elevations outside the damage location. A case with notional values of significant wave height of 4m and zero crossing period of 6.25s was chosen.

The experimental values of the mass of floodwater were estimated using the water heights within the Ro-Ro compartment measured using four wave probes. Fig.4 shows a comparison of the computed and experimentally measured time histories for the mass of floodwater within the vessel. Extrapolation of the wave probe measurement of water height to obtain the overall volume of floodwater in the experiment gives a noisy graph with unfeasibly high inflow/outflow rates, but does allow the average values of the mass of floodwater to be compared.

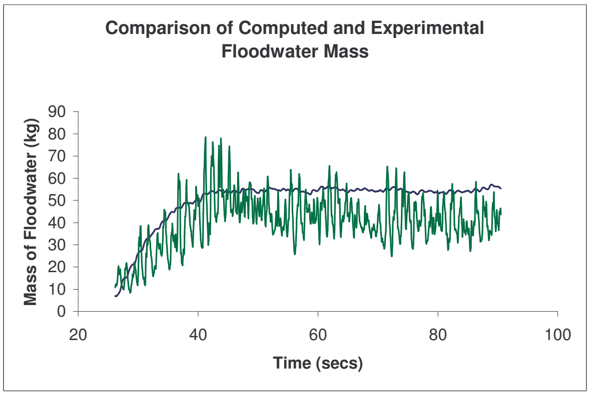

Fig.4. Fixed ship flooding: Comparison of computed and experimentally measured time histories. Upper, approximately steady line: Simulation; Lower, noisy line: experiments.

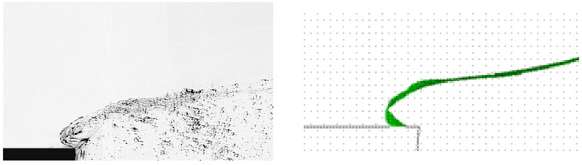

Experiment Simulation

Fig.5: Comparison of water surface profiles.

2.2. Ship fixed flooding tests 2

Flooding tests and particle image velocimetry (PIV) measurements of floodwater dynamics were carried out as part of the NEREUS project. As can be seen in Fig.5, during the flooding cycle the water surface profiles in the simulation compare well with those photographed in the experiments.

3. Sensitivity Studies

Following model testing, a number of factors thought likely to have a significant effect on the flooding rate, final mass of floodwater on deck, or capsize were tested in a parametric sensitivity study. Since there were few detailed experimental data to compare each of these cases with directly this was not intended to be a validation exercise. However, the results obtained were broadly in line with expectations based on previous experience. The results in some cases were strongly dependent on the relationship between several of the key parameters, but it is by no means expected that these dependencies will be universal. Rather, the approach is to identify those factors having a significant effect on the flooding and capsize so that their effect within a larger parameter space can be identified in further research. The parameters studied were:

- Number of degrees of freedom
- Heading
- Significant wave height (Hs) and zero crossing period (Tz).
- KG
- Damage size and geometry
- Vehicles on deck
- Inclusion of side casings
- Inclusion of lower compartments, both full width and wing-tanks
- Cross-flooding
- Scale

A series of experiments carried out previously at the University of Strathclyde provided the majority of the data on floodwater behaviour for this project [2]. The model used for these tests was a 1:42 scale model of a RoRo vessel, used extensively in previous model testing. The main particulars of which are shown in Table 2.

In the tests used in the present study, the vehicle deck was open to the sea in all damage configurations. Some compartments below the bulkhead deck were either considered filled with floodwater, but not in communication with the sea (in order to achieve the freeboard desired), or were initially empty and allowed to fill through the damage and remain in communication with the vehicle deck. The damage is located amidships and has the form of a trapezoidal opening, according to a 100% SOLAS damage opening.

The model was tested in irregular beams seas (JONSWAP Spectrum; $\gamma = 3.3$) with the damaged side exposed to the incoming waves. The experimental rig is constructed such that it is possible to constrain one or more degrees of freedom, or hold the vessel such that is was fixed.

Table 2: Main particulars of the vessel

Dimensions	Full-Scale	Model
Length, L_{BP}	131.0m	3117mm
Breadth, B	26.0m	619mm
Draught, T	6.1m	145mm
Initial Displacement	12200 tons	164kg

A total of 35 simulations were carried out in the present study, each with typical duration of 12-20 minutes of real time at full scale. The same wave realisation (H_s=4.0m, T_z=6.25s) at the origin was used for all the cases, to allow direct comparison of the effects of each parameter. The wave elevation time history experienced by the vessel is shown in Fig.6, together with the roll and heave motion time histories for the reference case in Fig.7(a) and (b) and the corresponding time history for the mass of floodwater on deck is shown in Fig.7(c). In this case, only the vehicle deck was open to flooding, though a full width lower compartment was assumed fully flooded (though not in communication with the deck) with 4400 tons of floodwater to give a damaged freeboard of 0.2m before flooding of the vehicle deck started. In this case the undamaged vessel KG was 10m. With a KG of 10m, the undamaged GM was 4m, which means the undamaged vessel is stiffer than is usual in this type of vessel. This stiffness is reflected in some of the behaviour of the vessel and the effects of changing some parameters in the sensitivity study.

The effect of the floodwater on the motion of the vessel can be seen clearly in Fig.7. The vessel sank lower in the water and the amplitude of the roll motions decreased as the mass of floodwater on deck increased, and the vessel also acquired a steady loll away from the damage of approximately 3° after about 500s.

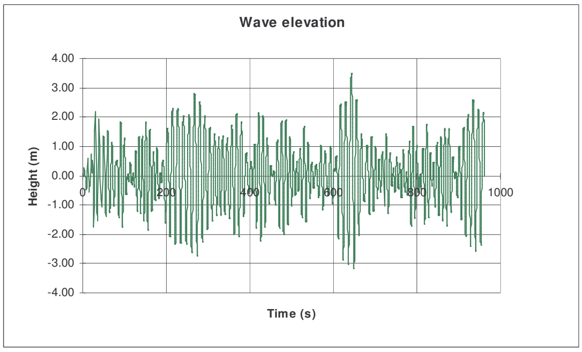

Fig.6: Time history of the wave elevation.

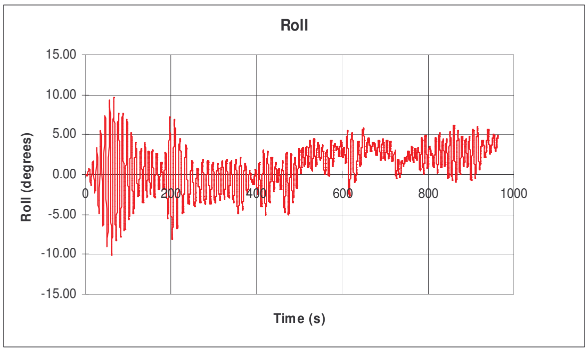

Fig.7(a): Time history of roll motion.

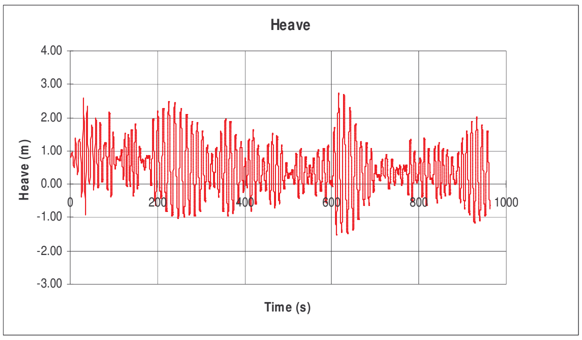

Fig.7(b): Time history of heave motion.

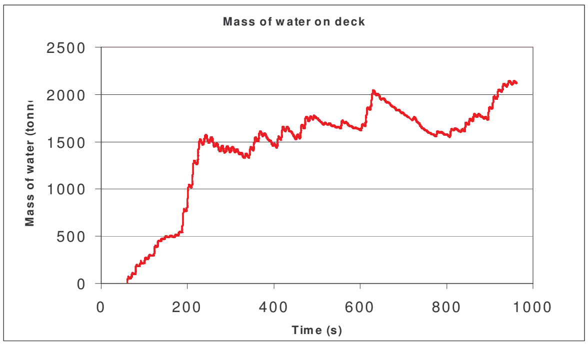

Fig.7 (c): Time history of floodwater.

For the cases which had been covered by previous experimental systematic studies, principally the first four in the table above, the final volumes of floodwater predicted were in line with those measured (taking into account both the likely experimental error bounds and differences in model set up). This provides confidence in the compatibility of the numerical and experimental results. No experimental data were available for comparison with the remaining factors. However, there was a consistency in the results achieved which allowed plausible explanations of the observed results based on sound principles of dynamics and fluid mechanics. The principal results obtained from this study were:

1. A two-stage pattern of flooding was identified, consisting of an initial flooding phase followed by a phase during which the mass of floodwater on deck remained approximately steady. During this second ‘steady’ phase, inflow and outflow continued, but were approximately equal such that the rate of change of the depth of water on deck with time was low.

2. All the parameters tested caused significant changes to the initial flooding rate.

3. Parameters causing the greatest changes to the ‘steady’ mass of water on deck were KG, Hs, Tz, and flooding of lower compartments.

4. The vessel’s KG was shown to have a significant effect on the dynamic roll response of the vessel, such that small changes in KG caused significant changes in both the initial flooding rate and the final ‘steady’ mass of water on deck. Significantly, in the cases tested here, vessels with lower KG accumulated greater volumes of water on deck.

5. The final mass of floodwater was dependent on both Hs and Tz – the dependence of the mass of floodwater on Tz was an important indication of the importance of the vessel dynamics on the mass of floodwater on deck.

6. The width and geometry of the damage opening had a strong effect on the initial flooding rate, but not on the final mass of water on deck.

7. The presence of vehicles in the form of fixed obstructions on the vehicle deck caused both the initial flooding rate and the final ‘steady’ mass of floodwater to be reduced. The presence of obstructions reduced the rate at which water on deck near the damage could flow across the deck away from the damage, thereby reducing the overall

flooding rate, while the presence of the 'fixed' vehicles reduced the area available for flooding.

8. It was demonstrated that all compartments open to flooding should be included in the flooding simulation domain, the modelling of flooded lower compartments as fixed 'closed' masses of water was not a good assumption when communication through large openings was possible.

9. Side casings, while reducing the overall mass of floodwater on deck, allowed the vessel to continue to respond dynamically.

10. The effect of scale on flooding processes was not found to be significant. Apart from the need to treat overall roll damping with great care, this research indicates that reduced scale tank testing is viable

11. Repeat testing with cross-flooding ducts of different cross-sectional areas allowed the effects of this parameter on the vessel's ability to survive to be quantified. Concerning the overall dynamics of the problem, two points become clear. Firstly that when capsize occurred, it was rapid compared with the length of time allowed for cross-flooding which is 1200s, and at no time did the vessel reach an equilibrium steady position. In each case insufficient equalisation had occurred to prevent capsize. However, there remained a cross-sectional area above which capsize was prevented. This area was sufficiently large that equalisation could occur within 100-150s. The second point is that the continuing motions of the vessel prevent and reverse the cross-flow of floodwater in the cross-flooding duct. While the provision may be adequate in a quasi-equilibrium sense, the continuing motions may disrupt the flow to such an extent that little equalisation takes place in practice.

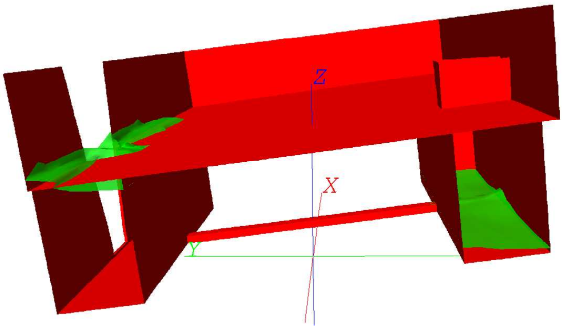

Fig.9: Section through the vehicle deck and lower compartments looking forward, showing the vessel position and water surface at one instant during the simulation.

Acknowledgements

This research was funded by the MCA (Research Project 424) and by the EC (RTD Project NEREUS).

References

[1] L. Letizia; D. Vassalos, "Formulation of a Non-linear Mathematical Model for a Damaged Ship with Progressive Flooding", Int. Symp. on Ship Safety in a Seaway, Kaliningrad, 1995.

[2] L. Letizia, "Damage Survivability of Passenger Ships in a Seaway", PhD Thesis, Univ. of Strathclyde, Glasgow, 1996.

[3] Y. Himeno, "Prediction of Ship Roll Damping: State of the Art", Dept. NAME, Univ. of Michigan Report No. 239, Ann Arbor, Mich. 1981.

[4] V. Armenio; A. Francescutto; M. La Rocca, "On the Hydrodynamic Coupling between Ship Roll Motion and Liquid Sloshing in a Flooded Tank", Univ. of Trieste Internal Report.

[5] V. Armenio; M. La Rocca, "Numerical and Experimental Analysis of the Roll Motion of a Ship with Free Surface Liquids Shipped on Board", Int. Symp. Ship Hydrodyn., St. Petersburg, 1995.

Simulation of Ship Maneuvering in Viscous Flow with Free Surface

Yan Xing-Kaeding and Gerhard Jensen

Fluid Dynamics and Ship Theory Section
Technical University of Hamburg-Harburg
Lämmersieth 90, D-22305 Hamburg, Germany
email: yan.xing@tu-harburg.de, g.jensen@tu-harburg.de

Milovan Perić

Computational Dynamics, CD adapco Group
Dürrenhofstraße 4, D-90402 Nürnberg, Germany
email: m.peric@cd-germany.de

1 Introduction

During ship operations in confined waters or in following seas, safety and functionality of the ship depend on the maneuvering performance. The path of the ship strongly depends on the fluid flow, wind field and the resulting forces acting on the hull, rudder and propeller or other maneuvering devices from the fluid flow. Viscous and turbulent effects and the interaction between ship and flow play an important roll here. The complexity of the problem requires a method, which can predict the hydrodynamic forces and ship motion accurately. So far, methods developed to predict the maneuvering motion of a ship are mostly based on empirical relations, theoretical or numerical methods, which ignore the viscous effect of the water. Due to the importance of viscosity during maneuvering, three dimensional CFD simulation solving RANS Equations appeared in the 1990s to improve the accuracy of the prediction of hydrodynamic coefficients[1-2]. The computations were mostly limited to steady flow computation around a ship with a constant inflow angle. By the late 1990s, RANSE results with free surface deformation and the generation of the waves[3-5] have been shown. The simulation of ship maneuvering considering the interaction of the maneuvering motion of the ship and the turbulent free surface flow around the ship has been seldom presented.

In previous NuTTSs, we have presented a numerical method, which considers the viscous and turbulent effect, free surface deformation and the interaction of fluid flow and flow-induced ship motion. The ship motion module follows rigid body dynamics for six degrees of freedom and has been integrated into the commercial package 'Comet' for fluid flow. The detailed description of the method and computational results compared to the experiments have been presented in previous NuTTSs[6-7].

In this paper, we will focus on the application of this method in ship maneuvering simulation. The propeller is simulated by applying a body force on a layer of cells in the propeller plane[8]. The rudder is modeled geometrically and a random rudder angle can be set using the technique of the sliding interfaces. Three type of computations related to ship maneuvers are under way in our numerical tank: ship running in oblique waves, turning circle and Z-maneuvers. Some preliminary results will be presented in this paper.

2 Numerical Method

The finite volume method incorporated in the ”Comet” code is used here to simulate incompressible viscous flows with free surface. The conservation equations for mass, momentum, and scalar quantities (e.g. energy or chemical species) are solved in their integral from. When the grid is moving, the so-called *space conservation law* (SCL) has to be satisfied. Interface-capturing method and High-Resolution Interface Capturing (HRIC) [3] scheme have been used to simulate the free-surface effects. In addition to the conservation equations for mass and momentum, a transport equation for void fraction of the liquid phase c has been introduced. Due to the limit of space, these basic equations will not be introduced here; for more detail, see [3,8-9].
The motions of the rigid body are computed following the dynamics of rigid bodies, which will not be repeated here. The forces and moments acting on a floating body are obtained from the fluid flow around the body. However, the flow itself is influenced by the body motion and both problems have to be considered simultaneously. For the prediction of the body motion, a predictor-corrector method which can be easily coupled with the iterative procedure for flow prediction (SIMPLE-algorithm) has been used here. For more details about the integration scheme, see [5].

3 Numerical Grid and Boundary Conditions

The block of surface-fitted grid surrounding the ship has a shape of a rectangular block and is made of a finite number of control volumes, which can have more than 6 faces. All variables are stored at the center of each control volume. Structured as well as unstructured grids with multi-blocks can be employed. As mentioned before, sliding interfaces, which allow a random rudder angle, have been taken between the block containing the rudder and the blocks surrounding the rudder block. Numerical beaches have been generated at some boundaries of the domain, which are far from the ship, to avoid the unexpected reflection of the waves at the boundaries. For the moderate roll, pitch and heave motions of the ship, a block around the ship (including the block with the rudder) can be moved together with the ship and the grid far way from the ship is kept unchanged; the block in between has to be smoothed or regenerated in three dimensions. For large yaw motion(e.g. in the case of turning circle), either the whole computational domain can be moved with the ship or additional body forces corresponding to the rotation should be applied to the whole domain instead of grid moving.

Great care should be taken to set boundary conditions correctly since the fluid could be flowing in or out from the same border of the domain at different time instances during ship maneuvering. Here a pressure boundary condition has been combined with the inlet boundary condition at the corresponding inflow and outflow parts of the border. No-slip wall condition has been applied to the ship hull as well as the surface of the rudder. At the bottom of the domain, slip wall condition or symmetry condition can be applied if it doesn’t exist physically. At the top of the domain, static air pressure can be applied or other corresponding conditions can be set up if the wind is considered.

4 Results and Discussions

4.1 Ship motions in oblique waves

One of the first test cases in the numerical tank is the computation of the ship motions in oblique waves. Waves are generated by specifying the velocities according to the linear wave theory at the corresponding inlet boundaries. The angle between waves propagation direction and the ship running direction is 170 degree. The heave, pitch and roll motions of the ship are set free; the surge, sway and yaw motions are kept fixed since the rudder/propeller is not modeled in this case. Figure

1 shows the computed wave pattern and the resulted motions of the ship in the oblique waves at $F_n = 0.18$. What is to be mentioned, is that the time averaged roll angle is not zero degrees due to the effect of the oblique waves.

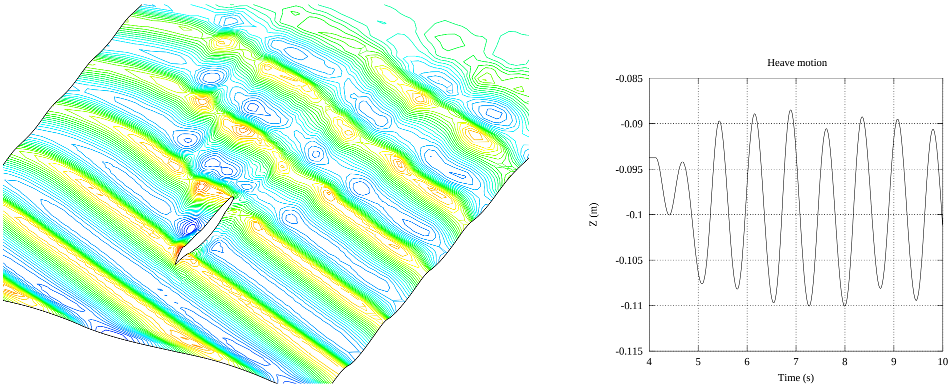

(a) wave pattern (b) heave motion

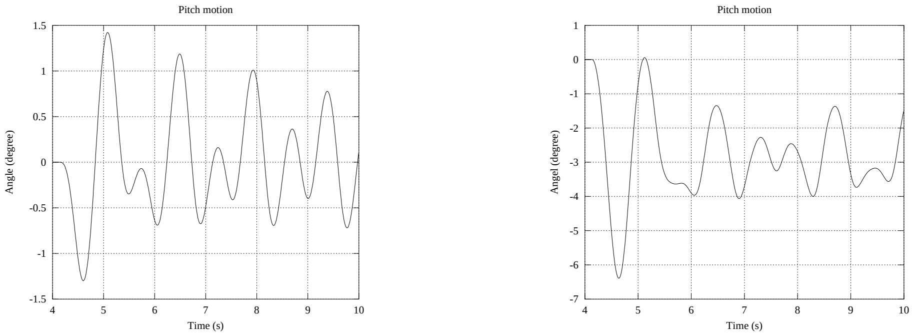

(a) pitch motion (b) roll motion

Fig. 1 Wave pattern and motions of the Wigley ship ($F_n = 0.18$) in oblique waves (170^o).

4.2 Turning circle maneuver

A captured turning circle test in calm water has been carried out in the numerical tank. The Wigley hull has been considered first due to its simple geometry. Boundary conditions are rather complex in this case. A combination of inlet and pressure boundary conditions is applied to the boundaries ahead of the ship and at the inner side of the turning circle. At the outer boundary of the turning circle and the boundary behind the ship, pressure boundary condition is employed. The grid around the ship is moved for the moderate motions(heave, pitch and roll) of the ship; for the large yaw motion during maneuvers and the motion due to ship's forward speed ($F_n = 0.29$, $r' = 0.4$), the corresponding body forces or field velocities are applied to the whole computational domain. Rudder is not modeled in this case, therefore the yaw motion is forced to follow the course of turning circle shown in Fig. 2(b). The computed wave pattern of the Wigley ship at a certain time instance is shown in Fig. 2(a).

Besides the Wigley ship, the turning circle has also been computed for the container ship 'CBOX'. The Rudder of 'CBOX' is geometrically modeled and can be turn to any desired rudder angle. The propeller is modeled by a body force model[10]. The ship is computed in model scale at the nondimensional yaw rate $r' = 0.6$ and $F_n = 0.23$ and expected to turn dramatically when the maximum ruder angel is set. Some preliminary results are shown in Fig. 3. The pressure distribution shown in Fig. 3(a) becomes asymmetric on the ship hull during the turning circle maneuvers. The

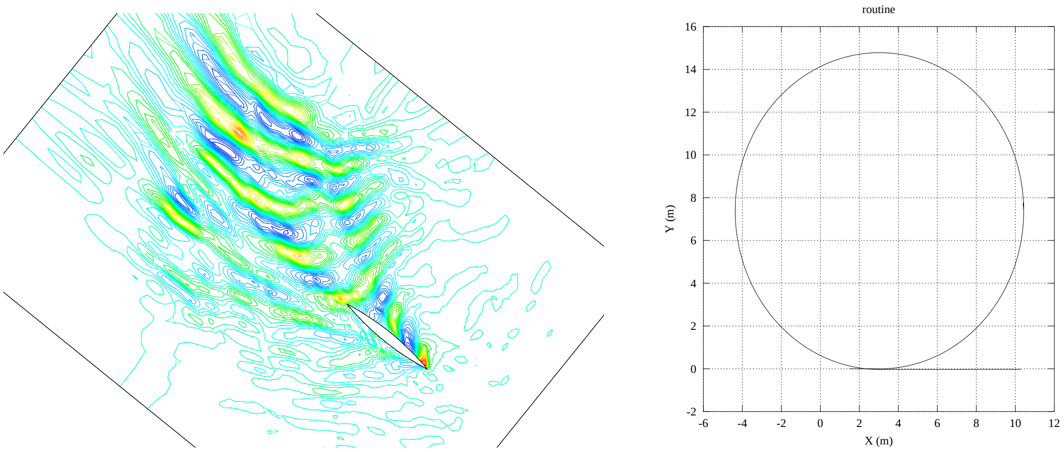

(a) wave pattern (b) course of the ship

Fig. 2 Turning circle maneuver of the Wigley ship ($r' = 0.4$).

computed wave pattern is presented in Fig. 3(b) giving a reasonable impression. The computation is running currently; more detailed results will be presented later.

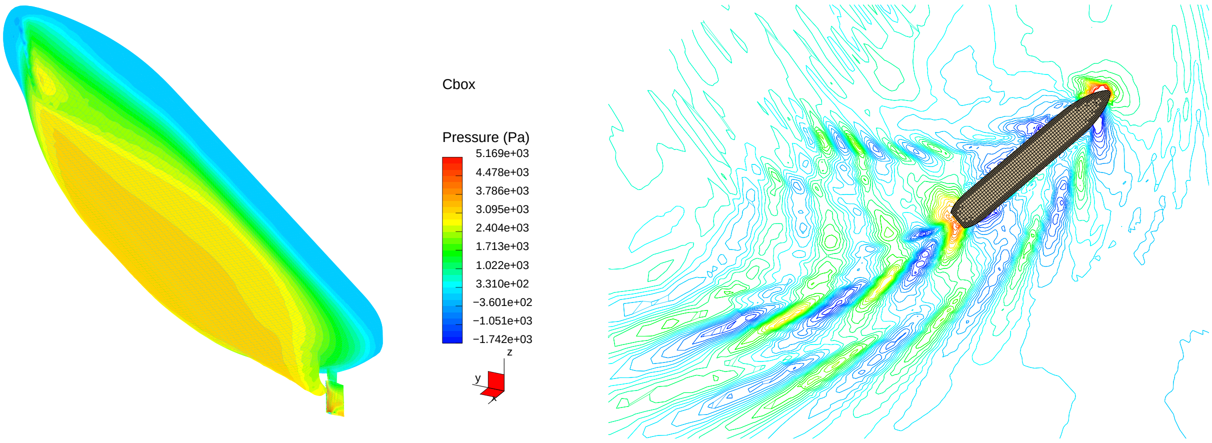

(a) pressure distribution (b) wave pattern

Fig. 3 Turning circle maneuver of the ship CBOX ($r' = 0.6$).

4.3 Z-maneuver

Using the same grid system as those employed to simulate ship motions in oblique waves and the turning circle maneuver, 25 degree Z-maneuver with the Wigley hull at average Froude number 0.18 has also been performed in the numerical tank. The resulting wave pattern at a selected time instance and the forced course and yaw angle of the ship are shown in Fig. 4.

5 Conclusion

The instaneous interaction between viscous free surface flow and flow-induced body motion has been computed using the finite volume method. Rigid body dynamics for six degrees of freedom has been integrated to the fluid solver to compute the body motion. The method has been tested and demonstated for ship motions in waves etc. in previous NuTTSs, showing good agreement with the experiment. Further application on maneuvring motion of a self-propelled ship has been intended in this paper. The rudder has been modeled geometrically in addition to the ship hull. The propeller has been simulated by a body force model. Some preliminay results about ship motions in oblique waves, turning circle maneuver and Z-maneuver have been presented. The computations will be futher analyzed and compared with the experiment in the future.

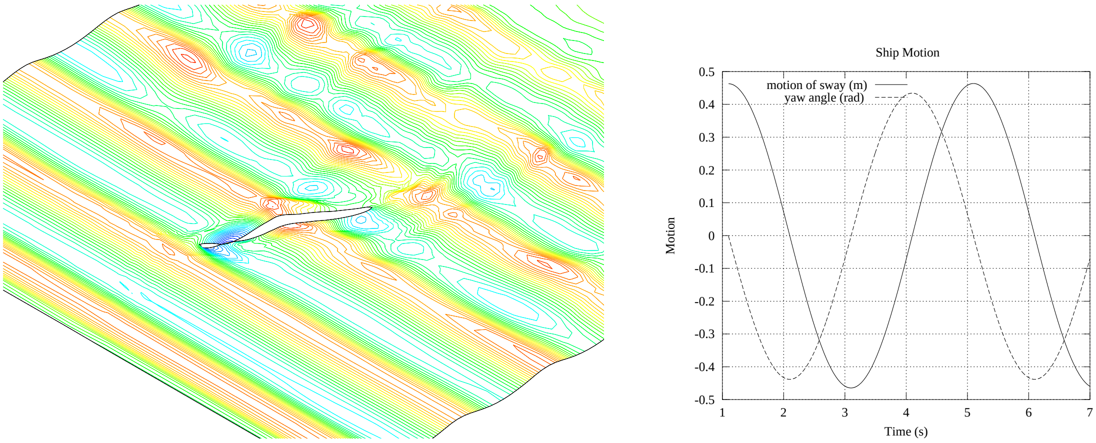

(a) wave pattern at time=7.0s (b) ship motion

Fig. 4 Z-maneuver (25^o) of the Wigley hull ($F_n = 0.18$).

References

[1] Cura Hochbaum A. Computation of the Turbulent Flow Around a Ship Model in Steady Turn and in Steady Oblique Motion, 22nd ONR Symp. on Naval Hydr., Washington D.C., 1998.

[2] Sato T., Izumi K. and Miyata H. Numerical Simulation of Maneuvring Motion, 22nd ONR Symp. on Naval Hydr., Washington D.C., 1998.

[3] Muzaferija S. and Perić M. Computation of free surface flow using interface-tracking and interface-capturing methods, Chap. 2 in O. Mahrenholtz and M. Markiewicz (eds.), Nonlinear Water Wave Interaction, pp. 59-100, WIT Press, Southampton, 1999.

[4] Cura Hochbaum A. and Vogt M. Efforts at HSVA in Predicting the Manoeuvrability of Ships using CFD Tools, Proc. Int. Workshop on Ship Manoeuvrability at the Hamburg Ship Model Basin, 2000.

[5] Hadzic I., Muzaferija S., Peric M. and Xing Y. Numerical Simulation of Interaction of a Floating Body and a Free-Surface Flow with Waves, Fifth World Congress on Computational Mechanics, Vienna/Austria, 2002.

[6] Xing, Y., Hadzic, I. and Peric, M. Predictions of Floating-Body Motions in Viscous Flow, Proc. 4th Numerical Towing Tank Symp., Hamburg/ Germany, 2001.

[7] Xing Y., Jensen G., Hadzic I. and Peric, M. An Approach to Ship Manouvering by Simultaneous Computation of Viscous Flow and Ship Motion, Proc. 5th Numerical Towing Tank Symp., Pornichet/, France, 2002.

[8] Demirdžić I. and Muzaferija S. Numerical method for coupled fluid flow, heat transfer and stress analysis using unstructured moving meshes with cells of arbitrary topology, Comput. Methods Appl. Mech. Eng., vol. 125, pp. 235-255, 1995.

[9] Demirdžić I., Muzaferija S. and Perić, M. Computation of turbulent flows in complex geometries, chap.$\tilde{7}$ in G. Tzabiras et al. (eds.), Calculation of Complex Turbulent Flows, pp.$\tilde{2}$49-299, WIT press, Southampton, 2000.

[10] Stern F., Kim H.T., Patel V.C. and Chen H.C. A viscous-flow approach to the computation of propeller-hull interaction, Journal of Ship Research, vol. 32, no. 4, pp. 246-262, 1988.

7th Numerical Towing Tank Symposium (NuTTS'04)

Hamburg, Germany
3-5 October 2004

Haus Rissen, Rissener Landstr 193, Hamburg-Rissen

Topics:

- Nonlinear flows around marine structures (LES, RANSE, Euler with or w/o free surface)
- Free-surface flows around marine structures (3-d seakeeping, free-surface viscous flows)
- Related topics (validation experiments, numerical techniques, grid generation, etc)

Deadlines:	Early feedback:	30 April 2004
	Extended Abstracts received:	**15 August 2004**
	Notification of acceptance:	22 August 2004
	Last possible update (for a fee):	19 September 2004

You are invited to participate in the above event. The objective of the event is to provide a forum for informal discussions among experts in the field and to disseminate latest results. The event will be held at Haus Rissen in the outskirts of Hamburg with all participants staying in the venue. All participants stay and have meals together to maximize interaction and discussion. The extended abstracts of the proposed talk will be directly reproduced in the proceedings. There will be no full paper as such. Proceedings will be in black and white. Work in progress, encountered problems, etc. should be discussed in an open, informal atmosphere (no ties!) among colleagues.

Extended abstracts are limited to 6 pages A4 format with 2.5 cm margin everywhere. The first page of the extended abstract should be headed with the title and authors' full names and email addresses in a compact form to economize on space. Font size shall not be less than 10pt times new roman. Academic titles and page numbers shall be omitted. The extended abstract shall neither contain an abstract of the abstract, nor keywords, nor further headers.

An early reply will help us in organizing the event better. For the early feedback, a tentative title or topic will suffice. An initial abstract may be as short as several lines.

Following the tradition of previous NuTTS events, the fees will be kept low to allow a maximum number of scientists to attend. The **fees including accommodation** (3 nights starting from Sunday night) **and meals** during the symposium will be:

200 Euro	PhD candidates and students (expected to share double)
300 Euro	authors (in single room)
400 Euro	others (in single room)

50% of above if hotel is not supplied.

30 Euro charge for update after 15 August

The fees are due cash on arrival.

Please note that the week before the HIPER conference (for fast ships) is held in Rome (27-29.9.) and the SMM (largest expo for ships in the world) is held in Hamburg (29.9.-2.10.) in Hamburg.

Heinrich Söding, h.soeding@tu-harburg.de
Volker Bertram, Volker.bertram@ensieta.fr